

PREPARED FOR SUBMISSION TO JHEP

Scale setting and the light baryon spectrum in $N_f = 2 + 1$ QCD with Wilson fermions



Gunnar S. Bali,^a Sara Collins,^a Peter Georg,^a Daniel Jenkins,^a Piotr Korcyl,^b
Andreas Schäfer,^a Enno E. Scholz,^a Jakob Simeth,^a Wolfgang Söldner,^a
Simon Weishäupl^a

^a*Institut für Theoretische Physik, Universität Regensburg,
93040 Regensburg, Germany.*

^b*Institute of Theoretical Physics, Jagiellonian University,
ul. Łojasiewicza 11, 30–348 Kraków, Poland.*

E-mail: gunnar.bali@ur.de, sara.collins@ur.de, peter.georg@ur.de,
daniel.jenkins@ur.de, piotr.korcyl@uj.edu.pl, andreas.schaefer@ur.de,
enno.scholz@ur.de, jakob.simeth@ur.de, wolfgang.soeldner@ur.de,
simon.weishaeupl@ur.de

ABSTRACT: We determine the light baryon spectrum on ensembles generated by the Coordinated Lattice Simulations (CLS) effort, employing $N_f = 2 + 1$ flavours of non-perturbatively improved Wilson fermions. The hadron masses are interpolated and extrapolated within the quark mass plane, utilizing three distinct trajectories, two of which intersect close to the physical quark mass point and the third one approaching the SU(3) chiral limit. The results are extrapolated to the continuum limit, utilizing six different lattice spacings ranging from $a \approx 0.10$ fm down to below 0.04 fm. The light pion mass varies from $M_\pi \approx 429$ MeV down to 127 MeV. In general, the spatial extent is kept larger than four times the inverse pion mass and larger than 2.3 fm, with additional small and large volume ensembles to investigate finite size effects. We determine the Wilson flow scales $\sqrt{t_{0,\text{ph}}} = 0.1449^{(7)}_{(9)}$ fm [1] and $t_0^* \approx t_{0,\text{ph}}$ [2] from the octet cascade (Ξ baryon). Determining the light baryon spectrum in the continuum limit, we find the nucleon mass $m_N = 941.7^{(6.5)}_{(7.6)}$ MeV and the other stable baryon masses to agree with their experimental values within sub-percent level uncertainties. Moreover, we determine SU(3) and SU(2) chiral perturbation theory low energy constants, including the octet and the Ω baryon sigma terms $\sigma_{\pi N} = 43.9(4.7)$ MeV, $\sigma_{\pi \Lambda} = 28.2^{(4.3)}_{(5.4)}$ MeV, $\sigma_{\pi \Sigma} = 25.9^{(3.8)}_{(6.1)}$ MeV, $\sigma_{\pi \Xi} = 11.2^{(4.5)}_{(6.4)}$ MeV and $\sigma_{\pi \Omega} = 6.9^{(5.3)}_{(4.3)}$ MeV, as well as various parameters, renormalization factors and improvement coefficients that are relevant for simulations with our lattice action.

KEYWORDS: Lattice QCD, light baryon spectroscopy, light quark masses, baryon chiral perturbation theory, nucleon sigma term

Contents

1	Introduction	1
2	Overview of the ensembles	4
3	Wilson flow scales and the determination of action-specific parameters	11
3.1	Order a improvement of the coupling constant	11
3.2	The critical hopping parameter and combinations of renormalization constants and improvement coefficients	13
3.3	The scale parameter t_0	17
3.4	The quark mass dependence of the t_0 - and the t_0^*/a^2 -values	19
3.4.1	Survey of the t_0/a^2 data	20
3.4.2	Interpolating formula for t_0^*/a^2	21
3.4.3	Global interpolation of t_0/a^2	22
3.5	Summary of the main results for t_0 , a and the low energy constant k_1	25
3.6	The symmetric point parameters	26
4	Physical point extrapolation strategy	29
4.1	The continuum limit	29
4.2	Parametrization of the quark mass, lattice spacing and volume dependence	31
4.3	Finite size effects	33
5	The continuum limit dependence of baryon masses on the meson masses	35
5.1	Linear: NLO BChPT	35
5.2	BChPT: NNLO BChPT	37
5.3	Octet-decuplet BChPT: including the small scale expansion	39
5.4	GMO: Taylor expansion about an SU(3) symmetric point	40
6	Results for the scale $t_{0,\text{ph}}$, the spectrum and the low energy constants	42
6.1	Fits carried out and the naming conventions used	42
6.2	Fit strategy and data cuts	43
6.3	Illustration of the scale setting procedure	44
6.4	Determination of the scale parameter $\sqrt{8t_{0,\text{ph}}}$	47
6.5	The baryon spectrum	51
6.6	The σ terms of the octet baryons and the Ω baryon	57
6.7	SU(3) and SU(2) (H)BChPT low energy constants	59
6.8	Discussion of $t_{0,\text{ph}}$, the baryon spectrum and $\sigma_{\pi N}$	64
7	Summary of the main results	67
7.1	Results that are specific to the lattice action	67
7.2	The σ terms and the BChPT low energy constants	68
7.3	The scale parameter t_0	69

7.4	The light baryon spectrum	70
8	Conclusions and outlook	72
A	Correcting for electrical and mass isospin breaking effects	73
B	Finite size effects on baryon masses	76
C	The σ terms	78
C.1	The σ terms from the meson mass dependence	79
C.2	Impact of corrections to the GMOR relations on the σ terms	80
D	SU(2) BChPT low energy constants	83
E	Details of the spectrum and quark mass determinations	84
E.1	Hadron interpolators and smearing	84
E.2	Source positions and extraction of the masses	88
E.3	Tables of the masses and t_0/a^2	95
F	Statistical analysis	100
F.1	Resampling: jackknife and bootstrap analysis	100
F.2	Binning and autocorrelation times	103
F.3	Examples of infinite bin size extrapolations	106
F.4	Least squares fits with errors on the arguments and priors	111
G	HMC simulation parameters and reweighting towards the target action	112
G.1	Technical HMC parameters	114
G.2	Reweighting	114

1 Introduction

Lattice QCD calculations have become indispensable for the theoretical understanding of Standard Model processes and beyond that involve reactions with quarks that are bound inside hadrons. An essential step in the analysis is the scale setting, assigning a physical value to the lattice spacing a . This is achieved by equating a lattice observable, computed at the physical point in terms of the quark masses, to the corresponding experimental value. Ideally, both the experimental value and the results of the lattice simulations should be known as precisely as possible. Some of the most accessible of such observables are hadron masses and decay constants. In the past, for instance the Ω baryon mass [3–8], the Ξ baryon mass [9, 10], the nucleon mass [11, 12], the average octet baryon mass [13], bottomonium mass splittings [14], the pion decay constant [12, 15, 16], the kaon decay constant [17] and combinations of the pion and kaon decay constants [2, 18–20] were employed to set the scale.

Basing the scale setting on pseudoscalar decay constants assumes knowledge of the Cabibbo–Kobayashi–Maskawa (CKM) matrix elements V_{ud} or V_{us} . Moreover, extracting decay constants from experimental decay rates of electrically charged particles requires some understanding of the role of electromagnetic interactions and soft photons (for a discussion in the context of Lattice QCD, see, e.g., refs. [21–23]). Pseudoscalar decay constants can, however, be determined with high statistical accuracy. Regarding the spectrum of hadrons that do not undergo strong decay, the experimental input is cleaner. However, for heavy-light meson or quarkonium masses also the heavy quark mass needs to be matched to experiment and, to achieve a controlled continuum limit, very fine lattice spacings are required, whereas for light baryon masses the statistical errors are a limiting factor.

Often results are not available exactly at the physical point so that an extrapolation or an interpolation is required. In view of this, it is useful to introduce an intermediate scale parameter to relate between different lattice spacings, that can be determined very precisely, shows little dependence on the quark masses and can be computed at a reference point in the quark mass (hyper)plane where simulations are computationally more affordable than at the physical point. For an overview of different reference scale parameters, see ref. [24]. One such quantity is the Wilson flow scale t_0 [1] and, in particular, its value t_0^* [2], obtained at equal quark masses for a reference value of the squared pion mass in units of t_0 . One can use the combination a^2/t_0^* to translate between different lattice spacings, however, to determine the physical scale and the correct quark mass values, experimental input is still required. Here we determine the combination $\sqrt{t_{0,\text{ph}}}m_\Xi$ at the experimental values of M_π/m_Ξ and M_K/m_Ξ (where m_Ξ , M_π and M_K are the masses of the Ξ baryon, the pion and the kaon, respectively) in the continuum limit. This procedure assigns physical units to the lattice scale $t_{0,\text{ph}}$ and, extrapolating the ratio $t_0^*/t_{0,\text{ph}}$ to the continuum limit, also to t_0^* .

Apart from setting the scale, the light baryon spectrum in itself and its dependence on the light and strange quark masses are of great interest: comparison with experiment serves as a check that all systematics for the lattice setup are under control, before more complicated observables are considered, while from the quark mass dependence the validity ranges of chiral effective theories can be estimated and the related low energy constants (LECs) determined. There exists a long history of lattice studies of the light hadron spectrum including baryons, starting with calculations in the quenched approximation [25–40], with $N_f = 4$ [41, 42] and $N_f = 2$ [43–55] mass-degenerate sea quark flavours, with $N_f = 2 + 1$ flavours [3, 9, 10, 56–65], with $N_f = 2 + 1 + 1$ flavours [8, 66, 67] and including electromagnetic and mass isospin breaking effects [68–70]. Motivated by the fact that effects due to a charm sea quark can essentially be integrated out [71, 72], in this first high statistics study with a large number of independent gauge ensembles, covering a significant region of the parameter space in terms of the lattice spacing, quark mass combinations and the volume, we restrict ourselves to $N_f = 2 + 1$ sea quark flavours.

In terms of observables, in this article we compute the spectrum of the light baryons and flavour non-singlet pseudoscalar mesons at the physical point. In particular, we determine the masses of all positive parity octet and decuplet baryons, i.e. the N , the Σ , the Λ and the Ξ , as well as the $\Delta(1232)$, the $\Sigma^*(1385)$, the $\Xi^*(1530)$ and the Ω . We remark that our results for the Δ , the Σ^* and the Ξ^* , that strongly decay into $N\pi$, $\Lambda\pi/\Sigma\pi$ and $\Xi\pi$ in

nature, demonstrate the limitations of the conventional approach. A more refined study of strongly decaying baryons would require a finite volume scattering analysis, also including baryon-meson-type operators into the interpolator basis. In addition to determining the spectrum, we map out the dependence of the baryon masses on the pion and kaon masses in the continuum limit and determine chiral perturbation theory (ChPT) LECs as well as the baryon σ terms.

Lattice simulations require an extrapolation to the continuum and infinite volume limits. In particular, a controlled extrapolation to the continuum limit is challenging, as has been emphasized recently in ref. [73]. Clearly, several simulation points are necessary, all employing inverse lattice spacings that are larger than any of the physical scales that need to be resolved. The present computations are carried out for a multitude of quark mass combinations at six different values of the lattice spacing, ranging from $a \lesssim 0.098$ fm down to $a < 0.039$ fm, covering a factor larger than 6 in terms of a^2 . Simulating at our smallest lattice spacing at the physical pion mass while maintaining a sufficiently large volume would require a linear spatial lattice dimension larger than 150 points. In view of the computational effort, near-physical quark masses are only realized at $a \approx 0.064$ fm and $a \approx 0.085$ fm. Values of the lattice spacing even smaller than $a = 0.039$ fm may be desirable in future studies, e.g., of heavy quark physics or of nucleon structure observables that require large momenta.

Irrespective of the computational cost, in general it is difficult to tune the simulation parameters to exactly match the physical quark mass point. Therefore, usually an interpolation or extrapolation, reweighting [3, 74–76] or a Taylor expansion (computing derivatives with respect to the quark masses [2]) is carried out. We implement the first strategy. One novelty of our simulations is the excellent coverage of the plane spanned by the light and strange quark masses. Most simulations involve the light quark mass being reduced while the strange quark mass is kept almost constant. Here we combine two trajectories that intersect close to the physical point, one keeping the average quark mass constant [77, 78] and one keeping the strange quark mass approximately constant [79], which tightly constrains the extrapolation. As a by-product, we also obtain the strange and light quark masses, which will be subject of a separate publication. Additional ensembles along the symmetric $m_s = m_\ell$ line are realized that approach the SU(3) chiral limit. These are essential for the determination of ChPT LECs.

We employ $N_f = 2 + 1$ flavours of non-perturbatively order a improved Wilson fermions and the tree-level Symanzik improved gauge action. For details on the action, see ref. [78]. To avoid freezing of the topological charge at small lattice spacings [80], most ensembles utilize open boundary conditions in time [81], and, in particular, all ensembles at our smallest two values of a . In addition to the baryon spectrum and ChPT LECs, we determine a number of observables like t_0^*/a^2 , the critical hopping parameter and combinations of coefficients of order a improvement terms as functions of the lattice coupling. These are important for the planning of future simulation points.

The article is organized as follows. In section 2, an overview of the gauge ensembles analysed is provided. Then, in section 3, combinations of renormalization constants and improvement coefficients are determined, employing global fits, updating earlier results [79]

and adding new ones. In addition, the scale parameter t_0/a^2 is computed and interpolating formulae are given for a number of related quantities. In section 4, the procedure of extrapolating the baryon masses to the physical limit is explained: details of the continuum limit extrapolations (maintaining full order a improvement) are described in section 4.1, followed by section 4.2, where the extrapolation and interpolation strategy in the quark mass plane is explained, and section 4.3, where finite volume corrections are considered. In section 5, the relevant continuum limit expectations and parametrizations in terms of SU(3) LECs as well as polynomial expansions are introduced. Subsequently, in section 6, extrapolations to physical quark masses in the infinite volume continuum limit are illustrated and the lattice scale as well as the baryon spectrum are determined and the systematics are quantified. Moreover, values of the σ terms and various LECs are computed and the results discussed. The main results are then highlighted in section 7, before we conclude in section 8.

For the non-specialist reader the figures and tables of section 2 are of interest as is the general extrapolation strategy of section 4. On first reading, the reader may wish to skip section 5, which details the continuum limit parametrizations, as these are referred to in the results section 6. All the main results are summarized in section 7 with references to where to find these in the body of the article.

Several appendices are provided: expectations for hadron masses in an isospin symmetric world are given in appendix A. In appendix B the parametrizations that are used for the finite volume effects of the baryon masses are presented, whereas in appendix C the σ terms are related to the dependence of the baryon masses on the quark masses and the pseudoscalar meson masses. Moreover, some NLO LECs of mesonic SU(3) ChPT are determined. In appendix D we describe how we obtain SU(2) (H)BChPT LECs from their SU(3) (H)BChPT counterparts. In appendix E, the extraction of the masses from the relevant two-point functions is discussed in detail, illustrative examples are provided and the masses are tabulated. All the statistical methods employed are discussed in appendix F, where autocorrelations in Monte Carlo time as well as correlations between different masses within each individual ensemble are addressed. These methods are used to extract the hadron and quark masses from two-point functions and to determine fit parameters, which describe, e.g., the dependence of baryon masses on the pseudoscalar masses, the volume and the lattice spacing. Some of the technical Hybrid Monte Carlo (HMC) simulation parameters are presented in appendix G, where we also discuss how the results, obtained from simulations with a small twisted mass term, are reweighted to the target action.

2 Overview of the ensembles

As mentioned above, we employ $N_f = 2 + 1$ flavours of non-perturbatively order a improved Wilson fermions [82, 83] and the tree-level Symanzik improved gauge action [84]. For details on the action and the simulation, see ref. [78]. Since that publication many new CLS ensembles have been generated and we discuss the present status below.¹ A few ensembles

¹For an up-to-date CLS configuration status, see <https://www-zeuthen.desy.de/alpha/public-cls-nf21/>.

are also included, which are not part of the CLS effort since these have been generated using the BQCD code [85], all with periodic boundary conditions in time and equal quark masses. These are labelled as “rqcd0mn” below. Six values of the inverse coupling constant $\beta = 6/g^2$ are realized, corresponding to lattice spacings ranging from $a \approx 0.098$ fm down to $a \approx 0.039$ fm. The scale t_0^* [2], defined in section 3.3 below, was used for the conversion into physical units. Our result $\sqrt{8t_0^*} \approx 0.4097$ fm is presented in section 3.5.

For Wilson fermions the so-called vector Ward identity (or lattice) quark mass of a flavour j is related to the corresponding hopping parameter κ_j that appears in the action as follows:

$$m_j = \frac{1}{2a} \left(\frac{1}{\kappa_j} - \frac{1}{\kappa_{\text{crit}}} \right), \quad (2.1)$$

where $m_1 = m_2 = m_\ell$ and $m_3 = m_s$ are the light and strange quark masses, respectively, and κ_{crit} is the critical hopping parameter. One can also use the axial Ward identity (AWI) to define unrenormalized non-singlet AWI masses:

$$\tilde{m}_j + \tilde{m}_k = \frac{i\partial_0 \langle 0 | A_0^{jk} | \pi^{jk} \rangle}{\langle 0 | P^{jk} | \pi^{jk} \rangle}, \quad (2.2)$$

where $A_\mu^{jk} = A_\mu^{jk,0} - iac_A \partial_\mu P^{jk}$ with $A_\mu^{jk,0} = \bar{\psi}_j \gamma_\mu \gamma_5 \psi_k$ is the order a improved non-singlet axial current for flavours $j \neq k$ and $P^{jk} = \bar{\psi}_j i \gamma_5 \psi_k$ is the corresponding pseudoscalar current. The improvement constant $c_A(g^2)$ has been determined in ref. [86]. The critical value of the hopping parameter $\kappa_{\text{crit}}(g^2)$, that appears in eq. (2.1), is defined by the requirement that the lattice quark mass along the symmetric line $m_s = m_\ell$ vanishes at the same point as the AWI mass $\tilde{m}_s = \tilde{m}_\ell$. The above quark masses can be converted into renormalized quark masses \hat{m}_j in a standard continuum scheme, e.g., the $\overline{\text{MS}}$ scheme at the scale $\mu = 2$ GeV. For the AWI masses, the conversion (including order a improvement) reads

$$\hat{m}_j = \frac{Z_A}{Z_P} \left\{ 1 + a \left[3 \left(\tilde{b}_A - \tilde{b}_P \right) \bar{m} + (b_A - b_P) m_j \right] \right\} \tilde{m}_j, \quad (2.3)$$

where

$$\bar{m} := \frac{1}{3} (2m_\ell + m_s) = \frac{1}{3} \text{Tr } M \quad (2.4)$$

denotes the average sea quark mass and $\text{Tr } M$ the trace of the quark mass matrix. The ratio of axial over pseudoscalar renormalization factors $Z_A(g^2)/Z_P(\mu a, g^2)$ was, for instance, determined in ref. [87] and the mass-dependent improvement coefficients $b_A(g^2)$, $b_P(g^2)$, $\tilde{b}_A(g^2)$ and $\tilde{b}_P(g^2)$ in ref. [88]. Since these order a correction terms are numerically small, keeping \tilde{m}_s constant will result in an almost constant \hat{m}_s . Our strategy for keeping the AWI strange quark mass near its physical value was introduced in ref. [79].

Table 1: Parameters of the analysed CLS and RQCD ensembles. Mass plane trajectory, ensemble name, open (o) or (anti-)periodic (p) boundary conditions (bc), hopping parameter κ , the number of lattice points $N_t \cdot N_s^3$, the number of molecular dynamics units (MDUs) used in the spectrum analysis, N_{MD} , and the number of MDUs between measurements, Δ_{MD} . For the determination of t_0/a^2 and its autocorrelation time $\tau_{t_0, \text{int}}$, in some cases a larger number of MDUs and a different Δ_{MD} (in brackets) was employed. Italics indicate that the autocorrelation time is only estimated, due to a short Monte Carlo time series. The resulting t_0/a^2 -values are listed in tables 17 and 18. Ensembles A653, U103, H101, B450, H200, N202, N300 and J500 are both on the $\bar{m} = m_{\text{symm}}$ and the $m_s = m_\ell$ lines while D150 and E250 are approximately on both the $\bar{m} = m_{\text{symm}}$ and the $\hat{m}_s \approx \hat{m}_{s, \text{ph}}$ lines. For H102 there exist two runs, H102a and H102b with slightly different algorithmic parameters (H102r001 and H102r002 in table 2 of ref. [78]).

trajectory	id	bc	(κ_ℓ, κ_s)	$N_t \cdot N_s^3$	N_{MD}	Δ_{MD}	$\frac{\tau_{t_0, \text{int}}}{\text{MDU}}$
$\beta = 3.34$							
$m_s = m_\ell$	A651	p	(0.1365, 0.1365)	$48 \cdot 24^3$	20400	4	$78(\frac{15}{12})$
	A652	p	(0.1365695, 0.1365695)	$48 \cdot 24^3$	19980	4	$48(\frac{7}{6})$
	A650	p	(0.1366, 0.1366)	$48 \cdot 24^3$	18624	4	$64(\frac{12}{9})$
$\bar{m} = m_{\text{symm}}$	A653	p	(0.1365716, 0.1365716)	$48 \cdot 24^3$	20200	4	$44(\frac{6}{5})$
	A654	p	(0.13675, 0.136216193)	$48 \cdot 24^3$	20268	4	$99(\frac{27}{19})$
$\beta = 3.4$							
$m_s = m_\ell$	rqcd019	p	(0.1366, 0.1366)	$32 \cdot 32^3$	1686	1	$18(\frac{7}{4})$
	rqcd021	p	(0.136813, 0.136813)	$32 \cdot 32^3$	1541	1	$0.8(\frac{0.2}{0.2})$
	rqcd017	p	(0.136865, 0.136865)	$32 \cdot 32^3$	1849	1	$7(\frac{2}{2})$
$\bar{m} = m_{\text{symm}}$	U103	o	(0.13675962, 0.13675962)	$128 \cdot 24^3$	19800	8(4)	$44(\frac{6}{5})$
	H101	o	(0.13675962, 0.13675962)	$96 \cdot 32^3$	8000	4	$45(\frac{9}{8})$
	U102	o	(0.136865, 0.136549339)	$128 \cdot 24^3$	17680	8(4)	$53(\frac{10}{8})$
	H102a	o	(0.136865, 0.136549339)	$96 \cdot 32^3$	3720	4	$34(\frac{10}{8})$
	H102b	o	(0.136865, 0.136549339)	$96 \cdot 32^3$	3948	4	$33(\frac{8}{6})$
	U101	o	(0.13697, 0.13634079)	$128 \cdot 24^3$	6624	4	$40(\frac{10}{8})$
	H105	o	(0.13697, 0.13634079)	$96 \cdot 32^3$	7944	4	$40(\frac{6}{5})$
	N101	o	(0.13697, 0.13634079)	$128 \cdot 48^3$	5824	4	$50(\frac{12}{9})$
	S100	o	(0.13703, 0.136222041)	$128 \cdot 32^3$	3932	4	$44(\frac{19}{12})$
	C101	o	(0.13703, 0.136222041)	$96 \cdot 48^3$	9368	4	$28(\frac{4}{4})$
	D101	o	(0.13703, 0.136222041)	$128 \cdot 64^3$	1292	4	$144(\frac{2}{2})$
	D150	p	(0.137088, 0.13610755)	$128 \cdot 64^3$	2408	4	$35(\frac{20}{11})$
	H107	o	(0.13694566590798, 0.136203165143476)	$96 \cdot 32^3$	6256	4	$46(\frac{11}{8})$
	H106	o	(0.137015570024, 0.136148704478)	$96 \cdot 32^3$	6212	4	$32(\frac{5}{5})$
	C102	o	(0.13705084580022, 0.13612906255557)	$96 \cdot 48^3$	6000	4	$35(\frac{7}{6})$
$\beta = 3.46$							
$m_s = m_\ell$	rqcd029	p	(0.1366, 0.1366)	$64 \cdot 32^3$	1476	1	$22(\frac{18}{7})$
	rqcd030	p	(0.1369587, 0.1369587)	$64 \cdot 32^3$	1224	1	$20(\frac{18}{7})$
	X450	p	(0.136994, 0.136994)	$64 \cdot 48^3$	1600	4	$17(\frac{7}{5})$
$\bar{m} = m_{\text{symm}}$	B450	p	(0.13689, 0.13689)	$64 \cdot 32^3$	6448	4	$56(\frac{17}{12})$
	S400	o	(0.136984, 0.136702387)	$128 \cdot 32^3$	11488	4	$40(\frac{7}{6})$
	N401	o	(0.1370616, 0.1365480771)	$128 \cdot 48^3$	4376	4	$32(\frac{7}{6})$
	D450	p	(0.137126, 0.136420428639937)	$128 \cdot 64^3$	2488	4	$98(\frac{2}{2})$
$\tilde{m}_s = \tilde{m}_{s, \text{ph}}$	B451	p	(0.136981435679729, 0.136408545268417)	$64 \cdot 32^3$	7996	4	$44(\frac{12}{8})$

Continued on next page

Table 1: Parameters of analysed ensembles (continued).

trajectory	id	bc	(κ_ℓ, κ_s)	$N_t \cdot N_s^3$	N_{MD}	Δ_{MD}	$\frac{\tau_{t0,\text{int}}}{\text{MDU}}$
	B452	p	(0.1370455, 0.136378044)	$64 \cdot 32^3$	7772	4	$29^{(6)}_{(4)}$
	N450	p	(0.1370986, 0.136352601)	$128 \cdot 48^3$	4524	4	$43^{(16)}_{(10)}$
	D451	p	(0.13714, 0.136337761)	$128 \cdot 64^3$	1828	4	$38^{(26)}_{(13)}$
$\beta = 3.55$							
$m_s = m_\ell$	B250	p	(0.1367, 0.1367)	$64 \cdot 32^3$	1776	4	$34^{(17)}_{(11)}$
	X250	p	(0.13705, 0.13705)	$64 \cdot 48^3$	1380	4	$70^{(161)}_{(35)}$
	X251	p	(0.1371, 0.1371)	$64 \cdot 48^3$	1744	4	$53^{(64)}_{(22)}$
$\overline{m} = m_{\text{symm}}$	H200	o	(0.137, 0.137)	$96 \cdot 32^3$	8000	4	$33^{(6)}_{(5)}$
	N202	o	(0.137, 0.137)	$128 \cdot 48^3$	3536	4	$63^{(26)}_{(16)}$
	N203	o	(0.13708, 0.136840284)	$128 \cdot 48^3$	6172	4	$23^{(3)}_{(3)}$
	N200	o	(0.13714, 0.13672086)	$128 \cdot 48^3$	6848	4	$34^{(6)}_{(5)}$
	S201	o	(0.13714, 0.13672086)	$128 \cdot 32^3$	8372	4	$22^{(3)}_{(2)}$
	D200	o	(0.1372, 0.136601748)	$128 \cdot 64^3$	7996	4	$28^{(5)}_{(4)}$
	E250	p	(0.137232867, 0.136536633)	$192 \cdot 96^3$	1956	4	$67^{(114)}_{(30)}$
$\tilde{m}_s = \tilde{m}_{s,\text{ph}}$	N204	o	(0.137112, 0.136575049)	$128 \cdot 48^3$	6000	4	$45^{(11)}_{(8)}$
	N201	o	(0.13715968, 0.136561319)	$128 \cdot 48^3$	6000	4	$38^{(7)}_{(6)}$
	D201	o	(0.1372067, 0.136546844)	$128 \cdot 64^3$	4312	4	$34^{(9)}_{(7)}$
$\beta = 3.7$							
$m_s = m_\ell$	N303	o	(0.1368, 0.1368)	$128 \cdot 48^3$	2000	4	$26^{(10)}_{(7)}$
	N300	o	(0.137, 0.137)	$128 \cdot 48^3$	6080	4	$44^{(11)}_{(9)}$
$\overline{m} = m_{\text{symm}}$	N302	o	(0.137064, 0.1368721791358)	$128 \cdot 48^3$	8804	4	$41^{(7)}_{(6)}$
	J303	o	(0.137123, 0.1367546608)	$192 \cdot 64^3$	7992	8	$77^{(20)}_{(16)}$
	E300	o	(0.137163, 0.1366751636177327)	$192 \cdot 96^3$	1992	8(4)	$38^{(15)}_{(10)}$
$\tilde{m}_s = \tilde{m}_{s,\text{ph}}$	N305	o	(0.137025, 0.136676119)	$128 \cdot 48^3$	8000	4	$37^{(9)}_{(7)}$
	N304	o	(0.137079325093654, 0.136665430105663)	$128 \cdot 48^3$	6136	4	$39^{(11)}_{(8)}$
	J304	o	(0.13713, 0.1366569203)	$192 \cdot 64^3$	6076	4	$56^{(22)}_{(14)}$
$\beta = 3.85$							
$m_s = m_\ell$	N500	o	(0.13672514, 0.13672514)	$128 \cdot 48^3$	3760	4	$57^{(35)}_{(18)}$
$\overline{m} = m_{\text{symm}}$	J500	o	(0.136852, 0.136852)	$192 \cdot 64^3$	6008	8	$75^{(15)}_{(12)}$
	J501	o	(0.1369032, 0.136749715)	$192 \cdot 64^3$	5988	4	$79^{(23)}_{(16)}$

Table 2: Overview of the physical parameters of the analysed CLS and RQCD ensembles. Mass plane trajectory, ensemble name, spatial lattice extent L in physical units and in units of the pion mass as well as the pion and the kaon masses (which are volume corrected, see section 4.3). The physical units have been assigned using $\sqrt{8t_0^*} = 0.4097$ fm. Statistical errors are not shown in this overview table. The lattice spacings including errors are given in table 5, see also section 3.4 for details, while the raw pion and kaon mass data including errors can be found in tables 17 and 18.

trajectory	id	L/fm	LM_π	M_π/MeV	M_K/MeV
$\beta = 3.34, a = 0.098$ fm					
$m_s = m_\ell$	A651	2.34	6.6	556	556
	A652	2.34	5.13	432	432
	A650	2.34	4.39	371	371
$\overline{m} = m_{\text{symm}}$	A653	2.34	5.09	429	429
	A654	2.34	4.0	338	459

Continued on next page

Table 2: Physical parameter values (continued).

trajectory	id	L/fm	LM_π	M_π/MeV	M_K/MeV
$\beta = 3.4, a = 0.085 \text{ fm}$					
$m_s = m_\ell$	rqcd019	2.72	8.4	608	608
	rqcd021	2.72	4.7	340	340
	rqcd017	2.72	3.26	236	236
$\bar{m} = m_{\text{symm}}$	U103	2.04	4.35	420	420
	H101	2.72	5.85	423	423
	U102	2.04	3.7	357	445
	H102a	2.72	4.95	359	444
	H102b	2.72	4.89	354	442
	U101	2.04	2.81	271	464
	H105	2.72	3.88	281	468
	N101	4.09	5.82	281	467
	S100	2.72	2.95	214	476
	C101	4.09	4.6	222	476
	D101	5.45	6.13	222	476
	D150	5.45	3.51	127	482
$\tilde{m}_s = \tilde{m}_{s,\text{ph}}$	H107	2.72	5.09	368	550
	H106	2.72	3.77	273	520
	C102	4.09	4.62	223	504
$\beta = 3.46, a = 0.075 \text{ fm}$					
$m_s = m_\ell$	rqcd029	2.41	8.72	713	713
	rqcd030	2.41	3.9	319	319
	X450	3.62	4.86	265	265
$\bar{m} = m_{\text{symm}}$	B450	2.41	5.15	421	421
	S400	2.41	4.33	354	445
	N401	3.62	5.27	287	464
	D450	4.82	5.28	216	480
$\tilde{m}_s = \tilde{m}_{s,\text{ph}}$	B451	2.41	5.16	422	577
	B452	2.41	4.31	352	548
	N450	3.62	5.26	287	528
	D451	4.82	5.35	219	507
$\beta = 3.55, a = 0.064 \text{ fm}$					
$m_s = m_\ell$	B250	2.04	7.37	713	713
	X250	3.06	5.43	350	350
	X251	3.06	4.16	268	268
$\bar{m} = m_{\text{symm}}$	H200	2.04	4.36	422	422
	N202	3.06	6.42	414	414
	N203	3.06	5.39	348	445
	S201	2.04	3.0	290	471
	N200	3.06	4.43	286	466
	D200	4.08	4.18	202	484
	E250	6.12	4.05	131	493
$\tilde{m}_s = \tilde{m}_{s,\text{ph}}$	N204	3.06	5.48	353	549
	N201	3.06	4.44	287	527

Continued on next page

Table 2: Physical parameter values (continued).

trajectory	id	L/fm	LM_π	M_π/MeV	M_K/MeV
	D201	4.08	4.14	200	504
$\beta = 3.7, a = 0.049 \text{ fm}$					
$m_s = m_\ell$	N303	2.36	7.75	646	646
$\bar{m} = m_{\text{symm}}$	N300	2.36	5.1	425	425
	N302	2.36	4.17	348	455
	J303	3.15	4.14	259	479
	E300	4.73	4.22	176	496
$\tilde{m}_s = \tilde{m}_{s,\text{ph}}$	N305	2.36	5.14	428	584
	N304	2.36	4.24	353	558
	J304	3.15	4.18	261	527
$\beta = 3.85, a = 0.039 \text{ fm}$					
$m_s = m_\ell$	N500	1.85	5.69	604	604
$\bar{m} = m_{\text{symm}}$	J500	2.47	5.19	413	413
	J501	2.47	4.21	336	448

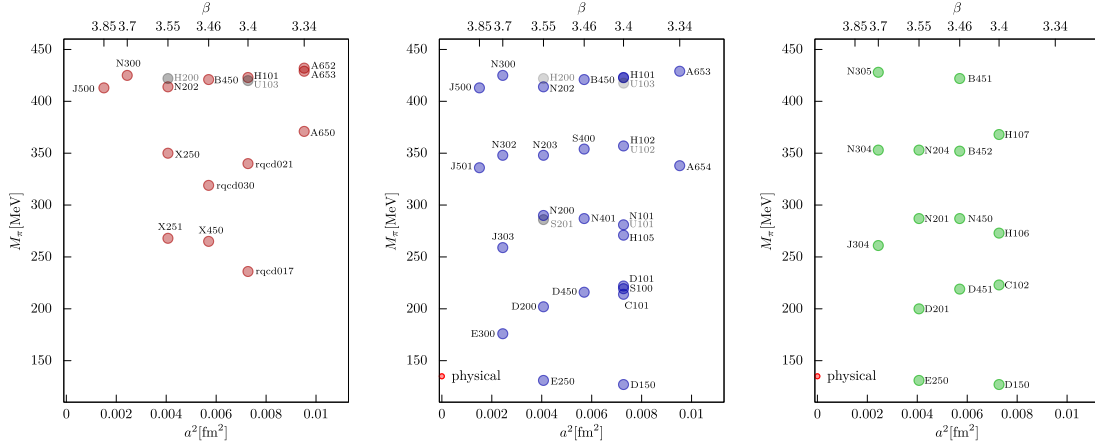


Figure 1. Overview of the analysed ensembles: three different quark mass trajectories (left: $m_s = m_\ell$, centre: $\text{Tr } M = \text{const}$, right: $\hat{m}_s \approx \text{const}$) have been analysed at six (four for $\hat{m}_s \approx \text{const}$) different lattice spacings. On the $m_s = m_\ell$ trajectory, six additional ensembles with $M_\pi > 450 \text{ MeV}$ exist (A651, rqcd019, rqcd029, B250, N303 and N500, see tables 1 and 2), which do not enter our hadron spectroscopy analysis. We also omit ensembles with $L < 2.3 \text{ fm}$ (grey circles).

At each value of β the simulations are carried out along three trajectories in the quark mass plane:

- The symmetric line: $m_s = m_\ell$, i.e. $\hat{m}_s = \hat{m}_\ell$.
- The $\text{Tr } M = \text{const}$ line: $a(2m_\ell + m_s) = 3am_{\text{symm}}$, i.e. $2\hat{m}_\ell + \hat{m}_s = \text{const} + \mathcal{O}(a)$. The constant is chosen such that the combination $(2M_K^2 + M_\pi^2)t_0^*$ is close to its physical value, assuming $\sqrt{8t_0^*} = 0.413 \text{ fm}$ [2]. The strategy of keeping the sum of quark masses constant was pioneered by QCDSF/UKQCD [77].

- The line of fixed strange quark mass: the renormalized strange quark mass is kept near its physical value [79].

We analyse a large number of ensembles along these three trajectories, most of which have open boundary conditions in time [81] in order to circumvent critical slowing down towards the continuum limit, due to the freezing of the topological charge [80]. The relevant simulation parameters are listed in table 1,² whereas the physical values of the lattice spacings, spatial lattice volumes and pseudoscalar meson masses are given in table 2. The t_0/a^2 -values are listed in tables 17 and 18 of appendix E.3. For some of the ensembles these have been determined previously [2, 78, 79]. In all these cases, within statistical errors, our determination agrees with the previous ones. An overview of the ensembles is shown in figure 1. Figure 2 illustrates our coverage of the quark mass plane within the region of interest.

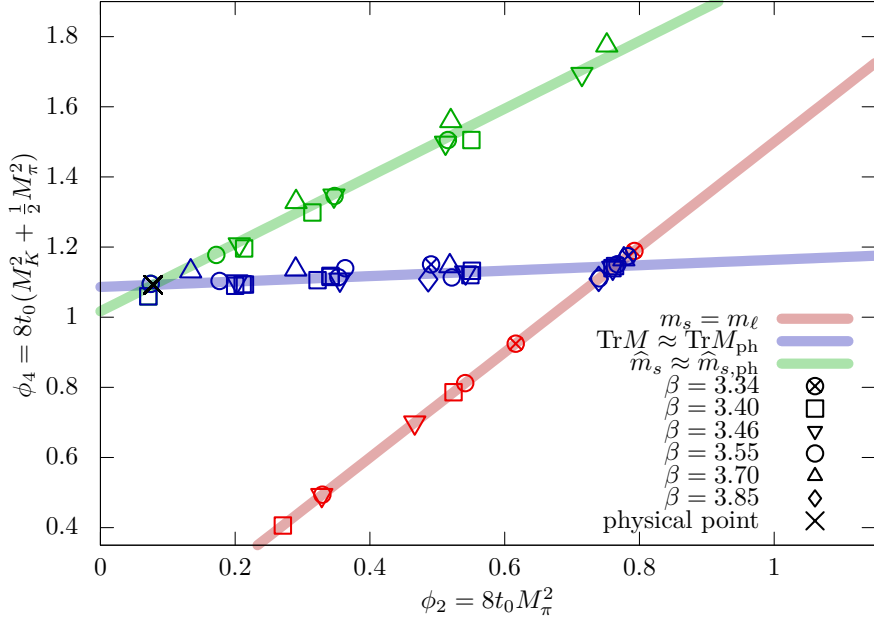


Figure 2. Overview of the analysed ensembles in the quark mass plane. The ordinate is (approximately) proportional to \hat{m}_ℓ , the abscissa to $2\hat{m}_\ell + \hat{m}_s$. The $\hat{m}_s \approx \text{const}$ and the $\text{Tr } M = \text{const}$ trajectories intersect close to the physical point (black cross), while the latter trajectory starts from the point on the symmetric $m_s = m_\ell$ line, where $M_\pi = M_K \approx 411$ MeV.

With three exceptions (rqcd017 for $m_s = m_\ell$, D150 for $\text{Tr } M = \text{const}$ and H106 for $\hat{m}_s \approx \text{const}$), at least one ensemble exists at each simulation point with a spatial lattice extent $L = N_s a > \max\{4/M_\pi, 2.3 \text{ fm}\}$. In some cases additional volumes were generated to enable the study of finite volume effects. Figure 3 provides an overview regarding this: the dark green areas correspond to $LM_\pi > 5$, light green to $5 \geq LM_\pi > 4$, yellow to $4 \geq LM_\pi$ and red to $L < 2.3 \text{ fm}$.

²The time $\tau_{t_0, \text{int}}$ is the largest autocorrelation time for the observables we have studied. It may be close to the exponential autocorrelation time of the system, see appendices F.2 and F.3.

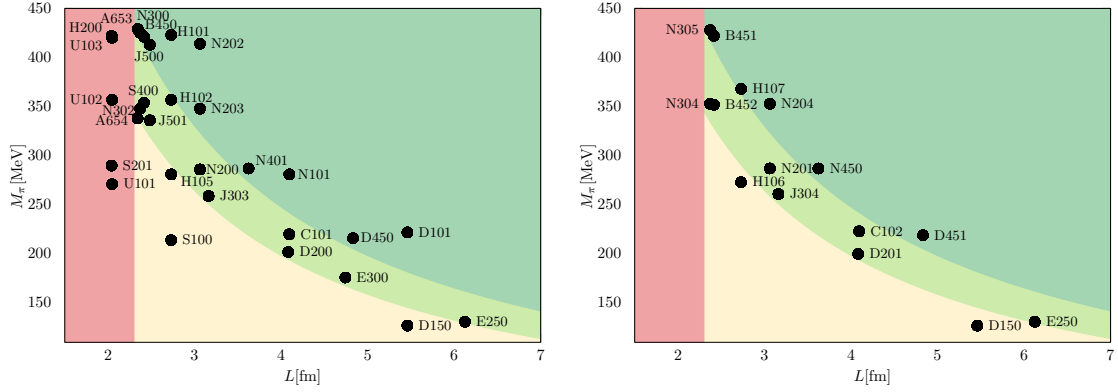


Figure 3. The spatial lattice extents L and the pion masses M_π for the two quark mass trajectories leading to the physical point. The coloured regions distinguish between $LM_\pi \leq 4$ (yellow), $4 < LM_\pi \leq 5$ (light green), $5 < LM_\pi$ (dark green) and $L < 2.3$ fm (red).

As mentioned above, details on the simulations performed by CLS using the OPENQCD code [89]³ can be found in ref. [78]. In appendix G we discuss the technical parameters for some of the more recently performed simulations.

3 Wilson flow scales and the determination of action-specific parameters

We start with a brief discussion of some of the subtleties related to order a improvement, before we determine the critical hopping parameter values and combinations of some of the relevant renormalization constants and improvement parameters. We then determine a reference point in the quark mass plane and compute different observables related to the scale parameter t_0 [1]. We give interpolating formulae for the dependence of all these quantities on g^2 and determine the continuum limit dependence of t_0 on the pseudoscalar masses. For each lattice spacing, the $\text{Tr } M = \text{const}$ trajectory starts from a point where $m_s = m_\ell$ and we determine the optimal start value for this trajectory to intersect the physical point. Finally, we determine the values κ^* and am^* associated with a reference point on the symmetric line, where t_0^* is defined.

3.1 Order a improvement of the coupling constant

The simulations are carried out at fixed values of the bare coupling $g^2 = 6/\beta$, however, the coupling undergoes order a improvement [90, 91],

$$\tilde{g}^2 = \tilde{g}^2(g^2, a\bar{m}) := g^2 [1 + b_g(g^2)a\bar{m}] , \quad (3.1)$$

with an as yet unknown improvement coefficient function $b_g(g^2)$. In order to implement order a Symanzik improvement, when varying the average quark mass \bar{m} , naively one would keep \tilde{g}^2 fixed, as is assumed, e.g., in ref. [92]. Since $b_g > 0$ (at least in perturbation theory) this means g^2 should be reduced as \bar{m} is increased. We find this impractical and instead

³Publicly available at <http://luscher.web.cern.ch/luscher/openQCD>.

keep g^2 fixed, thereby changing the improved coupling \tilde{g}^2 as $a\bar{m}$ is varied. As a result of this choice, the lattice spacing — although defined in the $N_f = 3$ chiral limit — acquires a dependence on $a\bar{m}$: $a(\tilde{g}^2) = a(\tilde{g}^2(g^2, a\bar{m}))$. We can determine the order a difference between this lattice spacing, corresponding to a fixed value of the improved coupling \tilde{g}^2 , and that corresponding to a constant g^2 , $a(g^2)$, by expanding

$$a(\tilde{g}^2) = a(g^2(1 + b_g a\bar{m})) = a(g^2)(1 + b_a a\bar{m} + \dots). \quad (3.2)$$

Integrating the β -function gives⁴

$$a(g^2)\Lambda_L = h(g^2) = \exp\left[-\frac{8\pi^2}{\beta_0 g^2} - \frac{\beta_1}{2\beta_0^2} \ln \frac{\beta_0 g^2}{16\pi^2} + \mathcal{O}(g^2)\right]. \quad (3.3)$$

Plugging $a(\tilde{g}^2)$ into this equation allows us to relate b_a and b_g :

$$b_a(g^2) = \frac{d \ln h(g^2)}{d g^2} g^2 b_g(g^2). \quad (3.4)$$

The one-loop result $b_g^{(1)} = 0.012000(2)N_f g^2$ [91], setting $N_f = 3$, translates into

$$b_a^{(1)} = \frac{8\pi^2}{\beta_0 g^2} b_g^{(1)} = 0.31583(5). \quad (3.5)$$

For simplicity of notation, below we will refer to $a(\tilde{g}^2)$ as a while we refer to the lattice spacing that we will approach in the chiral limit when keeping g^2 fixed as a_0 , i.e.

$$a_0(g^2) = a(\tilde{g}^2(g^2, a\bar{m}))(1 - b_a a\bar{m}). \quad (3.6)$$

Hadron masses determined in lattice units Ma are subject to quark mass-dependent order a effects since we do not simulate at fixed values of \tilde{g}^2 , whereas combinations $Ma_0 = Ma(1 - b_a a\bar{m})$ are free of such contributions. In the analysis we will use dimensionless combinations of physical observables to circumvent this complication. This is necessary to maintain order a improvement when including points in the quark mass plane that are not on the $\text{Tr } M = \text{const}$ trajectory. Another subtle issue concerns the definition of quark masses in the lattice scheme eq. (2.1). In this case κ_{crit} as a function of the improved coupling \tilde{g}^2 should be used. Nevertheless, we employ $\kappa_{\text{crit}}(g^2)$. The difference is of order $g^4 a\bar{m}$ and can be absorbed into the definition of the improvement coefficients \tilde{b}_m and \tilde{d}_m [79].

Finally, we remark that keeping g^2 fixed rather than \tilde{g}^2 means that we use the renormalization constant $Z_J(g^2)$ to renormalize a current $J(g^2, am_\ell, am_s)$, instead of $Z_J(\tilde{g}^2(g^2, a\bar{m}))$ in equations such as eq. (2.3). This substitution can be implemented consistently but alters some of the $\mathcal{O}(a)$ terms, as discussed in refs. [79, 88, 93]. Again, we remark that Z_J remains the same function of g^2 but, unlike ref. [92], we keep its argument constant as the quark masses are varied.

⁴ Λ_L is the QCD Λ parameter in the lattice scheme defined by our action and we use the normalization

$$\beta_0 = 11 - \frac{2}{3}N_f = 9, \quad \beta_1 = 102 - \frac{38}{3}N_f = 64.$$

3.2 The critical hopping parameter and combinations of renormalization constants and improvement coefficients

Following ref. [79], we parameterize the dependence of the AWI quark masses on the hopping parameter values as follows,

$$a\tilde{m}_s - a\tilde{m}_\ell = \frac{Z}{2} \left(\frac{1}{\kappa_s} - \frac{1}{\kappa_\ell} \right) \left[1 - \frac{\mathcal{A}}{12} \left(\frac{1}{\kappa_s} - \frac{1}{\kappa_\ell} \right) - \mathcal{B}_0 a\overline{m} \right], \quad (3.7)$$

$$a\overline{\tilde{m}} = r_m Z \left[a\overline{m} - \frac{\mathcal{C}_0}{36} \left(\frac{1}{\kappa_s} - \frac{1}{\kappa_\ell} \right)^2 - \frac{\mathcal{D}_0}{2} (a\overline{m})^2 \right]. \quad (3.8)$$

The two AWI quark mass combinations on the left hand sides, at each value of β , depend on six parameters: Z , $r_m Z$, κ_{crit} (implicit in the average lattice quark mass), \mathcal{B}_0 , \mathcal{C}_0 and \mathcal{D}_0 , while \mathcal{A} is already known non-perturbatively [88, 93]. The combination of flavour non-singlet renormalization constants Z is defined as

$$Z = \frac{Z_m Z_P}{Z_A} = 1 + 0.05274 C_F g^2 + \mathcal{O}(g^4), \quad (3.9)$$

where the one-loop result was obtained in refs. [94, 95] and $C_F = 4/3$. While flavour non-singlet combinations of lattice quark masses renormalize with $Z_m = Z_S^{-1}$, the average sea quark mass renormalizes with $Z_m^s = r_m Z_m$, for details, see, e.g., refs. [79, 92].

The parameters \mathcal{A} , \mathcal{B}_0 , \mathcal{C}_0 and \mathcal{D}_0 are normalized such that these are unity in the free field case. They correspond to combinations of improvement coefficients that are defined in ref. [92] (for the difference between \tilde{b}_P and \bar{b}_P etc., see refs. [79, 93]):

$$\mathcal{A} = b_P - b_A - 2b_m, \quad (3.10)$$

$$\mathcal{B}_0 = -(r_m + 1)(b_P - b_A) - 2b_m - 3(\tilde{b}_P - \tilde{b}_A + \tilde{b}_m), \quad (3.11)$$

$$\mathcal{C}_0 = -\frac{1}{2r_m}(b_P - b_A) - 2d_m, \quad (3.12)$$

$$\mathcal{D}_0 = -2(b_P - b_A + d_m) - 6(\tilde{b}_P - \tilde{b}_A + \tilde{d}_m). \quad (3.13)$$

The combination \mathcal{A} has been determined in ref. [93] and is not fitted here. Also \mathcal{B}_0 was computed in this reference, however, we choose to re-determine this here. We repeat the analysis of ref. [79] and obtain the values displayed in table 3. The larger set of ensembles at our disposal enables us to fit all the parameters. In general \mathcal{D}_0 is not well constrained by the data. In order to discriminate Z from the combination $Z\mathcal{B}_0$, at least two ensembles with $m_s \neq m_\ell$ at different values of $2m_\ell + m_s$ are necessary. Such sets of ensembles are not available at $\beta = 3.34$ and $\beta = 3.85$, where the number of different ensembles is smaller than at the intermediate four lattice spacings. Therefore, in these cases we estimate \mathcal{B}_0 , extrapolating from the other lattice spacings as described below. At $\beta = 3.85$, in addition \mathcal{C}_0 is obtained from an extrapolation. We then use these values and their errors as input. At $\beta = 3.85$ we also vary $\mathcal{D}_0 = 1 \pm 10$. The input parameter variations are implemented as pseudo-bootstrap samples in the cases of \mathcal{A} , \mathcal{B}_0 and \mathcal{D}_0 while we can add the constraint on \mathcal{C}_0 as a prior, without overly biasing the result. Different combinations of extrapolating some parameters and fitting the remaining ones were carried out, with consistent results.

Table 3. Results of fits to our AWI quark mass data according to eqs. (3.7) and (3.8). The \mathcal{A} -values were determined in ref. [93]. In addition to the fit parameters obtained separately at each β -value, we list the results from the global interpolations eqs. (3.17), (3.18), (3.19) and (3.21) as “(int)”. In the cases where the reduced χ^2 -value turned out to be larger than one, we multiplied our errors with its square root. Due to the smaller number of ensembles available, determining the parameters B_0 and C_0 via such a fit was not possible at $\beta = 3.85$, while B_0 could not be predicted at $\beta = 3.34$. Therefore, in these cases the result from the interpolation, obtained at the remaining five or four lattice spacings, was used as an input. At $\beta = 3.85$, in addition, we constrained $\mathcal{D}_0 = 1 \pm 10$. The values for $\beta = 3.4$ and 3.55 below supersede those that we published in ref. [79]. We also include an independent determination of r_m [96], interpolated to the same lattice spacings, for comparison.

β	3.34	3.4	3.46	3.55	3.7	3.85
χ^2/N_{DF}	1.8/2	41.1/13	32.6/11	20.9/12	13.0/8	3.9/1
Z	0.8061(218)	0.8705(127)	0.9186(84)	0.9819(41)	1.0514(19)	1.0843(23)
Z (int)	0.7924(167)	0.8681 (88)	0.9246(56)	0.9857(41)	1.0493(26)	1.0861(28)
r_m	3.818(958)	2.625(156)	1.848(65)	1.550(15)	1.300(14)	1.170(117)
r_m (int)	4.594(551)	2.437 (68)	1.879(23)	1.541(12)	1.317 (9)	1.216(35)
r_m [96]		2.335 (31)	1.869(19)	1.523(14)	1.267(16)	1.149(33)
κ_{crit}	0.1366944(218)	0.1369112(45)	0.1370657(28)	0.1371709(11)	0.1371532(14)	0.1369768(84)
κ_{crit} (int)	0.1366938(45)	0.1369153 (9)	0.1370613(10)	0.1371715(10)	0.1371530 (9)	0.1369767(26)
\mathcal{A}	2.058(49)	2.026(47)	1.995(45)	1.952(43)	1.886(40)	1.828(37)
\mathcal{B}_0		-1.11(3.20)	-1.56(1.62)	-1.17(83)(1)	0.11(36)	
\mathcal{B}_0 (int)	-4.41(6.78)	-2.42(2.26)	-1.44(95)	-0.65(42)	-0.01(33)	0.32(31)
\mathcal{C}_0	5.42(69)	4.03(30)	2.57(42)	2.45(20)	2.10(33)	
\mathcal{C}_0 (int)	5.60(58)	3.80(19)	3.04(16)	2.47(14)	2.02(11)	1.79(9)
\mathcal{D}_0	-31(542)	6(14)	-5(7)	2.7(1.3)	4.8(2.1)	

We will use the interpolated results “(int)” of table 3 in our analysis. The parameters \mathcal{B}_0 and \mathcal{C}_0 start out at very small and very large values, respectively, but steadily approach unity as β is increased. In the case of \mathcal{D}_0 the $\beta < 3.55$ results are compatible with zero within their large errors as the data are not very sensitive with respect to this parameter. Only at $\beta \geq 3.55$ we are able to obtain positive, non-zero values.

For our action to one-loop order [94] the above combinations of improvement coefficients read [79]⁵

$$\mathcal{A} = 1 + 0.1538(2) g^2, \quad (3.14)$$

$$\mathcal{B}_0 = \mathcal{D}_0 = 1 + 0.1501(4) g^2, \quad (3.15)$$

$$\mathcal{C}_0 = 1 + 0.1520(2) g^2. \quad (3.16)$$

This motivates fits of $\mathcal{O} \in \{\mathcal{B}_0, \mathcal{C}_0\}$ to the interpolating ansatz:

$$\mathcal{O} = 1 + b_{\mathcal{O}}^{\text{one-loop}} g^2 \frac{1 + \gamma_{\mathcal{O}} g^2}{1 + \delta_{\mathcal{O}} g^2}. \quad (3.17)$$

⁵There is one subtlety here: it turns out that the effect of b_g already propagates at $\mathcal{O}(g^2)$ into the \tilde{b}_J and \tilde{d}_J improvement coefficients for currents with an anomalous dimension, see Ref. [93] for details. However, since $\tilde{b}_m = -\tilde{b}_S$ and $2\tilde{d}_m + 6\tilde{d}_m = -b_S - 3\tilde{b}_S - 3\tilde{d}_S$, the anomalous dimension contributions cancel from the combinations \mathcal{B}_0 and \mathcal{D}_0 , as they should.

Table 4. Parameters of fits of the $3.4 \leq \beta \leq 3.7$ data to eq. (3.17), using the one-loop coefficients of ref. [94], see eqs. (3.15) and (3.16).

Coefficient	$b_{\mathcal{O}}^{\text{one-loop}}$	$\gamma_{\mathcal{O}}$	$\delta_{\mathcal{O}}$	$\text{cov}(\gamma_{\mathcal{O}}, \delta_{\mathcal{O}})$
\mathcal{B}_0	0.1501	$-0.946(223)$	$-0.537(34)$	-0.918
\mathcal{C}_0	0.1520	$-0.308(48)$	$-0.542(4)$	0.928

The resulting fit parameters are displayed in table 4. For the \mathcal{B}_0 interpolation we obtain $\chi^2/N_{\text{DF}} = 0.67/2$ and for \mathcal{C}_0 $\chi^2/N_{\text{DF}} = 1.99/3$. In figure 4 we show the data for \mathcal{B}_0 and \mathcal{C}_0 , along with the interpolating parametrizations eq. (3.17) and the one-loop expectations, which are indistinguishable on the scale of the figure. We also include the parametrization $\mathcal{A} = 1 + 0.1538 g^2 + 0.242(15) g^4$ of ref. [93]. The non-perturbatively determined values differ substantially from the one-loop expectations (grey curves).

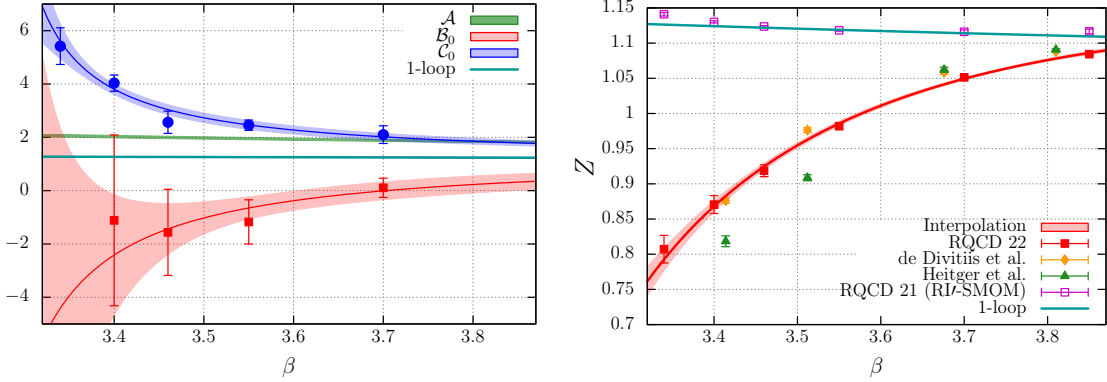


Figure 4. Left: \mathcal{A} [93], \mathcal{B}_0 and \mathcal{C}_0 along with the one-loop expectations (3.14)–(3.16) and the parametrization eq. (3.17) with the parameter values of table 4. Right: the renormalization constant combination $Z = Z_m Z_P / Z_A$, together with the one-loop expectation and the parametrization eq. (3.18). Also shown are the “LCP-0” results for Z of ref. [97] (de Divitiis et al.) and the “ $Z^{(T/3)}$ ” definition of ref. [96] (Heitger et al.) as well as the RI'-SMOM determination of ref. [98] (RQCD 21), using “ Z'_A ”, with leading lattice artefact subtraction and the fixed scale method.

In the right panel of figure 4 we show our data for $Z = Z_m Z_P / Z_A$ in comparison to different literature results [96–98]. Up to order a^2 effects, the different sets should approach each other towards large β -values. For instance, in figure 20 of ref. [98] it has been demonstrated that the ratios between the results for Z from refs. [98] and [97] are consistent with this expectation, when plotted as a function of a^2 . We note that the former non-perturbative set of results, obtained using the RI'-SMOM scheme (RQCD 21 [98]), is quite close to the one-loop expectation but differs substantially from the three other sets within our window of β -values. For $3.34 \leq \beta \leq 3.85$, our data for Z can be parameterized

with $\chi^2/N_{\text{DF}} = 3.79/3$ as follows:

$$Z(g^2) = 1 + 0.07032 g^2 \frac{1 + 0.4896 g^2 - 0.6473 g^4}{1 - 0.4857 g^2}. \quad (3.18)$$

We refrain from stating the covariance matrix and the errors of the fit parameters, however, the accuracy of the interpolation (about 1% at $\beta = 3.4$ and 2‰ at $\beta = 3.7$) can be read off table 3. We also show the above interpolation in the figure.

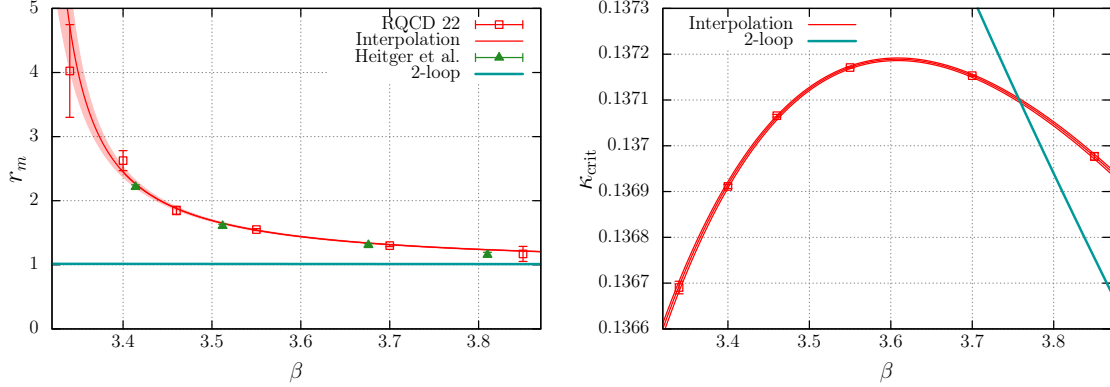


Figure 5. Left: the ratio of the singlet over the non-singlet quark mass renormalization constant $r_m = Z_m^s/Z_m$, along with the parametrization eq. (3.19) and the two-loop expectation. Also shown is the recent determination of ref. [96], using their “ $\nu, Z, T/3$ ” prescription. Right: the critical hopping parameter κ_{crit} , together with the interpolation eq. (3.21) and the two-loop expectation eq. (3.20).

Regarding r_m , we obtain the interpolation

$$r_m(g^2) = 1 + 0.004630 g^4 \frac{1 + 0.128(72) g^2}{1 - 0.5497(13) g^2}, \quad (3.19)$$

where the two-loop coefficient 0.004630(2) was computed in ref. [99]. We obtain $\chi^2/N_{\text{DF}} = 3.91/4$ and the correlation between the two fit parameters reads 0.844. The numerical values are compiled in table 3. The result is also shown, along with the interpolating formula and the two-loop expectation, in the left panel of figure 5. We compare this to the recent determination of Heitger et al. [96]. The two sets can in principle, differ by order a^2 effects. With the exception of $\beta \approx 3.7$, the data sets are compatible with one another (see table 3), however, the respective interpolations intersect (not shown). Note that — similarly to r_m — also the data for Z of Heitger et al. cross our results inbetween $\beta = 3.512$ and $\beta = 3.676$, as can be seen in figure 4. The error obtained at $\beta = 3.85$ for our interpolation was quite small compared to the actually measured uncertainty at this point (0.007 vs. 0.117). This is due to the perturbation theory constraint for $\beta \rightarrow \infty$. Therefore, to be on the safe side, we inflated the error given for the interpolation of r_m at this end point by a factor of five to bring this more in line with the statistical uncertainties.

The critical hopping parameter for our action is known to two-loops [100]: for the one-loop coefficient we insert the values of table II into eq. (20) of that reference, setting $c_{\text{sw}} = 1$. At the two-loop level we combine this result with the one-loop correction to c_{sw} ,

$0.19624449(1)g^2$ [101] (see also ref. [102]), and add the two-loop results of tables III–VII of ref. [100], setting $c_{\text{sw}} = 1$ and $c_2 = 0$:

$$\frac{1}{\kappa_{\text{crit}}} = 8 - 0.402453622(12)g^2 - 0.024893(5)g^4 + \mathcal{O}(g^6). \quad (3.20)$$

We use these results to fit κ_{crit} :

$$\frac{1}{\kappa_{\text{crit}}} = 8 - 0.402454g^2 \frac{1 + 0.28955g^2 - 0.1660g^6}{1 + 0.22770g^2 - 0.2540g^4}. \quad (3.21)$$

This interpolation with $\chi^2/N_{\text{DF}} = 3.67/3$, also shown in figure 5, is valid for $3.34 \leq \beta \leq 3.85$ and has the two-loop asymptotic large β limit built in. Its relative accuracy ranges from approximately $3 \cdot 10^{-5}$ at $\beta = 3.34$ to $2 \cdot 10^{-5}$ at $\beta = 3.85$ and is more precise inbetween these end points. The relevant numbers are included in table 3. The slow approach towards the two-loop expectation is striking.

Note again that Z and $r_m = r_m Z/Z$ can differ by $\mathcal{O}(a^2)$ terms if determined following a different prescription while the improvement coefficients \mathcal{A} , \mathcal{B}_0 , \mathcal{C}_0 and \mathcal{D}_0 have ambiguities of order a .

3.3 The scale parameter t_0

The parameter t_0 , introduced in ref. [1], corresponds to the Wilson flow time t at which the equality

$$t^2 E(t)|_{t=t_0} = 0.3, \quad E(t) = \frac{1}{V_4} \int_{V_4} d^4x \frac{1}{4} G_{\mu\nu}^a(x, t) G_{\mu\nu}^a(x, t) \quad (3.22)$$

holds, where we employ the clover leaf definition of the average action density $E(t)$ and the integration scheme of ref. [1]. For lattices with open boundary conditions in time, $E(t)$ is only averaged over the central temporal region of the lattice, $V_4 \approx 1 \text{ fm} \cdot (aN_s)^3$. Otherwise, we employ the whole lattice volume $V_4 = a^4 N_t N_s^3$. In figure 6 we show the Monte Carlo history in MDUs of $E(t)$ at $t \approx t_0$,⁶ for different ensembles with $M_\pi \approx 350 \text{ MeV}$ along the $\text{Tr } M = \text{const}$ line, see figure 1. The lattice spacing decreases from the left ($a \approx 0.098 \text{ fm}$) to the right ($a \approx 0.039 \text{ fm}$). This observable is known to have very large autocorrelation times [81] and indeed some slowing down is clearly visible. Nevertheless, even at the finest lattice spacing we are able to sufficiently sample the action density at this flow time.

Using an intermediate scale derived from t_0 to translate between different lattice spacings is a convenient choice since all its mass dependence is due to sea quark effects. Therefore, one would expect t_0/a^2 to vary only moderately at each β -value. At the same time the t_0/a^2 -values carry tiny statistical errors. In section 3.4 we study the quark mass dependence of t_0/a^2 and find that in the continuum limit this combination remains constant along trajectories where the sum of quark masses is kept fixed, within our present uncertainties.

We introduce four related scales:

- The ratio $t_{0,\text{symm}}/a^2$ refers to t_0 in lattice units at the point along our $\text{Tr } M = \text{const}$ lines where $m_s = m_\ell$. Note that $t_{0,\text{symm}}$ (in physical units) differs slightly between different β -values.

⁶Note that the data shown are only approximately at $t = t_0$. In the actual scale setting analysis we interpolate $E(t)$ between available flow times to determine the correct value of t_0/a^2 .

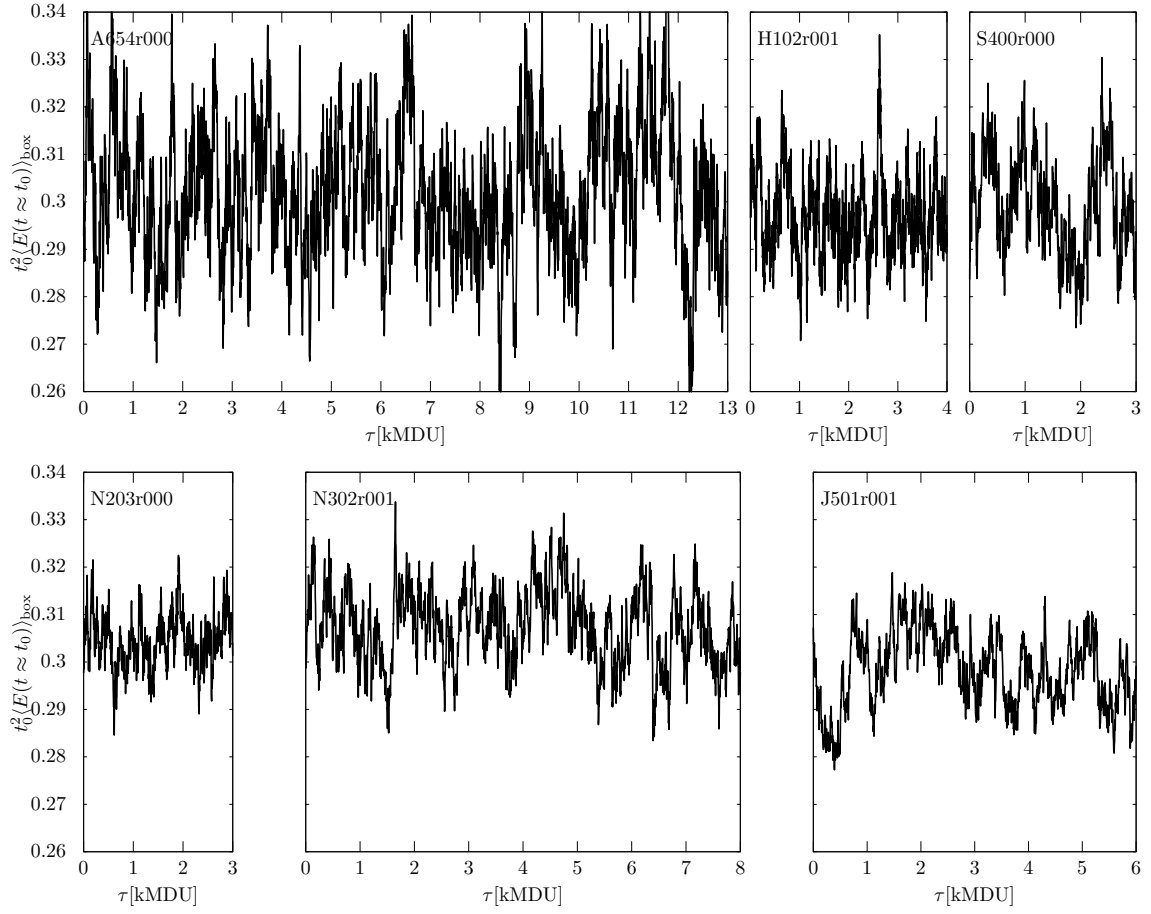


Figure 6. History of the Wilson flow action density, multiplied by t_0^2 [1], at a flow time close to t_0 , inside a sub-volume V_4 of approximately $1 \text{ fm} \cdot (aN_s)^3$ (except for A654 with periodic boundary conditions, where we employ the whole volume), along a line of $M_\pi \approx 350 \text{ MeV}$ (for $\text{Tr } M = \text{const}$) from coarse to fine lattice spacings. The amplitude of the fluctuation varies, e.g., due to somewhat different physical volumes. Autocorrelations increase from top left to bottom right, with the exception of A654 at $\beta = 3.34$ where we observe larger autocorrelation times than at $\beta = 3.4$. For the cases where more than one Monte Carlo chain exists, only one replica is shown.

- The scale t_0^* [2] is defined as the value of t_0 at the point in the quark mass plane where, along the symmetric $m_s = m_\ell$ line,

$$\phi_4^* = 8t_0^* \left(M_K^2 + \frac{M_\pi^2}{2} \right) = 12t_0^* M_\pi^2 := 1.110. \quad (3.23)$$

This is close to $t_{0,\text{symm}}$ and the combination t_0^*/a^2 can be obtained by a small interpolation or by reweighting nearby simulation points [2]. If at this point $2M_K^2 + M_\pi^2$ had the same value as at the physical quark mass point this definition would imply $\sqrt{8t_0^*} = 0.413 \text{ fm}$. However, we stress that the above choice can always be made, independent of any such assumption.

- The scale $t_{0,\text{ph}}$ refers to the value of t_0 at the physical values of M_π and M_K .
- Finally, the scale $t_{0,\text{ch}}$ refers to t_0 in the chiral limit $M_\pi = M_K = 0$.

We will frequently use the above sub- and superscripts also for other quantities taken at the respective points in the quark mass plane. $t_{0,\text{symm}}(\beta)/a^2$ is specific to our set of ensembles. These values are in general close to t_0^*/a^2 , however, the corresponding $\text{Tr } M = \text{const}$ lines do not always touch the physical point. Unlike t_0 at unphysical positions in the quark mass plane, the scale $t_{0,\text{ph}}$ can be determined from an experimental input quantity, e.g., the mass of the cascade baryon. ChPT LECs are defined in the chiral limit and, if dimensionful, obtain their scale from $t_{0,\text{ch}}$. For this purpose, the ratio $t_{0,\text{ch}}/t_{0,\text{ph}}$ is needed. Precise determinations of $t_{0,\text{ph}}$ and of $t_{0,\text{ch}}$ require ensembles with small pion masses. In contrast, t_0^*/a^2 can be determined easily with pseudoscalar masses around 400 MeV. It is therefore an ideal intermediate scale to relate different lattice spacings.

Below we will determine the dependence of $t_0(\sqrt{8t_0}M_\pi, \sqrt{8t_0}M_K, a)/a^2$ on the pion and kaon masses as well as on the lattice spacing, which will enable us to translate between all the above-mentioned scales. We will also extract $t_0^*/a^2(g^2, m^*)$ as a function of $g^2 = 6/\beta$.

3.4 The quark mass dependence of the t_0 - and the t_0^*/a^2 -values

It turns out to be convenient to define the following pseudoscalar meson mass combinations:

$$\overline{M}^2 := \frac{2M_K^2 + M_\pi^2}{3}, \quad \delta M^2 := 2(M_K^2 - M_\pi^2), \quad (3.24)$$

which we correct for finite volume effects in next-to-leading order (NLO) ChPT as described in section 4.3. With few exceptions⁷ these corrections are much smaller than our statistical errors.

The dependence of the continuum limit $t_0(\overline{M}, \delta M)$ on the pseudoscalar masses has been computed to next-to-next-to leading order (NNLO) in SU(3) ChPT in ref. [103]. To NLO only a term proportional to \overline{M}^2 appears while to NNLO M^4 and $M^4 \ln(M/\mu)$ terms contribute. Within the present precision, at the three finest lattice spacings we find our t_0 data to be insensitive to δM : at $\beta = 3.4$ the variation of t_0/a^2 along the $\overline{m} = m_{\text{symm}}$ line amounts to less than 3% and this decreases further with increasing β . Along the other lines in the quark mass plane we are unable to detect any deviation from a linear dependence on \overline{M}^2 , the relative slope of which decreases towards the continuum limit. Therefore, we assume the continuum limit behaviour [103]

$$t_0(\overline{M}, \delta M) = t_{0,\text{ch}} \left(1 + k_1 \frac{3\overline{M}^2}{(4\pi F_0)^2} \right) \approx t_{0,\text{ch}} \left(1 + \tilde{k}_1 8t_0 \overline{M}^2 \right), \quad (3.25)$$

where $k_1 = \tilde{k}_1 \cdot 8t_{0,\text{ch}}(4\pi F_0)^2/3$.

⁷For H105, H106, B452, N302, N304, J303 and J304 the pion mass correction becomes larger than half of the statistical error, but in no case does it exceed it.

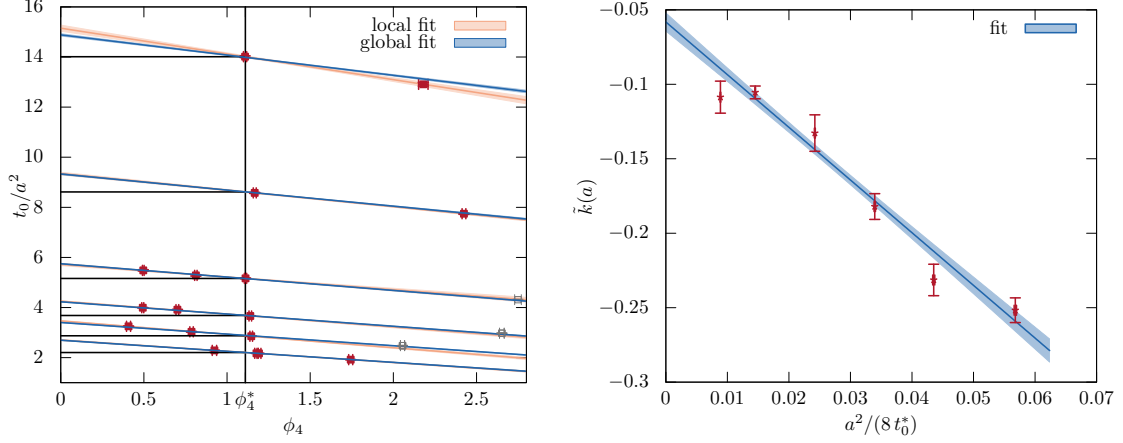


Figure 7. Left: linear interpolation of t_0/a^2 for $m_s = m_\ell$ for each value of the coupling, from $\beta = 3.34$ (bottom) to $\beta = 3.85$ (top), cf. eq. (3.26) (local fit). Also shown is the result of the global fit including all quark mass trajectories, see eqs. (3.32), (3.33), (3.35) and (3.36). The vertical line marks the value of the ϕ_4^* reference point and horizontal lines the resulting values of t_0^*/a^2 . Right: the slope \tilde{k} , as a function of $a^2/(8t_0^*)$ from the global fit, together with a quadratic continuum limit extrapolation.

3.4.1 Survey of the t_0/a^2 data

At a non-vanishing lattice spacing we will encounter mass-dependent order a lattice corrections $t_0/a^2 = (1 - 2b_a a\bar{m})t_0/a_0^2$ (see eq. (3.6)) and higher order corrections. The order a^2 contributions are proportional to either a constant, Λ^2 , the average squared pion mass \bar{M}^2 or to δM^2 . As a first step, along our $m_s = m_\ell$ lines (where $\delta M = 0$), we attempt fits of the form

$$\frac{t_0}{a^2} \approx \frac{t_{0,\text{ch}}}{a_0^2} \left[1 + \tilde{k}(a) 8t_0(\bar{M}, 0)\bar{M}^2 \right] \quad (3.26)$$

with a different set of parameters $t_{0,\text{ch}}/a_0^2$ and $\tilde{k}(a)$ for each value of the coupling. These fits effectively describe our data as is demonstrated in figure 7 (local fit). We list the results of this simplest way of extracting $t_0^*/a^2 \approx (t_{0,\text{ch}}/a_0^2)[1 + \frac{2}{3}\tilde{k}(a)\phi_4^*]$ in the first line of table 5 as “linear”. To minimize a possible bias due to higher order correction terms, in the cases where more than three well-separated data points were available, i.e. at $\beta = 3.4, 3.46$ and 3.55 , we excluded the heaviest pion mass from the fit. It turns out that the resulting t_0^*/a^2 -values are most sensitive with respect to the value of the data point $t_0/a^2 = t_{0,\text{symm}}/a^2$ closest to t_0^*/a^2 . The results compare well with the previous determination of ref. [2], updated in ref. [104], that we show in the third row of table 5. We also list the lattice spacings in this table, using the result of this article, $\sqrt{8t_0^*} = 0.4097_{(25)}^{(20)}$ fm for the conversion. The errors of a across the β -values are correlated because of this and are dominated by the scale setting uncertainty. When performing continuum limit extrapolations, we will use the globally interpolated t_0^*/a^2 -values of the second row of the table instead.

We plot the resulting slopes $\tilde{k}(a)$ as a function of $a^2/(8t_0^*)$ in the right panel of figure 7.

Table 5. Results for t_0^* in lattice units from this work (lines 1 and 2), in comparison to the respective numbers of ref. [2] (updated in ref. [104], line 3). We consider the global fit results of the second line as the most reliable ones. Also shown is the value of t_0 in the chiral limit, $t_{0,\text{ch}}(a)$. The continuum limit ratio $t_0^*/t_{0,\text{ch}}$ is shown in eq. (3.40). The first errors are statistical, the second errors reflect the uncertainty of the improvement coefficient b_a (that is related to b_g). In the last line we list the lattice spacings obtained through $\sqrt{8t_0^*} = 0.4097_{(25)}^{(20)}$ fm, see eq. (3.42) below, where we added all errors in quadrature after symmetrizing the scale error.

β	3.34	3.4	3.46	3.55	3.7	3.85
t_0^*/a^2 , linear fit	2.204(5)	2.872(10)	3.682(12)	5.162(16)	8.613(25)	14.011(39)
t_0^*/a^2 , global fit	2.204(4)(4)	2.888(4)(7)	3.686(4)(10)	5.157(5)(14)	8.617(7)(21)	13.988(19)(28)
t_0^*/a^2 [2, 104]		2.862(5)	3.662(12)	5.166(15)	8.596(27)	13.880(220)
$t_{0,\text{ch}}/a_0^2$, global fit	2.695(13)(2)	3.402(11)(1)	4.228(10)(5)	5.749(12)(1)	9.329(27)(4)	14.885(57)(14)
a/fm	0.09757(56)	0.08524(49)	0.07545(44)	0.06379(37)	0.04934(28)	0.03873(22)

Combining eqs. (3.6), (3.25) and (3.26), we obtain

$$\tilde{k}(a) = \tilde{k}_1 - \frac{2b_a a \overline{m}}{8t_0 \overline{M}^2} + \mathcal{O}(a^2). \quad (3.27)$$

However, we are unable to detect any linear contribution in the figure. Instead, a clearly quadratic dependence on a^2 is visible. Adding any other power of a to the quadratic continuum limit extrapolation results in a coefficient that is compatible with zero. The failure to resolve a term proportional to a reflects the fact that within our range of lattice spacings the combination $a\overline{m}$ remains almost constant when keeping the average renormalized quark mass $\widehat{\overline{m}} = r_m Z_m m \propto \overline{M}^2$ fixed because the factor r_m decreases rapidly with β , as can be seen in the left panel of figure 5. This also means that, unlike the coefficients r_m , \mathcal{A} , \mathcal{B}_0 , \mathcal{C}_0 or \mathcal{D}_0 , b_a cannot depend strongly on β ; otherwise there would have been visible corrections to the quadratic behaviour. Therefore, from now on we will assume that b_a coincides with its one-loop value $b_a^{(1)}$ within a 100% error band: $b_a = 0.32(32)$. Note that $b_a^{(1)}$ is independent of g^2 , see eqs. (3.3)–(3.5). The naive quadratic continuum limit extrapolation gives

$$\tilde{k} = \tilde{k}(a=0) = -0.0600(85). \quad (3.28)$$

Motivated by the above considerations, below we will attempt a global fit to our data according to the effective parametrization

$$\frac{t_0}{a^2} = \frac{t_{0,\text{ch}}}{a_0^2}(g^2) \left(1 + \tilde{k} 8t_0 \overline{M}^2\right) + \bar{c} 8t_0 \overline{M}^2 + \delta c 8t_0 \delta M^2, \quad (3.29)$$

with the parameters \bar{c} and δc , in addition to \tilde{k} . To set the stage for this global fit, we first interpolate the t_0/a^2 -values at each β -value locally via a linear fit to determine t_0^*/a^2 .

3.4.2 Interpolating formula for t_0^*/a^2

For very small values of the coupling g^2 the dependence of t_0^*/a^2 on g^2 is controlled by the perturbative β function. Its three-loop coefficient β_2 is at present not known for our action.

However, the ratio of Λ parameters,

$$\frac{\Lambda_L}{\Lambda_{\overline{\text{MS}}}} = 0.2887542, \quad (3.30)$$

was calculated in ref. [105]. Combining this with the recent determination [106]

$$\Lambda_{\overline{\text{MS}}} \sqrt{8t_0^*} = 0.712(24) \quad (3.31)$$

for the three flavour theory, we arrive at the expectation

$$\frac{t_0^*}{a^2(g^2)} = \frac{t_0^*}{a_0^2(g^2)} [1 - 2b_a(g^2)am^*] = [f(g^2) + c_{t_0} + d_{t_0}f^{-1/2}(g^2)] [1 - 2b_a(g^2)am^*], \quad (3.32)$$

where

$$f(g^2) = \frac{t_0^* \Lambda_L^2}{h^2(g^2)} = 0.00528(36) \exp \left(\frac{16\pi^2}{\beta_0 g^2} + \frac{\beta_1}{\beta_0^2} \ln \frac{\beta_0 g^2}{16\pi^2} - b_{t_0} g^2 + \dots \right). \quad (3.33)$$

The coefficient $b_{t_0} \approx (\beta_1^2 - \beta_0 \beta_2)/(16\pi^2 \beta_0^3)$ effectively parameterizes higher order perturbative contributions, c_{t_0} describes the leading $\mathcal{O}(a^2)$ lattice correction to eq. (3.31) and d_{t_0} a subleading $\mathcal{O}(a^3)$ correction. Setting $b_a = 0$, the resulting fit parameters read

$$c_{t_0} = 0.18(12), \quad d_{t_0} = -1.43(16), \quad b_{t_0} = 0.9293(46), \quad \chi^2/N_{\text{DF}} = 2.1/3. \quad (3.34)$$

3.4.3 Global interpolation of t_0/a^2

Having determined t_0^*/a^2 from individual fits to data obtained at the different β -values and having obtained an interpolating formula, we may also attempt a global fit to all the available data, utilizing this parametrization. Substituting t_0^*/a^2 for $t_{0,\text{ch}}/a_0^2$ (using eqs. (3.6) and (3.25)) and \tilde{k}_1 for \tilde{k} (using eq. (3.27)), from eq. (3.29) we obtain

$$\begin{aligned} \frac{t_0}{a^2} &= \frac{t_0^*}{a^2}(g^2) \left[1 + \tilde{k}_1 A - 2b_a(a\overline{m} - am^*) \right] + \bar{c}A + \delta c 8t_0 \delta M^2 \\ &= [f(g^2) + c_{t_0} + d_{t_0}f^{-1/2}(g^2)] \left(1 + \tilde{k}_1 A - 2b_a a\overline{m} \right) + \bar{c}A + \delta c 8t_0 \delta M^2, \end{aligned} \quad (3.35)$$

where

$$A = 8t_0 (\overline{M}^2 - M^{*2}). \quad (3.36)$$

In the second step above we used eqs. (3.32) and (3.33) to parameterize $t_0^*/a^2(g^2)$. This adds the parameters b_{t_0} , c_{t_0} and d_{t_0} , such that the total number of parameters for this combined fit across different values of g^2 is 6. Note that when inserting this parametrization the term that is proportional to $2b_a am^*$ cancels from the above equation but it resurfaces within the relation eq. (3.32) between t_0^*/a^2 and $f(g^2)$.

As discussed above, the effect of b_a cannot be isolated within our range of lattice spacings (see figure 7) as $a\overline{m}$ is approximately proportional to $t_0 \overline{M}^2$. This is shown in the left panel of figure 8, where we plot the ratio as a function of ϕ_4 . The $\text{Tr } M = \text{const}$ ensembles can be found in the vicinity of the vertical $\phi_4 = \phi_4^*$ line. There is no detectable dependence of this ratio on δM . The slopes with respect to $\overline{M}^2 \propto \phi_4$ decrease with the lattice spacing,

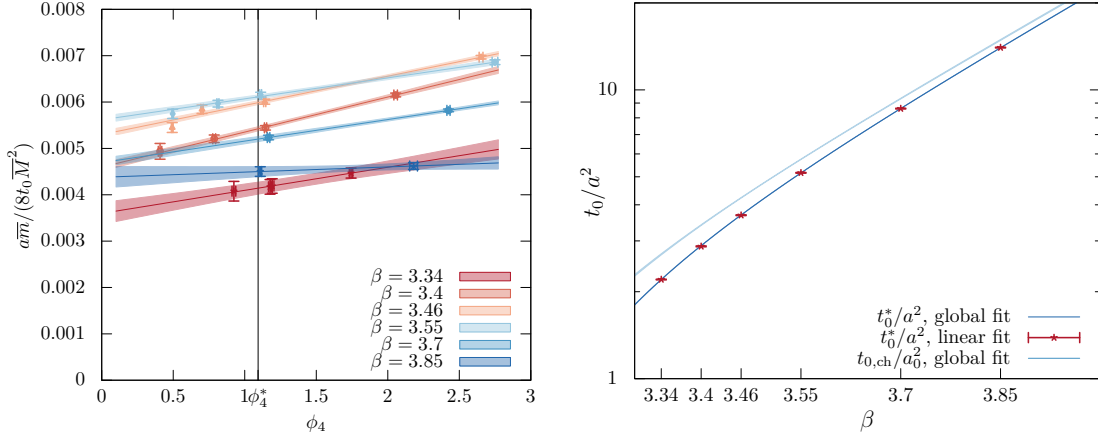


Figure 8. Left: the ratio of the average lattice quark mass in lattice units over the square of the average pseudoscalar mass, including all three quark mass trajectories. This ratio varies by only 20%. This makes it impractical to discriminate between terms proportional to $a\bar{m}$ and terms $\propto 8t_0\bar{M}^2$. Right: global fit results (cf. eq. (3.35)) for t_0^*/a^2 and $t_{0,\text{ch}}/a_0^2$, together with results for t_0^*/a^2 taken from separate linear fits (cf. eq. (3.26)) to the $m_s = m_\ell$ data only.

indicating that the dominant violations of the GMOR relation $\bar{m}/\bar{M}^2 = \text{const}$ are due to lattice artefacts. However, as already discussed above, the ratio $a\bar{m}/[8t_0\bar{M}^2]$ at ϕ_4^* itself does not decrease linearly with a . Instead, between $\beta = 3.34$ and $\beta = 3.4$ it first increases and only from $\beta = 3.46$ onwards it decreases as the parameter r_m slowly approaches unity.

Since the $a\bar{m}$ dependence is hard to distinguish from the \bar{M}^2 dependence, within the global fit we fix b_a to its one-loop value eq. (3.5), $b_a = b_a^{(1)} \approx 0.3158$. The relation (3.27) between \tilde{k}_1 and \tilde{k} will enable a cross-check with the previous fit result eq. (3.28) that was obtained by extrapolating the individual slopes $\tilde{k}(a)$ of eq. (3.26) to the continuum limit. In addition to this central fit, we carry out a second fit, setting $b_a = 0$ and interpret the difference between the resulting parameters as a systematic uncertainty. This second fit also allows for a comparison not only with eq. (3.28) but also with the earlier results shown in eq. (3.34). The difference of the b_a -values used in eq. (3.32) only slightly affects the parameters b_{t_0} , c_{t_0} and d_{t_0} and the impact on the t_0^*/a^2 -values is even smaller.

Since not only t_0/a^2 but also the variables $t_0\bar{M}^2$ and $t_0\delta M^2$ carry errors, in these fits (as well as in the previous fit to eq. (3.26)) we use the generalized least squares fit method described in appendix F.4, where we also take into account the correlation among the arguments. However, we neglect correlations between these variables and the t_0/a^2 -values on the left hand side of the equation. This is justified by the fact that the relative errors of t_0/a^2 are much smaller than those of the pseudoscalar meson masses.

We demonstrate in figure 9 that the data are well described by the fit with $b_a = b_a^{(1)}$ and remark that the picture looks very similar for $b_a = 0$. The fit curve itself is shown for

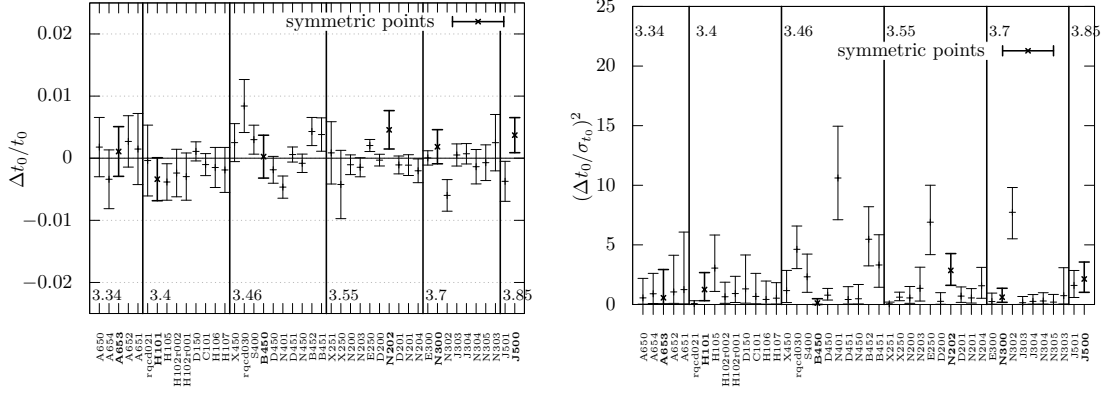


Figure 9. Deviations $\Delta t_0/a^2 = t_0/a^2(g^2, \overline{M}^2, \delta M^2) - t_0/a^2$ between the values postdicted by the fit eq. (3.35) and the data are typically below one per cent (left) or of the order of the statistical error (right), with only a few exceptions. The ensembles are sorted from left to right in terms of decreasing lattice spacing and increasing values of the average \overline{M}^2 . Boldface ensemble names correspond to the “symmetric” points, i.e. those closest to the position of ϕ_4^* .

the $m_s = m_\ell$ points in figure 7 (left). The respective fit parameters read

$$\begin{aligned}
 \tilde{k}_1(b_a = b_a^{(1)}) &= -0.0466(62), & \tilde{k}_1(b_a = 0) = \tilde{k} &= -0.0506(63), \\
 \bar{c}(b_a = b_a^{(1)}) &= -0.560(27), & \bar{c}(b_a = 0) &= -0.560(27), \\
 \delta c(b_a = b_a^{(1)}) &= 0.0213(28), & \delta c(b_a = 0) &= 0.0210(28), \\
 b_{t_0}(b_a = b_a^{(1)}) &= 0.9336(26), & b_{t_0}(b_a = 0) &= 0.9340(26), \\
 c_{t_0}(b_a = b_a^{(1)}) &= 0.286(63), & c_{t_0}(b_a = 0) &= 0.254(63), \\
 d_{t_0}(b_a = b_a^{(1)}) &= -1.567(84), & d_{t_0}(b_a = 0) &= -1.515(84), \\
 \chi^2/N_{\text{DF}}(b_a = b_a^{(1)}) &= 59.4/38, & \chi^2/N_{\text{DF}}(b_a = 0) &= 58.7/38,
 \end{aligned} \tag{3.37}$$

where the errors have been obtained from the bootstrap distributions of the parameters and scaled with $\sqrt{\chi^2/N_{\text{DF}}}$. In the right panel of figure 8 we compare the global fit to the t_0^*/a^2 -values obtained from the linear (local) interpolation results above. In addition, we show the chiral limit of this ratio.

The differences between the central values of the two columns of eq. (3.37) constitute the systematic errors from varying b_a from zero to its one-loop value. As expected, the slope parameter \tilde{k}_1 is most affected by this change. For $b_a = 0$, one has $\tilde{k}_1 = \tilde{k}$ and the above result still agrees within errors with our first estimate (3.28) of \tilde{k} . We remark that the difference between the above two values is consistent with eq. (3.27): combining the $b_a = 0$ result with the typical value $am^* = 0.004$ (see the left panel of figure 8 and table 6), we obtain $\tilde{k}_1 \approx \tilde{k} + 3b_a m^*/\phi_4^* \approx -0.0472(63)$, which indeed is very close to the result of the $b_a = b_a^{(1)}$ fit $\tilde{k}_1 = -0.0466(62)$. Moreover, the parameters b_{t_0} , c_{t_0} and d_{t_0} agree within errors with the determination (3.34), based on the local fit results.

We used the central value $\Lambda_{\overline{\text{MS}}}\sqrt{8t_0^*} = 0.712$ from the determination of ref. [106] [eq. (3.31)] as an input. Instead, we could have included the normalization as a free fit parameter. Carrying out such a fit, we find $\Lambda_{\overline{\text{MS}}}\sqrt{8t_0^*} = 0.68(17)$, in agreement with the more precise result that was obtained employing the step scaling function within the Schrödinger functional framework [106].

3.5 Summary of the main results for t_0 , a and the low energy constant k_1

We summarize the t_0^*/a^2 results from the global fit in the second line of table 5, where the first error is statistical and the second one reflects the impact of the uncertainty of b_a . Similarly, in the fourth line of the table we list $t_{0,\text{ch}}/a_0^2$, where naturally the statistical uncertainty is larger while the uncertainty of the b_a -value has less of an impact. In general, the t_0^*/a^2 results from the global fit agree well with those obtained at the individual β -values. Comparing with the results of refs. [2, 104], we only find deviations of about 2.5 and 1.5 standard deviations, respectively, at $\beta = 3.4$ and $\beta = 3.46$. Also in our case there is some difference between the linear (local) and the global fit results at $\beta = 3.4$, which is mainly due to the t_0/a^2 -value determined on ensemble H101. We regard the results from the global interpolation where statistical fluctuations average out to some extent as more robust and we will use these values.

The t_0^*/a^2 -values are well described by the interpolating formula

$$\begin{aligned} \frac{t_0^*}{a^2}(g^2) &= f_{\text{eff}}(g^2) + 0.285 - 1.566 f_{\text{eff}}^{-1/2}(g^2), \quad \text{where} \\ f_{\text{eff}}(g^2) &= \exp(17.54596 g^{-2} - 7.507 + 0.790123 \ln(g^2) - 0.9334 g^2). \end{aligned} \quad (3.38)$$

The relative errors are below 0.3% over the entire fitted range $3.34 \leq \beta \leq 3.85$. This more convenient parametrization was obtained by refitting the result, setting $b_{t_0} = 0$ but keeping the g^{-2} and $\ln(g^2)$ coefficients fixed. Within the errors of the Λ parameter of ref. [106], this interpolation converges towards the two-loop running of the scale at small values of g^2 , making this formula particularly useful for predictions regarding future runs at smaller lattice spacings. For the values at already existing simulation points we refer the reader to the second row of table 5.

The slope parameter [103] defined in eq. (3.25) has the numerical value

$$\tilde{k}_1 = -0.0466(62), \quad k_1 = \tilde{k}_1 \cdot \frac{8t_{0,\text{ch}}(4\pi F_0)^2}{3} \approx -0.055(8), \quad (3.39)$$

where we used the globally fitted \tilde{k}_1 with the effect of b_a and its uncertainty included in the central value and the error. For the last conversion, we used $\sqrt{8t_{0,\text{ch}}}F_0 = 0.1502_{(29)}^{(56)}$ [107].

Plugging the result for \tilde{k}_1 above as well as $\phi^* = 1.11$ into eq. (3.25) gives the continuum limit relations

$$t_0^* = \left(1 + \frac{2}{3}\tilde{k}_1\phi_4^*\right)t_{0,\text{ch}} = 0.9655(46)t_{0,\text{ch}}, \quad (3.40)$$

$$t_0^* = \left[1 + \frac{2}{3}\tilde{k}_1(\phi_4^* - \phi_{4,\text{ph}})\right]t_{0,\text{ph}} = 0.99947(7)t_{0,\text{ph}}. \quad (3.41)$$

In the second equation we used the result of this work $\phi_{4,\text{ph}} = 1.093_{(14)}^{(10)}$, which is due to $\sqrt{8t_{0,\text{ph}}} = 0.4098_{(25)}^{(20)} \text{ fm} < 0.413 \text{ fm}$ (see eq. (6.2)). This then implies

$$\sqrt{8t_0^*} = 0.99974(4)\sqrt{8t_{0,\text{ph}}} = 0.4097_{(25)}^{(20)} \text{ fm}. \quad (3.42)$$

Note that at a non-vanishing lattice spacing, the above relations between the t_0 -values at different points in the quark mass plane depend on the action used and, in the case of $t_0^*/t_{0,\text{ph}}$, also on the exact definition of the physical point. However, in the continuum limit (up to the treatment of isospin breaking effects), the results should be universal. Within this study, we use $a^2/(8t_0^*)$ only to relate different lattice spacings within our continuum limit extrapolation. In the end the scale is set by $t_{0,\text{ph}}$, as obtained from the mass of the Ξ baryon at the physical point, in the continuum limit. The lattice spacings of table 5 are computed using $a^2/(8t_0^*)$ with the physical value of t_0^* set by the continuum limit ratio $t_{0,\text{ph}}/t_0^*$.

In principle, along the line with $\text{Tr } M = \text{const}$ there could be a dependence of ϕ_4 on the mass difference δM^2 , which we have neglected above. This would then result in a correction to the above relation between $\sqrt{8t_0^*}$ and $\sqrt{8t_{0,\text{ph}}}$. The relative statistical uncertainty of the latter quantity is of size 0.5%. A correction of a comparable size to eqs. (3.41) and (3.42) would require ϕ_4 to vary by more than 30% along this line between $\delta M = 0$ and the physical point, due to the smallness of the parameter \tilde{k}_1 . As we will see in the following subsection, we are unable to detect any corrections to $\phi_4(\delta M)$ in the continuum limit that would exceed our statistical accuracy of about 1%. Therefore, the above value for $\sqrt{8t_0^*}$ and its error remain unaffected.

3.6 The symmetric point parameters

Above, we have defined the parameter $\phi_4 = 12t_0^2\overline{M}^2$. Several values of ϕ_4 are of relevance:

- $\phi_{4,\text{ph}}$, the value at the physical point in the continuum limit,
- $\phi_4^* = 1.11$, which — together with $M_K = M_\pi$ — defines the reference point for the determination of t_0^*/a^2 ,
- $\phi_{4,\text{symm}}(a)$, the starting point, where for each lattice spacing a our actual $\text{Tr } M = \text{const}$ trajectory branches off the symmetric $m_s = m_\ell$ line,
- $\phi_{4,\text{opt}}(a)$, the branch point that should be chosen such that the $\text{Tr } M = \text{const}$ trajectory touches the physical point for the lattice spacing a and
- $\phi_{4,\text{opt}}$, the corresponding starting point in the continuum limit.

Note that in general there is some degree of mistuning so that $\phi_{4,\text{symm}}(a) \neq \phi_{4,\text{opt}}(a)$. The optimal values $\phi_{4,\text{opt}}(a)$ will depend somewhat on how the physical point is defined. Here we match the kaon and pion masses in units of $\sqrt{8t_0}$ to their experimental values, where $t_{0,\text{ph}}$ is obtained from m_Ξ in the continuum limit.

Other parameters of interest are the lattice quark mass at this point am^* and the corresponding hopping parameter κ^* . To determine κ^* and am^* , at each β -value we carry

Table 6. Results for the critical hopping parameter κ_{crit} and for the hopping parameter at the $N_f = 3$ symmetric point, where $\phi_4 = \phi_4^* = 1.11$, κ^* , together with the bare quark mass at this point, $am^* = (\kappa^{*-1} - \kappa_{\text{crit}}^{-1})/2$.

β	κ_{crit}	κ^*	am^*
3.34	0.1366938(45)	0.1365791(23)	0.00307(10)
3.4	0.1369153 (9)	0.1367647(11)	0.00402 (3)
3.46	0.1370613(10)	0.1368948(13)	0.00444 (3)
3.55	0.1371715(10)	0.1370013(10)	0.00453 (3)
3.7	0.1371530 (9)	0.1370081(13)	0.00385 (4)
3.85	0.1369767(26)	0.1368518(39)	0.00333 (8)

out a simple phenomenological fit to the $m_s = m_\ell$ ensembles using the previously determined κ_{crit} -values as an input:

$$am = p_1\phi_4 + p_2\phi_4^2. \quad (3.43)$$

am^* is then the value of this interpolation at $\phi_4 = \phi_4^*$. The fit is depicted in the left panel of figure 8, where we plot $(3/2)am/\phi_4$ versus ϕ_4 for the symmetric ensembles. The results are collected in table 6, where we also display the critical hopping parameter values.

Starting at the symmetric point ($\delta M^2 = 0$) and reducing the pion mass, keeping the sum of lattice quark masses constant, results in a decreasing $\phi_4(\delta M_{\text{ph}}, a)$: in order to simulate on a trajectory that goes through the physical point, at a given lattice spacing a , one has to start from values $\phi_{4,\text{opt}}(a)$ somewhat larger than $\phi_{4,\text{ph}}$. Along lines of constant $\text{Tr } M$, in the continuum limit ϕ_4 cannot depend linearly on δM^2 [103], but this is not so regarding lattice artefacts. Therefore, for the data taken along such trajectories, we make the ansatz:

$$\phi_4(\delta M, a) = \phi_4(0, a) + \delta c_\phi \frac{a^2}{t_0^*} 8t_0 \delta M^2 + [c_\phi + d_\phi (\phi_4(0, a) - \phi_{4,\text{ph}})] (8t_0 \delta M^2)^2. \quad (3.44)$$

We added the term proportional to d_ϕ to compensate for the effect that the starting point $\phi_4(0, a) = \phi_{4,\text{symm}}(a)$ is not kept constant across the six lattice spacings, see the fourth column of table 7.

In this article we find the central value of $\phi_{4,\text{ph}} = \phi_4(\delta M_{\text{ph}}, 0) = 1.093_{(13)}^{(11)}$ to be smaller than $\phi_4^* = 1.110$ by almost 2%, corresponding to about 1.6 standard deviations, due to $\sqrt{8t_{0,\text{ph}}} < 0.413 \text{ fm}$. Furthermore, we obtain $8t_0 \delta M_{\text{ph}}^2 = 1.950_{(24)}^{(19)}$. Setting $\phi_4(\delta M_{\text{ph}}, a) = \phi_{4,\text{ph}}$ in eq. (3.44) then gives $\phi_4(0, a) = \phi_{4,\text{opt}}(a)$:

$$\phi_{4,\text{opt}}(a) = \phi_{4,\text{ph}} - \frac{\delta c_\phi \frac{a^2}{t_0^*} 8t_0 \delta M_{\text{ph}}^2 + c_\phi \left(8t_0 \delta M_{\text{ph}}^2\right)^2}{1 + d_\phi \left(8t_0 \delta M_{\text{ph}}^2\right)^2}. \quad (3.45)$$

We carry out correlated one-, two- and three-parameter fits to eq. (3.44), setting $c_\phi = d_\phi = 0$, $c_\phi = 0$, $d_\phi = 0$ and leaving all parameters free, respectively. In total we have

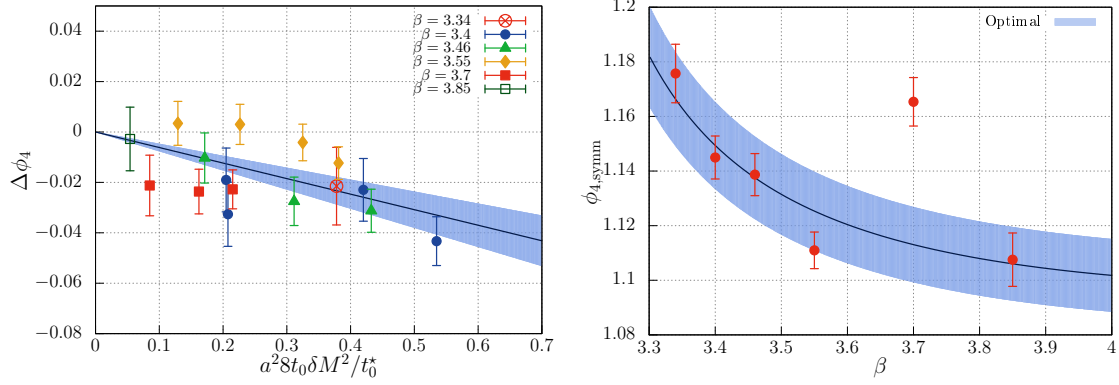


Figure 10. Left: the differences defined in eq. (3.47) as a function of $(a^2/t_0^*)8t_0\delta M^2$. The curve and error band correspond to a two-parameter fit of the $\text{Tr } M = \text{const}$ data with $m_s \neq m_\ell$ to eq. (3.44), setting $c_\phi = 0$. Right: the optimal starting values of ϕ_4 at the symmetric point that should be used in order to obtain $\phi_{4,\text{ph}} = 1.093_{(13)}^{(11)}$ at the physical point (blue error band), along with the actually simulated values of $\phi_{4,\text{symm}}(a)$.

Table 7. The values of $\phi_{4,\text{symm}}(a)$ and $\phi_{4,\text{opt}}(a)$ and the corresponding hopping parameter-values.

β	κ_{symm}	κ_{opt}	$\phi_{4,\text{symm}}(a)$	$\phi_{4,\text{opt}}(a)$
3.34	0.1365715	0.1365725(30)	1.1757(109)	1.166(17)
3.4	0.13675962	0.1367585(28)	1.1450 (78)	1.149(16)
3.46	0.13689	0.1368901(29)	1.1387 (76)	1.138(15)
3.55	0.137	0.1369988(26)	1.1110 (66)	1.125(14)
3.7	0.137	0.1370077(24)	1.1653 (88)	1.113(14)
3.85	0.136852	0.1368523(43)	1.1075 (96)	1.106(13)

15 large volume simulation points along the $\text{Tr } M = \text{const}$ lines with $m_\ell \neq m_s$ (see the central panel of figure 1). We omit D150 from this counting and the fits since $LM_\pi < 4$ in this case. Taking into account the fact that we have two data points that correspond to the H102 parameters, this then gives 15, 14, 14 and 13 degrees of freedom, respectively, for the four fits. Regarding the one-parameter fit, we find $\delta c_\phi = -0.0839(76)$ with $\chi^2/N_{\text{DF}} = 1.30$. Allowing for $d_\phi \neq 0$, we find

$$\delta c_\phi = -0.062(14), \quad d_\phi = -0.062(33), \quad \chi^2/N_{\text{DF}} = 1.21. \quad (3.46)$$

We define

$$\Delta\phi_4(\delta M, a) = \phi_4(\delta M, a) - \phi_4(0, a) - d_\phi (\phi_4(0, a) - \phi_{4,\text{ph}}) (8t_0\delta M^2)^2 \quad (3.47)$$

and plot the resulting fit for these shifted differences as a function of $(a^2/t_0^*)t_0\delta M^2$ in the left panel of figure 10. Additionally including the parameter c_ϕ slightly decreases the fit quality

($\chi^2/N_{\text{DF}} = 1.22$) and gives $c_\phi = 0.0029(27)$ while $\delta c_\phi = -0.070(14)$ and $d_\phi = -0.114(54)$ remain unchanged within errors, relative to eq. (3.46). Setting $d_\phi = 0$ but including c_ϕ gives $c_\phi = -0.0017(16)$ with $\chi^2/N_{\text{DF}} = 1.33$. Also in this case $\delta c_\phi = -0.069(17)$ agrees with the other fit results.

We conclude that we are unable to discriminate c_ϕ from zero and we actually obtain the best fit quality when removing this parameter. Therefore, within errors $\phi_{4,\text{opt}} = \phi_{4,\text{ph}}$ in the continuum limit. Of particular interest is also $\phi_{4,\text{opt}}(a)$, which can be obtained from eq. (3.45). In the right panel of figure 10 we compare this to the actual simulation points $\phi_{4,\text{symm}}$. The error of the prediction, also included in table 7, is dominated by the uncertainty of the scale $t_{0,\text{ph}}$. It turns out that, with the exception of $\beta = 3.7$, the simulated $\text{Tr } M = \text{const}$ trajectories are within the target range. The continuum limit agreement of $\phi_{4,\text{opt}}$ at the symmetric line with $\phi_{4,\text{ph}}$ within the present errors is a universal feature of $N_f = 2 + 1$ QCD. However, we remark again that $\phi_{4,\text{opt}}(a)$ as depicted in the figure will depend on the input quantities used to define the physical point at non-vanishing values of the lattice spacing.

Finally, we predict the hopping parameter values that correspond to the optimal $m_s = m_\ell$ starting point,

$$\frac{1}{\kappa_{\text{opt}}(a)} = 2 [p_1 \phi_{4,\text{opt}}(a) + p_2 \phi_{4,\text{opt}}^2(a)] + \frac{1}{\kappa_{\text{crit}}}, \quad (3.48)$$

where p_1 and p_2 are defined in eq. (3.43). These κ -values are also included in table 7.

4 Physical point extrapolation strategy

We detail our strategy to extrapolate the hadron masses to the physical point in the quark mass plane, and to the continuum and infinite volume limits. In particular, we wish to maintain full order a improvement within the continuum limit extrapolation. Since the scale should be set by comparing to an experimental measurement at the physical quark mass point, the exact position of which in turn depends on the scale setting, some care needs to be taken. First we explain how we retain order a improvement in the continuum limit extrapolation. Then, in section 4.2, we give the general framework of our combined chiral and continuum limit extrapolations, before discussing how we account for eventual finite volume effects in section 4.3.

4.1 The continuum limit

Naive Wilson fermions have order a cut-off effects. Here we implement a complete, non-perturbative order a improvement programme. This consists of improving the action and — for the determination of the AWI quark masses — also the axial and pseudoscalar currents. To improve the action, the Sheikholeslami-Wohlert (clover) term [82] is added, with its coefficient c_{sw} determined in ref. [83] for the tree-level Symanzik improved gluon action [84] that we use. Most of our gauge ensembles have open boundary conditions in time [81] where the boundary terms are not order a improved. However, measurements are only taken in the bulk, far away from these boundaries, see appendix E.2, exponentially suppressing such

residual order a effects. Also the quark masses and the coupling constant appearing in the action need to be improved. The former does not affect the position of the physical point in terms of the kaon and pion masses but was relevant for the vector Ward identity quark mass determination of section 3.2 (with the combinations of improvement coefficients \mathcal{A} , \mathcal{B}_0 , \mathcal{C}_0 and \mathcal{D}_0).

As mentioned above and discussed in section 3.1, the bare coupling $g^2 = 6/\beta$ undergoes order a improvement [90, 91]: $\tilde{g}^2 = g^2(1 + b_g a \bar{m})$, where \bar{m} denotes the average sea quark mass eq. (2.4). Instead of simulating at fixed values of \tilde{g}^2 , thereby keeping the lattice spacing a constant, we simulate at specified values of g^2 . This will imply order a cut-off effects on lattice hadron mass values Ma , unless the average quark mass is kept constant. Along two of our quark mass plane trajectories, namely $m_s = m_\ell$ and $\hat{m}_s \approx \hat{m}_{s,\text{ph}}$, we vary \bar{m} and therefore care needs to be taken.

Assuming that the combination ϕ_4 of eq. (3.23) remains constant along the $2/\kappa_\ell + 1/\kappa_s = \text{const}$ line (i.e. the line of a constant average lattice quark mass $\bar{m} = m_{\text{symm}}$) and setting $\sqrt{8t_0^*} \approx 0.413 \text{ fm}$ gives the value $\phi_4^* = 1.11$. Previous lattice studies gave results consistent with this value of t_0 , either at the ϕ_4^* position [2] or at the physical point [5]. In section 3.6 we confirm that ϕ_4 remains constant within our present statistical errors as long as $\text{Tr } M$ is kept constant, up to lattice artefacts. However, we will find a somewhat lower value for $\sqrt{8t_0^*}$, giving $\phi_{4,\text{ph}} = 1.093_{(13)}^{(11)}$. Nevertheless, we will keep the value $\phi_4 = \phi_4^* = 1.11$ in order to define the “*” reference point. Given our good coverage of the quark mass plane, whether this reference value exactly coincides with the value of ϕ_4 at the physical point is not relevant for our scale and mass determinations.

In the end the scale needs to be set independently, i.e. a physical value has to be assigned, e.g., to $t_{0,\text{ph}}$ or t_0^* in the continuum limit, that is consistent with our physical point definition. In the absence of stable light mesons other than the π and the K , the remaining possibilities of input quantities include baryon masses as well as pion and kaon decay constants.⁸ In the former case statistical errors are larger, while the accuracy of the latter observables is limited by the precision of the determination of the renormalization factor Z_A , the accuracy of the experimental input (converted into an isospin symmetric world without soft photon effects) and using phenomenological values for the CKM matrix elements V_{ud} and, in particular, V_{us} . These values in turn depend on previous lattice QCD determinations by other groups.

Within this subsection we denote a hadron mass of the continuum theory as M . Lattice simulations give dimensionless combinations $Ma(g^2, a\bar{m}) = Ma_0(g^2)(1 + b_a a\bar{m})$, see eq. (3.6). This $a\bar{m}$ correction term cancels from ratios of masses determined at the same value of \bar{m} . These will then approach the continuum limit without any linear dependence on a , which holds for hadron masses obtained at different positions along the $\bar{m} = m_{\text{symm}} = \text{const}$ quark mass plane trajectory. However, in general ratios between hadron masses at different points in the quark mass plane will not be order a improved since $M_1 a(g^2, a\bar{m}_1) / [M_2 a(g^2, a\bar{m}_2)] = (M_1/M_2)[1 + b_a a(\bar{m}_1 - \bar{m}_2)]$. The average quark mass varies along the $m_s = m_\ell$ and

⁸The ϕ meson is reasonably narrow too, however, it has the same quantum numbers as the lighter, less stable ω meson. Including input from heavy hadrons, e.g., charmed baryons, while statistically precise, would require to simultaneously fix the charm quark mass.

$\hat{m}_s \approx \text{const}$ trajectories. Order a effects will, however, cancel if dimensionless combinations $Ma\sqrt{8t_0}/a = M\sqrt{8t_0}$, where t_0 is computed on the same ensemble as M , are taken.

Extrapolating $\sqrt{8t_0}M$ combinations mixes the continuum limit quark mass dependence of t_0 with that of M . This is unproblematic since we have already determined the continuum limit functional dependence of t_0 on the pseudoscalar masses in section 3.4, see eqs. (3.25) and (3.39), allowing us to disentangle the two effects. Also physical point extrapolated masses will remain unaffected. We remark that the $\bar{m} = m_{\text{symm}}$ trajectory is a notable exception in our extrapolation strategy since in this case the ratio of lattice numbers $(t_0^*/a^2)/(t_{0,\text{ph}}/a^2)$ taken at different points does not receive any order a contributions, at least if we assume that this trajectory (that starts out from somewhere near ϕ_4^*) goes through the physical point. Moreover, in this case t_0 only varies at NNLO in ChPT [103].

4.2 Parametrization of the quark mass, lattice spacing and volume dependence

It is convenient not only to define the average sea quark mass eq. (2.4) but also to introduce the quark mass difference

$$\delta m := m_s - m_\ell = 3(\bar{m} - m_\ell) = -\frac{3}{2}(\bar{m} - m_s). \quad (4.1)$$

The leading order (LO) SU(3) GMOR relations read

$$M_\pi^2 = 2B_0\hat{m}_\ell + \mathcal{O}(\hat{m}_\ell^2), \quad M_K^2 = B_0(\hat{m}_s + \hat{m}_\ell) + \mathcal{O}(\hat{m}_s^2, \hat{m}_\ell^2, \hat{m}_s\hat{m}_\ell), \quad (4.2)$$

where $B_0 = \Sigma_0/F_0^2$ and $\Sigma_0 = -\langle \bar{u}u \rangle > 0$ and F_0 are the (negative) chiral condensate and the pion decay constant, respectively, in the limit of $N_f = 3$ massless quarks. We remind the reader that the renormalized quark masses in a continuum scheme are denoted as \hat{m}_ℓ and \hat{m}_s . The GMOR relations also link the meson mass combinations of eq. (3.24) to corresponding quark mass combinations:

$$\bar{M}^2 = \frac{2M_K^2 + M_\pi^2}{3} \approx 2B_0\bar{m}, \quad \delta M^2 = 2(M_K^2 - M_\pi^2) \approx 2B_0\delta\hat{m}, \quad (4.3)$$

where $\delta m = m_s - m_\ell$, see eq. (4.1).

In section 4.1 we discussed how to avoid order a lattice artefacts. We implement this programme by employing the fit strategy outlined below. We distinguish between t_0^* , defined at the position $\phi_4 = 1.11$ along the $m_s = m_\ell$ flavour symmetric line and $t_{0,\text{ph}}$, defined at the physical point in the quark mass plane. The ratio of these two quantities is unity to NLO in ChPT [103]. Note that the combination $\sqrt{8t_0^*}/a$ can be employed to translate between lattice spacings obtained at different values of the inverse coupling constant β , without the need to know the corresponding $\sqrt{8t_{0,\text{ph}}}/a$ -values.

The fit strategy consists of first defining parametrizations (here for the example of the Ξ mass):

$$\sqrt{8t_0}m_\Xi = f_\Xi(\sqrt{8t_0}M_\pi, \sqrt{8t_0}M_K, L/\sqrt{8t_0}, a^2/(8t_0^*)). \quad (4.4)$$

In principle, we could have chosen $a^2/(8t_{0,\text{ph}})$ as the last argument on the right hand side, however, this is not known prior to the fit while we have already determined $a^2/(8t_0^*)$ in

section 3.4, see the second line of table 5. We also remark that in the last argument we replaced a_0^2 by $a^2 = a_0^2(1 + 2b_a am^*)$, the difference being of order a^3 .

In view of eq. (4.4) it is convenient to define the dimensionless quantities

$$\mathfrak{m}_B = \sqrt{8t_0} m_B, \quad \overline{\mathbb{M}} = \sqrt{8t_0} \overline{M}, \quad \delta\mathbb{M} = \sqrt{8t_0} \delta M, \quad \mathbb{L} = \frac{L}{\sqrt{8t_0}}, \quad \mathfrak{a} = \frac{a}{\sqrt{8t_0^*}}, \quad (4.5)$$

where $B \in \{N, \Lambda, \Sigma, \Xi, \Delta, \Sigma^*, \Xi^*, \Omega\}$. Other quantities such as $\mathbb{M}_\pi = \sqrt{8t_0} M_\pi$ are rescaled analogously. Note that we choose to rescale a into units of $\sqrt{8t_0^*}$ rather than $\sqrt{8t_0}$.

The above products of hadron masses and $\sqrt{8t_0}$, determined at the same lattice coupling and quark mass values, have no linear lattice spacing dependence. Therefore, the leading lattice spacing effects are of orders $a^2 \Lambda^2$, $a^2 \Lambda \overline{m}$, $a^2 \Lambda \delta m$, $a^2 \overline{m}^2$, $a^2 \overline{m} \delta m$ and $a^2 \delta m^2$. We will also investigate corrections $\propto a^3$.⁹ Omitting these latter terms, converting the quark masses into pseudoscalar meson masses and truncating the dependence of lattice artefacts at quadratic order in the pseudoscalar masses,¹⁰ the fit function for the baryon octet can be factorized as follows:

$$\mathfrak{m}_O(\mathbb{M}_\pi, \mathbb{M}_K, \mathbb{L}, \mathfrak{a}) = \mathfrak{m}_O(\mathbb{M}_\pi, \mathbb{M}_K, \mathbb{L}) \left[1 + \mathfrak{a}^2 (c_O + \bar{c}_O \overline{\mathbb{M}}^2 + \delta c_O \delta \mathbb{M}^2) \right]. \quad (4.6)$$

While c_O and \bar{c}_O are independent of the baryon in question, the δc_O will be different for different baryons $O \in \{N, \Lambda, \Sigma, \Xi\}$. The same applies to decuplet baryons with the replacements $\mathfrak{m}_O \mapsto \mathfrak{m}_D$, $c_O \mapsto c_D$, $\bar{c}_O \mapsto \bar{c}_D$, $\delta c_O \mapsto \delta c_D$ and $D \in \{\Delta, \Sigma^*, \Xi^*, \Omega\}$. We summarize possible continuum limit parametrizations of $\mathfrak{m}_B(\mathbb{M}_\pi, \mathbb{M}_K, \mathbb{L}) = \mathfrak{m}_B(\mathbb{M}_\pi, \mathbb{M}_K, \mathbb{L}, 0)$ in section 5 below. We remark that since our lattice action breaks chiral symmetry at any non-vanishing value of the lattice spacing, there are no obvious SU(3) constraints, relating the δc_B parameters for different baryons B .

Our physical point is defined as the position in the quark mass plane where $M_{\pi, \text{ph}} = 134.8(3)$ MeV and $M_{K, \text{ph}} = 494.2(3)$ MeV. We use $m_{\Xi, \text{ph}} = 1316.9(3)$ MeV as the input to set the scale in the continuum limit. We refer to appendix A for a discussion of these numbers and specifically to table 14. Using these values, the scale $t_{0, \text{ph}}$ can be obtained via the relation

$$\sqrt{8t_{0, \text{ph}}} = \frac{\mathfrak{m}_\Xi(\mathbb{M}_\pi = 0.10236(22)\mathfrak{m}_\Xi, \mathbb{M}_K = 0.37528(24)\mathfrak{m}_\Xi, 0)}{1316.9(3) \text{ MeV}}. \quad (4.7)$$

Subsequently, also at $a > 0$ we may define the physical point as the position where

$$\mathbb{M}_K = \sqrt{8t_{0, \text{ph}}} 494.2(3) \text{ MeV}, \quad \frac{\mathbb{M}_\pi}{\mathbb{M}_K} = \frac{M_{\pi, \text{ph}}}{M_{K, \text{ph}}} = 0.2728(6). \quad (4.8)$$

⁹In principle, the a^2 effects are accompanied by different powers $g^{2\Gamma_i}$ with the anomalous dimensions Γ_i determined by the Symanzik counterterms [73]. However, for our action it was found for the minimal dimension Γ_{\min} that $\Gamma_{\min} \approx 0.247$ without and $\Gamma_{\min} = -0.111$ with quark mass terms [108]. In fact, the dominant contribution is expected to be $\propto g^{1.52} a^2$ [108]. Therefore, ignoring the anomalous dimensions should be a conservative and safe assumption for our lattice action, in particular, since the Γ_i are positive and g^2 varies only by a factor of 1.15, whereas the lattice spacing a changes by a factor of 2.5.

¹⁰This is justified by the fact that our parametrizations of the dependence on pseudoscalar masses in the continuum limit will not exceed $\mathcal{O}(M^4)$. Moreover, one would expect that $\overline{m} \lesssim m_s/3 \ll \Lambda$ and $\delta m < m_s \ll \Lambda$.

Finally, if needed, the continuum limit ratio $t_0^*/t_{0,\text{ph}}$ can be determined via eqs. (3.39) and (3.41), see eq. (3.42).

4.3 Finite size effects

Within section 4.2 we have assumed infinite volume hadron masses. Here we use ChPT as a guide to study the impact of potential finite size effects. To be safely within the so-called p -regime of ChPT we not only restrict the linear box size to $L \gg M_\pi^{-1}$ but we also require this to be much larger than the inverse pseudo-critical temperature. To this end, in the latest Flavour Lattice Averaging Group (FLAG) Review [109] an extent $L > 2\text{ fm}$ is advocated. Here we set the somewhat stricter limit $L > 2.3\text{ fm}$. Any remaining finite size effects are expected to be suppressed at least exponentially with the mass gap, in proportion to $\exp(-LM_\pi)$.

The pseudoscalar meson masses, which we are able to determine very precisely, can, in principle, be affected by finite size effects in a statistically significant way. To limit the number of parameters and also to be consistent with the order, i.e. $\mathcal{O}(p^3)$, that we use in the chiral expansion of the baryon masses, we only consider finite size effects to NLO (order p^2) in mesonic ChPT, where no order p^3 corrections exist. For $N_f = 3$ mass-degenerate light quark flavours one obtains in a finite volume [110, 111]:

$$M_\pi^2(L) = M_\pi^2 \left[1 + \frac{1}{N_f} h(\lambda_\pi, M_\pi^2) + \dots \right], \quad (4.9)$$

where $\lambda_\pi = LM_\pi$ and

$$h(\lambda_\pi, M_\pi^2) = \frac{4M_\pi^2}{(4\pi F_0)^2} \sum_{\mathbf{n} \neq \mathbf{0}} \frac{K_1(\lambda_\pi |\mathbf{n}|)}{\lambda_\pi |\mathbf{n}|}. \quad (4.10)$$

Above, $\mathbf{n} \in \mathbb{Z}^3$ are integer component vectors and $K_1(x)$ is the modified Bessel function of the second kind.

For non-degenerate quark masses, one obtains (see, e.g., eq. (16) of ref. [112], where also the NNLO corrections can be found)

$$M_\pi^2(L) = M_\pi^2 \left[1 + \frac{1}{2} h(\lambda_\pi, M_\pi^2) - \frac{1}{6} h(\lambda_{\eta_8}, M_{\eta_8}^2) \right], \quad (4.11)$$

$$M_K^2(L) = M_K^2 \left[1 + \frac{1}{3} h(\lambda_{\eta_8}, M_{\eta_8}^2) \right], \quad (4.12)$$

where we made use of

$$M_{\eta_8}^2 \approx \frac{4M_K^2 - M_\pi^2}{3} = \overline{M}^2 + \frac{1}{3} \delta M^2, \quad (4.13)$$

which holds to this order in ChPT. In figure 11 we compare the pion mass data to this expectation for two pion masses where simulations at three different volumes exist. In these cases the deviation of the smallest volume points from the large volume limit seems to have the wrong sign, however, the deviation from the NLO ChPT expectation is smaller than two standard deviations. Note that the smallest volume shown (U101) does not enter our analysis since $L < 2.3\text{ fm}$ in this case. For the kaon mass we do not detect any statistically

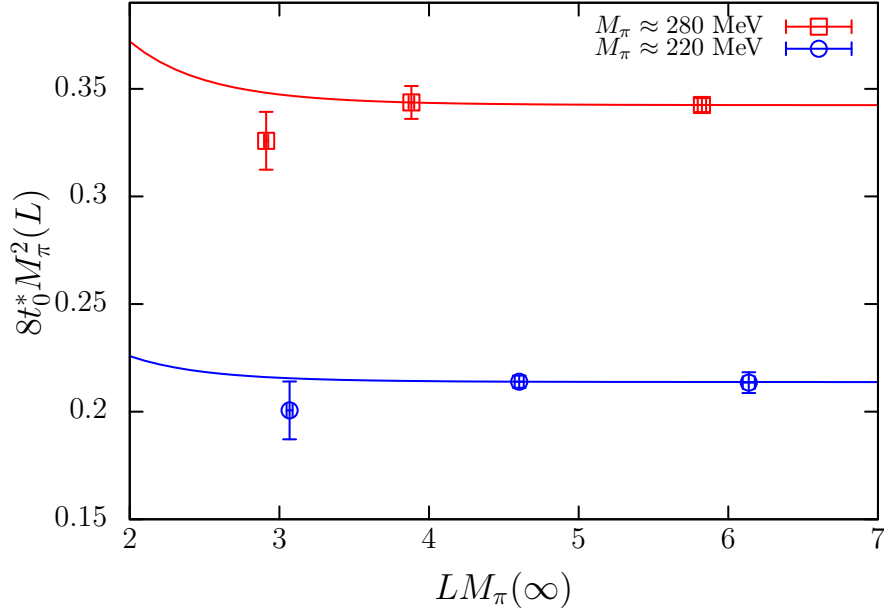


Figure 11. Dependence of the pion mass on the lattice extent at $\beta = 3.4$. The $M_\pi \approx 280$ MeV data correspond to ensembles U101, H105 and N101 (in order of increasing L), the $M_\pi \approx 220$ MeV data to ensembles S100, C101 and D101. The curves, that are normalized with respect to the most precise data point, correspond to the parametrization eq. (4.11), where we made use of eqs. (4.10) and (4.13).

significant finite volume effects. In this case, away from the $m_s = m_\ell$ line, both the predicted finite size effects and the relative statistical errors are smaller than for the pion.

To be on the safe side, we correct all pion and kaon masses for the finite volume effect eqs. (4.10)–(4.13). Since these equations only encapsulate the leading non-trivial order, we add in quadrature half of the difference between finite volume and infinite volume extrapolated results as a systematic error to the statistical error of the pion and kaon masses. In practice, this is done by adding uncorrelated Gaussian distributed random variables to the existing bootstrap samples. We remark that except for some small volume ensembles that do not enter our extrapolations, e.g., U101, the finite size correction is always smaller than the statistical error and, for the vast majority of ensembles, much smaller.

The analytical expressions for finite volume effects of the baryon masses are discussed in appendix B. These are included into the functional form of the fit to $\mathbf{m}_B(\mathbf{M}_\pi, \mathbf{M}_K, \mathbb{L})$. In general, we expect finite volume effects in the baryon sector to be much smaller than our statistical errors, at least for $L \gtrsim \max\{4M_\pi^{-1}, 2.3 \text{ fm}\}$. In figure 12 we compare nucleon and cascade masses with the order p^3 BChPT expectation eq. (B.1), matching this in each case to the first data point with $LM_\pi > 4$. The coefficients $g_{N,P}/(4\pi F_0)^2$ and $g_{\Xi,P}/(4\pi F_0)^2$ (see eq. (5.15)) and the scale m_0 , all defined in the chiral limit, are taken from our best global continuum limit BChPT fit to the octet baryon spectrum, see section 6.5 and table 11. M_{η_8} is computed via eq. (4.13). The curves are subject to systematics that are due to truncating at order p^3 , omitting effects of decuplet baryon loops and the uncertainties of

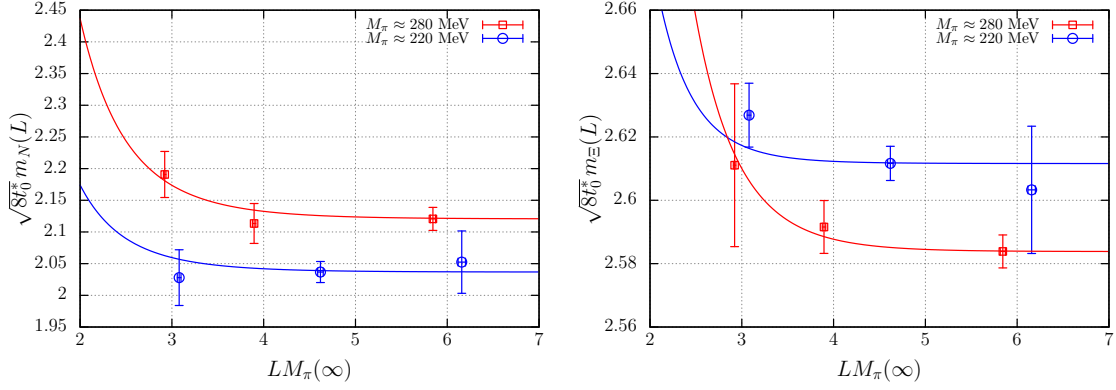


Figure 12. Dependence of the nucleon (left) and Ξ baryon (right) mass on the lattice extent. The masses are determined on the ensembles that are displayed in figure 11. The curves, that are normalized with respect to the most precise data point, correspond to the parametrization (B.1).

the low energy constants. Similar results are obtained for the other baryons and at different simulation points. The figure qualitatively confirms our expectation: some of the $LM_\pi \approx 3$ points appear to give larger masses than the large volume data, while we see no significant differences between the $LM_\pi \gtrsim 4$ points.

5 The continuum limit dependence of baryon masses on the meson masses

In the preceding section, we discussed our combined chiral, continuum and infinite volume limit extrapolation strategy. The generic form of our fits is given in eq. (4.6), see also the definitions eqs. (4.3) and (4.5). We remark that for analysing $m_s = m_\ell$ ensembles alone, the parameters $\delta c_{O|D}$ are not needed since $\delta \bar{M} = 0$. Likewise, only one of the coefficients $c_{o|d}$ or $\bar{c}_{o|d}$ is required when considering only the $\bar{m} = \text{const}$ data, where $\bar{M} \approx \text{const}$. If only $\hat{m}_s \approx \hat{m}_{s,\text{ph}}$ data are used, the effect of $\bar{c}_{o|d}$ can be absorbed into $c_{o|d}$ and $\delta c_{O|D}$. However, here we attempt a joint analysis of all the ensembles and we therefore include all six discretization coefficients both for the octet and for the decuplet baryons.

Below we define the relevant parametrizations of the quark mass dependence in the continuum limit. These are based on SU(3) ChPT, i.e. an expansion about $m_s = m_\ell = 0$, as well as on a Taylor expansion about points on the $m_s = m_\ell$ line. The volume dependence (that does not contain additional LECs) is detailed in appendix B. We start the discussion with a linear dependence of the baryon masses on the quark masses, i.e. NLO ChPT. The fits that we will carry out are based on NNLO BChPT in extended-on-mass-shell (EOMS) regularization, NNLO BChPT, including transitions between octet and decuplet baryons (small scale expansion (SSE)), and a Taylor expansion up to quadratic order in the quark masses about points on the symmetric line $m_s = m_\ell$. The heavy baryon limit (HBChPT) is also discussed.

5.1 Linear: NLO BChPT

Terms proportional to quark masses are quadratic in the pseudoscalar meson masses due to the GMOR relations. Therefore, to lowest non-trivial order the infinite volume continuum

limit expectations for octet and decuplet baryon masses read

$$m_O(M_\pi, M_K) = m_0 + \bar{b} \bar{M}^2 + \delta b_O \delta M^2, \quad (5.1)$$

$$m_D(M_\pi, M_K) = m_{D0} + \bar{t} \bar{M}^2 + \delta t_D \delta M^2, \quad (5.2)$$

respectively, where $O \in \{N, \Lambda, \Sigma, \Xi\}$, $D \in \{\Delta, \Sigma^*, \Xi^*, \Omega\}$ and m_0 and $m_{D0} = m_0 + \delta$ are the baryon masses in the SU(3) chiral limit. The remaining parameters are related to the three standard octet SU(3) LECs b_0 , b_D and b_F and the two decuplet LECs t_{D0} and t_D as follows (where we deviate from the standard notation to distinguish the LEC t_{D0} from the scale parameter t_0),

$$\bar{b} = -6b_0 - 4b_D, \quad \bar{t} = 3t_{D0} + 3t_D, \quad (5.3)$$

$$\delta b_N = \frac{2}{3}(3b_F - b_D), \quad \delta b_\Lambda = -\frac{4}{3}b_D, \quad \delta b_\Sigma = \frac{4}{3}b_D, \quad \delta b_\Xi = -\frac{2}{3}(3b_F + b_D), \quad (5.4)$$

$$\delta t_\Delta = -t_D, \quad \delta t_{\Sigma^*} = 0, \quad \delta t_{\Xi^*} = t_D, \quad \delta t_\Omega = 2t_D. \quad (5.5)$$

One parameter encapsulates the dependence on the average quark mass (b_0 and t_{D0} or, equivalently, \bar{b} and \bar{t}) while the quark mass splittings depend on two parameters or one parameter only (b_D and b_F or t_D , respectively), which is due to SU(3) constraints. Note that the above functional forms are consistent with the Gell-Mann–Okubo mass splitting relations [113, 114].

Based on these continuum relations, we employ the ansatz

$$\mathfrak{m}_O(\mathbb{M}_\pi, \mathbb{M}_K) = \mathfrak{m}_0 + \bar{\mathfrak{b}} \bar{\mathbb{M}}^2 + \delta \mathfrak{b}_O \delta \mathbb{M}^2, \quad (5.6)$$

$$\mathfrak{m}_D(\mathbb{M}_\pi, \mathbb{M}_K) = \mathfrak{m}_{D0} + \bar{\mathfrak{t}} \bar{\mathbb{M}}^2 + \delta \mathfrak{t}_D \delta \mathbb{M}^2 \quad (5.7)$$

for the dimensionless combinations eq. (4.5) for octet and decuplet baryons, respectively, where \mathfrak{m}_0 and \mathfrak{m}_{D0} are the products of m_0 and m_{D0} with $\sqrt{8t_{0,\text{ch}}}$ in the $N_f = 3$ chiral limit. Again, we have the SU(3) constraints

$$\delta \mathfrak{b}_N = \frac{2}{3}(3\mathfrak{b}_F - \mathfrak{b}_D), \quad \delta \mathfrak{b}_\Lambda = -\frac{4}{3}\mathfrak{b}_D, \quad \delta \mathfrak{b}_\Sigma = \frac{4}{3}\mathfrak{b}_D, \quad \delta \mathfrak{b}_\Xi = -\frac{2}{3}(3\mathfrak{b}_F + \mathfrak{b}_D), \quad (5.8)$$

$$\delta \mathfrak{t}_\Delta = -\mathfrak{t}_D, \quad \delta \mathfrak{t}_{\Sigma^*} = 0, \quad \delta \mathfrak{t}_{\Xi^*} = \mathfrak{t}_D, \quad \delta \mathfrak{t}_\Omega = 2\mathfrak{t}_D. \quad (5.9)$$

To this order, $t_0(M_\pi, M_K)$ in the continuum limit only depends on \bar{M}^2 but not on the mass splitting, see eq. (4.10) of ref. [103]. Therefore, \mathfrak{b}_F , \mathfrak{b}_D and \mathfrak{t}_D can be obtained by trivially rescaling the baryonic low energy constants. However, the slopes $\bar{\mathfrak{b}}$ and $\bar{\mathfrak{t}}$ will contain an additive term, due to the dependence of $\sqrt{8t_0}$ on \bar{M}^2 (see eq. (3.25)):

$$b_F = \sqrt{8t_{0,\text{ch}}} \mathfrak{b}_F, \quad b_D = \sqrt{8t_{0,\text{ch}}} \mathfrak{b}_D, \quad t_D = \sqrt{8t_{0,\text{ch}}} \mathfrak{t}_D, \quad (5.10)$$

$$\bar{b} = \sqrt{8t_{0,\text{ch}}} \left(\bar{\mathfrak{b}} - \frac{\tilde{k}_1}{2} \mathfrak{m}_0 \right), \quad \bar{t} = \sqrt{8t_{0,\text{ch}}} \left(\bar{\mathfrak{t}} - \frac{\tilde{k}_1}{2} \mathfrak{m}_{D0} \right), \quad (5.11)$$

$$b_0 = \sqrt{8t_{0,\text{ch}}} \left(\mathfrak{b}_0 + \frac{\tilde{k}_1}{12} \mathfrak{m}_0 \right), \quad t_{D0} = \sqrt{8t_{0,\text{ch}}} \left(\mathfrak{t}_{D0} - \frac{\tilde{k}_1}{6} \mathfrak{m}_{D0} \right), \quad (5.12)$$

where eq. (5.12) follows from eqs. (5.10) and (5.11) and the definitions (5.3) of \bar{b} and \bar{t} .

Linear octet baryon fits would contain a total of 10 parameters: the six parameters of eq. (4.6) describing the lattice spacing dependence ($c_o, \bar{c}_o, \delta c_N, \delta c_\Lambda, \delta c_\Sigma, \delta c_\Xi$) and four parameters describing the chiral behaviour in the continuum limit (m_0, \bar{b}, b_D, b_F). The decuplet masses only depend on nine parameters ($m_{D0}, \bar{t}, t_D, c_d, \bar{c}_d, \delta c_\Delta, \delta c_{\Sigma^*}, \delta c_{\Xi^*}, \delta c_\Omega$).

5.2 BChPT: NNLO BChPT

We label the $\mathcal{O}(1)$ and $\mathcal{O}(p^2)$ baryon ChPT as LO and NLO, respectively, and the $\mathcal{O}(p^3)$ covariant baryon ChPT (BChPT) [115] as NNLO.¹¹ This leading one-loop order includes the usual sunset self-energy diagrams. We regulate the loop-function according to the EOMS scheme [116–118] for removing terms that break the power counting. For a review of different ChPT approaches, see, e.g., ref. [119]. The infinite volume mass dependence for octet baryons reads [120]

$$m_O(M_\pi, M_K) = m_0 + \bar{b} \bar{M}^2 + \delta b_O \delta M^2 + \frac{m_0^3}{(4\pi F_0)^2} \left[g_{O,\pi} f_O \left(\frac{M_\pi}{m_0} \right) + g_{O,K} f_O \left(\frac{M_K}{m_0} \right) + g_{O,\eta_8} f_O \left(\frac{M_{\eta_8}}{m_0} \right) \right], \quad (5.13)$$

where the δb_O are the same as above, see eq. (5.4), the η_8 mass to this order is given by eq. (4.13) and the EOMS loop-function reads

$$f_O(x) = -2x^3 \left[\sqrt{1 - \frac{x^2}{4}} \arccos \left(\frac{x}{2} \right) + \frac{x}{2} \ln(x) \right]. \quad (5.14)$$

The dimensionless couplings $g_{O,P}$ are given as¹²

$$\begin{aligned} g_{N,\pi} &= \frac{3}{2}(D+F)^2, & g_{N,K} &= \frac{5}{3}D^2 - 2DF + 3F^2, & g_{N,\eta_8} &= \frac{1}{6}(D-3F)^2, \\ g_{\Lambda,\pi} &= 2D^2, & g_{\Lambda,K} &= \frac{2}{3}D^2 + 6F^2, & g_{\Lambda,\eta_8} &= \frac{2}{3}D^2, \\ g_{\Sigma,\pi} &= \frac{2}{3}D^2 + 4F^2, & g_{\Sigma,K} &= 2D^2 + 2F^2, & g_{\Sigma,\eta_8} &= \frac{2}{3}D^2, \\ g_{\Xi,\pi} &= \frac{3}{2}(D-F)^2, & g_{\Xi,K} &= \frac{5}{3}D^2 + 2DF + 3F^2, & g_{\Xi,\eta_8} &= \frac{1}{6}(D+3F)^2, \end{aligned} \quad (5.15)$$

where D and F are the usual SU(3) LECs describing the LO baryon-meson-baryon coupling. For instance, $g_{N,\pi} = (3/2)(D+F)^2 = (3/2)\hat{g}_A^2$ is related to the axial charge of the nucleon in the chiral limit \hat{g}_A^2 . Note that truncating the loop-function (5.14) at $\mathcal{O}(x^3)$, i.e. expanding about $m_0 = \infty$, results in the HBChPT [115] expression [121, 122]

$$f_O(x) = -\pi x^3 + \mathcal{O}(x^4). \quad (5.16)$$

¹¹Note that in the naming conventions that are usually employed within HBChPT, this order is labelled as “NLO”. Also note that in NNLO BChPT the baryon masses are accurate to $\mathcal{O}(m_q^{3/2})$ in the quark masses $m_q \sim p^2$. Due to the absence of such terms in the mesonic sector, NLO meson ChPT already contains all $\mathcal{O}(p^4)$ terms, while the LO GMOR relations are accurate at $\mathcal{O}(p^2)$. Consequently, both within NLO and NNLO BChPT it is sufficient to employ the GMOR relations to convert quark masses into meson masses. NLO meson ChPT is only needed in conjunction with BChPT at NNNLO.

¹²The $g_{O,P}$ satisfy the constraints $g_{O,\pi} + g_{O,K} + g_{O,\eta_8} = 2(5D^2 + 9F^2)/3$ and $2g_{N,P} + g_{\Lambda,P} + 3g_{\Sigma,P} + 2g_{\Xi,P} = 2c_P(5D^2 + 9F^2)/3$, where the couplings $g_{O,P}$ already include the meson multiplicities c_P ($c_\pi = 3$, $c_K = 4$, $c_{\eta_8} = 1$).

We remark that the NNNLO BChPT expression is also known [123].

The functional form above, when rescaled, reads

$$\begin{aligned} m_O(\mathbb{M}_\pi, \mathbb{M}_K) = m_0 + \bar{\mathbb{b}} \bar{\mathbb{M}}^2 + \delta \mathbb{b}_O \delta \mathbb{M}^2 \\ + g_{O,\pi} f_O \left(\frac{\mathbb{M}_\pi}{m_0} \right) + g_{O,K} f_O \left(\frac{\mathbb{M}_K}{m_0} \right) + g_{O,\eta_8} f_O \left(\frac{\mathbb{M}_{\eta_8}}{m_0} \right). \end{aligned} \quad (5.17)$$

If we were to go to the next order then we would have to include corrections to the GMOR relations when replacing the quark masses by the meson masses, as well as additional terms arising from the $\mathcal{O}(p^4)$ chiral expansion of t_0 .

The couplings $g_{O,P}$ are related to the original ones $g_{O,P}$ by substituting $D \mapsto \mathbb{D}, F \mapsto \mathbb{F}$, where

$$D^2 = \frac{(4\pi \mathbb{F}_0)^2}{m_0^3} \mathbb{D}^2, \quad F^2 = \frac{(4\pi \mathbb{F}_0)^2}{m_0^3} \mathbb{F}^2. \quad (5.18)$$

In total our NNLO fit to the octet baryon masses has only 12 parameters: the six parameters describing the lattice spacing dependence of eq. (4.6) ($c_o, \bar{c}_o, \delta c_N, \delta c_\Lambda, \delta c_\Sigma, \delta c_\Xi$), the four parameters describing the linear, NLO chiral continuum limit behaviour ($m_0, \bar{\mathbb{b}}, \mathbb{b}_D, \mathbb{b}_F$) and, in addition, \mathbb{F} and \mathbb{D} that parameterize the 12 couplings $g_{O,P}$.

Decuplet baryon masses have been computed in SU(3) HBChPT in ref. [124], to NNLO in covariant SU(2) BChPT with infrared cut-off (IR BChPT) [125] as well as in SU(3) EOMS BChBT to NNLO in ref. [126] and to NNNLO in ref. [127]. Restricting ourselves to self-energy diagrams that do not contain octet baryon exchanges, the relevant infinite volume expression reads

$$\begin{aligned} m_D(M_\pi, M_K) = m_{D0} + \bar{t} \bar{M}^2 + \delta t_D \delta M^2 \\ + \frac{m_{D0}^3}{(4\pi F_0)^2} \left[g_{D,\pi} f_D \left(\frac{M_\pi}{m_{D0}}, \frac{M_\pi}{m_0} \right) + g_{D,K} f_D \left(\frac{M_K}{m_{D0}}, \frac{M_K}{m_0} \right) \right. \\ \left. + g_{D,\eta_8} f_D \left(\frac{M_{\eta_8}}{m_{D0}}, \frac{M_{\eta_8}}{m_0} \right) \right]. \end{aligned} \quad (5.19)$$

The decuplet loop-function in the EOMS regularization [126] reads:¹³

$$f_D(x, y) = -2x^3 \left\{ \left(1 - \frac{x^2}{4} \right)^{5/2} \arccos \left(\frac{x}{2} \right) + \frac{x}{64} [17 - 2x^2 + 2(30 - 10x^2 + x^4) \ln(y)] \right\}, \quad (5.20)$$

where we use the same renormalization scale $\mu = m_0$ as in the octet baryon case. This is the reason for the two arguments of the loop function. Truncating f_D at $\mathcal{O}(x^3)$ again gives the HBChPT result [124]

$$f_D(x) = -\pi x^3. \quad (5.21)$$

¹³It is derived in the IR regularization in ref. [125].

The decuplet couplings $g_{D,P}$ are given as¹⁴ [124, 126]

$$\begin{aligned}
g_{\Delta,\pi} &= \frac{25}{54}\mathcal{H}^2, & g_{\Delta,K} &= \frac{5}{27}\mathcal{H}^2, & g_{\Delta,\eta_8} &= \frac{5}{54}\mathcal{H}^2, \\
g_{\Sigma^*,\pi} &= \frac{20}{81}\mathcal{H}^2, & g_{\Sigma^*,K} &= \frac{40}{81}\mathcal{H}^2, & g_{\Sigma^*,\eta_8} &= 0 \\
g_{\Xi^*,\pi} &= \frac{5}{54}\mathcal{H}^2, & g_{\Xi^*,K} &= \frac{5}{9}\mathcal{H}^2, & g_{\Xi^*,\eta_8} &= \frac{5}{54}\mathcal{H}^2 \\
g_{\Omega,\pi} &= 0, & g_{\Omega,K} &= \frac{10}{27}\mathcal{H}^2, & g_{\Omega,\eta_8} &= \frac{10}{27}\mathcal{H}^2.
\end{aligned} \tag{5.22}$$

This means that the NNLO fit to the decuplet baryon masses has 10 parameters: the six parameters describing the lattice spacing dependence (c_d , \bar{c}_d , δc_Δ , δc_{Σ^*} , δc_{Ξ^*} , δc_Ω), the three parameters describing the linear NLO chiral continuum limit behaviour (\mathfrak{m}_{D0} , $\bar{\mathfrak{t}}$, \mathfrak{t}_D) and, in addition, a parameter \mathbb{H} that is related to the LEC \mathcal{H} in analogy to eq. (5.18):

$$\mathcal{H}^2 = \frac{(4\pi F_0)^2}{\mathfrak{m}_{D0}^3} \mathbb{H}^2. \tag{5.23}$$

If fitting the decuplet baryons alone, one could also have set $\mu = m_{D0}$, thereby removing one of the arguments of the loop function eq. (5.20). However, for the decuplet baryons octet baryon loops cannot be neglected. This is discussed in the following subsection. Note that including finite volume effects in the parametrization does not involve additional LECs, see appendix B.

5.3 Octet-decuplet BChPT: including the small scale expansion

For most of our data points the gap between octet and decuplet masses is of a similar size as the pion mass. Hence, we should also consider that at NNLO the decuplet self-energies receive contributions from octet baryon plus meson loops and the octet energies receive contributions from decuplet loops. In particular, this effect cannot be neglected when discussing decuplet baryons since (with the exception of the Ω) these strongly decay into octet baryons and mesons at the physical quark mass point. The small scale expansion (SSE) [125, 128, 129] is the theoretical framework to incorporate these baryon loop effects. This was first worked out for the Δ baryon in refs. [130] and [131] in SU(2) HBChPT and in SU(2) BChPT, respectively, and later generalized to SU(3), employing EOMS BChPT [126]. It turns out that these effects can be accounted for to NNLO with just one additional LEC, \mathcal{C} .¹⁵

$$m_B \mapsto m_B + \mathcal{C}^2 \frac{\delta^3}{(4\pi F_0)^2} \left[\xi_{B,\pi} h_B \left(\frac{M_\pi}{\delta} \right) + \xi_{B,K} h_B \left(\frac{M_K}{\delta} \right) + \xi_{B,\eta_8} h_B \left(\frac{M_{\eta_8}}{\delta} \right) \right], \tag{5.24}$$

where the coefficients $\xi_{B,P}$ are listed in table 8 and in the usual SSE power counting $\delta = m_{D0} - m_0 = \mathcal{O}(p)$ is an additional small scale.

In general, the loop functions [126] will separately depend on M/m_0 and on δ . However, for simplicity, for these transition terms we will only consider the HBChPT limit [132–134],

¹⁴For the LEC \mathcal{H} we use the normalization of ref. [124]. The decuplet couplings satisfy the SU(3) constraints $g_{D,\pi} + g_{D,K} + g_{D,\eta_8} = 20\mathcal{H}^2/27$ and $4g_{\Delta,P} + 3g_{\Sigma^*,P} + 2g_{\Xi^*,P} + g_{\Omega,P} = 25c_P\mathcal{H}^2/27$ where $c_\pi = 3$, $c_K = 4$, $c_{\eta_8} = 1$.

¹⁵For the LEC \mathcal{C} we use the normalization of refs. [63, 132, 133], where $\mathcal{C}^2 = g_{\Delta N}^2$ [134].

Table 8. The coefficients $\xi_{B,P}$ of eq. (5.24).

	N	Λ	Σ	Ξ	Δ	Σ^*	Ξ^*	Ω
π	$\frac{4}{3}$	1	$\frac{2}{9}$	$\frac{1}{3}$	$\frac{1}{3}$	$\frac{5}{18}$	$\frac{1}{6}$	0
K	$\frac{1}{3}$	$\frac{2}{3}$	$\frac{10}{9}$	1	$\frac{1}{3}$	$\frac{2}{9}$	$\frac{1}{3}$	$\frac{2}{3}$
η_8	0	0	$\frac{1}{3}$	$\frac{1}{3}$	0	$\frac{1}{6}$	$\frac{1}{6}$	0

in which the respective functions for octet and decuplet baryons read:

$$h_O(x) = -(2 - 3x^2) \ln\left(\frac{x}{2}\right) - \frac{1}{2}x^2 - 2w(x), \quad (5.25)$$

$$h_D(x) = (2 - 3x^2) \ln\left(\frac{x}{2}\right) + \frac{1}{2}x^2 - 2w(-x), \quad (5.26)$$

$$w(x) = \begin{cases} (x^2 - 1)^{3/2} \arccos(x^{-1}) & , |x| \geq 1 \\ (1 - x^2)^{3/2} \ln\left(|x^{-1} + \sqrt{x^{-2} - 1}|\right) & , |x| < 1 \end{cases}. \quad (5.27)$$

For $w(x)$ we encounter both cases since we cover simulation points with $M_\pi < 300 \text{ MeV} \approx \delta$ as well as with $M_\pi > \delta$. In the first case, the poles of the decuplet baryon propagators will acquire imaginary parts in an infinite volume, due to the possibility of a real p -wave decay into a pseudoscalar meson and an octet baryon. For a detailed discussion of the situation in a finite volume, see, e.g., ref. [135]. We take the real part of the logarithm — hence the modulus in its argument — and we will only include stable decuplet baryons into our fits. Again, our rescaled parameter \mathbb{C} is trivially related to the LEC \mathcal{C} :

$$\mathcal{C}^2 = \frac{(4\pi\mathbb{F}_0)^2}{(\mathfrak{m}_{D0} - \mathfrak{m}_0)^3} \mathbb{C}^2. \quad (5.28)$$

The joint NNLO octet and decuplet fits have a total of 23 free parameters: the 12 parameters of the octet parametrization, the 10 parameters of the decuplet parametrization plus \mathbb{C} . Twelve of these are used to parameterize the lattice spacing dependence. Like for the fits of section 5.2 without octet-decuplet transitions, incorporating finite volume effects does not involve additional LECs, see appendix B.

5.4 GMO: Taylor expansion about an SU(3) symmetric point

Instead of expanding about the chiral limit using BChPT, one can also Taylor expand, e.g., about the symmetric point (where $M_K = M_\pi = M^*$), implementing group theoretical constraints [62] that generalize the Gell-Mann–Okubo relations [113, 114]. In this case the only assumptions we make are that SU(3) flavour symmetry is broken by the quark masses and that to leading order these quark masses are proportional to squared pseudoscalar meson masses. This is less restrictive than ChPT as no additional assumption about the symmetries of interactions mediated by Goldstone bosons is made. Therefore, the Taylor expansion will involve a larger number of parameters. In principle, one can expand, employing the same

formulae, about any point along the symmetric line, however, the domain of analyticity cannot extend beyond $M_{\eta_8} \geq M_K \geq M_\pi \geq 0$.

At quadratic order in the quark masses we obtain

$$\begin{aligned} m_O(M_\pi, M_K) &= m^* + \bar{b}^* (\bar{M}^2 - M^{*2}) + \bar{d} (\bar{M}^2 - M^{*2})^2 \\ &\quad + \delta b_O^* \delta M^2 + \delta d_O \delta M^2 (\bar{M}^2 - M^{*2}) + \delta e_O \delta M^4, \end{aligned} \quad (5.29)$$

$$\begin{aligned} m_D(M_\pi, M_K) &= m_D^* + \bar{t}^* (\bar{M}^2 - M^{*2}) + \bar{u} (\bar{M}^2 - M^{*2})^2 \\ &\quad + \delta t_D^* \delta M^2 + \delta u_D \delta M^2 (\bar{M}^2 - M^{*2}) + \delta v_D \delta M^4, \end{aligned} \quad (5.30)$$

for the octet and decuplet baryons, respectively, where $M^{*2} = \frac{2}{3}\phi_4^* = 0.740$ is chosen such that it is close to \bar{M}_{ph}^2 . Since the above is a polynomial in $(\bar{M}^2 - M^{*2})$, we can absorb the dependence on M^{*2} into the coefficients of the expansion. At the above order this amounts to the replacements

$$m^* = m_0 + \bar{b} M^{*2} + \bar{d} M^{*4} \quad \bar{b}^* = \bar{b} + 2\bar{d} M^{*2}, \quad \delta b_O^* = \delta b_O + \delta d_O M^{*2}, \quad (5.31)$$

$$m_D^* = m_{D0} + \bar{t} M^{*2} + \bar{u} M^{*4}, \quad \bar{t}^* = \bar{t} + 2\bar{u} M^{*2}, \quad \delta t_D^* = \delta t_D + \delta u_D M^{*2}. \quad (5.32)$$

In terms of the new parameters, eqs. (5.29) and (5.30) read

$$m_O(M_\pi, M_K) = m_0 + \bar{b} \bar{M}^2 + \delta b_O \delta M^2 + \bar{d} \bar{M}^4 + \delta d_O \delta M^2 \bar{M}^2 + \delta e_O \delta M^4, \quad (5.33)$$

$$m_D(M_\pi, M_K) = m_{D0} + \bar{t} \bar{M}^2 + \delta t_D \delta M^2 + \bar{u} \bar{M}^4 + \delta u_D \delta M^2 \bar{M}^2 + \delta v_D \delta M^4, \quad (5.34)$$

respectively, where at linear order in the quark masses, one recovers eqs. (5.1)–(5.5), reducing the dependence to four and three SU(3) BChPT LECs for the octet and decuplet baryons, respectively. While the expansions above are valid near any point along the symmetric line, they can only converge for positive pion masses, i.e. for $\delta M^2 < 3\bar{M}^2$. This explicitly excludes the chiral limit and also explains the absence of terms that are non-analytic functions of the quark masses; beyond the linear order, the above expansions are incompatible with BChPT. However, all our points, including the physical point, are far away from the chiral limit so that the above parametrizations may still accurately represent the data, as long as the ratio $\delta M^2/\bar{M}^2$ is sufficiently small.

The parameters δb_O and δt_D satisfy the SU(3) constraints (5.4) and (5.5) and analogous relations also apply to δd_O and δu_D :

$$\delta d_N = \frac{2}{3}(3d_F - d_D), \quad \delta d_\Lambda = -\frac{4}{3}d_D, \quad \delta d_\Sigma = \frac{4}{3}d_D, \quad \delta d_\Xi = -\frac{2}{3}(3d_F + d_D), \quad (5.35)$$

$$\delta u_\Lambda = -u_D, \quad \delta u_{\Sigma^*} = 0, \quad \delta u_{\Xi^*} = u_D, \quad \delta u_\Omega = 2u_D. \quad (5.36)$$

There are no SU(3) constraints [62] regarding the octet baryon parameters δe_O . In this case we end up with a total of 11 parameters ($m_0, \bar{b}, b_D, b_F, \bar{d}, d_D, d_F, \delta e_N, \delta e_\Lambda, \delta e_\Sigma, \delta e_\Xi$), in addition to the 6 parameters of eq. (4.6) parameterizing the lattice spacing dependence ($c_o, \bar{c}_o, \delta c_N, \delta c_\Lambda, \delta c_\Sigma, \delta c_\Xi$).

For the decuplet baryons one of the parameters accompanying the $\mathcal{O}(\delta M^4)$ terms can be eliminated [62]: we rewrite the δv_D as

$$\delta v_\Delta = v_F - v_D, \quad \delta v_{\Sigma^*} = v_G, \quad \delta v_{\Xi^*} = v_G + v_D, \quad \delta v_\Omega = v_F + 2v_D, \quad (5.37)$$

such that we count $8 + 6$ parameters in total ($m_{D0}, \bar{t}, t_D, \bar{u}, u_D, v_D, v_F, v_G$ as well as $c_d, \bar{c}_d, \delta c_\Delta, \delta c_{\Sigma^*}, \delta c_{\Xi^*}, \delta c_\Omega$).

6 Results for the scale $t_{0,\text{ph}}$, the spectrum and the low energy constants

The methods used to compute baryonic two-point functions and to obtain the masses from these are detailed in appendix E. The statistical analysis methods, taking into account autocorrelations in Monte Carlo time and correlations between different masses obtained on the same ensemble, are described in appendix F. We carry out fully correlated fits according to the parametrizations introduced in sections 4 and 5. In section 6.1 we introduce the naming scheme of the fit functions that we employ. We continue with explaining the fit strategy and cuts on the data in section 6.2. We then illustrate this for the example of one parametrization in section 6.3, before we determine the scale parameter $\sqrt{8t_{0,\text{ph}}}$ from the mass of the Ξ baryon in section 6.4, where we also detail our model averaging procedure and investigate the systematics. In section 6.5 we determine the spectrum of octet and decuplet baryons and compare this to expectations. Then, in section 6.6, we compute the strange and light quark σ terms of the octet and the Ω baryons. In section 6.7 we determine the SU(3) (H)BChPT LECs and for the nucleon also the LO SU(2) BChPT LECs. Finally, we compare the results for the scale parameter, the baryon spectrum and the pion-nucleon σ term to literature values in section 6.8.

6.1 Fits carried out and the naming conventions used

We find that linear fits (section 5.1) poorly describe the data and do not consider these further. When employing the (H)BChPT parametrizations (sections 5.2 and 5.3), we only fit the decuplet baryon masses together with the octet masses (SSE, section 5.3). Fitting the decuplet masses alone would amount to ignoring loops involving an octet baryon and a meson. In contrast, the GMO Taylor expansions (section 5.4) for octet and decuplet baryons are independent of one another.

We label fits generically as “**multiplet(s) parametrization (FV) ($\text{SC}^{L|\infty}$)**”, where

- “**octet (H)BChPT**” refers to eq. (5.17) with the loop-functions eq. (5.14) and eq. (5.16) for BChPT and HBChPT, respectively. The order p^2 coefficients can be expressed in terms of $\overline{\mathbb{b}}$, $\mathbb{b}_{\mathbb{D}}$ and $\mathbb{b}_{\mathbb{F}}$, see eq. (5.8), whereas the p^3 coefficients can be written in terms of \mathbb{D} and \mathbb{F} via eq. (5.15). In addition, the (rescaled) mass parameter \mathfrak{m}_0 represents the mass of the octet in the SU(3) chiral limit.
- “**octet-decuplet (H)BChPT**” refers to simultaneous (SSE) fits utilizing eqs. (5.17), (5.19) and (5.24) (with rescaled variables) of sections 5.2 and 5.3. For BChPT the loop-functions eqs. (5.14), (5.20) and (5.25)–(5.27) are used, while for HBChPT the former two are replaced by the one defined in eq. (5.16). There are five independent order p^2 coefficients, see eqs. (5.8) and (5.9), namely $\overline{\mathbb{b}}$, \mathbb{b}_D , \mathbb{b}_F , $\overline{\mathfrak{t}}$ and \mathfrak{t}_D . The order p^3 coefficients depend on the rescaled parameters \mathbb{D} , \mathbb{F} , \mathbb{H} and \mathbb{C} , see eqs. (5.15) and (5.22) and table 8. The relations between the rescaled parameters and the corresponding LECs are given in eqs. (5.18), (5.23) and (5.28). In addition to the nine above parameters, we have the chiral octet and decuplet baryon masses \mathfrak{m}_0 and \mathfrak{m}_{D0} .
- “**octet GMO**” and “**decuplet GMO**” correspond to eqs. (5.33) and (5.34) of section 5.4, respectively, with the SU(3) constraints eqs. (5.8)–(5.9) and (5.35)–(5.37).

This amounts to 11 and 8 free parameters for the continuum limit parametrizations of the octet and decuplet masses, respectively.

An appended “**FV**” means that the (H)BChPT finite volume effects of appendix B are included. For “octet BChPT FV” and “octet HBChPT FV” fits these are eqs. (B.1) and (B.2), respectively. Regarding “octet-decuplet BChPT FV” and “octet-decuplet HBChPT FV”, also eqs. (B.3)–(B.6) and (B.7)–(B.8) are added, respectively. These expressions do not include any additional parameters. For “octet GMO FV” fits, the octet baryon masses are first corrected for finite volume effects using estimates from the octet BChPT FV fits. We do not carry out any “decuplet GMO FV” fits as the finite volume effects are very small.

We either append “**SC[∞]**” or “**SC^L**” to the fits involving the decuplet masses, referring to stability cuts. In the former case all decuplet baryons that will become unstable at the given pseudoscalar masses in an infinite volume are excluded from the fit, while in the latter case only the decuplet baryons that are unstable in the box of volume L^3 are disregarded.

For the lattice spacing dependence of the baryon masses, we follow eq. (4.6), which amounts to the six fit parameters each for the octet ($c_o, \bar{c}_o, \delta c_N, \delta c_\Lambda, \delta c_\Sigma, \delta c_\Xi$) and decuplet baryons ($c_d, \bar{c}_d, \delta c_\Delta, \delta c_{\Sigma^*}, \delta c_{\Xi^*}, \delta c_\Omega$). This implies a total of 12, 23, 17 and 14 free parameters, respectively, for the octet (H)BChPT, octet-decuplet (H)BChPT, octet GMO and decuplet GMO fits. We also investigate the significance of the individual discretization effects, adding or removing terms. Further details are given in section 6.4.

6.2 Fit strategy and data cuts

We carry out a number of fits to the pseudoscalar meson mass, volume and lattice spacing dependence of the octet and decuplet baryon masses. The continuum limit parametrizations are introduced in sections 5.1–5.4 and the finite volume expressions are collected in appendix B. The lattice spacing dependence is parameterized according to eq. (4.6). The naming scheme for different fit ansätze is explained in section 6.1 above. We exclude ensembles with $M_\pi > 450$ MeV or $L < 2.3$ fm from all fits. We will use the mass of the Ξ baryon to fix the scale. The masses of the pion and the kaon are then employed to determine the physical point in the quark mass plane.

In order to explore the systematics, we vary the continuum limit parametrization and, in addition, we explore the lattice spacing dependence by including additional lattice spacing dependent terms and/or by setting some of the discretization terms to zero. Moreover, we vary the fit ranges, excluding small volumes, excluding the coarsest lattice spacing or — for the (H)BChPT fits — excluding ensembles with large average pion masses. The latter mass cuts are illustrated in figure 13, which also provides an overview of the ensembles used. The mass cuts are not applied when carrying out the GMO fits. As explained in section (5.4), in this case δM^2 is the parameter that governs the convergence properties. Since this is maximal for our two physical point ensembles and we wish to obtain the spectrum for physical quark masses, it does not make sense to impose a cut on δM^2 . Regarding the (H)BChPT fits, the two ensembles in the top right corner of the figure are always excluded, i.e. we only include ensembles with $\phi_4 < 1.6$. These two ensembles are, however, always included in the GMO fits.

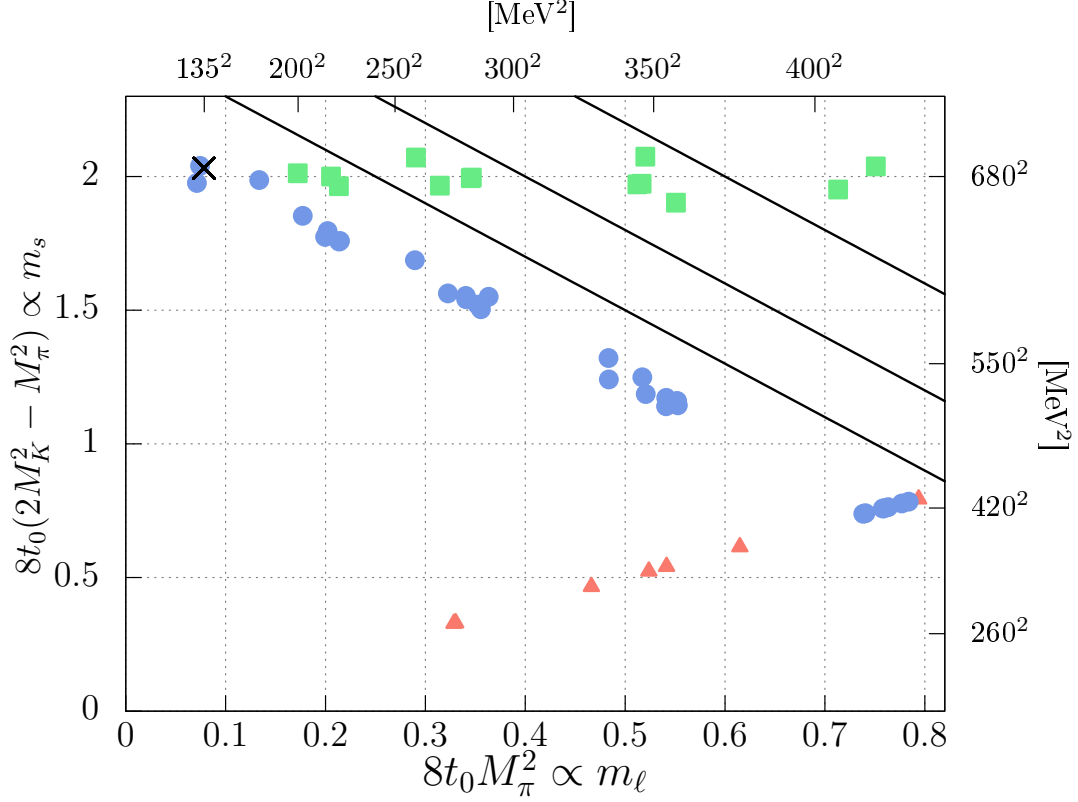


Figure 13. The ensembles used for the six different lattice spacings shown in the quark mass plane. The green squares indicate the ensembles on the trajectory where the strange quark mass is kept constant, the blue circles indicate ensembles with a constant sum of the $N_f = 2 + 1$ quark masses and the red triangles are ensembles on the symmetric $m_s = m_\ell$ line. The latter two sets of points intersect near $8t_0 M_\pi^2 = 2\phi_4^*/3 = 0.74$. The cross indicates the physical point and the black lines correspond to mass cuts at $\phi_4 = 12t_0 \bar{M}^2 = 1.25, 1.4$ and 1.6 , respectively. The physical point is at $\phi_4 \approx 1.093$.

We start with one fit to illustrate the scale setting procedure, the physical point determination and how the data that depend on M_K , M_π , L and a are shifted to enable their visualization in two-dimensional figures. We then investigate the systematics and we present final results on the scale parameter, the octet and the decuplet baryon masses at the physical point.

6.3 Illustration of the scale setting procedure

We start with an order p^3 (NNLO) BChPT fit of the octet baryon masses obtained on the 44 ensembles with $\phi_4 < 1.6$, $M_\pi < 450$ MeV and $L > 2.3$ fm, including the finite volume corrections eq. (B.1) (the octet BChPT FV fit, see section 6.1). Fourteen of these ensembles are on the $m_s = m_\ell$ line. For the remaining 30 ensembles, the four octet baryon masses are non-degenerate. In total this amounts to 134 data points. These are fitted by 12 parameters, which correspond to c_o , \bar{c}_o , δc_N , δc_Λ , δc_Σ and δc_Ξ , accounting for lattice spacing effects, and to the LECs m_0 , b_0 , b_D , b_F , F and D , describing the quark mass and the volume

dependence.¹⁶ We obtain the value $\chi^2/N_{\text{DF}} = 1.16$, taking into account all correlations between the four baryon and the two meson masses. Note that the 6×6 covariance matrices reduce to 2×2 matrices on the symmetric line $m_s = m_\ell$. The quality of this fit suggests that our data cannot resolve the additional LECs that would appear at order p^4 .

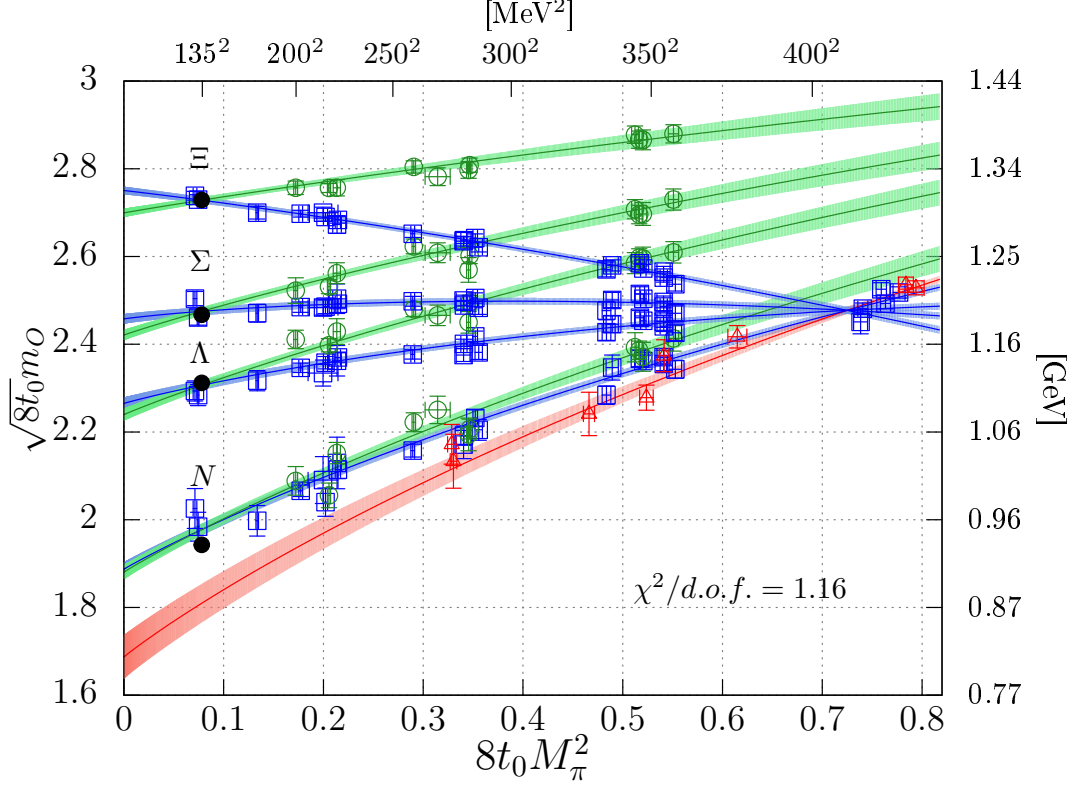


Figure 14. Octet BChPT FV fit (see section 6.1 for the naming convention and references to the equations used) for $\phi_4 < 1.6$. The data points are corrected for the fitted lattice spacing and finite volume effects. The blue squares ($\text{Tr } M = \text{const}$) and the green circles ($\hat{m}_s \approx \text{const}$) are in addition shifted according to the fit to kaon masses that correspond to constant values of $\phi_4 = 12t_0\overline{M}^2$ and $8t_0(2M_K^2 - M_\pi^2)$, respectively, which coincide with those at the physical point. The red triangles denote the symmetric $m_s = m_\ell$ line, i.e. $M_K = M_\pi$. The curves with error bands are the projections of the continuum limit fit onto these trajectories. The black circles are the experimental masses, corrected for QCD and QED isospin breaking effects, where m_Ξ was used to set the scale, see eqs. (4.7) and (4.8). The red band approaches the SU(3) chiral limit.

The resulting dependence on the pion mass, with the data points shifted to the infinite volume and continuum limits, is shown in figure 14. The scale $t_{0,\text{ph}}$ is then computed from the continuum limit parametrization of the Ξ baryon mass as a function of the squared pion and kaon masses (all in units of $8t_0$), according to eqs. (4.7) and (4.8) via an iterative procedure. The uncertainties of the experimental hadron masses that have been corrected regarding the up and down quark mass splitting and electrical charge effects (see appendix A) are implemented via pseudo-bootstrap distributions in the error analysis. Once $t_{0,\text{ph}}$ has been

¹⁶We have already corrected the meson masses for volume effects, see section 4.3.

determined, the physical point on the $8t_0 M_\pi^2$ axis is known too. For comparison, we also show the (pseudo-)experimental values, with isospin breaking effects removed, of table 14 as solid black circles in the figure. While the agreement with the experimental value of m_Ξ — that has been used to set the scale — is trivial, the other three masses are predicted. The red curve with $m_s = m_\ell$ approaches the value $\sqrt{8t_{0,\text{ch}}}m_0$ in the chiral limit. The kaon masses along the blue curves are such that $8t_0(2M_K^2 + M_\pi^2) = 8t_{0,\text{ph}}(2M_{K,\text{ph}}^2 + M_{\pi,\text{ph}}^2)$, i.e. \overline{M}^2 is kept constant in units of t_0 , while the green curves correspond to $8t_0(2M_K^2 - M_\pi^2) = 8t_{0,\text{ph}}(2M_{K,\text{ph}}^2 - M_{\pi,\text{ph}}^2)$, i.e. the strange quark mass is kept approximately fixed. These two sets of curves intersect at the physical point. The original data are not exactly aligned along these two sets, therefore, the blue squares and green circles depicted in the figure have been shifted somewhat, according to the fit, to the respective kaon masses.

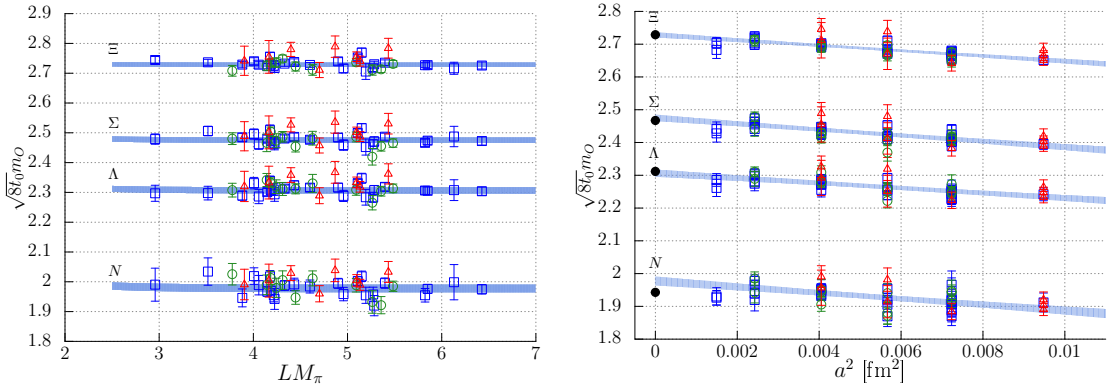


Figure 15. The volume dependence (left) and the lattice spacing dependence (right) of the four octet baryon masses. The underlying octet BChPT FV fit (see section 6.1) is identical to the one shown in figure 14. Again, red triangles, blue squares and green circles correspond to the $m_s = m_\ell$, $\text{Tr } M = \text{const}$ and $\hat{m}_s \approx \text{const}$ quark mass trajectories, respectively.

We show other projections of the same fit in figure 15. In this case all the data are projected to the physical point in terms of the pion and kaon masses. On the left, additionally, these are also projected to the continuum limit and shown as a function of the linear spatial lattice dimension in units of the inverse pion mass. The blue bands correspond to the fit. The data look rather flat and also the volume dependence suggested by the BChPT FV fit is mild. Nevertheless, we will see that omitting finite volume effects deteriorates the fit quality, without reducing the number of parameters. In the right panel of figure 15 the dependence of the data (projected onto the physical quark masses and infinite volume) on the squared lattice spacing is shown. This is significant, however, the slope of $\sqrt{8t_0}m_O$ as a function of a^2 is similar for all four baryons. It is also obvious from this figure that there is some tension between the nucleon mass determined by the fit and the experimental point on the level of two to three standard deviations. However, for the fit discussed above, the χ^2 -value is larger than the number of degrees of freedom. We will vary the fit ranges and parametrization to explore the systematics. We start by determining the scale.

6.4 Determination of the scale parameter $\sqrt{8t_{0,\text{ph}}}$

In order to explore the systematics, we first impose different cuts on the data for the octet BChPT FV fit (defined in section 6.1) and then we consider different parametrizations. Regarding the fit ranges,

- we include or exclude our coarsest **lattice spacing**,
- we impose the **volume** cuts $LM_\pi > 4$, $LM_\pi > 3.5$ or we use all our data with $L > 2.3$ fm and
- we impose the cuts on the average **meson mass** $12t_0\overline{M}^2 < 1.6$, $12t_0\overline{M}^2 < 1.4$ or $12t_0\overline{M}^2 < 1.25$, see figure 13, where $12t_0\overline{M}^2 \approx 1.09$ at the physical point.

This gives a total of 18 different fits with values χ^2/N_{DF} ranging from 0.94 (with the cuts $LM_\pi > 4$ and $12t_0\overline{M}^2 < 1.25$) to $\chi^2/N_{\text{DF}} = 1.20$ (with the cuts $a < 0.09$ fm and $12t_0\overline{M}^2 < 1.6$ but no cut on the volume, except for $L > 2.3$ fm).

We use the Akaike Information Criterion (AIC) [136] to assign a weight

$$w_j = A \exp \left[-\frac{1}{2} (\chi_j^2 - N_{\text{DF},j} + k_j) \right] \quad (6.1)$$

to the result of each fit $j \in \{1, \dots, N_M\}$, see, e.g., eq. (161) of the e-print version of ref. [137] and references therein.¹⁷ The normalization A is such that $\sum_i^{N_M} w_i = 1$. χ_j^2 denotes the χ^2 -value of the fit j , k_j the number of fit parameters and $N_{\text{DF},j} = n_j - k_j$ the number of degrees of freedom. The above equation extends the AIC to also include fits where the number of data points n_j is varied and not only the fit function. It assumes no correlations between the removed and the remaining data points. Moreover, the parametrization should not vary with the included data. Both criteria are satisfied since we exclude whole ensembles from the analysis, while maintaining the same parametrizations. One concern with this procedure may be the preference for fits with low χ^2 -values, even if these are much smaller than N_{DF} . However, this is not a problem for our current analysis where for the “best” fit that enters the averaging we obtain $\chi^2/N_{\text{DF}} \approx 0.94$, which, given the error on the error, is not significantly different from one.

For each parameter a that we are interested in, we generate for each fit j a bootstrap distribution of a_j , $a_j(b)$, with N_b bootstrap samples b . We then determine the one- σ confidence interval by sorting the values $a_j(b)$ in ascending order and then determining the 15.9% and 84.1% percentiles, counting each entry $a_j(b)$ according to its weight w_j/N_b . The central values that we quote correspond to the median of this distribution. Usually, this is very close to the naive weighted average $\sum_j w_j a_j$.

The procedure is illustrated for $\sqrt{8t_{0,\text{ph}}}$, obtained from m_Ξ , and the nucleon mass m_N in figure 16, where the grey boxes with thin vertical lines (indicating the central values)

¹⁷Recently, instead of subtracting $N_{\text{DF}} - k$ from the χ^2 -value in the exponent, in ref. [138] it has been suggested to subtract $-2n_{\text{cut}} - 2k = \text{const} + 2N_{\text{DF}}$ instead, where n_{cut} is the number of removed data points. This seems counter-intuitive: for a good fit $\chi^2 \sim N_{\text{DF}}$, therefore, this change results in a very strong preference for fits that include as many data points as possible, even if the corresponding χ^2/N_{DF} -values are significantly larger.

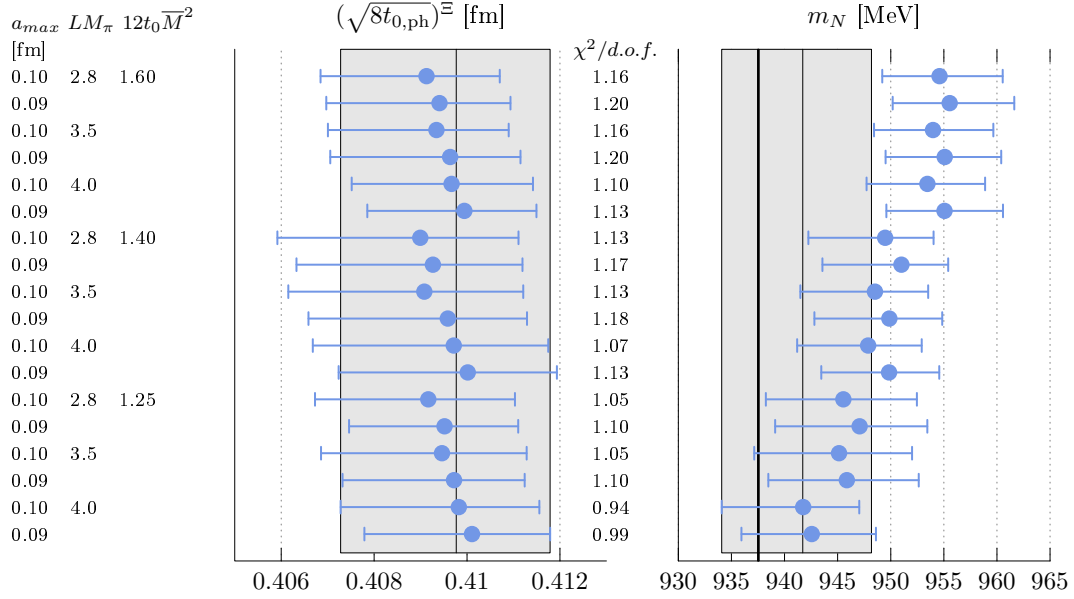


Figure 16. Results for $\sqrt{8t_{0,ph}}^\Xi$ determined from the mass of the Ξ baryon, together with results for the nucleon mass m_N from the BChPT FV fits (see section 6.1). On the left the cuts on the lattice spacing, the spatial lattice extent in units of the pion mass and the average pseudoscalar meson mass are indicated. In the centre the corresponding χ^2/N_{DF} -values are shown. The grey boxes correspond to the 68% confidence intervals of the AIC averaging procedure. Also indicated as a thick vertical line is the experimental nucleon mass, corrected for isospin breaking effects.

correspond to the outcome of the AIC averaging procedure. Also shown as a thick vertical line is the experimental nucleon mass, corrected for QCD and QED isospin breaking effects. Within our uncertainty of about 7 MeV, we are able to reproduce this mass. Note that the fit discussed in section 6.3 above corresponds to the first fit shown in figure 16 with $\chi^2/N_{DF} = 1.16$, which overestimates the nucleon mass by almost three standard deviations. While $t_{0,ph}$ is quite independent of the data cuts, the nucleon mass decreases systematically with the cut on $12t_0\overline{M}^2$. This can easily be understood from figure 14: the Ξ baryon data are quite precise and its physical point value is well constrained by the intersection of the two trajectories in the quark mass plane. Therefore, it depends only mildly on the parametrization and the cuts. In contrast, not only are the statistical errors of the nucleon mass data larger but also the two trajectories that intersect at the physical point are not very different from each other, resulting in a less precise determination.

We investigate different parametrizations of the lattice spacing dependence. For $O \in \{N, \Lambda, \Sigma, \Xi\}$, we assumed the generic form $(a^2/8t_0^*)(c_o + \bar{c}_o\overline{M}^2 8t_0 + \delta c_O \delta \overline{M}^2 8t_0)$, see eq. (4.6). We carry out our AIC procedure separately for 10 additional functional forms for these effects. The results are shown in figure 17. Within our standard octet BChPT FV fit ($c_o, \bar{c}_o, \delta c_O \neq 0$), δc_N is statistically compatible with zero. This motivates us to carry out an additional 11-parameter fit ($\delta c_N = 0$) and two 10-parameter fits ($\delta c_N = c_o = 0$ and $\delta c_N = \bar{c}_o = 0$). All these fits give somewhat larger nucleon masses but have little impact on

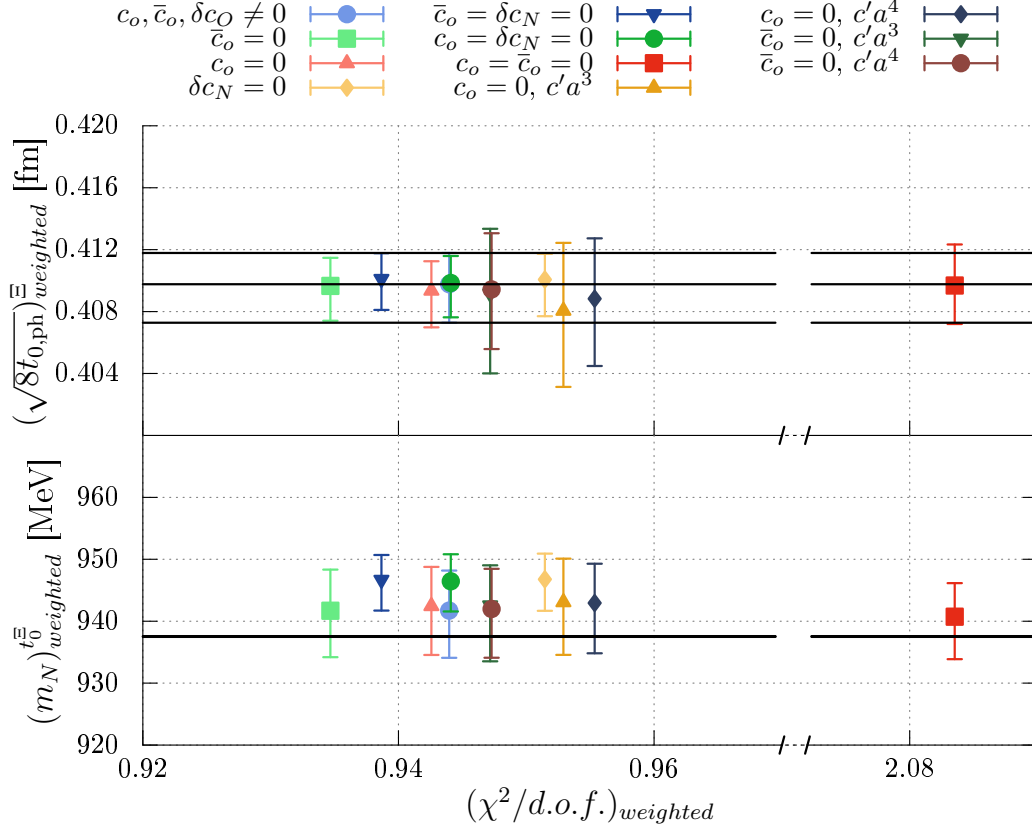


Figure 17. Results for $\sqrt{8t_{0,\text{ph}}}$ and the nucleon mass from the octet BChPT FV fit (see section 6.1), when varying the lattice spacing corrections, setting different discretization terms within eq. (4.6) to zero and/or adding a^3 or a^4 terms as indicated in the labelling. For each fit form the result from the AIC averaging over the 18 different ensemble cuts is plotted against the corresponding reduced χ^2 -value, also AIC averaged over the 18 cuts. The horizontal lines displayed for $\sqrt{8t_{0,\text{ph}}}$ correspond to our final result, obtained with $c_o, \bar{c}_o, \delta c_N, \delta c_\Lambda \delta c_\Sigma, \delta c_\Xi \neq 0$, also indicated by the blue circle. The isospin corrected experimental value of the nucleon mass is also shown as a black horizontal line.

$t_{0,\text{ph}}$. The latter two choices result in slightly smaller AIC weighted χ^2/N_{DF} -values than the original ansatz, due to the reduced number of parameters. Setting either $c_o = 0$ or $\bar{c}_o = 0$ alone gives even smaller χ^2/N_{DF} -values. In contrast, setting $c_o = \bar{c}_o = 0$ gives a very large χ^2 (red square): an a^2 correction term that does not depend on δM is required, however, the fit cannot discriminate between c_o and \bar{c}_o since, except for some less precise $m_s = m_\ell$ data points, $8t_0 \bar{M}^2$ varies only very little. This also means that it is impossible to achieve stable fits, when adding a^3 or a^4 lattice corrections without either setting $c_o = 0$ or $\bar{c}_o = 0$. Therefore, we replace either the c_o -term or the \bar{c}_o -term by $c'a^3(t_0^*)^{-3/2}$ or $c'a^4(t_0^*)^{-2}$. The two $c_o = 0$ choices somewhat decrease the quality of the fit while the two $\bar{c}_o = 0$ choices do not significantly affect χ^2/N_{DF} .

Carrying out the AIC procedure over all the 198 results that are obtained when combining the 18 cuts with the 11 different parametrizations gives similar values for $t_{0,\text{ph}}$ and m_N with slightly smaller errors than the original fit. All the fit forms that decrease the χ^2/N_{DF} are

based on reducing the number of parameters in a way that is physically not well motivated. It must be stressed, however, that (with the exception of the $c_o = \bar{c}_o = 0$ fit) the variations in terms of the reduced χ^2 -value are minimal. We conclude that the systematics regarding the continuum limit extrapolation are already covered within the AIC error bar of our original fit.

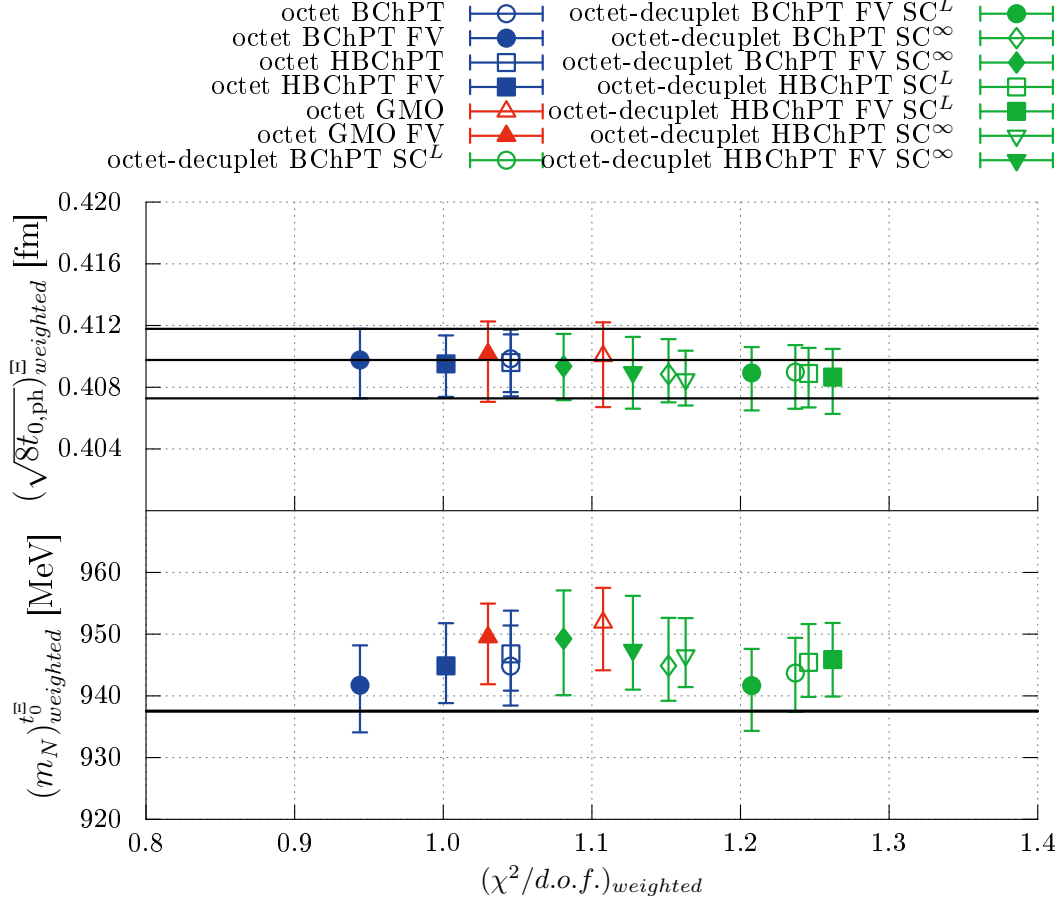


Figure 18. Results for $\sqrt{8t_{0,ph}}$ and the nucleon mass obtained from the AIC procedure for different continuum parametrizations, see section 6.1. Blue symbols correspond to the octet (H)BChPT parametrization, red symbols to the octet GMO fits and green symbols to simultaneous octet-decuplet (H)BChPT fits. Solid symbols include finite volume effects. Circles and diamonds correspond to BChPT, squares and downward triangles to HBChPT. Regarding the joint octet-decuplet fits, only data for stable decuplet baryons were included. We adopt two stability cuts: “ SC^L ” stands for stability in the finite volume, while “ SC^∞ ” denotes stability even for an infinite volume.

Finally, in figure 18 we investigate the impact of different parametrizations of the continuum dependence of the baryon masses on the meson masses and the volume. The naming conventions and references to the explicit parametrizations can be found in section 6.1. Solid symbols include finite volume (FV) effects, open symbols do not. The best fit (solid blue circle, octet BChPT FV) is the one discussed above. Its HBChPT equivalent is the next best fit. The GMO parametrization has a larger number of parameters (17 instead of

12) but also a larger χ^2/N_{DF} . This polynomial expansion does not include finite volume effects. Therefore, for the GMO FV fit we correct the data “by hand”, using the finite volume corrections from the octet BChPT FV fit discussed in section 6.3. Additionally, we display results from simultaneous octet-decuplet (H)BChPT fits, where we carry out two stability cuts regarding the Δ , Σ^* and Ξ^* baryons which at the physical point can strongly decay into $N\pi$, $\Lambda\pi$ or $\Sigma\pi$ and $\Xi\pi$, respectively, namely requiring stability in the infinite volume limit (SC^∞) or stability in the finite volume (SC^L). These fits contain 23 free parameters, 12 accounting for lattice artefacts, and 11 LECs. However, the number of data points is much larger since eight instead of four baryon masses are fitted simultaneously.

With one exception, the quality of the fits improves when finite volume effects are included. In principle, one could AIC average the HBChPT FV and the BChPT FV results, however, due to the better χ^2 -values, the result would be dominated by the EOMS BChPT parametrizations. Note that no AIC averaging can be carried out across the three classes of parametrizations, i.e. (H)BChPT, octet-decuplet (H)BChPT and GMO, because the data sets are not the same. Only in the octet-decuplet (H)BChPT fits do the decuplet masses contribute while within the GMO fits no cut on $\phi_4 = 12t_0\overline{M}^2$ is imposed and data with $\phi_4 > 1.6$ are included. Similarly, it is also not possible to average over the two classes of simultaneous octet-decuplet fits (SC^L and SC^∞) as different sets of data points are excluded per ensemble in each case. Finally, we remark that for each of the continuum parametrizations investigated, we also varied the form of the lattice spacing dependence as discussed above and reached similar conclusions as for the octet BChPT FV fits.

All methods give very consistent results and errors. Therefore, as our final result we quote the AIC average of the BChPT FV fit to the octet baryon masses:

$$\sqrt{8t_{0,\text{ph}}} = 0.4098_{(25)}^{(20)} \text{ fm}. \quad (6.2)$$

We find $\sqrt{8t_0^*}$ to be smaller by 10^{-4} fm than this value, see eq. (3.42).

6.5 The baryon spectrum

As a by-product of the scale setting procedure outlined above we also determine the baryon spectrum. The fits to the octet baryon masses and our AIC model averaging procedure have already been explained and discussed in sections 6.3 and 6.4. Examples for the nucleon mass were shown next to $\sqrt{8t_{0,\text{ph}}}$ in figures 16, 17 and 18. A fit to the whole octet was illustrated in figure 14. In the left panel of figure 19 we show the corresponding octet BChPT FV fit that carried the highest weight in the AIC averaging procedure, with the data shifted in the same way to $a = 0$, $L = \infty$ and to kaon masses corresponding to the correct physical point trajectories as in section 6.3. The data cuts for this fit with $\chi^2/N_{\text{DF}} = 0.94$ were $LM_\pi > 4$ and $\phi_4 > 1.25$. For comparison, in the right panel we show the continuum limit projection of our best polynomial fit (GMO FV, $\chi^2/N_{\text{DF}} = 1.02$). In this case, the volume was restricted to $LM_\pi > 4$ and all data with $8t_0M_\pi^2 < 0.8$ were included. No further cut in the quark mass plane was imposed since restricting the parameter governing the convergence of the expansion, δM^2 , would have excluded the physical point. In this fit form only group theory constraints are implemented but no assumption is made regarding the interactions.

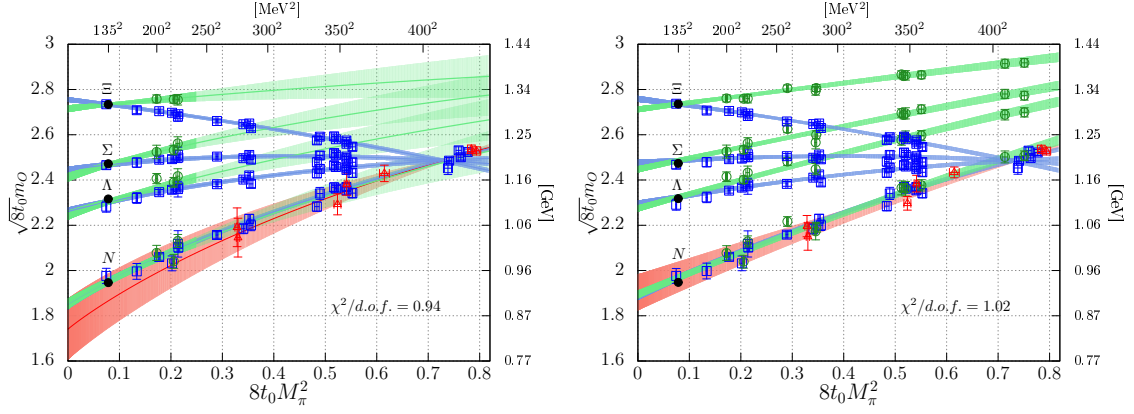


Figure 19. Left: the same octet BChPT FV fit as in figure 14 but with the cuts $\phi_4 > 1.25$ and $LM_\pi > 4$ that resulted in the smallest χ^2/N_{DF} . The lighter parts of the green error bands indicate the region that has been discarded from the fit. Right: the best polynomial fit (GMO FV) to the octet baryon spectrum. As in figure 14 the data points have been shifted to the continuum, infinite volume limit and to the kaon masses that correspond to the respective trajectories in the quark mass plane. References to the formulae used can be found in section 6.1.

Therefore, the number of parameters entering the continuum limit parametrization is 11 instead of 6, however, more data points are included in the fit. Both fit forms give adequate descriptions of the data and result in similar predictions regarding the scale parameter and the baryon masses. However, in terms of the fit quality, the BChPT parametrization seems to be preferred by the data.

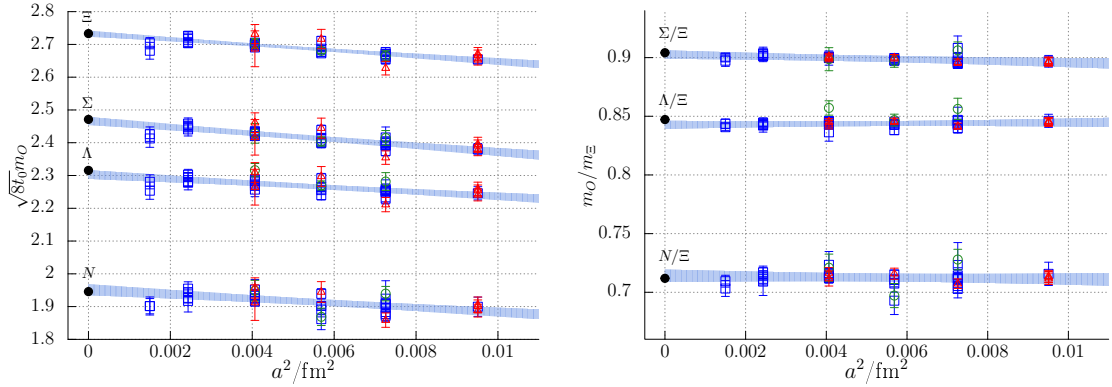


Figure 20. Continuum limit extrapolations for the octet baryon masses. The data are shifted to the infinite volume and the physical point in the quark mass plane according to the octet BChPT FV parametrization (see section 6.1), using the fit with the best quality ($\chi^2/N_{\text{DF}} = 0.94$). Red triangles, blue squares and green circles correspond to the $m_s = m_\ell$, $\text{Tr } M = \text{const}$ and $\hat{m}_s \approx \text{const}$ quark mass trajectories, respectively. Left: the lattice spacing dependence of the masses in units of $\sqrt{8t_{0,\text{ph}}}$. Right: the lattice spacing dependence of ratios of the baryon masses over the mass of the Ξ .

In the left panel of figure 20 we show for our best fit the dependence of the combinations $\sqrt{8t_0}m_O$ at the physical point in the infinite volume limit on the squared lattice spacing: there

is a difference of about 3% between the values obtained on our coarsest lattice ($a \approx 0.098$ fm) and the continuum limit. Note that in this representation we are only sensitive to four combinations of the six independent order a^2 terms since the pion and kaon masses are set to the physical ones. In the right panel we display ratios of the other octet baryon masses over the mass of the Ξ . We find that ratios of octet baryon masses have a much smaller dependence on a , which we cannot resolve within our present errors, than the combinations $\sqrt{8t_0}m_O$. Note that unlike in the fit shown in the right panel of figure 15, that carries a very small weight in the AIC averaging procedure, the nucleon mass agrees with the physical one within errors.

Finite volume effects have been discussed in sections 4.3 and illustrated for the baryons in figures 12 and 15. The corresponding analytical expression eq. (B.1) can be found in appendix B. These are generally mild for our lattice sizes, however, they can have an impact on the fit quality even for $LM_\pi > 4$ as can be seen in figure 18 above; with one exception the fits including the finite volume terms (full symbols) give smaller reduced χ^2 -values. Note that the number of fit parameters is not affected by this. In the approach of polynomially expanding in δM^2 and \overline{M}^2 (GMO), no statement can be made about finite volume effects. In this case, we just adjust the data for the effects predicted by BChPT, which results in smaller χ^2 -values for the GMO fits.

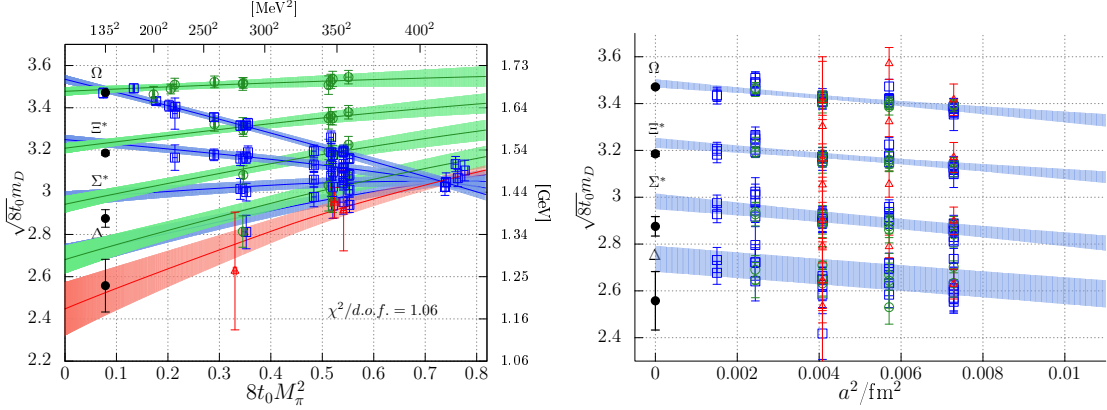


Figure 21. Results in the decuplet sector for a simultaneous octet-decuplet BChPT FV SC^∞ fit (see section 6.1). Shown is the fit with highest weight that enters the AIC procedure. The data cuts are $\phi_4 < 1.6$, $a < 0.09$ fm and $LM_\pi > 4$. Decuplet masses that can strongly decay into a pion and an octet baryon for an infinite volume (SC^∞) are ignored and not displayed. The experimental results (black circles) correspond to the Breit–Wigner masses plus and minus half the Breit–Wigner widths. Left: the continuum limit dependence on M_π^2 . Right: the dependence on a^2 .

In figure 21 we show the results of a simultaneous octet-decuplet BChPT FV SC^∞ fit for the decuplet sector (for details, see section 6.1). The corresponding results for the octet baryons are very similar to those shown in previous figures. The scale is set self-consistently by requiring that m_Ξ assumes the physical mass at the physical point, see eqs. (4.7) and (4.8). Not shown or fitted are masses of decuplet baryons that can strongly decay to a pion and an octet baryon in an infinite volume since this goes beyond the formalism that we apply here. The Ω baryon mass agrees with the expectation. In principle, we could also have used this

to set the scale. However, the error is larger than for the Ξ baryon. The results for the other three baryons are slightly above the sums of the Breit–Wigner masses and the half-widths: in the regime in which we discard the data also the prediction has to be taken with a grain of salt since we neglect that the poles of the resonances acquire imaginary parts.

In the right panel of figure 21 we show the a^2 dependence of $\sqrt{8t_0}m_D$ at the physical point. Also in this case the difference between the results at our coarsest lattice spacing (not included into this particular fit) and in the continuum limit are about 3%. Again, ratios comprised of a decuplet baryon mass divided by an octet baryon mass (not shown), are independent of a within our present errors.

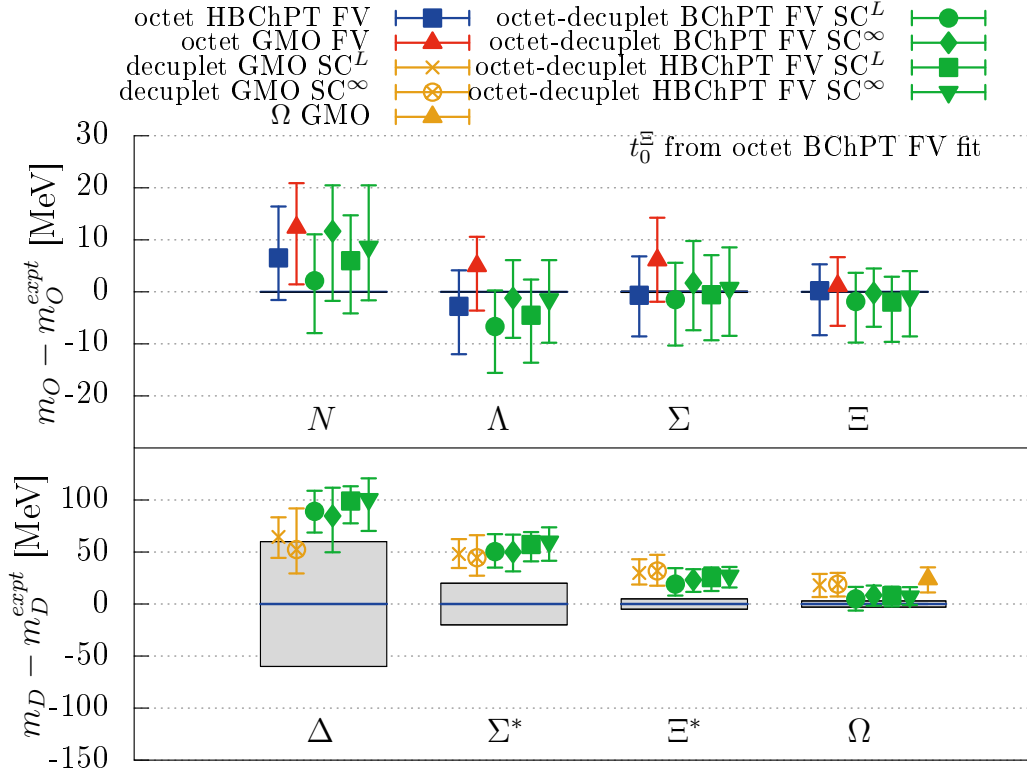


Figure 22. Comparison of the various fit results for the light baryon masses with the experimental values. The scale is set using the m_Ξ mass from the octet BChPT FV fit. For the fit forms already covered, the symbols are the same as those used in figure 18 and the labelling corresponds to that of section 6.1. For the Ω baryon alone we carry out an additional nine parameter fit (Ω GMO) with terms proportional to \overline{M}^2 , δM^2 , $\overline{M}^2 \delta M^2$, \overline{M}^4 , δM^4 , a^2 , $a^2 \overline{M}^2$ and $a^2 \delta M^2$.

In figure 22 we compare our results for the baryon masses from various fits to our expectations, subtracting the (pseudo)-experimental values m_B^{expt} . For the (H)BChPT parametrizations, we always include finite volume effects. The symbols are the same as those used in figure 18. Again, for the decuplet baryons we implement two cuts (in addition to those on the maximal ϕ_4): only considering baryons that are stable in the finite volume (SC^L) and baryons that are stable in the infinite volume (SC^∞). In addition, we carry

Table 9. Comparison of our physical point continuum limit predictions for the lower lying light baryon masses (with all systematics included in the error) with the “experimental” expectations of iso-symmetric QCD (table 14). For orientation, for the unstable baryons Δ , Σ^* and Ξ^* , we give the Breit–Wigner masses, with the respective half-widths as errors. The Ξ baryon mass of the octet BChPT FV fits was used to set the scale. The fit functions are referenced in section 6.1.

fit	m_N	m_Λ	m_Σ	m_Ξ
octet BChPT FV	$941.7^{(6.5)}_{(7.6)}$	$1110.0^{(4.2)}_{(4.2)}$	$1188.4^{(4.8)}_{(3.5)}$	—
octet-decuplet BChPT FV SC^∞	$949.2^{(8.8)}_{(13.4)}$	$1114.5^{(7.3)}_{(7.7)}$	$1192.4^{(8.1)}_{(9.1)}$	$1316.7^{(4.7)}_{(6.5)}$
expt.	$937.54(6)$	$1115.68(1)$	$1190.66(12)$	$1316.9(3)$
fit	m_Δ	m_{Σ^*}	m_{Ξ^*}	m_Ω
octet-decuplet BChPT FV SC^∞	$1314.6^{(27.2)}_{(34.9)}$	$1432.9^{(16.8)}_{(18.5)}$	$1555.2^{(10.3)}_{(11.6)}$	$1678.0^{(9.3)}_{(10.0)}$
expt.	$1230(60)$	$1383(20)$	$1532(5)$	$1669.5(3.0)$

out GMO fits to the decuplet baryon masses (orange symbols). We also show the result of such a fit, using the Ω baryon mass alone (orange triangle). The results of the octet BChPT FV fits and of the octet-decuplet BChPT FV SC^∞ fits are displayed in table 9 and shown in the summary figure 29 below. For all the results shown in figure 22, the scale $\sqrt{8t_{0,\text{ph}}}$ was set from the mass of the Ξ baryon, obtained via the octet BChPT FV fits. In general we see good agreement between the different results and for the octet baryons also with the experimental masses. Regarding the Ω baryon, with the decuplet GMO fits there is a tension on the level of 1.5 to 2 standard deviations with experiment, while the octet-decuplet BChPT and HBChPT fits agree. The values of table 9 indicate that within our errors of 4 MeV (for the Λ and Σ), 7 MeV (for the nucleon) and 10 MeV (for the Ω), we reproduce the experimental masses. The differences regarding the unstable decuplet baryons have already been addressed above.

Finally, we investigate the breaking of SU(3) flavour symmetry in the baryon masses. Following ref. [62], we define the averages

$$X_N = \frac{1}{3}(m_N + m_\Sigma + m_\Xi), \quad X_\Lambda = \frac{1}{2}(m_\Lambda + m_\Sigma), \quad X_\pi^2 = \frac{1}{3}(M_\pi^2 + 2M_K^2) = \overline{M}^2 \quad (6.3)$$

that do not receive any linear contributions in the flavour breaking parameter $\delta m = m_s - m_\ell$. In figure 23 we show continuum limit results for X_N and X_Λ as functions of M_π^2 along the line where the flavour averaged pseudoscalar mass is fixed to its experimental value $X_\pi = 411$ MeV. This approximately corresponds to our $\text{Tr } M = \text{const}$ trajectory in the quark mass plane. Shown are the results of the best BChPT FV fit (blue bands) and the best polynomial fit (GMO FV, red bands) for X_N (top) and X_Λ (bottom). Since b_D and b_F cancel from these combinations and b_0 is fixed for $X_\pi = \text{const}$, any dependence on M_π^2 is due to F and D in the BChPT case and the two combinations $\delta e_N + \delta e_\Sigma + \delta e_\Xi$ and $\delta e_\Lambda + \delta e_\Sigma$ for the GMO parametrization eq. (5.29). The scale was set from the mass of the Ξ baryon, using the octet BChPT FV fit, which explains why the experimental values (black

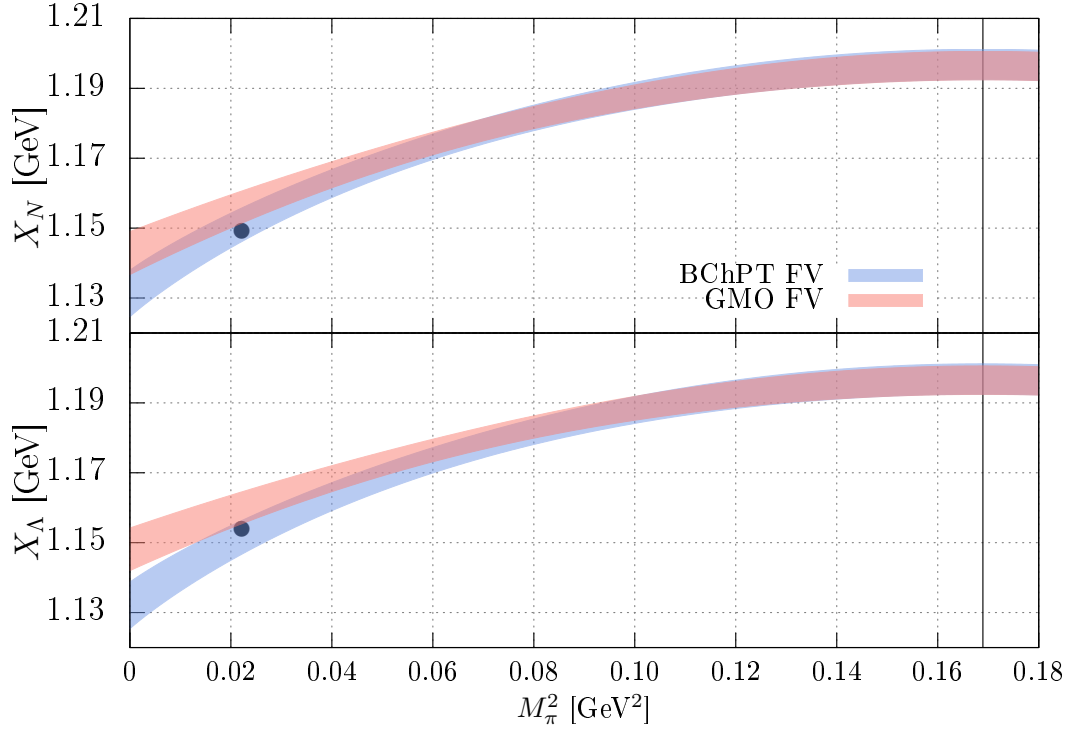


Figure 23. The mass averages X_N (top) and X_Λ (bottom) defined in eq. (6.3) as functions of M_π^2 , keeping $3X_\pi^2 = 3\overline{M}^2 = 2M_K^2 + M_\pi^2 = 2M_{K,\text{ph}}^2 + M_{\pi,\text{ph}}^2$ fixed, in the continuum limit. Shown are the results of the best BChPT FV (blue bands) and GMO FV (red bands) fits to the baryon octet. The vertical line denotes the flavour symmetric point $M_\pi = M_K = 411$ MeV where all baryon masses are equal. The black points are the experimental values. The parametrizations used are referenced in section 6.1.

circles) are not in the centre of the error bands. The vertical line denotes the symmetric point $M_\pi = M_K = X_\pi$, where all the octet baryon masses agree. As we have not carried out the AIC averaging but just selected the fit ranges that gave the smallest χ^2/N_{DF} , the error bands do not include all systematics. The difference, however, is not big; as an example one may compare the grey band to the entry with $\chi^2/N_{\text{DF}} = 0.94$ in the right panel of figure 18.

The BChPT parametrizations of X_N and X_Λ are not identical but they are extremely close to each other, whereas differences between the GMO curves are visible. As for the individual baryon masses, the curvature suggested by BChPT is somewhat larger than that of the polynomial expansion. However, in the range $M_\pi > 127$ MeV where we have data, the parametrizations agree within errors. The difference between X_N and X_Λ at the physical point cannot be resolved within our present accuracy but both predictions agree with experiment (solid circles). The experimental value for this difference reads $X_N - X_\Lambda \approx -5$ MeV. This is related to the Gell-Mann–Okubo relation [113, 114]

$$\frac{m_N + m_\Xi}{2} - \frac{3\Lambda + \Sigma}{4} = \frac{3}{2}(X_N - X_\Lambda) \approx 0 \quad (6.4)$$

and expected to be small since the average masses only differ by quadratic and higher order terms in the SU(3) symmetry breaking parameter δm from their values at the symmetric

point, where these must agree. However, we see that both averages at the physical point differ by over 40 MeV from the value at $m_s = m_\ell$ (vertical line). There is no obvious (group theoretical or other) reason why this effect has the same sign or a similar size for both averages, X_N and X_Λ . In view of the size of the observed higher than linear order corrections, the accuracy of the GMO relation is somewhat surprising. It could easily have been violated by as much as 50 MeV rather than 5 MeV. One may speculate that the variation of X_N and X_Λ as a function of M_π^2 when $\bar{M} = X_\pi$ is kept constant may dominantly be due to SU(3) breaking effects in the mesonic sector. However, this is hard to reconcile with section 3.6, where we found $\phi_{4,\text{opt}} \approx \phi_{4,\text{ph}}$ ($\phi_4 = 12t_0 X_\pi^2$).

6.6 The σ terms of the octet baryons and the Ω baryon

We define the baryon sigma terms as

$$\sigma_{qB} = m_q \frac{\partial m_B}{\partial m_q}, \quad \sigma_{\pi B} = \sigma_{uB} + \sigma_{dB}. \quad (6.5)$$

Following appendix C, we extract these terms from the dependence of the mass of baryons B on the pion and kaon masses, using the GMOR relations. We carry this out for all the octet baryons as well as for the Ω baryon. We distinguish between $\tilde{\sigma}_{\pi B}$ and $\sigma_{\pi B}$ as well as between $\tilde{\sigma}_{sB}$ and σ_{sB} , where the $\tilde{\sigma}$ terms refer to the logarithmic derivatives with respect to squared pion masses, see their definition eq. (C.2), while the usual σ terms are the derivatives with respect to the quark masses as defined above (and in eq. (C.1)). The difference is due to the corrections to the GMOR relations that are worked out in appendix C.2,¹⁸ where we also determine the required combinations of mesonic NLO LECs, see eq. (C.26). As can be seen from the results in table 10, the differences between assuming the GMOR relations and accounting for the violations are negligible for the pion σ terms. While the differences between σ_{sB} and $\tilde{\sigma}_{sB}$ are sizeable for the less-well constrained strange σ terms, also in this case these are much smaller than the respective errors.

To the order of BChPT implemented here, it is consistent to ignore corrections to the GMOR relations. Nevertheless, we choose to remove this small source of systematic uncertainty (see appendix C.2), in particular, since these corrections are visible in the squared meson mass data as functions of the quark masses. Regarding the baryon mass dependence on the pseudoscalar masses, within the present statistical errors we do not need to go beyond $\mathcal{O}(p^3)$, as we have seen above. The results shown in table 10 are consistent with the naive expectation that (a) the sum of the σ terms becomes bigger with the baryon mass and (b) that baryons with a larger number of strange valence quarks have bigger strange σ terms but smaller pion σ terms. Within errors the σ terms for the Λ , the Σ and the Ξ baryons agree with previous lattice determinations [139, 140]. We refrain from predicting the σ terms of the unstable decuplet baryons and we are unaware of previous lattice calculations of the σ terms for the Ω baryon. However, predictions from fits to collections of lattice data on octet and decuplet baryon masses can also be found, e.g., in refs. [123, 126, 127, 141, 142].

¹⁸We take into account the leading dependence of t_0 on the meson masses when determining $\tilde{\sigma}$ from the rescaled variables (see eq. (C.5)). For σ we also include the higher order terms eq. (C.7) (as well as the NLO corrections to the GMOR relations).

Table 10. The σ terms for the octet baryons and for the Ω baryon. The $\tilde{\sigma}_{\pi B}$ and $\tilde{\sigma}_{sB}$ are obtained from the pseudoscalar mass dependence of the baryon masses, assuming the GMOR relations to be valid. The usual σ terms take violations of the GMOR relations into account. The results are obtained using the octet BChPT FV and, for the Ω baryon, the octet-decuplet BChPT FV parametrizations (see section 6.1), including AIC averaging analogous to figure 16.

B	$\tilde{\sigma}_{\pi B}/\text{MeV}$	$\sigma_{\pi B}/\text{MeV}$	$\tilde{\sigma}_{sB}/\text{MeV}$	σ_{sB}/MeV
N	$44.0^{(4.4)}_{(4.7)}$	$43.9^{(4.7)}_{(4.7)}$	$4^{(59)}_{(61)}$	$16^{(58)}_{(68)}$
Λ	$27.6^{(4.3)}_{(4.9)}$	$28.2^{(4.3)}_{(5.4)}$	$113^{(63)}_{(60)}$	$144^{(58)}_{(76)}$
Σ	$24.9^{(4.6)}_{(5.0)}$	$25.9^{(3.8)}_{(6.1)}$	$194^{(68)}_{(61)}$	$229^{(65)}_{(70)}$
Ξ	$10.1^{(4.4)}_{(5.4)}$	$11.2^{(4.5)}_{(6.4)}$	$267^{(70)}_{(68)}$	$311^{(72)}_{(83)}$
Ω	$5.8^{(5.5)}_{(3.8)}$	$6.9^{(5.3)}_{(4.3)}$	$391^{(92)}_{(56)}$	$421^{(89)}_{(59)}$

We discuss $\sigma_{\pi N}$ in more detail in section 6.8 below. It is evident from our distribution of ensembles, see, e.g., figure 13, that the strange quark mass is varied very little close to the physical point. Therefore, the strange σ terms at present are not very well constrained. This can be improved upon by direct determinations of the respective matrix elements [143].

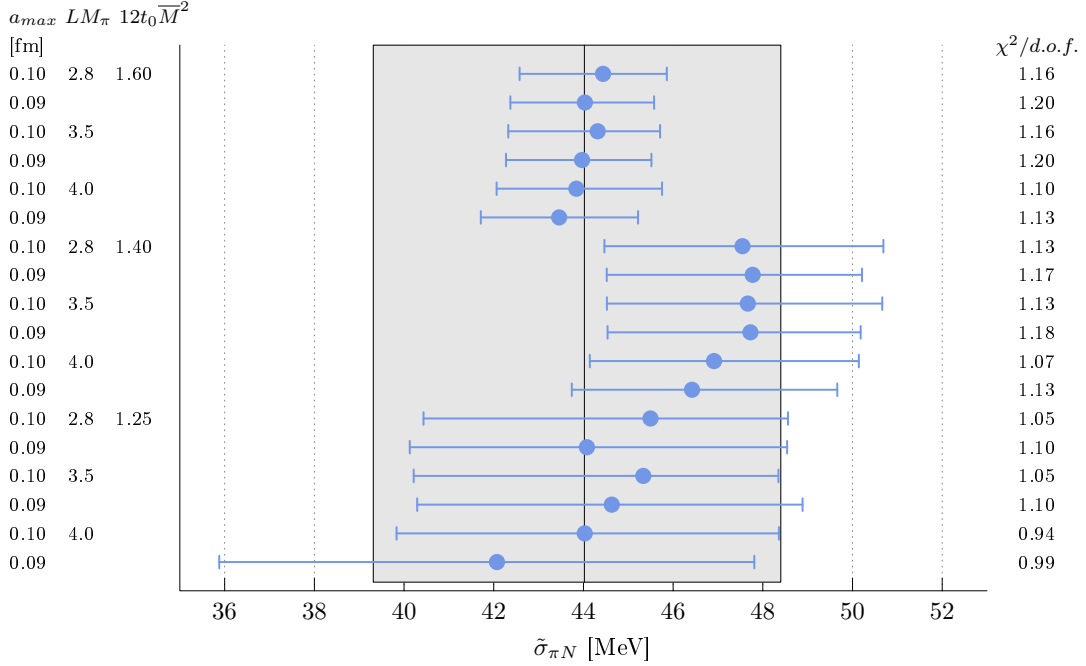


Figure 24. The same as figure 16 for $\tilde{\sigma}_{\pi N}$. The grey band represents the final result obtained via the AIC averaging procedure. The underlying BChPT FV parametrization is referenced in section 6.1 and the data cuts are explained in section 6.4.

In the statistical analysis we follow section 6.4, also regarding the cuts and model

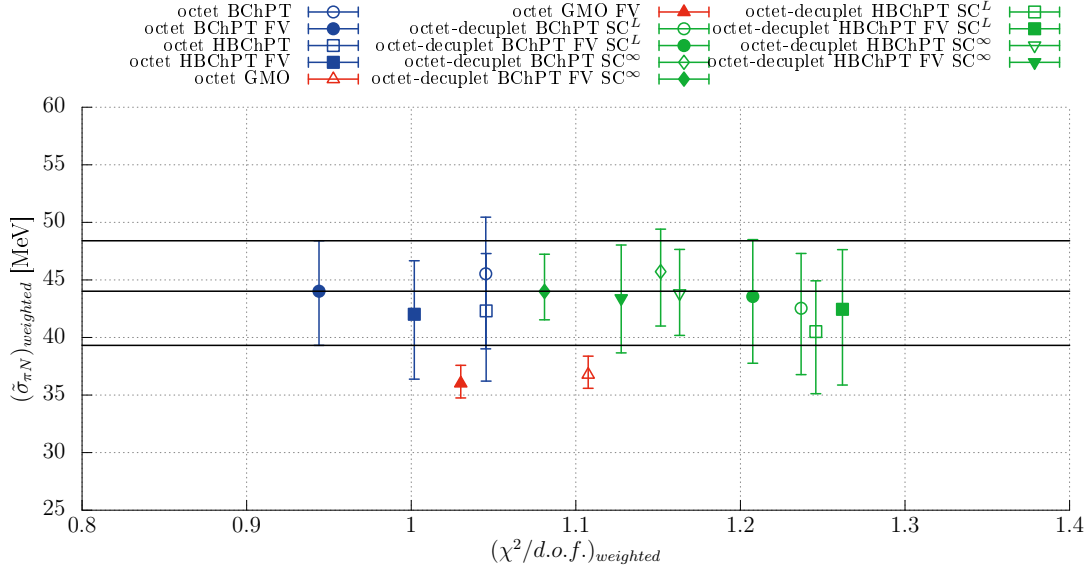


Figure 25. The same as figure 18 for $\tilde{\sigma}_{\pi N}$. The parametrizations are referenced in section 6.1.

variation. We illustrate the dependence on different cuts with respect to the lattice spacing, the volume and the average squared pseudoscalar mass for the example of the $\tilde{\sigma}_{\pi N}$ in figure 24. As mentioned above, the difference between $\tilde{\sigma}_{\pi N}$ and the pion-nucleon σ term $\sigma_{\pi N}$ is negligible, see table 10. Unlike the nucleon mass shown in figure 16, $\tilde{\sigma}_{\pi N}$ shows very little dependence on the data cuts, apart from an increase in the statistical error as the set of ensembles is reduced. We also investigated whether setting the scale using the nucleon mass rather than the cascade mass had any impact on the σ terms, and, in particular, on $\sigma_{\pi N}$. However, the resulting shifts only amounted to negligible fractions of the errors.

In figure 25 we investigate the dependence on the parametrization: all fits give very consistent results, with the exception of the GMO ansätze that carry much smaller errors and give lower central values. This is related to a reduced curvature of these baryon mass parametrizations near the physical point, relative to the (H)BChPT fits, see figure 19. A similarly consistent picture arises for the remaining octet baryon σ terms. The σ terms of the Ω baryon in table 10 are determined via the simultaneous octet-decuplet BChPT FV SC^∞ fit. The GMO fits give very similar results for $\sigma_{s\Omega}$ but with somewhat smaller errors.

6.7 SU(3) and SU(2) (H)BChPT low energy constants

Our continuum limit extrapolated results include some of the SU(3) and SU(2) (H)BChPT LECs. To determine these and to estimate their uncertainties, we employ the methods explained in the previous subsections. For the SU(2) LECs see also appendix D. We carry out the analysis using the octet(-decuplet) BChPT FV (SC^∞) as well as the octet(-decuplet) HBChPT FV (SC^∞) parametrizations (see section 6.1). For comparison we also give the leading terms m_0 and m_{D0} and the linear coefficients of the octet GMO FV and the decuplet GMO SC^∞ fits. Note that for the linear coefficients, we have taken into account the mass dependence of $\sqrt{8t_0}$, see eqs. (5.10)–(5.12).

Table 11. The LO SU(3) octet and decuplet LECs. BChPT is employed as well as HBChPT. For the decuplet baryons we only carry out (H)BChPT fits including octet baryon loops, while the octet baryons are fitted with and without the decuplet baryons. We also include m_0 and m_{D0} determined via the $\mathcal{O}(M^4)$ GMO expansions. The relevant equations are referenced in section 6.1.

fit	χ^2/N_{DF} (weighted)	m_0 [MeV]	$F/(4\pi F_0)$ [GeV ⁻¹]	$D/(4\pi F_0)$ [GeV ⁻¹]	F/D
octet	0.94	821 ⁽⁷¹⁾ ₍₅₃₎	0.383 ⁽³⁹⁾ ₍₅₁₎	0.638 ⁽⁵²⁾ ₍₅₁₎	0.606 ⁽⁸³⁾ ₍₉₇₎
BChPT FV					
octet	1.00	836 ⁽⁸⁶⁾ ₍₆₁₎	0.287 ⁽³³⁾ ₍₃₀₎	0.460 ⁽⁴¹⁾ ₍₄₂₎	0.617 ⁽¹⁰⁵⁾ ₍₇₇₎
HBChPT FV					
octet-decuplet	1.08	809 ⁽³³⁾ ₍₄₅₎	0.324 ⁽⁵⁹⁾ ₍₄₂₎	0.509 ⁽¹⁰⁹⁾ ₍₉₁₎	0.641 ⁽¹⁵⁵⁾ ₍₁₂₇₎
BChPT FV SC [∞]					
octet-decuplet	1.13	818 ⁽⁶⁰⁾ ₍₆₉₎	0.255 ⁽⁴⁸⁾ ₍₅₁₎	0.378 ⁽⁹⁹⁾ ₍₈₄₎	0.677 ⁽¹⁶⁶⁾ ₍₁₃₈₎
HBChPT FV SC [∞]					
octet	1.03	896 ⁽³⁴⁾ ₍₃₁₎			
GMO FV					
		m_{D0} [MeV]	$ \mathcal{H} /(4\pi F_0)$ [GeV ⁻¹]	$ \mathcal{C} /(4\pi F_0)$ [GeV ⁻¹]	δ [MeV]
octet-decuplet	1.08	1147 ⁽⁷⁴⁾ ₍₉₁₎	0.66 ⁽⁵⁹⁾ ₍₆₆₎	0.45 ⁽¹⁴⁾ ₍₁₅₎	333 ⁽⁷⁹⁾ ₍₈₄₎
BChPT FV SC [∞]					
octet-decuplet	1.13	1128 ⁽¹¹⁸⁾ ₍₂₈₉₎	0.02 ⁽⁷⁴⁾ ₍₂₎	0.47 ⁽¹⁵⁾ ₍₁₈₎	305 ⁽¹¹³⁾ ₍₃₀₄₎
HBChPT FV SC [∞]					
decuplet	0.88	1249 ⁽¹¹²⁾ ₍₁₁₈₎			
GMO SC [∞]					

All results for the LO and NLO LECs are shown in tables 11 and 12. Differences between the different (H)BChPT parametrizations are indicative of higher order effects. We find consistent values for the LO LEC m_0 . The LECs F and D , while formally also of leading order, only appear within the loop corrections when considering the baryon self-energies. Therefore, these are subject to uncertainties larger than 10%. Both have the tendency to be smaller when using the HBChPT FV compared to the BChPT FV parametrization. Including decuplet loops reduces their values too. The ratio F/D , however, is quite stable, albeit with large errors. Regarding the additional LECs related to the decuplet baryons, m_{D0} is basically the same when using HBChPT and BChPT while \mathcal{H} is compatible with zero within errors that are as large as the central value of D . We find \mathcal{C} to be small too but to differ from zero by three standard deviations. The GMO fits give larger central values for the baryon masses in the chiral limit, m_0 and m_{D0} , but the results are compatible with the

Table 12. The NLO SU(3) octet and decuplet LECs. BChPT is employed as well as HBChPT. For the decuplet baryons we only carry out (H)BChPT fits including octet baryon loops, while the octet baryons are fitted with and without the decuplet baryons. In addition, we list the corresponding linear coefficients of the GMO expansion, truncated at $\mathcal{O}(M^4)$. The relevant equations are referenced in section 6.1.

fit	χ^2/N_{DF} (weighted)	b_0 [GeV $^{-1}$]	b_D [GeV $^{-1}$]	b_F [GeV $^{-1}$]
octet	0.94	$-0.739^{(70)}_{(84)}$	$0.056^{(43)}_{(39)}$	$-0.440^{(40)}_{(26)}$
BChPT FV				
octet	1.00	$-0.649^{(80)}_{(75)}$	$0.052^{(30)}_{(34)}$	$-0.399^{(35)}_{(24)}$
HBChPT FV				
octet-decuplet	1.08	$-0.706^{(56)}_{(69)}$	$0.083^{(33)}_{(35)}$	$-0.384^{(28)}_{(44)}$
BChPT FV SC $^\infty$				
octet-decuplet	1.13	$-0.662^{(73)}_{(78)}$	$0.080^{(27)}_{(37)}$	$-0.377^{(43)}_{(28)}$
HBChPT FV SC $^\infty$				
octet	1.03	$-0.389^{(49)}_{(53)}$	$0.092^{(9)}_{(7)}$	$-0.243^{(6)}_{(9)}$
GMO FV				
		t_{D0} [GeV $^{-1}$]	t_D [GeV $^{-1}$]	
octet-decuplet	1.08	$0.42^{(22)}_{(17)}$	$0.33^{(12)}_{(64)}$	
BChPT FV SC $^\infty$				
octet-decuplet	1.13	$0.44^{(57)}_{(22)}$	$0.28^{(9)}_{(3)}$	
HBChPT FV SC $^\infty$				
decuplet	0.88	$0.10^{(36)}_{(35)}$	$0.32^{(3)}_{(2)}$	
GMO SC $^\infty$				

(H)BChPT results within one standard deviation. The larger values are due to the smaller curvatures of the corresponding fits.

Our parametrizations only depend on the ratios D/F_0 , F/F_0 , \mathcal{C}^2/F_0^2 and \mathcal{H}^2/F_0^2 . In ref. [107] some of us determined the combination $\sqrt{8t_{0,\text{ch}}F_0} = 0.1502^{(56)}_{(29)}$ by analysing the quark mass dependence of the pseudoscalar meson mass and its decay constant along the symmetric line, as well as $\sqrt{8t_{0,\text{ch}}}m_0 = 1.57^{(5)}_{(6)}$, when carrying out an analogous analysis for the octet baryon mass and the axial charges. Combining this with our result $\sqrt{8t_{0,\text{ch}}} = 0.4170^{(22)}_{(27)} \text{ fm}$ (see eqs. (3.40) and (3.42)) gives

$$4\pi F_0 = 893^{(34)}_{(18)} \text{ MeV} \quad (6.6)$$

and $m_0 = 743^{(24)}_{(29)} \text{ MeV}$. This value of m_0 , which is compared to literature values in figure 11

of ref. [107], is by about 1.4 standard deviations smaller than the BChPT value of table 11,

$$m_0 = 821_{(53)}^{(71)} \text{ MeV}. \quad (6.7)$$

Note that while in the present study we have included a larger number of ensembles with a better coverage of the quark mass plane, the work [107] is based on a joint analysis of the octet baryon axial charges and its mass, which better constrains F and D . In particular, the result $F/D = 0.612_{(12)}^{(14)}$ was obtained which compares well with the values shown for this ratio in table 11. Ideally, one would repeat such a simultaneous analysis incorporating all available ensembles.

Using the value eq. (6.6) for the combination $4\pi F_0$ gives

$$F = 0.34_{(5)}^{(4)}, \quad D = 0.57(5), \quad |\mathcal{C}| = 0.40(13), \quad |\mathcal{H}| = 0.59_{(59)}^{(53)}, \quad (6.8)$$

where for F and D we quote the result of the octet BChPT FV fits while for \mathcal{C} and \mathcal{H} we have chosen the octet-decuplet BChPT FV SC^∞ result. The SU(6) quark model expectation reads $6D = 9F = -2\mathcal{H} = -3\mathcal{C}$ (see, e.g., ref. [132]), which is consistent with the large- N_c limit [144]. Our results satisfy the first equality within errors. However, both $|\mathcal{H}|$ and $|\mathcal{C}|$ are smaller than expected. The axial charge in the chiral limit is obtained as $\hat{g}_A = F + D \approx 0.8$, which is quite small too, given that $g_A \approx 1.27$ [145] at the physical point. Using the axial charges, albeit only along the $m_s = m_\ell$ line, in ref. [107] some of us obtained the larger values $F = 0.447(7)$ and $D = 0.730(11)$. Using these values, within a preliminary analysis of directly determined σ terms [143], it was only possible to describe the data if a larger value for the chiral decay constant F_0 was admitted. The same appears to hold in the present analysis of the baryon spectrum. We conclude that the data are well described by the BChPT parametrization at $\mathcal{O}(p^3)$, however, there appears to be some tension with the axial charges on the level of 20%, regarding the LECs. This hints at contributions from higher order corrections that can only be resolved by simultaneously analysing a larger set of observables. Values for F and D from other determinations can be found in figure 12 of ref. [107].

From our preferred simultaneous fits to the octet and decuplet baryon masses (octet-decuplet BChPT FV SC^∞), we obtain

$$m_{D0} = 1147_{(91)}^{(74)} \text{ MeV}, \quad \delta = 333_{(84)}^{(79)} \text{ MeV} \quad (6.9)$$

and $m_0 = 818_{(69)}^{(60)} \text{ MeV}$, which agrees well with the value extracted from the octet baryons alone, see eq. (6.7). The central value of δ differs slightly from that of $m_{D0} - m_0$ since we quote the median of the respective sum of AIC weighted bootstrap histograms.

Regarding the linear NLO coefficients of table 12, the differences between BChPT and HBChPT are rather small. The central values of b_D and b_F are somewhat larger when including the decuplet loops. However, in the GMO fits b_0 comes out by almost a factor of two smaller, while b_F is systematically larger than in the (H)BChPT fits. We remark that the data are not well described by the linear $\mathcal{O}(p^2)$ parametrization. To get the physics right, the inclusion of $\mathcal{O}(p^3)$ terms is necessary within (H)BChPT, which increases b_0 by a

factor of two. From our preferred fits (octet BChPT FV for b_0 , b_D and b_F and octet-decuplet BChPT FV SC^∞ for t_{D0} ,¹⁹ and t_D) we obtain:

$$b_0 = -0.739_{(84)}^{(70)}, \quad b_D = 0.056_{(39)}^{(43)}, \quad b_F = -0.440_{(26)}^{(40)}, \quad (6.10)$$

$$t_{D0} = 0.42_{(17)}^{(22)}, \quad t_D = 0.33_{(64)}^{(12)}. \quad (6.11)$$

Table 13. The SU(2) LECs m_N^0 and c_1 for the nucleon, using BChPT and HBChPT both with and without the inclusion of decuplet loops. The relevant parametrizations are referenced in section 6.1. The relation to the SU(3) LECs is worked out in appendix D and the LECs are defined in eq. (D.1).

fit	χ^2/N_{DF} (weighted)	m_N^0 [MeV]	c_1 [GeV ⁻¹]
octet BChPT FV	0.94	$893.2_{(8.6)}^{(9.3)}$	$-0.920_{(96)}^{(59)}$
octet HBChPT FV	1.00	$898.3_{(12.0)}^{(11.7)}$	$-0.817_{(75)}^{(59)}$
octet-decuplet BChPT FV SC^∞	1.08	$888.1_{(10.4)}^{(12.1)}$	$-0.924_{(84)}^{(66)}$
octet-decuplet HBChPT FV SC^∞	1.13	$894.9_{(10.6)}^{(12.1)}$	$-0.823_{(74)}^{(55)}$

We now address the SU(2) LECs. Following appendix D, we determine m_N^0 , i.e. the nucleon mass in the SU(2) chiral limit, as well as c_1 , the coefficient of the linear contribution to $m_N(M_\pi^2)$ at a fixed physical strange quark mass, $-4c_1 M_\pi^2$, see equation (D.1). The results from the (H)BChPT fits with and without decuplet loops are displayed in table 13. While m_N^0 is very stable across the four classes of fits, c_1 comes out systematically smaller in the HBChPT parametrizations. However, the decuplet loops appear to have little impact, as was the case for b_0 which is the dominant contribution to c_1 , see eq. (D.4). The results from our preferred octet BChPT FV fits read

$$m_N^0 = 893.2_{(8.6)}^{(9.3)} \text{ MeV}, \quad c_1 = -0.920_{(96)}^{(59)} \text{ GeV}^{-1}. \quad (6.12)$$

The nucleon mass in the SU(2) chiral limit m_N^0 is much better constrained than the nucleon mass in the SU(3) chiral limit, $m_0 = 821_{(53)}^{(71)} \text{ MeV}$, since we have many ensembles close to the former point in the quark mass plane. Note that Hoferichter et al. [146] predict $c_1 \sim -1.1 \text{ GeV}^{-1}$ (see table 7 of that reference), which is somewhat larger in magnitude than our result. Consistent with this, they also obtain a larger $\sigma_{\pi N}$ -value [147] (see below).

Assuming that $m_N(M_\pi^2)$ at a fixed value of the strange quark mass is a concave function, one can easily derive the inequalities

$$898 \text{ MeV} \approx m_N - \tilde{\sigma}_{\pi N} > m_N^0 = 893.2_{(8.6)}^{(9.3)} \text{ MeV}, \quad (6.13)$$

$$44 \text{ MeV} \approx \tilde{\sigma}_{\pi N} < -4c_1 M_{\pi, \text{ph}}^2 = 67_{(7)}^{(4)} \text{ MeV}, \quad (6.14)$$

¹⁹We renamed this LEC to avoid confusion with the scale parameter t_0 .

which are both satisfied. On the one hand, increasing $\sigma_{\pi N}$ would violate the first inequality, unless the nucleon mass in the SU(2) chiral limit was smaller. On the other hand, $\sigma_{\pi N}/M_\pi^2$ must be larger in the SU(2) chiral limit than at the physical point, which results in another, less stringent upper limit for $\sigma_{\pi N}$.

6.8 Discussion of $t_{0,\text{ph}}$, the baryon spectrum and $\sigma_{\pi N}$

Above we determined the scale parameter $t_{0,\text{ph}}$ from the mass of the Ξ baryon, see eq. (6.2). In section 6.4 we have demonstrated that this result is robust against variations of the parametrizations of the mass dependence, finite volume effects and continuum limit extrapolation as well as regarding different cuts imposed on the data. The input quantities used to fix the physical point and to set the scale, i.e. M_π , M_K and m_Ξ , are also very precisely known, even after correcting these for isospin breaking effects. We found the lattice spacing dependence of $\sqrt{8t_{0,\text{ph}}}m_\Xi$ to be less pronounced than that observed using the same lattice action when determining the pseudoscalar decay constants in units of $\sqrt{8t_0}$ [2, 20]. However, it is still significant: on our coarsest lattice, the combination $\sqrt{8t_{0,\text{ph}}}m_\Xi$ differs by a bit more than 3% from the continuum limit value, see the left panel of figure 20. Nevertheless, with six lattice spacings at our disposal, this extrapolation is well controlled so that the most dominant uncertainty of our determination of t_0 is by far the statistical error, in particular, of the mass of the Ξ baryon.

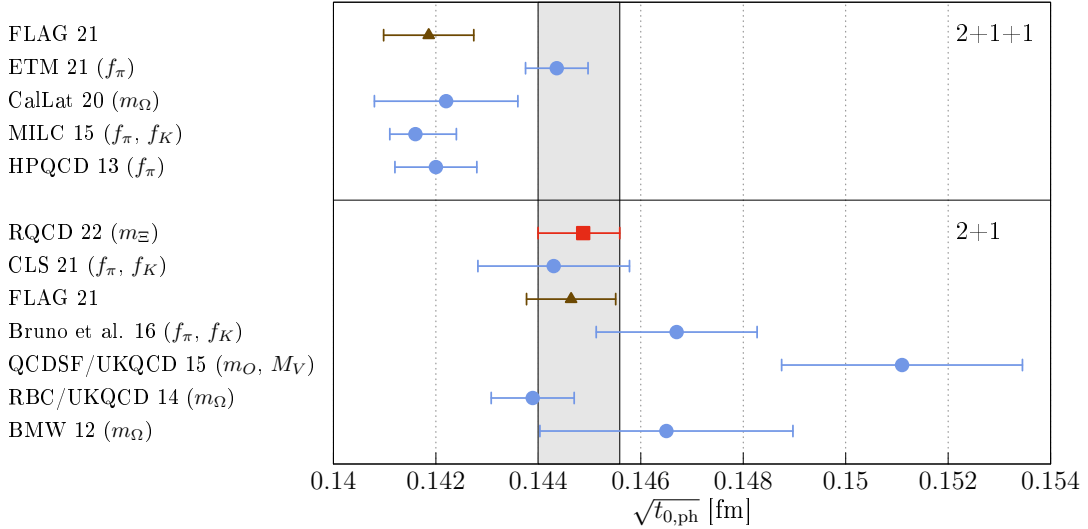


Figure 26. Comparison of our determination of $\sqrt{t_{0,\text{ph}}}$ from the Ξ baryon mass (red square and shaded grey region) to other determinations of this quantity with $N_f = 2 + 1$ flavours (CLS 21 [20], Bruno et al. 16 [2], QCDSF/UKQCD 15 [13], RBC/UKQCD 14 [6] and BMW 12 [5]) and $N_f = 2 + 1 + 1$ flavours (ETM 21 [16], CalLat 20 [8], MILC 15 [18] and HPQCD 13 [15]). The experimental quantities used as an input to set the scale are indicated in brackets. Also shown as green triangles are the averages of the FLAG Review 2021 [109].

The scale parameter $t_{0,\text{ph}}$ has been determined previously in $N_f = 2 + 1$ QCD [2, 5, 6, 13, 20] and $N_f = 2 + 1 + 1$ QCD [8, 15, 16, 18], using different input quantities and

different extrapolation strategies. In figure 26 we compare our result (red square and shaded grey region) with previous determinations as well as with the 2021 FLAG averages [109]. HPQCD [15] and ETM [16] used the pion decay constant to set the scale while MILC [18], Bruno et al. [2] as well as CLS [20] (both on CLS ensembles) used combinations of the pion and kaon decay constants. MILC carried out an interpolation to a decay constant of a hypothetical meson with two quarks of mass $0.4m_s$ and used this to set the scale while the two CLS-based determinations extrapolated/interpolated the flavour averaged combination $\sqrt{t_0}f_{\pi K} := \sqrt{t_0}(2f_K + f_\pi)/3$ to the physical point in the continuum limit. In contrast BMW [5], RBC/UKQCD [6] and CalLat [8] used the mass of the Ω baryon to set the scale. Finally, QCDSF/UKQCD [13] averaged a result from the average octet baryon mass with a result from the average vector meson mass. This is not entirely unproblematic since the ρ meson at the physical point has quite a substantial decay width. All in all, with the exception of this last result, there is agreement within 1.6σ or less between any pair of $N_f = 2 + 1$ determinations, regardless of whether the Ω mass, the Ξ mass or pseudoscalar decay constants were used. Also the $N_f = 2 + 1 + 1$ determination with twisted mass fermions (ETM 21 [16]) is consistent with our result. However, the three $N_f = 2 + 1 + 1$ determinations that were obtained using the highly improved staggered quark (HISQ) sea quark action (CalLat 20 [8], MILC 15 [18] and HPQCD 13 [15]) appear to suggest a somewhat lower value.

In figure 27 we compare our spectrum of strongly stable baryons with previous determinations in $N_f = 2 + 1(+1)$ QCD where a continuum limit extrapolation was attempted. The most comprehensive study so far was carried out for $2 + 1$ fermions by BMW 08 [9], who also set the scale using the mass of the Ξ baryon. In that case 18 ensembles were employed across three lattice spacings $a \approx 0.125$ fm, $a \approx 0.085$ fm and $a \approx 0.065$ fm with pion masses $M_\pi > 190$ MeV and statistics typically between 1000 and 2000 MDUs. Apart from having longer HMC runs, employing almost 50 ensembles (see table 1), we significantly vary the strange quark mass too, cover six lattice spacings 0.039 fm $\lesssim a \lesssim 0.098$ fm and go down to the physical pion mass (see table 2 and figures 1–3). While BMW 08 also employed Wilson quarks, our action is non-perturbatively order a improved. All of this, together with the improved quark smearing used (see appendix E.1), enables very significant reductions of the errors, see figure 27. Another comprehensive study was carried out by ETM 14 [66] using $2 + 1 + 1$ twisted mass fermions. In that case the nucleon mass was used to set the scale and the Ω mass was employed to match the strange quark mass and could therefore not be predicted. Ten ensembles across three lattice spacings 0.065 fm $\lesssim a \lesssim 0.094$ fm were realized with pion masses $M_\pi > 210$ MeV. Additional continuum limit results on either the nucleon mass (χ QCD 18 [148], PNDME 19 [149], MILC 19 [151] and Mainz 22 [153]) or the cascade mass (Miller et al. 22 [8]) alone are included too. For details on the scale input, see the caption of figure 27. These determinations employed overlap fermions on top of $N_f = 2 + 1$ domain wall fermions [148], Wilson-clover fermions on top of $N_f = 2 + 1 + 1$ HISQ [149], $N_f = 2 + 1 + 1$ HISQ [151] and a subset of the $N_f = 2 + 1$ CLS ensembles that we use [153].

In figure 28 we compare our result on $\sigma_{\pi N}$ (RQCD 22, red square and the shaded

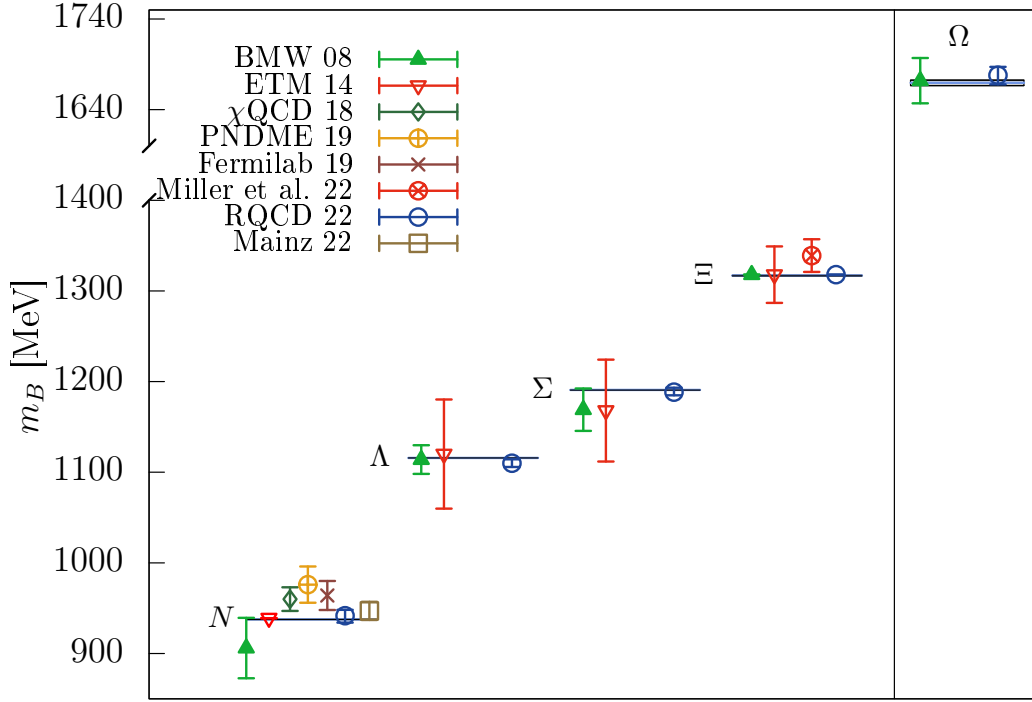


Figure 27. Comparison of our spectrum of strongly stable baryons (RQCD 22, blue circles) with other $N_f = 2 + 1$ and $N_f = 2 + 1 + 1$ continuum limit extrapolated results. BMW 08 [9] ($N_f = 2 + 1$) also used the Ξ baryon mass to set the scale, whereas ETM 14 [66] ($N_f = 2 + 1 + 1$) employed the nucleon mass and no prediction of the Ω baryon mass was made since this was used to fix the strange quark mass. Other determinations of either the nucleon or the cascade mass include χ QCD 18 [148] ($N_f = 2 + 1$, scale from the Ω baryon mass [6]), PNDME 19 [149] ($N_f = 2 + 1 + 1$, scale from ref. [150], indirectly using the pion and kaon decay constants), Fermilab 19 [151] ($N_f = 2 + 1 + 1$, scale from ref. [152] using the value of the parameter w_0 [5], determined in HPQCD 13 [15] from the pion decay constant), Miller et al. 22 [67] ($N_f = 2 + 1 + 1$, scale set from the Ω mass of CalLat 20 [8]), Mainz 22 [153] ($N_f = 2 + 1$, scale set via t_0 from the pion and kaon decay constants by Bruno et al. 16 [2]).

grey region) with other determinations.²⁰ The lattice determinations are all statistically consistent with our result. Only JLQCD 18 [159] suggest a much smaller central value, while ETM 14 [66] (however, superseded in part by ETM 19 [161]) and, more recently, Gupta et al. [163] suggest quite large values for this parameter. We refer the reader to the FLAG 2021 Review [109] for a more detailed comparison of the different lattice results. Also shown in the figure are the FLAG 21 averages as well as determinations using $N\pi$ scattering data. Note that refs. [147, 155] take account of isospin breaking effects, while all the lattice

²⁰Further efforts to determine the σ terms from fits to collections of lattice baryon mass data can be found, e.g., in refs. [123, 126, 127, 141, 142]. Particularly puzzling results (also for the LECs) were obtained in a recent fit [164] to the same baryon mass data that we present here: not only the value found for $\sigma_{\pi N}$ is much larger than ours but also the error given is three and a half-fold smaller, while the strangeness σ term is reported to be significantly negative ($\sigma_{sN} \approx -316(76)$ MeV)!

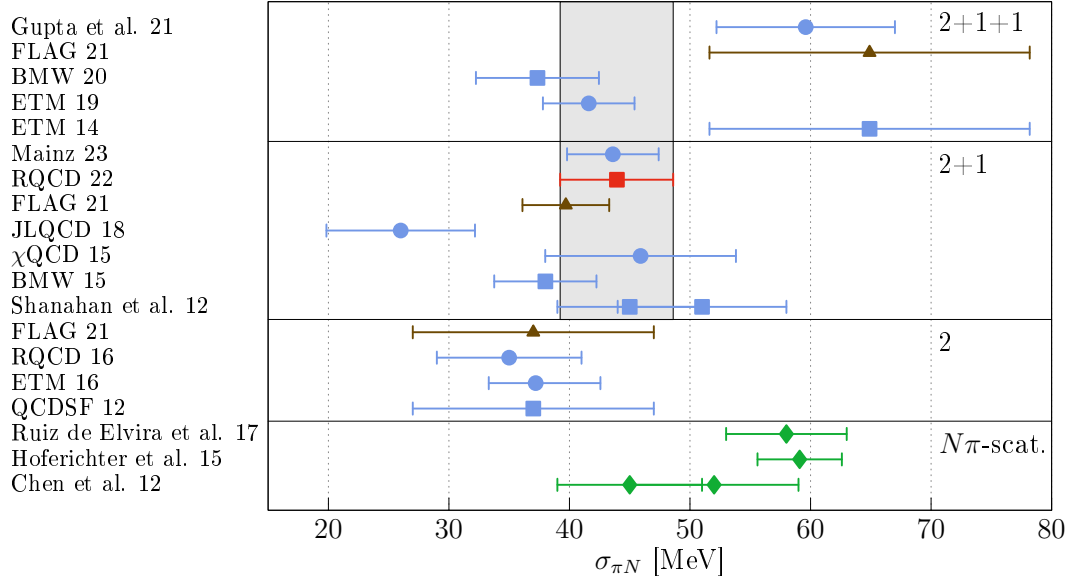


Figure 28. Comparison of our determination of $\sigma_{\pi N}$ (red square and shaded grey region) to recent determinations of this quantity from pion-nucleon scattering data (Chen et al. 12 [154], Hoferichter et al. 15 [147], Ruiz de Elvira et al. 17 [155]), lattice simulations with $N_f = 2$ flavours (QCDSF 12 [11], ETM 16 [156], RQCD 16 [157]), $N_f = 2 + 1$ flavours (Shanahan et al. 12 [139], BMW 15 [140], χ QCD 15 [158], JLQCD 18 [159]), Mainz 23 [160] and $N_f = 2 + 1 + 1$ flavours (ETM 14 [66], ETM 19 [161], BMW 20 [162], Gupta et al. 21 [163]). Also shown as brown triangles are the averages of the FLAG Review 2021 [109]. Circles correspond to direct determinations, squares to fits to the quark mass dependence of the nucleon mass.

results refer to iso-symmetric QCD. In ref. [147] isospin effects are estimated to increase the pion-nucleon σ term by about 3 MeV. The magnitude of this effect is not unexpected since to leading non-trivial order the σ term is proportional to the squared pion mass and, for instance, $M_{\pi^+}^2/M_{\pi^0}^2 \approx 1.07$. Nevertheless, even when adding 3 MeV to our iso-symmetric QCD prediction,

$$\sigma_{\pi N} = (43.9 \pm 4.7) \text{ MeV}, \quad (6.15)$$

this is still by more than 1.6 standard deviations smaller than the latest determination from pion-nucleon scattering data, $\sigma_{\pi N} = 58(5) \text{ MeV}$ [155]. An earlier determination by the same authors gave $\sigma_{\pi N} = 59.1(3.5) \text{ MeV}$ [147].

7 Summary of the main results

We summarize our findings, starting with results that are specific to our lattice action, continuing with the σ terms, the LECs and the scale setting parameter, and concluding with the light baryon spectrum.

7.1 Results that are specific to the lattice action

We employed non-perturbatively order a improved Wilson fermions [82, 83] and the tree-level Symanzik improved gauge action [84]. For details on the action and the implementation for

$N_f = 2 + 1$ fermions, see ref. [78]. We determined the scale parameter t_0^* in lattice units as a function of the inverse lattice coupling $\beta = 6/g^2$. This parameter is defined at the point in the quark mass plane where $m_u = m_d = m_s$ and $\phi_4^* = 12t_0^*M_\pi^2 = 1.11$. Within the range $3.34 \leq \beta \leq 3.85$, $(t_0^*/a^2)(g^2)$ is given by the interpolating formula (3.38), which approaches the perturbative two-loop expectation at large β . The dependence on β is visualized in the right panel of figure 8, where in addition we show t_0/a^2 at the SU(3) chiral point. The results for the β -values at which we carried out the simulations are displayed in table 5, along with the lattice spacings that are obtained using $\sqrt{8t_0^*} = 0.4097_{(25)}^{(20)}$ fm.

An interpolating formula for the $N_f = 3$ critical hopping parameter value $\kappa_{\text{crit}}(g^2)$ is given in eq. (3.21) and shown in the right panel of figure 5. This interpolation will approach the two-loop result at large β -values. The corresponding values, as well as κ^* and $am^* = \frac{1}{2}(1/\kappa^* - 1/\kappa_{\text{crit}})$, are displayed in table 6. In table 7 we list the starting points on the $m_s = m_\ell$ line for the different β -values of trajectories of constant $m_u + m_d + m_s$ that will touch the physical point in terms of κ_{opt} and $\phi_{4,\text{opt}}$. The physical point is defined by $M_{\pi,\text{ph}} = 134.8(3)$ MeV and $M_{K,\text{ph}} = 494.2(3)$ MeV, where the scale is set using $\sqrt{8t_{0,\text{ph}}} = 0.4098_{(25)}^{(20)}$ fm.

We give interpolating formulae for the combination of renormalization factors $Z(g^2) = (Z_m Z_P/Z_A)(g^2)$ and the ratio of singlet and octet mass renormalization constants $r_m(g^2) = (Z_m^s/Z_m^{ns})(g^2)$ in eqs. (3.18) and (3.19), respectively. The former is compared to results from the literature in the right panel of figure 4 and the latter in the left panel of figure 5. The interpolating formulae are such that $Z(g^2)$ and $r_m(g^2)$ will approach the perturbative one- and two-loop expectations, respectively, at small values of g^2 . The numerical values at our simulation points are tabulated in table 3. We include the combinations of $\mathcal{O}(a)$ improvement coefficients \mathcal{A} , \mathcal{B}_0 , \mathcal{C}_0 and \mathcal{D}_0 that are defined in eqs. (3.10)–(3.13) (see also eqs. (3.7) and (3.8)) in the same table. The corresponding interpolations for \mathcal{B}_0 and \mathcal{C}_0 are given in eq. (3.17) (with the coefficients of table 4) and plotted in the left panel of figure 4. These interpolations also approach the respective one-loop expectations at small values of g^2 . Finally, estimates of integrated autocorrelation times for t_0 can be found in the last column of table 1.

7.2 The σ terms and the BChPT low energy constants

All the pion-baryon and strange-baryon σ terms for the nucleon, the Λ , the Σ , the Ξ and the Ω can be found in the third and fifth columns of table 10 with all systematics included in the error estimates. We refrain from determining the σ terms for the unstable resonances Δ , Σ^* and Ξ^* . The results, that are the first continuum limit determinations of σ terms other than for the nucleon, refer to iso-symmetric QCD. We compare $\sigma_{\pi N}$ (RQCD 22) to previous determinations in figure 28 and discuss this in section 6.8. The σ terms are computed from the dependence of the baryon masses on the pseudoscalar masses, also taking into account the dependence of the pseudoscalar masses on the quark masses. In particular, the strange σ terms are not very well constrained since we do not sufficiently vary the strange quark mass near the physical point. This will be improved upon in the near future by incorporating direct determinations of the scalar matrix elements [143].

In tables 11 and 12 we list the leading order and the NLO SU(3) LECs, employing BChPT in the EOMS regularization as well as HBChPT, both including and not including decuplet loops. In table 13 we also display the corresponding results for the nucleon mass in the SU(2) chiral limit and the SU(2) slope parameter c_1 . While the errors given also reflect the systematics due to different cuts regarding the lattice spacing, the volume and also the maximum average squared pseudoscalar mass, the results depend on the ChPT parametrization due to different higher order contributions. In terms of the reduced χ^2 -values, our data are better described by the BChPT expressions than by HBChPT.

We find $m_0 = 821_{(53)}^{(71)}$ MeV and $m_{D0} = 1147_{(91)}^{(74)}$ MeV from the preferred BChPT fits to the octet baryons and to the octet and decuplet baryons, respectively. This then gives $\delta = m_{D0} - m_0 = 333_{(84)}^{(79)}$ MeV. We display the corresponding values for F , D , $|\mathcal{C}|$ and $|\mathcal{H}|$ in eq. (6.8). From the baryon masses alone one can only determine ratios of these LECs with respect to the pseudoscalar decay constant in the $N_f = 3$ chiral limit, F_0 , for which we used the result of ref. [107]. In the same reference, where the baryon mass and the axial charges were analysed simultaneously, albeit only for the $m_s = m_\ell$ ensembles, m_0 comes out somewhat smaller and F and D somewhat larger than here. These ambiguities are most likely due to higher order terms in the chiral expansion, which we are unable to resolve within the present statistical uncertainties using the baryon spectrum alone. To investigate this more systematically, a simultaneous analysis of the baryon spectrum and the charges is planned.

The NLO LECs b_0 , b_D , b_F , t_{D0} (renamed from t_0 to avoid confusion with the scale parameter) and t_D are listed in table 12 and the values from the preferred fits displayed in eqs. (6.10) and (6.11). Due to the larger statistical errors of the decuplet masses and the smaller number of available data points for which these are stable, t_{D0} and t_D are subject to substantial errors. Regarding SU(2) BChPT, our preferred results for m_N^0 and c_1 are shown in eq. (6.12). Since we have many ensembles that are close to the $N_f = 2$ chiral limit, the SU(2) mass parameter $m_N^0 = 893.2_{(8.6)}^{(9.3)}$ MeV is well determined and robust against changes of the parametrization. Finally, we obtained the preliminary results in eq. (C.26) for the combinations of the mesonic SU(3) LECs $L_{85} = 2L_8 - L_5$ and $L_{64} = 2L_6 - L_4$.

7.3 The scale parameter t_0

We determined the scale parameter t_0 in $N_f = 2 + 1$ QCD using the mass of the Ξ baryon, along with M_π and M_K to define the physical quark mass point. Using this input, we observe that t_0 is quite robust against cuts in the data and changes of the parametrization with respect to the lattice spacing, the meson mass and the volume dependence, see figures 16, 17 and 18. To summarize our results, here we give values of t_0 at four different points in the quark mass plane,

- $t_{0,\text{ph}}$, the value at the physical point (where $\phi_4 = \phi_{4,\text{ph}} = 1.093_{(13)}^{(11)}$),
- t_0^* , the value at the point where $\phi_4 = \phi_4^* = 1.11$ and $m_s = m_\ell$,
- $t_{0,\text{ch}}$, the value in the $N_f = 3$ chiral limit (where $\phi_4 = 0$) and

- $t_{0,\text{ch2}}$, the value in the SU(2) chiral limit (where $\phi_4 = \phi_{4,\text{ch2}} = 1.014_{(13)}^{(11)}$):

$$\sqrt{8t_{0,\text{ph}}} = 0.4098_{(25)}^{(20)} \text{ fm}, \quad \sqrt{8t_0^*} = 0.4097_{(25)}^{(20)} \text{ fm}, \quad (7.1)$$

$$\sqrt{8t_{0,\text{ch}}} = 0.4170_{(27)}^{(22)} \text{ fm}, \quad \sqrt{8t_{0,\text{ch2}}} = 0.4108_{(25)}^{(22)} \text{ fm}. \quad (7.2)$$

All systematics are included in the error estimates. A comparison of $\sqrt{8t_{0,\text{ph}}}$ with other determinations of this parameter is shown in figure 26 and discussed in section 6.8. The leading meson mass dependence of t_0 in the continuum limit is given in eq. (3.25) and the respective LEC k_1 [103] is displayed in eq. (3.39). Within the present accuracy, we are unable to resolve any higher order corrections.

7.4 The light baryon spectrum

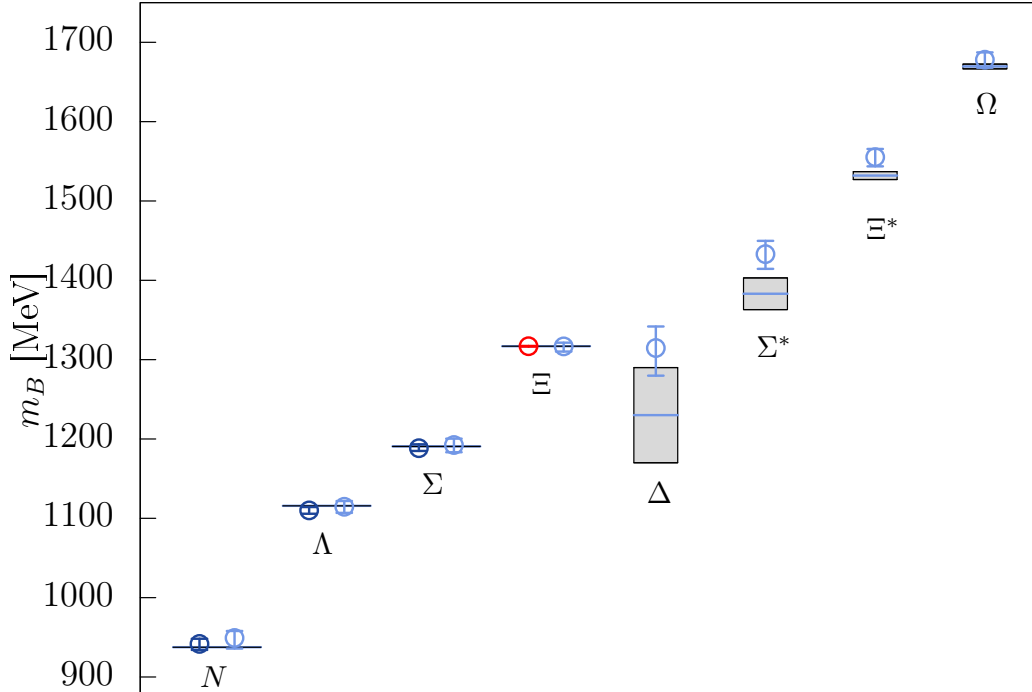


Figure 29. The continuum limit baryon spectrum at the physical point, obtained via the AIC averaging procedure. The dark blue symbols correspond to results obtained from the octet baryons. The mass of the Ξ baryon (red circle) was used to set the scale. The light symbols correspond to simultaneous BChPT fits to the octet and decuplet baryon spectrum. The lines and grey boxes depict the isospin violation corrected experimental values of table 14, including the uncertainties. The Δ , Σ^* and Ξ^* masses correspond to the maxima of the respective Breit–Wigner distributions and their errors reflect the widths of these distributions.

In figure 22 we investigate the impact of the parametrization of the continuum meson mass dependence on the baryon spectrum. The results from the preferred parametrization (BChPT including finite volume effects) are listed in table 9. In particular, we obtain for the

nucleon mass $m_N = 941.7^{(6.5)}_{(7.6)} \text{ MeV}$, which should be compared to the value 937.5 MeV that is obtained, when correcting the experimental proton and neutron masses for the isospin breaking QED and QCD effects. The other stable baryons also agree within errors with the expectations. Note that the uncertainty on the nucleon mass is just $\sim 7 \text{ MeV}$, i.e. less than 0.8%, while the uncertainties regarding the Λ and Σ baryon masses are $\sim 4 \text{ MeV}$, i.e. less than 0.4%. Our data driven approach with a very small residual dependence on the parametrization was possible due to the excellent coverage of the quark mass plane as well as by the availability of six lattice spacings with a^2 varying by a factor of more than six. In particular, the physical quark mass point is tightly constrained due to the intersection of the $\text{Tr } M = \text{const}$ and $\hat{m}_s \approx \text{const}$ trajectories, see, e.g., figures 14 and 19 for the octet baryon masses. The error reduction in comparison to previous continuum limit results, where the errors stated did not always include all sources of systematics, is evident from figure 27.

In figure 29 we visualize the results for the light octet and decuplet baryon masses given in table 9. The lines and boxes correspond to the experimental values, corrected for isospin breaking effects, of table 14, including the uncertainties of these estimates. For the Δ , the Σ^* and the Ξ^* we show the Breit–Wigner masses rather than the real parts of their poles, together with half the respective widths of the Breit–Wigner distributions as errors. The three dark circles are our predictions from the averaged fits to the octet baryon masses alone. The red circle is the corresponding Ξ baryon mass, which was used to set the scale for the other predictions. As mentioned above, we find agreement with experiment within sub-percent level errors. The light circles are the results of AIC averaged joint BChPT fits to the octet and decuplet baryons. Also here we find agreement with the expectation for the octet baryons, as well as for the Ω baryon.

Regarding the remaining decuplet resonances, namely the Δ , the Σ^* and the Ξ^* , our predictions from fits where only stable baryons are considered lie above the positions of the experimental resonances by slightly more than one decay width. This illustrates the limitations of determining “masses” and other properties of baryon resonances in the absence of a dedicated scattering study relating the spectrum of QCD in a finite volume to the resonance parameters [165], e.g., within the framework of (H)BChPT [166]. Such an investigation [167, 168] would require additional interpolators that specifically couple to octet baryons plus pions as well as additional volumes and/or non-zero momentum frames.

The Gell-Mann–Okubo mass relation for octet baryons implies that the flavour averaged mass combinations X_N and X_Λ defined in eq. (6.3) agree at linear order in the SU(3) symmetry breaking parameter δm if the average squared pseudoscalar mass is kept constant. Using the experimental masses, this relation is only violated by about 0.5%, which is consistent with our lattice data. This suggests that non-linear SU(3) symmetry breaking effects are similarly small at the physical point. One interesting observation is summarized in figure 23: the flavour breaking effects for these two mass combinations between the symmetric and the physical points turn out to be about 4%, an order of magnitude larger than the violation of the GMO relation. Since the correction is very similar for both averages shown, most of this effect cancels in the GMO relation.

8 Conclusions and outlook

This article is based on Coordinated Lattice Simulations (CLS) ensembles [78, 79, 169] that have been generated using the OPENQCD [89] code, employing the non-perturbatively $\mathcal{O}(a)$ improved Wilson action on top of the tree-level improved Symanzik gauge action. This study utilizes the unique combination of a large variation in the lattice spacing and good coverage of the quark mass plane: for the simultaneous continuum, infinite volume and physical mass point extrapolation we have determined two pseudoscalar and eight baryon masses (as well as t_0/a^2 and the quark masses) on almost 50 distinct gauge ensembles, encompassing six lattice spacings (covering a factor of more than six in terms of a^2) that are scattered around three distinct trajectories in the quark mass plane, including the physical point. The main results on the σ terms, SU(3) and SU(3) ChPT low energy constants, the scale parameter $t_{0,\text{ph}}$ and the light baryon spectrum are summarized in sections 7.2–7.4 above.

Since Wilson fermions provide an excellent compromise between theoretical rigour and computational affordability within the landscape of fermion formulations available in lattice QCD, further simulation points will be realized in the future. We determined interpolations for a number of parameters, e.g., the critical hopping parameter κ_{crit} , the ratio of the singlet over the non-singlet quark mass renormalization constants r_m , various combinations of order a improvement coefficients as well as the scale t_0^*/a^2 as functions of the inverse coupling parameter β , see section 7.1 for references to the relevant equations, figures and tables. Having mapped out the parameter space for our action will enable a very efficient planning of new simulation points. Another important result is the determination of the lattice scales $t_{0,\text{ph}}$ and t_0^* , see eq. (7.1), from the experimentally very well known Ξ baryon mass.

Following up on this work, we plan investigations of the quark masses, pseudoscalar decay constants and nucleon matrix elements. Of particular interest in this context is SU(3) ChPT. On the one hand, due to the heavier strange quark mass, its convergence properties at the physical point must be inferior to those of SU(2) ChPT. On the other hand, the increase of the number of LECs when going from SU(2) to SU(3) is much smaller than the increase of the number of independent observables that can be used to constrain these. Here we have demonstrated that within sub-percent level accuracy the mass and volume dependence of the whole octet baryon spectrum in the iso-symmetric continuum limit can be parameterized in terms of just six LECs, at least for $\overline{M}^2 = (2M_K^2 + M_\pi^2)/3 < (440 \text{ MeV})^2$ and $M_\pi > 130 \text{ MeV}$. In the future we plan a simultaneous baryon ChPT analysis of the axial charges [107, 170, 171], directly determined σ terms [143] and the baryon spectrum to establish the universality of the LECs and to arrive at increased precision regarding these observables and $t_{0,\text{ph}}$.

Acknowledgments

GB, SC and DJ acknowledge support through the European Union’s Horizon 2020 research and innovation programme under the Marie Skłodowska-Curie grant agreement no. 813942 (ITN EuroPLEx). SC and SW received support through the German Research Foundation

(DFG) grant CO 758/1-1. Part of the work of GB and SW was funded by the German Federal Ministry of Education and Research (BMBF) grant no. 05P18WRFP1. Additional support from the EU through grant agreement no. 824093 (STRONG 2020) is gratefully acknowledged, as well as initial stage funding through the DFG collaborative research centre SFB/TRR-55. This work was also supported by DFG grant NFDI 39/1 (PUNCH4NFDI).

We thank all our CLS colleagues for discussions and the joint production of the gauge ensembles. Moreover, we thank Benjamin Gläkle, Fabian Kaiser, Andreas Rabenstein, Philipp Wein and Thomas Wurm for their contributions at the beginning of this project regarding code development, the generation of some of the two-point functions and cross checks.

The authors gratefully acknowledge the [Gauss Centre for Supercomputing \(GCS\)](#) for providing computing time through the [John von Neumann Institute for Computing \(NIC\)](#) on the supercomputer JUWELS [172] and, in particular, on the Booster partition of the supercomputer JURECA [173] at [Jülich Supercomputing Centre \(JSC\)](#). GCS is the alliance of the three national supercomputing centres HLRS (Universität Stuttgart), JSC (Forschungszentrum Jülich), and LRZ (Bayerische Akademie der Wissenschaften), funded by the BMBF and the German State Ministries for Research of Baden-Württemberg (MWK), Bayern (StMWFK) and Nordrhein-Westfalen (MIWF). The authors also acknowledge the Interdisciplinary Centre for Mathematical and Computational Modelling (ICM) of the University of Warsaw for computer time on Okeanos (grant Nos. GA67-12, GA69-20 and GA72-26) and AGH Cyfronet Computing Center under Grant ID pionda, nspt, hadron-spectrum. Additional computations were carried out on the SFB/TRR-55 QPACE 2 [174] Xeon Phi installation and the iDataCool cluster in Regensburg, on the QPACE 3 Xeon Phi cluster of SFB/TRR-55 hosted at JSC and the Regensburg Athene 2 cluster. The authors also thank the JSC for their support and for providing services and computing time on the HDF Cloud cluster [175] at JSC, funded via the Helmholtz Data Federation (HDF) programme.

Most of the ensembles were generated using [OPENQCD](#) [89] within the [Coordinated Lattice Simulations \(CLS\)](#) effort. A few additional ensembles were generated employing the BQCD-code [85] on the QPACE supercomputer of SFB/TRR-55. For the computation of the correlation functions we used a modified version of the CHROMA [176] software package along with the LIBHADRONANALYSIS library and the multigrid solver implementation of Refs. [177, 178] (see also ref. [179]) as well as the IDFLS solver [180] of OPENQCD.

A Correcting for electrical and mass isospin breaking effects

In our simulations we neglect isospin breaking effects. Isospin breaking is controlled by two small parameters, the quark mass difference $(m_d - m_u)/\Lambda$ and the fine structure constant α_{fs} . Both parameters are of the size 10^{-2} . The factorization of isospin breaking into QCD and QED effects is not unique, see, e.g., refs. [181–183]. A popular way is to choose the $\overline{\text{MS}}$ scheme at the scale $\mu = 2 \text{ GeV}$ [183] in order to disentangle these effects. Regarding the baryons we will deviate from this prescription as the ambiguity between different procedures is smaller than the precision required here.

We match our simulation parameters to a world where isospin breaking effects are subtracted. The starting point is the splitting between neutral and charged pions. Unlike the charged pion, the neutral pion two-point function receives contributions from a disconnected quark line diagram. Formally, this is of second order in the QCD and QED isospin breaking parameters. Restricting ourselves to first order corrections, the mass difference is entirely electromagnetic in nature and the isospin corrected pion mass can be obtained, e.g., following the conventions outlined in ref. [183]. We use the so-obtained pion and kaon mass values of the FLAG 2016 Review [184] and define the physical point in the quark mass plane at each lattice spacing as the position where

$$M_{\pi,\text{ph}} = 134.8(3) \text{ MeV} \quad \text{and} \quad M_{K,\text{ph}} = 494.2(3) \text{ MeV}. \quad (\text{A.1})$$

These values correspond to electrically neutral isospin-averaged pions and kaons, see the discussion in Sections 3.1.1 and 3.1.2 of ref. [184].

Also in the case of a baryon B , isospin breaking effects can be parameterized in terms of QCD- and QED-related baryon mass shifts, Δm_B^{QED} and Δm_B^{QCD} : we start by decomposing the on-shell matrix element for the isovector vector current between baryons B^{Q+1} and B^Q (that differ by $\Delta I_3 = 1$ in their isospin) for $p' \approx p$ into formfactors:

$$\partial^\mu \langle B^{Q+1}(p') | \bar{d} \gamma_\mu u | B^Q(p) \rangle = \partial^\mu \bar{u}_{B^{Q+1}}(p') [g_{V,B} \gamma_\mu + \dots] u_{B^Q}(p), \quad (\text{A.2})$$

where $g_{V,B} = 1$ to leading order in the symmetry breaking parameters and the ellipses denote terms that vanish for $p' = p$. Combining this with the vector Ward identity $i\partial^\mu \bar{d} \gamma_\mu u = (m_u - m_d) \bar{d}u$, one obtains

$$\Delta m_B^{\text{QCD}} = g_{S,B} (m_u - m_d) \quad (\text{A.3})$$

as the QCD contribution to the mass difference, where $g_{S,B}$ denotes the isovector scalar charge in the iso-symmetric limit. Since we neither precisely know the isovector scalar charges $g_{S,B}$ nor the quark mass difference $m_u - m_d$, we resort to current algebra arguments — which is sufficient for the precision that is required in the present context. We assume that the splittings can be explained by two parameters, $\delta m^{\text{QED}} > 0$ and $\delta m^{\text{QCD}} > 0$, that are the same across an SU(3) multiplet, the former multiplying the difference of the squared electrical charges and the latter the isospin difference. This assumption implies the Coleman–Glashow theorem [185] $\Delta m_N - 2\Delta m_\Sigma + \Delta m_\Xi = 0$. It also corresponds to $\Delta m_B^{\text{QCD}} = -\delta m^{\text{QCD}}$, i.e. the scalar couplings $g_{S,B}$ are assumed to be independent of the baryon B . The proportionality of δm^{QED} to the square of the electric charge is consistent with the Dashen theorem [186]. In other words, to leading order in the isospin breaking effects, the masses of neutral particles do not receive QED contributions. We obtain

$$\Delta m_N = m_p - m_n \approx -\delta m^{\text{QCD}} + \delta m^{\text{QED}}, \quad (\text{A.4})$$

$$2\Delta m_\Sigma = m_{\Sigma^+} - m_{\Sigma^-} \approx -2\delta m^{\text{QCD}}, \quad (\text{A.5})$$

$$\Delta m_\Xi = m_{\Xi^0} - m_{\Xi^-} \approx -\delta m^{\text{QCD}} - \delta m^{\text{QED}}. \quad (\text{A.6})$$

The resulting Coleman–Glashow theorem was confirmed to hold within an accuracy of 0.13 MeV in ref. [69], while the experimental value reads 0.06(23) MeV [145].

Plugging in the experimental masses gives

$$\begin{aligned}\delta m^{\text{QED}} &= \frac{1}{2} (\Delta m_N - \Delta m_{\Xi}) = 2.78(11) \text{ MeV}, \\ &= \Delta m_N - \Delta m_{\Sigma} = 2.75(4) \text{ MeV},\end{aligned}\tag{A.7}$$

where we will use the second, more precise difference as our central value. However, as the Coleman–Glashow relation does not necessarily hold with the same accuracy, we will apply the larger error of 0.11 MeV.

We can now proceed to compute the mass of a hypothetical uncharged isospin symmetric Σ baryon:

$$m_{\Sigma} = \frac{1}{2} (m_{\Sigma^+} + m_{\Sigma^-}) - \delta m^{\text{QED}} = 1190.66(12) \text{ MeV}.\tag{A.8}$$

However, the charge-neutral Σ^0 baryon has the mass $m_{\Sigma^0} = 1192.64(2) \text{ MeV}$. In other words: computing $\frac{1}{2}(m_{\Sigma^+} + m_{\Sigma^-}) - m_{\Sigma^0} \approx 0.8 \text{ MeV}$ gives an estimate of δm^{QED} that is much smaller than the 2.75 MeV of eq. (A.7). Isospin breaking enables mixing between the two $I_3 = 0$ baryons Σ^0 and Λ . However, the impact of this on the baryon masses should be quadratic in the isospin breaking parameters and also there are numerical indications that the mixing angle is small [187, 188]. Therefore, the difference between the Σ^0 mass and eq. (A.8) strongly suggests that more than two parameters are needed to parameterize the isospin violations of the octet baryon masses, in spite of the experimental accuracy of the Coleman–Glashow relation: the spatial extension of a baryon and therefore its QED mass shift may depend on its strange quark content. Moreover, as we discussed above (see eq. (A.3)), the QCD mass shifts are proportional to the isovector scalar couplings $g_{S,B}$, which in general will depend on the strangeness of the baryon too. Indeed, in ref. [69] the Coleman–Glashow theorem was confirmed to hold, however, Δm_B^{QCD} was reported to differ between the octet baryons N , Σ and Ξ . Nevertheless, here we will use the value eq. (A.8) but we have to keep in mind that its uncertainty may be bigger than the suggested error, i.e. in the worst case it could be as large as 2 MeV.

In this article we use the cascade mass for the scale setting. We compute

$$m_{\Xi} := \frac{1}{2} (m_{\Xi^0} + m_{\Xi^-} - \delta m^{\text{QED}}) = 1316.9(3) \text{ MeV},\tag{A.9}$$

where we carry out the isospin average and correct the Ξ^- mass for the charge effect. Similarly, the isospin symmetric nucleon mass can be obtained as

$$m_N := \frac{1}{2} (m_n + m_p - \delta m^{\text{QED}}) = 937.54(6) \text{ MeV}.\tag{A.10}$$

Again, the errors displayed above may be underestimated: considering the deviation of the Σ^0 mass from the expectation, the real uncertainty of removing isospin breaking effects could be as large as 2‰, which, however, is much smaller than the uncertainty of 5‰ of the scale determination that we carry out here.

Regarding the decuplet, in this case only the Ω is a narrow resonance, while $\Xi^*(1530)$, $\Sigma^*(1385)$ and $\Delta(1232)$ have decay widths of about 10 MeV, 40 MeV and 120 MeV, respectively. For the real parts of the Ξ^* poles experiment gives

$$m_{\Xi^{*-}} - m_{\Xi^{*0}} = 3.2(6) \text{ MeV} \approx \delta m^{\text{QCD}} + \delta m^{\text{QED}}.\tag{A.11}$$

Table 14. (Pseudo-)experimental masses, corrected for the isospin breaking effects due to the light quark mass difference and electric charges. Note that for the baryons we have chosen one particular prescription so that an additional uncertainty of up to 2 MeV may exist. Regarding the three unstable decuplet baryons, we display their Breit–Wigner masses with the Breit–Wigner half-widths as errors.

mass	value/MeV
M_π	134.8(3)
M_K	494.2(3)
m_N	937.54(6)
m_Λ	1115.68(1)
m_Σ	1190.66(12)
m_Ξ	1316.9(3)
m_Δ	1230(60)
m_{Σ^*}	1383(20)
m_{Ξ^*}	1532(5)
m_Ω	1669.5(3.0)

For the octet we found $\delta m^{\text{QCD}} \approx 4 \text{ MeV}$. So the above difference is already saturated by the difference of the quark masses. This means that due to the presence of strong decay channels, we cannot reliably determine δm^{QED} for the decuplet baryons. Regarding the Ω , it is conceivable that this is spatially more compact than octet baryons, due to the heavier strange quark, so the octet value $\delta m^{\text{QED}} \approx 2.75(11) \text{ MeV}$ may be an underestimate. In view of the above, we subtract 3 MeV from the Ω^- baryon mass and add this as our systematic uncertainty, arriving at

$$m_\Omega = 1669.5(3.0) \text{ MeV}. \quad (\text{A.12})$$

Determining the other decuplet baryon poles reliably will require a dedicated scattering study. Since this is not carried out in the present article, we will compare our results to the experimental Breit–Wigner mass values of the Ξ^* , the Σ^* and the Δ decuplet baryons, with the errors given by half of the Breit–Wigner widths.

We summarize the masses of isospin symmetric QCD discussed above in table 14.

B Finite size effects on baryon masses

The expected dependence of the pseudoscalar masses on the spatial lattice extent L is presented in section 4.3. Here we provide the corresponding expressions regarding the octet and decuplet baryon masses. The finite volume effects in a cubic box of size L^3 have been computed in SU(2) and in SU(3) HBChPT and covariant BChPT, first at order p^3 and then at order p^4 [57, 123, 129, 133, 134, 189, 190], also including baryon loop effects [129, 134, 141, 142, 190]. To be consistent with the dependence on the pseudoscalar masses, here we will also only make use of the order p^3 results. Allowing for pseudoscalar

loops only, the volume dependence in BChPT is given as [123, 129, 189, 190]

$$m_B(L) = m_B + \frac{1}{(4\pi F_0)^2} \sum_{P \in \{\pi, K, \eta_8\}} g_{B,P} M_P^3 2 \int_0^\infty dx \sum_{\mathbf{n} \neq \mathbf{0}} K_0 \left(\lambda_M |\mathbf{n}| \sqrt{1 + x^2 - \frac{M_P}{m_0} x} \right), \quad (\text{B.1})$$

where the couplings $g_{B,P}$ are expressed in terms of the LECs D , F and \mathcal{H} in eqs. (5.15) and (5.22) and $\lambda_P = LM_P$. For the octet and decuplet baryons, m_0 and $m_{D0} = m_0 + \delta$ should be used, respectively, in the argument of the square root. The finite volume corrections are independent of the covariant ultraviolet regulator (e.g., the EOMS or the IR scheme), however, the HBChPT formulae differ somewhat since terms proportional to M_P/m_0 are consistently neglected in this case. In the heavy baryon limit the integration can be carried out analytically [57, 133, 134, 191]:

$$2 \int_0^\infty dx K_0 \left(\lambda_M |\mathbf{n}| \sqrt{1 + x^2 - \frac{M_P}{m} x} \right) \xrightarrow{m \rightarrow \infty} \pi \frac{e^{-\lambda_P |\mathbf{n}|}}{\lambda_P |\mathbf{n}|}. \quad (\text{B.2})$$

In addition, one encounters corrections from loops involving transitions between octet and decuplet baryons [129, 190]:

$$\begin{aligned} m_O(L) \mapsto m_O(L) + \frac{\mathcal{C}^2}{(4\pi F_0)^2} \frac{m_0^2}{m_{D0}^2} \sum_{P \in \{\pi, K, \eta_8\}} \xi_{O,P} M_P^2 \delta \int_0^\infty dy \left\{ \left[2 + \frac{\delta}{m_0} (1 - y) \right] g_O(y) \right. \\ \left. \times \sum_{\mathbf{n} \neq \mathbf{0}} \left[g_O(y) K_0(\lambda_P |\mathbf{n}| g_O(y)) - \frac{K_1(\lambda_P |\mathbf{n}| g_O(y))}{\lambda_P |\mathbf{n}|} \right] \right\} \end{aligned} \quad (\text{B.3})$$

with

$$g_O(y) = \sqrt{\left(1 - \frac{\delta^2}{M_P^2}\right) \left(1 - \frac{\delta}{m_0} y\right) + \frac{\delta^2}{M_P^2} (1 + y)^2}. \quad (\text{B.4})$$

The coefficients $\xi_{B,P}$ can be found in table 8. The decuplet masses receive similar octet loop corrections:

$$\begin{aligned} m_D(L) \mapsto m_D(L) + \frac{\mathcal{C}^2}{(4\pi F_0)^2} \frac{m_{D0}^2}{m_0^2} \sum_{P \in \{\pi, K, \eta_8\}} \xi_{O,P} M_P^2 \delta \int_0^\infty dy \left\{ \left[2 - \frac{\delta}{m_{D0}} (1 + y) \right] g_D(y) \right. \\ \left. \times \sum_{\mathbf{n} \neq \mathbf{0}} \left[g_D(y) K_0(\lambda_P |\mathbf{n}| g_D(y)) - \frac{K_1(\lambda_P |\mathbf{n}| g_D(y))}{\lambda_P |\mathbf{n}|} \right] \right\} \end{aligned} \quad (\text{B.5})$$

with

$$g_D(y) = \sqrt{\left(1 - \frac{\delta^2}{M_P^2}\right) \left(1 - \frac{\delta}{m_{D0}} y\right) + \frac{\delta^2}{M_P^2} (1 - y)^2}. \quad (\text{B.6})$$

The decuplet baryons may become unstable for $M_P < \delta$ and the infinite volume results as well as the finite volume corrections acquire imaginary parts. As for the infinite volume result,

we take the real part and restrict the fit to only include decuplet baryons that are stable. For imaginary $g_D(y)$, K_0 becomes imaginary while K_1 remains real, which means that the integrand is purely imaginary. Taking the real part, therefore, corresponds to omitting the part of the integration range where the argument of the square root in $g_D(y)$ is negative. The corresponding y -interval is symmetric about $y = 1 - \delta/(2m_{D0}) + M_P^2/(2m_{D0}\delta)$.

In the heavy baryon limit, the above integrals simplify to [57, 134]

$$\delta \int_0^\infty \dots \xrightarrow{m_0 \rightarrow \infty} 2\delta \int_0^\infty dy \left\{ f_\pm(y) \sum_{\mathbf{n} \neq \mathbf{0}} \left[f_\pm(y) K_0(\lambda_P |\mathbf{n}| f_\pm(y)) - \frac{K_1(\lambda_P |\mathbf{n}| f_\pm(y))}{\lambda_P |\mathbf{n}|} \right] \right\} \quad (\text{B.7})$$

with

$$f_\pm(y) = \sqrt{1 - \frac{\delta^2}{M_P^2} + \frac{\delta^2}{M_P^2} (y \pm 1)^2}, \quad (\text{B.8})$$

where the plus (minus) sign is for the octet (decuplet) baryons. For $M_P < \delta$, the integrand becomes imaginary in the range

$$y \in \left(1 - \sqrt{1 - \frac{M_P^2}{\delta^2}}, 1 + \sqrt{1 - \frac{M_P^2}{\delta^2}} \right), \quad (\text{B.9})$$

which we omit from the integration region.²¹ In the octet case, for $\lambda_P \gg 1$ the integral (B.7) has the limiting behaviour

$$\sqrt{2\pi} \delta \frac{M_P^2}{\delta^2} \sum_{\mathbf{n} \neq \mathbf{0}} \frac{e^{-\lambda_P |\mathbf{n}|}}{(\lambda_P |\mathbf{n}|)^{3/2}}, \quad (\text{B.10})$$

which one may further approximate, setting $|\mathbf{n}| = 1$ and replacing the sum by a factor of six. For small values of the ratio δ/M_P , this limit is only approached slowly. Here we use the full (H)BChPT expressions eqs. (B.7) and (B.8).

C The σ terms

We define the σ terms

$$\sigma_{qB} = m_q \left[\frac{\langle B | \bar{q} \mathbb{1} q | B \rangle}{2m_B} - V_3 \langle \Omega | \bar{q} \mathbb{1} q | \Omega \rangle \right] = m_q \frac{\partial m_B}{\partial m_q}, \quad (\text{C.1})$$

where $|\Omega\rangle$ denotes the vacuum, V_3 the spatial volume and the states at zero momentum are normalized as $\langle B | B \rangle = 2m_B V_3$. The σ terms can approximately be obtained from the dependence of the baryon masses m_B on the squared pseudoscalar meson masses M_P^2 . We discuss this below, as well as the corrections we encounter due to the mass rescaling $\mathfrak{m}_B = \sqrt{8t_0 m_B}$ and $\mathfrak{M}_P^2 = 8t_0 M_P^2$. We then further correct the formulae, taking into account violations of the GMOR relations, in appendix C.2, where we also determine the combinations of the mesonic SU(3) LECs $2L_8 - L_5$ and $2L_6 - L_4$.

²¹Note that in this case the integral from zero to the lower limit is equal to that from the upper limit to 2.

C.1 The σ terms from the meson mass dependence

In addition to the baryon masses and the LECs, it is also possible to obtain the σ terms: by relating the derivatives with respect to a quark mass m_q to derivatives with respect to squared pseudoscalar masses via the GMOR relations, it is easy to see that

$$\tilde{\sigma}_{\pi B} = M_\pi^2 \left(\frac{2}{3} \frac{\partial m_B}{\partial \overline{M}^2} - \frac{\partial m_B}{\partial \delta M^2} \right), \quad \tilde{\sigma}_{sB} = (2M_K^2 - M_\pi^2) \left(\frac{1}{3} \frac{\partial m_B}{\partial \overline{M}^2} + \frac{\partial m_B}{\partial \delta M^2} \right), \quad (\text{C.2})$$

where $\sigma_{\pi B} = \sigma_{uB} + \sigma_{dB}$ and $\sigma_{qB} = \tilde{\sigma}_{qB} [1 + \mathcal{O}(M^2)]$. The order M^2 corrections [192] to the GMOR relations will depend on the combinations $2L_8 - L_5$ and $2L_6 - L_4$ of the mesonic SU(3) LECs, in addition to F_0 and B_0 . This is discussed in appendix C.2 below. These NLO mesonic ChPT corrections should be taken into account when determining the derivatives using the GMO Taylor expansion, which includes order M^4 terms. Within the chiral power counting, formally these terms only need to be included in BChPT at NNNLO, whereas we only employ the NNLO expressions (which is sufficient to describe the baryon mass data). However, when fitting our quark masses as functions of the pion masses, it turns out that corrections to the GMOR relations need to be taken into account. Hence, for determining the σ terms, we will include them. We will distinguish between $\tilde{\sigma}_{qB}$, the σ terms determined assuming linear dependencies of the quark masses on the squared pseudoscalar masses, and σ_{qB} , the results that take into account the leading violations of the GMOR relations.

We remark that the LECs are defined in the SU(3) chiral limit while the σ terms are given at the physical point in the quark mass plane. Our fits are carried out for masses that are rescaled in units of $\sqrt{8t_0}$, which in turn depends on the meson masses. The leading dependence of t_0 on the pseudoscalar masses, eq. (3.25), results in the relations

$$\left. \frac{\partial \mathfrak{m}_{O|D}}{\partial \overline{M}^2} \right|_{\text{ph}} = \frac{1}{\sqrt{8t_0}} \left. \frac{\partial m_{O|D}}{\partial \overline{M}^2} \right|_{\text{ph}} + \frac{\tilde{k}_1}{2} \sqrt{8t_0} m_{0|D0} + \mathcal{O}(\overline{M}^2), \quad (\text{C.3})$$

$$\left. \frac{\partial \mathfrak{m}_B}{\partial \delta \overline{M}^2} \right|_{\text{ph}} = \frac{1}{\sqrt{8t_0}} \left. \frac{\partial m_B}{\partial \delta M^2} \right|_{\text{ph}} + \mathcal{O}(\overline{M}^2) \quad (\text{C.4})$$

between the derivatives of the fit formulae and those that we are interested in. Up to order \overline{M}^2 corrections, this amounts to

$$M_P^2 \frac{\partial m_{O|D}}{\partial \overline{M}^2} = \frac{\mathbb{M}_P^2}{\sqrt{8t_{0,\text{ph}}}} \left(\frac{\partial \mathfrak{m}_{O|D}}{\partial \overline{M}^2} - \frac{\tilde{k}_1}{2} \mathfrak{m}_{0|D0} \right), \quad (\text{C.5})$$

$$M_P^2 \frac{\partial m_B}{\partial \delta M^2} = \frac{\mathbb{M}_P^2}{\sqrt{8t_{0,\text{ph}}}} \frac{\partial \mathfrak{m}_B}{\partial \delta \overline{M}^2}, \quad (\text{C.6})$$

which is consistent with the relation (5.11) between $\overline{\mathfrak{b}}$ and \bar{b} (or between $\overline{\mathfrak{t}}$ and \bar{t} for the decuplet baryons) as well as with eq. (5.10). Within our statistical accuracy we cannot detect any higher order corrections to the dependence of t_0 on the pseudoscalar masses eq. (3.25). Since we will also include corrections to the GMOR relations, we expand eq. (C.5) one order higher (neglecting higher order contributions to t_0) and obtain for the case of the

octet baryons

$$M_P^2 \frac{\partial m_O}{\partial \overline{M}^2} = \frac{\mathbb{M}_P^2}{\sqrt{8t_{0,\text{ph}}}} \left[\frac{\partial \mathbb{m}_O}{\partial \overline{M}^2} - \frac{\tilde{k}_1}{2} (\mathbb{m}_0 + \overline{\mathbb{b}} \overline{M}^2 + \delta \mathbb{b}_O \delta \overline{M}^2) + \frac{\tilde{k}_1^2}{2} \overline{M}^2 \mathbb{m}_0 \right]. \quad (\text{C.7})$$

The expression for decuplet baryons is analogous, replacing $\mathbb{m}_0 \mapsto \mathbb{m}_{D0}$, $\overline{\mathbb{b}} \mapsto \overline{\mathbb{t}}$ and $\delta \mathbb{b}_O \mapsto \delta \mathbb{t}_D$. We will include this effect into our determinations of both $\tilde{\sigma}_{qB}$ and σ_{qB} .

C.2 Impact of corrections to the GMOR relations on the σ terms

The general strategy of determining the σ terms was outlined above, including the impact of rescaling all quantities in units of $\sqrt{8t_0}$, see eq. (C.7). Here we consider higher order corrections to eq. (C.2) due to violations of the GMOR relations.

The σ terms are defined in eq. (C.1):

$$\sigma_{qB} = m_q \frac{\partial m_B}{\partial m_q} = \sum_P m_q \frac{\partial M_P^2}{\partial m_q} \frac{\partial m_B}{\partial M_P^2}. \quad (\text{C.8})$$

For a linear dependence of the meson masses M_P^2 on the quark masses m_q this results in $\tilde{\sigma}_{qB} = \sigma_{qB}$, where $\tilde{\sigma}_{qB}$ is defined in eq. (C.2). At our level of precision, we find order p^4 terms to be necessary to describe the dependence of the meson masses on the quark masses, whereas the order p^3 BChPT expansion suffices to parameterize the baryon masses. Therefore, we wish to expand the right hand side of the above equation to order p^4 , even though this is not required in the BChPT power counting. For the GMO expansion, where we include terms proportional to M_P^4 , expanding the meson masses one order higher is necessary also for consistency.

Expanding eq. (C.8) to order p^4 , meson masses that appear within order p^3 terms (or order M_P^4 terms in the GMO expansion) can be substituted with the leading order expressions

$$M_\pi^2 = 2B_0 m_\ell, \quad M_K^2 = B_0 (m_\ell + m_s), \quad M_{\eta_8}^2 = B_0 \left(\frac{2}{3} m_\ell + \frac{4}{3} m_s \right). \quad (\text{C.9})$$

Using

$$M_{\eta_8}^2 = \frac{4}{3} M_K^2 - \frac{1}{3} M_\pi^2, \quad (\text{C.10})$$

the leading order derivatives with respect to the logarithms of the quark masses read

$$m_\ell \frac{\partial M_\pi^2}{\partial m_\ell} = M_\pi^2, \quad m_\ell \frac{\partial M_K^2}{\partial m_\ell} = \frac{1}{2} M_\pi^2, \quad m_\ell \frac{\partial M_{\eta_8}^2}{\partial m_\ell} = \frac{1}{3} M_\pi^2, \quad (\text{C.11})$$

$$m_s \frac{\partial M_\pi^2}{\partial m_s} = 0, \quad m_s \frac{\partial M_K^2}{\partial m_s} = \frac{1}{2} (2M_K^2 - M_\pi^2), \quad m_s \frac{\partial M_{\eta_8}^2}{\partial m_s} = \frac{2}{3} (2M_K^2 - M_\pi^2). \quad (\text{C.12})$$

Plugging this into eq. (C.8) gives eq. (C.2), where we replace the derivatives by eqs. (C.5) and (C.6). At order p^4 the σ terms will differ from the $\tilde{\sigma}$ terms, defined in eq. (C.2). We will consistently correct for this difference to order p^4 . This amounts to substituting eq. (C.5) with eq. (C.7) for the mass-dependence of t_0 and expanding eq. (C.9) to the next order,

substituting eqs. (C.11) and (C.12) with the corresponding derivatives of the higher order expression. These will depend on mesonic LECs that we shall also determine from the dependence of the quark masses on the pseudoscalar meson masses. Below we explain how the result is obtained.

The order p^4 corrections that we address below only affect the terms proportional to \bar{b} and δb_B (see, e.g., eq. (5.13)) and are therefore not required for $M_{\eta_8}^2$. We define

$$\mu_P^2 = \frac{1}{2} \frac{M_P^2}{(4\pi F_0)^2} \ln \left(\frac{M_P^2}{\mu^2} \right), \quad (\text{C.13})$$

which we will need for $P = \pi$ and $P = \eta_8$. Up to higher orders, we can carry out the replacements

$$\mu_\pi^2 = \frac{B_0}{(4\pi F_0)^2} m_\ell \ln \left(\frac{2B_0 m_\ell}{\mu^2} \right), \quad \mu_{\eta_8}^2 = \frac{B_0}{(4\pi F_0)^2} \frac{1}{3} (m_\ell + 2m_s) \ln \left[\frac{2}{3} \frac{B_0 (m_\ell + 2m_s)}{\mu^2} \right]. \quad (\text{C.14})$$

The order p^4 relations read [192]

$$M_\pi^2 = 2B_0 m_\ell \left\{ 1 + \mu_\pi^2 - \frac{1}{3} \mu_{\eta_8}^2 + \frac{16B_0}{F_0^2} [m_\ell L_{85} + (m_s + 2m_\ell) L_{64}] \right\}, \quad (\text{C.15})$$

$$M_K^2 = B_0 (m_s + m_\ell) \left\{ 1 + \frac{2}{3} \mu_{\eta_8}^2 + \frac{8B_0}{F_0^2} [(m_s + m_\ell) L_{85} + 2(m_s + 2m_\ell) L_{64}] \right\}, \quad (\text{C.16})$$

where

$$L_{85}(\mu) = 2L_8(\mu) - L_5(\mu), \quad L_{64}(\mu) = 2L_6(\mu) - L_4(\mu) \quad (\text{C.17})$$

are combinations of scale-dependent LECs. It is easy to see that

$$L_{85}(\mu') = L_{85}(\mu) - \frac{1}{12} \frac{1}{16\pi^2} \ln \left(\frac{\mu^2}{\mu'^2} \right), \quad L_{64}(\mu') = L_{85}(\mu) + \frac{1}{72} \frac{1}{16\pi^2} \ln \left(\frac{\mu^2}{\mu'^2} \right). \quad (\text{C.18})$$

Inverting eqs. (C.15) and (C.16) gives

$$2B_0 m_\ell = M_\pi^2 \left\{ 1 - \mu_\pi^2 + \frac{1}{3} \mu_{\eta_8}^2 - \frac{8}{F_0^2} [M_\pi^2 L_{85} + (2M_K^2 + M_\pi^2) L_{64}] \right\}, \quad (\text{C.19})$$

$$\begin{aligned} 2B_0 m_s = & (2M_K^2 - M_\pi^2) \left[1 - \frac{8}{F_0^2} (2M_K^2 + M_\pi^2) L_{64} \right] + M_\pi^2 \mu_\pi^2 - \frac{1}{3} (4M_K^2 + M_\pi^2) \mu_{\eta_8}^2 \\ & - \frac{8}{F_0^2} (2M_K^4 - M_\pi^4) L_{85}. \end{aligned} \quad (\text{C.20})$$

In order to compute the contributions to the σ terms according to eq. (C.8) consistently at order p^4 , we need to multiply the derivatives with respect to the quark mass of the squared pion masses eqs. (C.15) and (C.16) that accompany the coefficients \bar{b} and δb_B within eq. (5.13) by the quark masses eqs. (C.19) and (C.20). As discussed above, for the higher order corrections to the baryon masses it is sufficient to truncate according to eqs. (C.11)–(C.12). The respective expressions are generated automatically, using SYMPY [193].

In our fits we rescale m_q and M_P^2 into units of $\sqrt{8t_0}$. The LECs are all defined in the SU(3) chiral limit, in units of $\sqrt{8t_{0,\text{ch}}}$. This difference implies a shift of the LEC combination

L_{64} , due to $t_0 = t_{0,\text{ch}}(1 + \tilde{k}_1 8t_0 \overline{M}^2)$. We define \tilde{L}_{64} as the fitted LEC for the dependence of the quark masses on the squared meson masses given in units of $\sqrt{8t_0}$ and, starting from eq. (C.19), derive the relation

$$\begin{aligned} 2m_\ell B_0 &= \frac{\sqrt{t_0}}{\sqrt{t_{0,\text{ch}}}} M_\pi^2 \left\{ 1 - \mu_\pi^2 + \frac{1}{3} \mu_{\eta_8}^2 - \frac{8}{F_0^2} \left[M_\pi^2 L_{85} + (2M_K^2 + M_\pi^2) \tilde{L}_{64} \right] \right\} \\ &= M_\pi^2 \left\{ 1 + \dots - (2M_K^2 + M_\pi^2) \left(\frac{8}{F_0^2} \tilde{L}_{64} - \frac{1}{6} 8t_0 \tilde{k}_1 \right) \right\}. \end{aligned} \quad (\text{C.21})$$

Comparison with eq. (C.19) gives

$$L_{64} = \tilde{L}_{64} - \frac{\tilde{k}_1}{48} 8t_0 F_0^2. \quad (\text{C.22})$$

Within eq. (C.8) we need the derivatives of the pseudoscalar masses with respect to the quark mass. Therefore, within the analytic expression, L_{64} should be used instead of \tilde{L}_{64} . The difference is small but of a similar magnitude as L_{64} itself.

The combinations of LECs L_{85} and L_{64} turn out to be numerically small, however, they are accompanied by $1/F_0^2$, rather than by $1/(4\pi F_0)^2$ and $(4\pi)^2 \approx 158$. MILC [194] and HPQCD [15] give values at the scale $\mu = M_{\eta_8} \approx 576 \text{ MeV}$. Converting these results to the standard scale $\mu = M_\rho \approx 770 \text{ MeV}$ (see eq. (C.17)) results in

$$L_{85} = -0.20(11)_{(19)}^{(45)} \cdot 10^{-3}, \quad L_{64} = 0.04(24)_{(27)}^{(32)} \cdot 10^{-3} \quad (\text{C.23})$$

for MILC and

$$L_{85} = -0.15(20) \cdot 10^{-3}, \quad L_{64} = 0.23(17) \cdot 10^{-3} \quad (\text{C.24})$$

for HPQCD. L_6 and L_4 are suppressed in $1/N_c$ relative to L_8 and L_5 , which is not obvious from the above combinations which are all consistent with zero, due to cancellations. Some of us determined a value $L_{85} = 0.50(34) \cdot 10^{-3}$ in a large N_c NLO $U(3)$ ChPT analysis of the η/η' meson system [195]. In this approach, at this order $L_6 = L_4 = 0$ and there is no scale dependence of L_{85} . Finally, Bijens and Ecker [196] obtain the values

$$L_{85} = -0.12(21) \cdot 10^{-3}, \quad L_{64} = -0.02(10) \cdot 10^{-3} \quad (\text{C.25})$$

from a phenomenological fit (column BE14 of table 3 in their article, with a fixed value of L_4). Again, only upper limits could be set.

In the absence of precise and reliable literature values, we determined these parameters from our quark mass data. We obtain at the scale $\mu = 770 \text{ MeV} \approx 1.6/\sqrt{8t_0}$

$$\frac{L_{85}}{F_0^2} = 7.8(4.8) \cdot 10^{-9} \text{ MeV}^{-2}, \quad \frac{L_{64}}{F_0^2} = -1.5(3.2) \cdot 10^{-9} \text{ MeV}^{-2}. \quad (\text{C.26})$$

Setting, for instance, $F_0 = 71 \text{ MeV}$, the central values would correspond to $L_{85} \approx 0.04 \cdot 10^{-3}$ and $L_{64} \approx -0.008 \cdot 10^{-3}$. The smallness of these NLO LECs at this scale does not mean that the impact of the higher order is completely negligible since also the logarithmic terms μ_π^2 and $\mu_{\eta_8}^2$ enter the expressions.

D SU(2) BChPT low energy constants

The SU(2) (H)BChPT LECs can easily be derived from their SU(3) counterparts. Regarding the decuplet sector, the Δ appears to be the most interesting particle, however, due to its unstable nature, its self-energy acquires an imaginary part, whose inclusion is beyond the scope of the present study. Hence, we will restrict ourselves to the LECs that are governing the dependence of the nucleon mass on the pion mass, neglecting decuplet loops. In principle, similar LECs for the pion mass dependence of the Λ , the Σ and the Ξ can be obtained, however, we refrain from doing this since SU(3) BChPT is more adequate as a framework to study processes involving the different octet baryons. In SU(2) (H)BChPT the $\mathcal{O}(p^3)$ dependence is given as (see, e.g., ref. [189])

$$m_N(M_\pi) = m_N^0 - 4c_1 M_\pi^2 + \frac{3}{2} \frac{g_A^{02}}{(4\pi F_\pi^0)^2} m_N^{03} f_O \left(\frac{M_\pi}{m_N^0} \right), \quad (\text{D.1})$$

where m_N^0 , g_A^0 and F_π^0 denote the nucleon mass, the axial charge and the pion decay constant in the SU(2) chiral limit, respectively, at the physical strange quark mass. The loop function f_O for the EOMS regularization is defined in eq. (5.14). In the heavy baryon limit, $f_O(x) = -\pi x^3$. To our order in ChPT, keeping the strange quark mass fixed corresponds to varying the kaon mass as a function of the pion mass, according to

$$2M_K^2 - M_\pi^2 =: M_{ss}^2 = M_{ss,\text{ph}}^2 \approx (686 \text{ MeV})^2. \quad (\text{D.2})$$

Since $\overline{M}^2 = (M_{ss}^2 + 2M_\pi^2)/3$, this means that $\overline{M}_{\text{ph}}^2 - \overline{M}_{\text{ch2}}^2 = \frac{2}{3}M_{\pi,\text{ph}}^2$, where the subscript “ch2” indicates the SU(2) chiral limit. This then relates the t_0 parameters between the two points: using eqs. (3.25) and (3.39), we obtain

$$t_{0,\text{ph}} = \left[1 + \tilde{k}_1 8t_0 \left(\overline{M}_{\text{ph}}^2 - \overline{M}_{\text{ch2}}^2 \right) \right] t_{0,\text{ch2}} = 0.9976(3) t_{0,\text{ch2}}. \quad (\text{D.3})$$

Evaluating the parametrization (5.17) for $O = N$ at $M_\pi = 0$, $M_K = \sqrt{8t_{0,\text{ch2}}} M_{K,\text{ch2}}$ and $M_{\eta_8} = \sqrt{8t_{0,\text{ch2}}} M_{\eta_8,\text{ch2}}$, where $M_{K,\text{ch2}} = \sqrt{1/2} M_{ss,\text{ph}}$ and $M_{\eta_8,\text{ch2}} = \sqrt{2/3} M_{ss,\text{ph}}$, gives $m_N^0 = \sqrt{8t_{0,\text{ch2}}} m_N^0$, i.e. the nucleon mass in the SU(2) chiral limit in units of $\sqrt{8t_{0,\text{ch2}}}$. The conversion between $\sqrt{8t_{0,\text{ch2}}}$ and $\sqrt{8t_{0,\text{ph}}} = 0.4098_{(25)}^{(20)} \text{ fm}$ is given in eq. (D.3) above. Note that computing the expression (5.13) — that is given in physical units — for the pseudoscalar masses in the SU(2) chiral limit at order p^3 is equivalent to the above procedure.

Regarding the LEC c_1 , a comparison between eq. (D.1) and eq. (5.13) gives

$$c_1 = -\frac{1}{6}\bar{b} + \frac{1}{4}\delta b_N = b_0 + \frac{b_D}{2} + \frac{b_F}{2}. \quad (\text{D.4})$$

This is a relation between LECs that are all given in physical units. Therefore, in this case there exist no subtleties related to changes of t_0 between different points in the quark mass plane.

Note that to leading non-trivial order $\sigma_{\pi N} = -4c_1 M_{\pi,\text{ph}}^2$. Since the LECs F and D are not overly well-determined in the present study, we refrain from predicting g_A^0 , i.e. g_A in the SU(2) chiral limit. This is best left to simulations of the axial nucleon matrix element in the forward limit.

E Details of the spectrum and quark mass determinations

We define the interpolators that are used to create and destroy the pseudoscalar mesons and baryons. We then detail the quark smearing and the source positions employed. The latter are relevant regarding ensembles with open boundary conditions in time. After explaining the extraction of masses and their correlations from the resulting two-point functions, in appendix E.3 we tabulate the resulting hadron and AWI quark masses in lattice units as well as t_0/a^2 for all the ensembles.

E.1 Hadron interpolators and smearing

In our simulations the pseudoscalar mesons, the octet and the decuplet baryons are destroyed, respectively, using the relativistic interpolators

$$I_\pi = \bar{d}\gamma_5 u, \quad I_K = \bar{s}\gamma_5 u, \quad (E.1)$$

$$I_N = \epsilon_{abc} u_a [u_b^\top C \gamma_5 d_c], \quad I_\Lambda = \epsilon_{abc} s_a [u_b^\top C \gamma_5 d_c], \quad I_\Sigma = \epsilon_{abc} u_a [u_b^\top C \gamma_5 s_c], \quad (E.2)$$

$$I_\Xi = \epsilon_{abc} s_a [s_b^\top C \gamma_5 u_c],$$

$$I_\Delta = \epsilon_{abc} (2u_a [u_b^\top C \gamma_- d_c] + d_a [u_b^\top C \gamma_- u_c]),$$

$$I_{\Sigma^*} = \epsilon_{abc} (2u_a [u_b^\top C \gamma_- s_c] + s_a [u_b^\top C \gamma_- u_c]),$$

$$I_{\Xi^*} = \epsilon_{abc} (2s_a [s_b^\top C \gamma_- u_c] + u_a [s_b^\top C \gamma_- s_c]), \quad I_\Omega = \epsilon_{abc} s_a [s_b^\top C \gamma_- s_c]. \quad (E.3)$$

The superscript “ \top ” indicates the transpose in Dirac spinor space, $C = \gamma_2 \gamma_0$ is the charge conjugation matrix and $\gamma_- = \frac{1}{2}(\gamma_2 + i\gamma_1)$. The quark fields $u(x)$ and $d(x)$ need to be distinguished when carrying out the Wick contractions for the hadronic two-point functions but they share the same mass. The indices $a, b, c \in \{1, 2, 3\}$ run over fundamental colour. The spinor index of the baryonic interpolators is suppressed. Note that the above naive implementation of I_Λ also has overlap with the Σ^0 baryon. However, since $m_\Lambda < m_\Sigma$ this does not inhibit us from extracting the correct ground state signal. In addition we compute two-point functions, destroying the pseudoscalar mesons with the local axial currents $\bar{q}\gamma_0\gamma_5 u$, where $q \in \{d, s\}$, in order to determine the AWI quark masses.

Within these interpolators we employ either local or smeared quark field operators. For the baryons we only consider smeared-smeared two-point functions while for the mesons we analyse smeared-smeared as well as smeared-local two-point functions, the latter to determine the quark masses. We project all interpolators to zero momentum:

$$I_X(t) := \sum_{\vec{x}} I_X(\vec{x}, t). \quad (E.4)$$

Exploiting spatial translational invariance of two-point functions, in practice we only explicitly carry out the momentum projection at the sink (i.e. we utilize point-to-all propagators), however, some additional measurements are carried out using stochastic timeslice-to-all propagators.

The two-point function for a pseudoscalar meson P is given as

$$C_P(t) = \langle \Omega | I_P(t + t_0) I_P^\dagger(t_0) | \Omega \rangle, \quad (E.5)$$

where the vacuum expectation value on the right hand side is obtained as an ensemble average of the Wick-contracted two-point function and t_0 denotes the source position in Euclidean time. Defining the parity and spin projectors $\Gamma_{\text{unpol}} = \frac{1}{2}(\mathbb{1} + \gamma_0)$ and $\Gamma_{\text{pol}} = \frac{1}{2}\Gamma_{\text{unpol}}(\mathbb{1} + i\gamma_3\gamma_5)$, we compute the two-point functions

$$C_O(t) = \text{Tr} \left(\Gamma_{\text{unpol}} \langle \Omega | I_O(t + t_0) \bar{I}_O(t_0) | \Omega \rangle \right), \quad (\text{E.6})$$

$$C_D(t) = \text{Tr} \left(\Gamma_{\text{pol}} \langle \Omega | I_D(t + t_0) \bar{I}_D(t_0) | \Omega \rangle \right) \quad (\text{E.7})$$

for the octet and decuplet baryons, respectively. The trace is over spinor space, the time separation t is positive and the conjugation has the usual meaning: $\bar{I} = I^\dagger \gamma_0$. The phases are set such that all the two-point functions are positive.

The above interpolators are either local or Wuppertal smeared [197, 198], employing spatially APE smeared gauge links [199] as parallel transporters that are iteratively constructed via

$$U_i^{(n+1)}(\vec{x}) = P_{\text{SU}(3)} \left(U_i^{(n)}(\vec{x}) + \delta \sum_{|j| \neq i} U_j^{(n)}(\vec{x}) U_i^{(n)}(\vec{x} + \hat{j}) U_j^{\dagger(n)}(\vec{x} + \hat{i}) \right), \quad (\text{E.8})$$

where $i \in \{1, 2, 3\}$, $j \in \{\pm 1, \pm 2, \pm 3\}$ and \hat{j} denotes a vector of length a pointing into the direction j , i.e. the sum is over the four spatial “staples” surrounding the link that connects \vec{x} with $\vec{x} + \hat{i}$, $U_i(\vec{x})$. Note that $U_{-i}(\vec{x}) = U_i^\dagger(\vec{x} - \hat{i})$ and $\{U_i^{(0)}(\vec{x})\}$ is the original gauge field. Since the smearing is local in time, the time index is suppressed. $P_{\text{SU}(3)}$ is a gauge covariant projector onto the SU(3) group, defined by maximizing $\text{Re Tr}[A^\dagger P_{\text{SU}(3)}(A)]$. We iterate eq. (E.8) 25 times, using the weight factor $\delta = 0.4$. Using these smeared gauge transporters $\bar{U}_i(\vec{x}) = U_i^{(25)}(\vec{x})$, we Wuppertal smear the quark fields q , successively applying the smearing operator Φ that is defined as

$$(\Phi q)(\vec{x}) = \frac{1}{1 + 6\varepsilon} \left(q(\vec{x}) + \varepsilon \sum_{j=\pm 1}^{\pm 3} \bar{U}_j(\vec{x}) q(\vec{x} + \hat{j}) \right), \quad (\text{E.9})$$

either at the sink to propagators that have been obtained by solving the discretized Wilson–Dirac equation or to point sources $q_{a\alpha}(\vec{x}) = \delta_{\vec{x}\vec{0}} \delta_{aa_0} \delta_{\alpha\alpha_0}$ for $a_0 = 1, 2, 3$, where the smearing only needs to be carried out for one value of the spin index α since Φ commutes with the spin structure. The normalization $(1 + 6\varepsilon)^{-1}$ is arbitrary and is introduced to avoid numerical overflow for high iteration counts.

On a free field configuration, i.e. $\bar{U}_i(\vec{x}) = \mathbb{1}$, the root mean squared (rms) smearing radius for the gauge invariant combination $\|q(\vec{x})\| := \sqrt{q^\dagger(\vec{x})q(\vec{x})}$ for a large iteration count n in an infinite volume reads [200]

$$r = \sqrt{\frac{6\varepsilon}{1 + 6\varepsilon}} a \sqrt{n}, \quad (\text{E.10})$$

where ε should be positive. Here we set $\varepsilon = 0.25$. As can be seen from the above equation, to maintain a constant radius in physical units, the number of iterations n needs to be scaled in proportion to a^{-2} . Moreover, it turns out that an optimal ground state overlap requires r to be increased with decreasing quark mass.

Table 15: Numbers of smearing iterations n_ℓ and n_s for the light and strange quarks, respectively, as well as the corresponding root mean squared smearing radii r_ℓ and r_s . We also include the number of sources N_{src} employed for point-to-all propagators.

trajectory	id	M_π/MeV	M_K/MeV	n_ℓ	n_s	r_ℓ/fm	r_s/fm	N_{src}
$\beta = 3.34, a = 0.098 \text{ fm}$								
$m_s = m_\ell$	A651	556	556	120	120	0.55	0.55	3
	A652	432	432	150	150	0.62	0.62	3
	A650	371	371	160	160	0.64	0.64	3
$\bar{m} = m_{\text{symm}}$	A653	429	429	150	150	0.61	0.61	3
	A654	338	459	185	165	0.68	0.64	3
$\beta = 3.4, a = 0.085 \text{ fm}$								
$m_s = m_\ell$	rqcd019	608	608	150	150	0.54	0.54	3
	rqcd021	340	340	250	250	0.67	0.67	3
	rqcd017	236	236	320	320	0.73	0.73	3
$\bar{m} = m_{\text{symm}}$	U103	420	420	220	220	0.63	0.63	8
	H101	423	423	220	220	0.64	0.64	20
	U102	357	445	250	210	0.66	0.62	36
	H102a	359	444	250	210	0.66	0.62	20
	H102b	354	442	250	210	0.66	0.62	20
	U101	271	464	300	200	0.69	0.60	36
	H105	281	468	300	200	0.73	0.61	20
	N101	281	467	300	200	0.72	0.61	33
	S100	214	476	350	170	0.77	0.57	33
	C101	222	476	350	170	0.77	0.57	20
	D101	222	476	350	170	0.79	0.58	3
	D150	127	482	440	140	0.84	0.52	32
$\tilde{m}_s = \tilde{m}_{s,\text{ph}}$	H107	368	550	250	160	0.67	0.56	3
	H106	273	520	250	160	0.67	0.56	3
	C102	223	504	350	160	0.77	0.56	3
$\beta = 3.46, a = 0.075 \text{ fm}$								
$m_s = m_\ell$	rqcd029	713	713	180	180	0.52	0.52	3
	rqcd030	319	319	355	355	0.68	0.68	3
	X450	265	265	400	400	0.73	0.73	3
$\bar{m} = m_{\text{symm}}$	B450	421	421	270	270	0.61	0.61	16
	S400	354	445	310	260	0.66	0.61	20
	N401	287	464	375	250	0.72	0.60	20
	D450	216	480	480	200	0.78	0.55	32
$\tilde{m}_s = \tilde{m}_{s,\text{ph}}$	B451	422	577	270	200	0.62	0.54	3
	B452	352	548	310	200	0.65	0.54	3
	N450	287	528	375	200	0.70	0.54	3

Continued on next page

Table 15: List of smearing parameters (continued).

trajectory	id	M_π/MeV	M_K/MeV	n_ℓ	n_s	r_ℓ/fm	r_s/fm	N_{src}
	D451	219	507	480	200	0.78	0.54	32
$\beta = 3.55, a = 0.064 \text{ fm}$								
$m_s = m_\ell$	B250	713	713	250	250	0.44	0.44	3
	X250	350	350	445	445	0.65	0.65	3
	X251	268	268	540	540	0.71	0.71	3
$\overline{m} = m_{\text{symm}}$	H200	422	422	390	390	0.61	0.61	3
	N202	414	414	390	390	0.61	0.61	20
	N203	348	445	445	375	0.65	0.61	20
	S201	290	471	540	360	0.71	0.61	3
	N200	286	466	540	360	0.69	0.58	20
	D200	202	484	660	290	0.78	0.55	20
	E250	131	493	795	285	0.82	0.54	32
$\tilde{m}_s = \tilde{m}_{s,\text{ph}}$	N204	353	549	445	285	0.66	0.54	3
	N201	287	527	540	285	0.72	0.54	3
	D201	200	504	660	285	0.77	0.54	3
$\beta = 3.7, a = 0.049 \text{ fm}$								
$m_s = m_\ell$	N303	646	646	440	440	0.51	0.51	3
$\overline{m} = m_{\text{symm}}$	N300	425	425	640	640	0.59	0.59	18
	N302	348	455	750	620	0.64	0.59	20
	J303	259	479	950	525	0.70	0.55	3
	E300	176	496	800	310	0.67	0.44	16
$\tilde{m}_s = \tilde{m}_{s,\text{ph}}$	N305	428	584	640	465	0.60	0.52	3
	N304	353	558	750	465	0.62	0.51	3
	J304	261	527	950	465	0.70	0.52	3
$\beta = 3.85, a = 0.039 \text{ fm}$								
$m_s = m_\ell$	N500	604	604	650	650	0.48	0.48	3
$\overline{m} = m_{\text{symm}}$	J500	413	413	1000	1000	0.57	0.57	3
	J501	336	448	1225	1025	0.61	0.57	3

In table 15 we list our approximate pion and kaon masses as well as the number of smearing iterations n_ℓ and n_s for the light and strange quarks and the resulting rms smearing radii r_ℓ and r_s . These have been calculated numerically on time slices of a few gauge configurations via

$$r^2 = \frac{\left(\prod_{i=1}^3 \sum_{x_i/a=-N_s/2}^{N_s/2-1} \right) \|q(\vec{x})\| \vec{x}^2}{\sum_{\vec{x}} \|q(\vec{x})\|}. \quad (\text{E.11})$$

The results are slightly smaller than eq. (E.10) would suggest due to volume effects and also since the APE smeared gauge transporters are somewhat rougher than unit gauge fields. We

kept the radii approximately constant in physical units across the lattice spacings. The light quark radius r_ℓ depends on M_π^2 while the strange quark radius r_s depends on $2M_K^2 - M_\pi^2$.

E.2 Source positions and extraction of the masses

We distinguish between open boundary conditions (obc) and periodic boundary conditions (pbc) in time. Regarding obc, we expect order g^2a lattice artefacts as well as physical states of scalar quantum numbers (the lightest one having a mass of approximately $2M_\pi$) to propagate from the boundaries into the bulk. These contributions will be exponentially suppressed with the distance from the boundaries. Therefore, at some minimum separation t_{bound} , translational invariance in time is effectively restored for most of the two-point functions. Below we explain how we estimate t_{bound} , how two-point functions with different source and sink positions are combined in the analysis, how the fit ranges are chosen and how the pseudoscalar, AWI quark and baryon masses are extracted.

We employ several temporal source positions t_0 for point sources for each configuration as indicated in the last column of table 15. With pbc one can naively average the two-point functions over the source positions. In this case, for the mesons we can naively average forward and backward ($t \mapsto -t$) propagating two-point functions, while for the baryons, in addition, we have to replace $\gamma_0 \mapsto -\gamma_0$ within the projectors in eqs. (E.6) and (E.7). Also the backward propagating two-point functions for pseudoscalar mesons that are destroyed by local axial currents (which are used to compute the AWI quark masses, see eq. (2.2)) acquire a minus sign. We label the time slices as

$$t' = 0, a, \dots, T - a, \quad \text{where} \quad T = N_t a. \quad (\text{E.12})$$

With pbc the temporal dimension of the lattice is T , while with obc it is $T - a$. In the latter case, the two-point function starting at t_0 , propagating in the forward direction, can be averaged with that starting at $T - a - t_0$, propagating in the backward direction, as above. Other than this, we keep the source positions separate throughout the analysis, enabling us to detect any violation of translational invariance. Moreover, the source and sink positions $t' = t_0$ and $t' = t_0 + t$ (with t positive or negative), respectively, should be restricted to $t_{\text{bound}} \leq t' \leq T - a - t_{\text{bound}}$ with t_{bound} yet to be determined (see below). This means that for large values of $|t|$ a smaller number of sources contributes than indicated in table 15.

In the case of pbc, the spatial and temporal source positions are selected randomly for each configuration, while for obc we employ fixed temporal (but random spatial) positions, where for each source at $t' = t_0$, we also place a source at $t' = T - a - t_0$.

Regarding the pseudoscalar (and pseudoscalar-axial) two-point functions, additional measurements have been carried out employing the “one-end-trick” [201, 202], using spin-explicit [203, 204] stochastic complex \mathbb{Z}_2 -sources. These techniques were first combined in ref. [205]. It turns out to be advantageous in terms of the signal over noise ratio not to seed the stochastic source on the whole time slice t_0 but just on a subset [201]. We carry out this “thinning” in a random pattern (to exclude overlap with non-zero momentum contributions), with the occupation ratio 0.02. Each source consists of one random vector for each of the four spin components with support on the thinned set of points. In the case of obc, the

Table 16. Ranges for the separation t_{bound} from the boundaries of obc ensembles.

β	3.4	3.46	3.55	3.7	3.85
t_{bound}/a	24–29	31–32	31–40	31–43	45–55
$t_{\text{bound}}/\text{fm}$	2–2.5	2.3–2.4	2–2.5	1.5–2.1	1.7–2.1

temporal positions of the one-end sources usually are $t_0 = a$ and $t_0 = T - 2a$, one time slice away from the boundary, at the positions of the first non-trivial spatial links. In some cases the distance was chosen somewhat larger. We employ two stochastic estimates for each of the two time slices. For pbc on each configuration we use four different randomly selected time slices. The sources and sinks of the one-end two-point functions used in this analysis are local, without quark smearing applied. We separately analyse the mesonic two-point functions from the conventional point sources and from the one-end sources and find consistent results. Whenever this leads to an error reduction, we carry out a combined fit to the data obtained using the two methods.

When determining the boundary region on obc ensembles, we observe by varying the source position, t_0 , that the pion two-point function is more sensitive with respect to the proximity of the source or the sink to the boundaries than any other two-point function. Moreover, if the pion source is placed in the centre of the lattice, ground state dominance is achieved at smaller source-sink separations t than for the one-end sources near the boundaries. Therefore, we define t_{bound} as the minimum separation of the sink from the boundary for the local-local pion two-point function with the source placed at $t_0 = a$, that is needed for the boundary/excited state contributions to become smaller than one quarter of the statistical error. In this determination we follow the strategy that we also employ for the ground state mass extractions that is described below. All the point source positions that we use are outside of the respective boundary regions, defined in terms of t_{bound} . An overview of the resulting ranges is provided in table 16. Note that none of the $\beta = 3.34$ ensembles have obc, while at $\beta = 3.46$ only two ensembles with obc exist, where one-end source measurements were taken (S400 and N401).

Our mass determinations follow a two step procedure: first we determine a time range of ground state dominance and then we carry out one-state fits for the hadron and AWI quark masses. We carry out both uncorrelated and correlated fits. The latter fits are utilized to monitor the fit quality in terms of the χ^2/N_{DF} -values. However, in many cases the statistics is insufficient for a reliable determination of the large covariance matrices between the values of the two-point functions at different times. Therefore, the final results are obtained from uncorrelated fits and the errors computed via the bootstrap procedure, also taking autocorrelations into account, see appendix F. We remark that the mean values for correlated and uncorrelated fits are in good agreement in almost all of the cases.

Starting from the mesonic two-point functions with pbc, we carry out fits according to

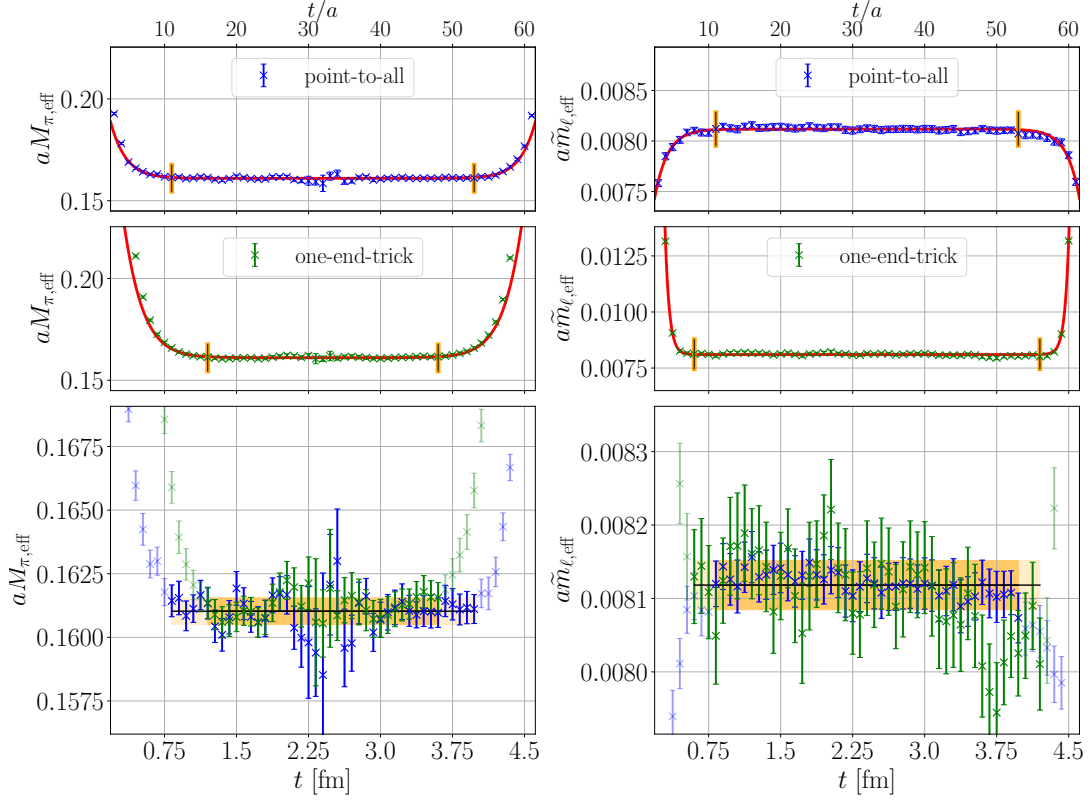


Figure 30. Left: the effective mass $aM_{\pi,\text{eff}}$ of the pion for ensemble B450 (pbc, $a \approx 0.075$ fm, $M_\pi \approx 420$ MeV, see table 2). The upper plot shows the “point-to-all” smeared-smeared data and the middle plot the “one-end-trick” local-local data. The two-point functions have been averaged over sixteen and four source positions, respectively. The red line corresponds to the fit result of the two-state ansatz given in eq. (E.13). The vertical orange bars indicate the resulting fit ranges for one-state fits (setting $B_P = 0$), see the main text for details. In the last row the effective masses for both data sets are shown, together with the final (one-state) fit result, where the solid black line with orange error band indicates the result. The data that are not included in the fit are shown as light symbols. Right: the corresponding figures for the AWI quark mass, using the parametrization eq. (E.14) and setting $B_m = 0$ for the ground state fit. In this case the point-to-all two-point functions are smeared-local and the one-end ones local-local.

the ansatz

$$C_P(t) = A_P \cosh [M_P(t - T/2)] + B_P \cosh [M'_P(t - T/2)] \quad (\text{E.13})$$

with the fit parameters A_P , B_P , M_P and M'_P , increasing the minimum t -value until we find an acceptable representation of the data (by means of the correlated χ^2/N_{DF} -value). In the spirit of ref. [206], we determine the minimum value t_{\min} as the value from which onwards the (effective) contribution of the excited state term (proportional to B_P) to the two-point function $C_P(t)$ becomes smaller than one quarter of the statistical error of the data. Note that whenever more than one two-state fit was found to adequately represent the data, the largest resulting value for t_{\min} is chosen. To obtain the ground state mass, we subsequently fit $C_P(t)$ within the range $t_{\min} \leq t \leq t_{\max} = T - t_{\min}$ to the ground state only, i.e. we set

$B_P = 0$ within eq. (E.13). The analogous procedure is implemented for the ratio eq. (2.2) of smeared pseudoscalar-local axial over smeared pseudoscalar-local pseudoscalar two-point functions to obtain AWI quark masses,

$$\tilde{m}_{\text{eff}}(t) = \tilde{m} + B_m \cosh [m'(t - T/2)], \quad (\text{E.14})$$

where the second term is a lattice artefact ($B_m = \mathcal{O}(a^2)$) and $m' \approx M'_P - M_P$. Once the region of ground state dominance has been determined, $\tilde{m}(t)$ is averaged over this region.

The above procedure is illustrated for the pbc ensemble B450 in figure 30, where we show data both for point sources (smeared-smeared for the pion, smeared-local for the AWI quark mass) and for stochastic one-end sources (local-local in both cases, hence the larger values of t_{min} for the pion). In the left of the figure, the effective mass

$$M_{P,\text{eff}} = \frac{1}{2a} \left| \text{arccosh} \left(\frac{C_P(t-a)}{C_P(T/2)} \right) - \text{arccosh} \left(\frac{C_P(t+a)}{C_P(T/2)} \right) \right| \quad (\text{E.15})$$

is compared to $|(d/dt) \text{arccosh}[C_P(t)/C_P(T/2)]|$. Both expressions will approach M_P in the limit $T \gg t \gg 0$.

Regarding obc, the above expression is replaced by

$$C_P(t) = A_P [\exp(-M_P t) - \exp(-M_P(2T' - t))] + B_P \exp(-M'_P t) \quad (\text{E.16})$$

with an additional fit parameter $T' \approx T$. The forward and backward propagating two-point functions are symmetrized as explained above so that $t > 0$. The ground state mass is then extracted via a fit to

$$C_P(t) = A_P \exp(-M_P t), \quad (\text{E.17})$$

for the fit range $t_{\text{min}} \leq t \leq t_{\text{max}}$. The start time t_{min} is determined in the same way as described above as the time where the excited state contribution, proportional to B_P , becomes smaller than one quarter of the statistical error of $C_P(t)$. The upper limit of the fit range, $t_{\text{max}} < T - a - t_{\text{bound}}$, corresponds to the time at which $A_P e^{M_P(t-2T')}$ becomes larger than one quarter of the statistical error. Since the resulting values of t_{min} and t_{max} will depend on the statistical error of the two-point function, one danger of this procedure is that for each individual source position a value for t_{min} may be suggested that is smaller than if the correlators for all the different sources were averaged. For pbc we average the two-point functions over all the source positions in any case. The same is carried out for obc data with one-end sources since these are always placed at the same distance from the boundaries. Regarding obc two-point functions with point sources, we first reconfirm that translational invariance is effectively restored within the region $t_{\text{bound}} \leq t + t_0 \leq T - a - t_{\text{bound}}$ for the different source positions t_0 , before we average two-point functions obtained for nearby values of t_0 into up to four groups. We then determine the fit range for each of this smaller number of groups. We implement the same procedure for the baryonic two-point functions.

In the left of figure 31, the determination of the fit ranges is shown for the pion mass on ensemble D200. The one-state fit to determine the ground state mass (shown in the bottom left of the figure) is carried out simultaneously for the different source positions, using the

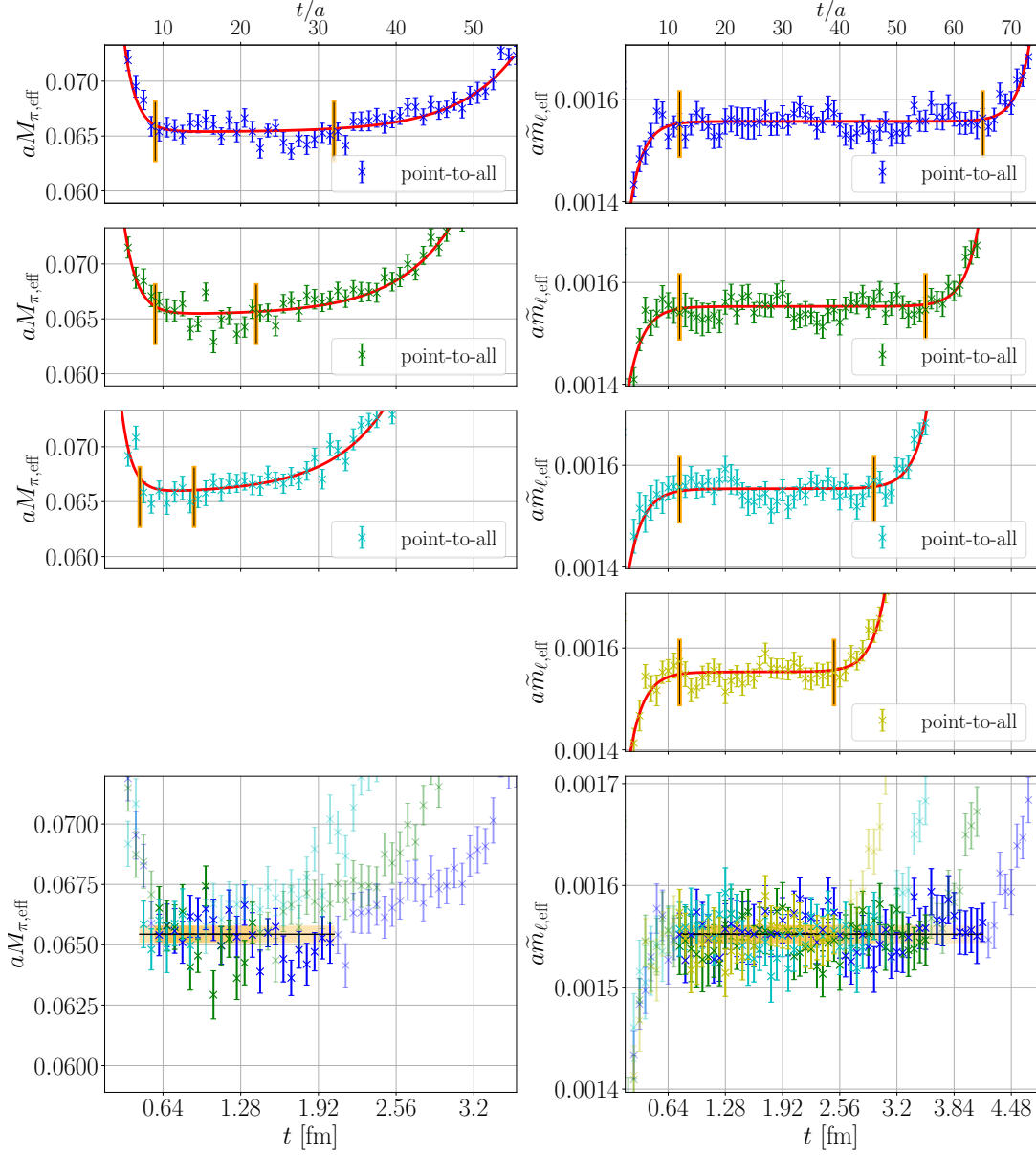


Figure 31. Left: the effective mass of the pion for ensemble D200 (obc, $a \approx 0.064$ fm, $M_\pi \approx 200$ MeV, see table 2). Data from eighteen point source positions are shown, which are pairwise forward/backward averaged between t_0 and $T - a - t_0$. Within each panel, in addition we average data from three nearby source positions. The red lines, orange bars, black line and orange error band in the four panels have the same meaning as in figure 30, however, the fit form defined in eq. (E.16) is used for the two-state fit and eq. (E.17) for the one-state fit. Right: the same for the light AWI quark mass, where two additional source positions (shown in the fourth row) are within the range that we average over. The fit range is determined using eq. (E.19).

respective fit ranges. The effective mass

$$M_{P,\text{eff}}(t) = \frac{1}{a} \ln \left(\frac{C_P(t - a/2)}{C(t + a/2)} \right) \quad (\text{E.18})$$

is compared to the derivative of the parametrization $-(d/dt) \ln C_P(t)$. Both expressions will approach M_P at large values of t .

Turning to the AWI quark mass with obc, we encounter, in addition to the usual lattice artefacts, also contributions from the boundary. This motivates the ansatz

$$\tilde{m}_{\text{eff}}(t) = \tilde{m} + B_m \exp(-m't) + D_m \exp(m''t) \quad (\text{E.19})$$

with the fit parameters \tilde{m} , B_m , D_m , $m' \approx M'_P - M_P$ and $m'' \approx 2M_\pi$, where \tilde{m} is the AWI quark mass of interest, the second term describes the usual lattice spacing effects or, if one-end sources are used, also boundary effects and the last term encapsulates the boundary effects at large times. Using this ansatz, we determine t_{\min} and t_{\max} in the same way as above and carry out the fit to a constant for the resulting range. This is shown for the example of point sources for ensemble D200 in the right of figure 31. As with pbc, smeared-local and local-local two-point functions are used to obtain the AWI quark masses with point sources and with one-end sources (not shown), respectively.

As was already noticed and explained in appendix B of ref. [207] (see also ref. [208]), the relative error of two-point functions other than for the pseudoscalar mesons increases exponentially with t . In view of this, we use the ansatz

$$C_B(t) = A_B \exp(-m_B t) + B_B \exp(-m'_B t) \quad (\text{E.20})$$

for the baryons, both for obc and pbc, to determine the value of t_{\min} for the subsequent one-state fit, where $t_{\text{bound}} \leq t_{\min}$ and $t_{\max} \leq T - a - t_{\text{bound}}$. In addition, we restrict t_{\max} to values where the noise over signal ratio of the two-point function satisfies the condition $\Delta C_B(t)/C_B(t) < 0.25$. In figure 32, we show the effective masses for the nucleon on ensemble B450 as well as for the nucleon, the Ξ and the Ω baryons on ensemble D200. Also shown are the two-state fits, used to determine t_{\min} , and the results of the subsequent ground state fits. The data shown are averaged over the different source positions. For the baryon spectroscopy only smeared-smeared two-point functions with point sources are employed.

Note that t_{\min} is determined on binned data, where a suitable bin size is chosen in order to account for autocorrelations. The data shown in figures 30–32 are binned accordingly. The final statistical errors of the masses and derived quantities are computed from bootstrap distributions, as detailed in appendix F.1. The widths of these distributions are rescaled, taking autocorrelations into account by means of a binning analysis, see appendices F.2 and F.3. Note that the mean values are always extracted from unbinned data, while the error bands shown for the masses resulting from the one-state fits correspond to the infinite bin size. In addition, for each ensemble a normalized covariance matrix between all the meson, baryon and AWI quark masses is computed as explained in appendix F.3, which also incorporates the autocorrelation effects. For $m_s = m_\ell$ the dimension of this matrix is four (meson mass, quark mass, octet baryon mass and decuplet baryon mass), while for $m_s \neq m_\ell$ it is twelve (two meson and two quark masses each, as well as four octet and four decuplet baryon masses). For fits of the baryon masses as functions of the meson masses we take correlations between the two mesons, the four octet baryons and the four decuplet baryons into account as well as between the baryons and the mesons, see appendix F.4.

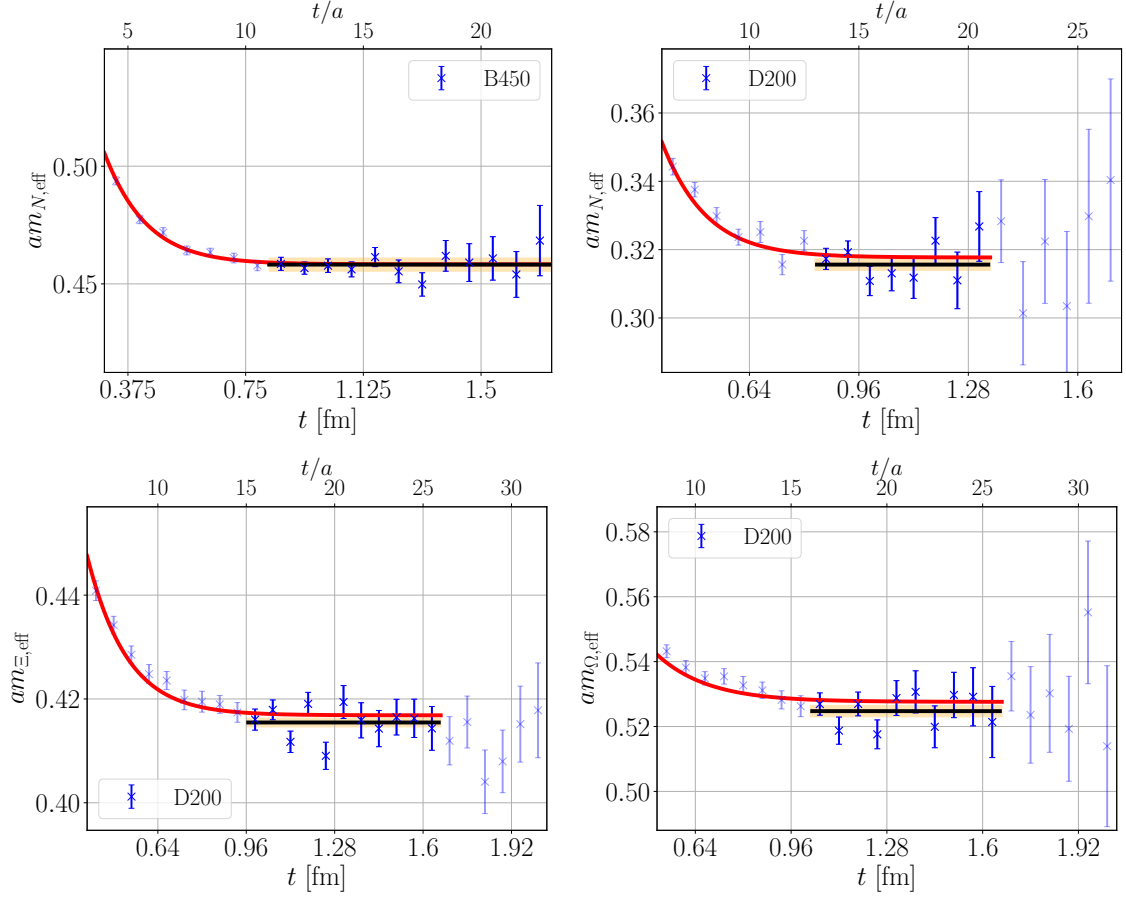


Figure 32. Effective masses for the nucleon for ensembles B450 (pbc, $a \approx 0.075$ fm, $M_\pi \approx 420$ MeV) and D200 (obc, $a \approx 0.064$ fm, $M_\pi \approx 200$ MeV) are shown (top left and top right panel, respectively) as well as for the Ξ and the Ω baryon for D200 (lower left and lower right panel, respectively). For B450 the two-point function has been averaged over sixteen sources. For D200 twenty sources have been used within the range $37a \leq t_0 \leq 90a$, where for the average over the two-point functions also the sink positions $t_0 + t$ are restricted to the same range. The red lines and the orange bands have the same meaning as in figure 30, however, the fit form defined in eq. (E.20) is used for the two-state fit and B_B is set to zero within this equation for the one-state fit.

We have kept the smearing radii almost constant across the different lattice spacings, however, the fit ranges will also depend on the quark masses and, in particular, on the statistics. In addition, at least for the AWI masses, t_{\min} will decrease with the lattice spacing. This complicates a systematic comparison of fit ranges across the different ensembles. In figure 33 we show the t_{\min} values for the nucleon and the cascade baryon for ensembles where we have particularly good statistics. These are sorted in the order of a decreasing lattice spacing. Within each lattice spacing group (distinguishable by the first numerical digit of the ensemble id, see table 2), the squared pion mass $M_\pi^2 \propto 3m_\ell$ decreases from left to right for the nucleon, while the squared η_8 mass $M_{\eta_8}^2 \propto 2m_s + m_\ell$, which is more relevant for the Ξ baryon, increases. Regarding the cascade, we omit ensembles with $m_s = m_\ell$, since

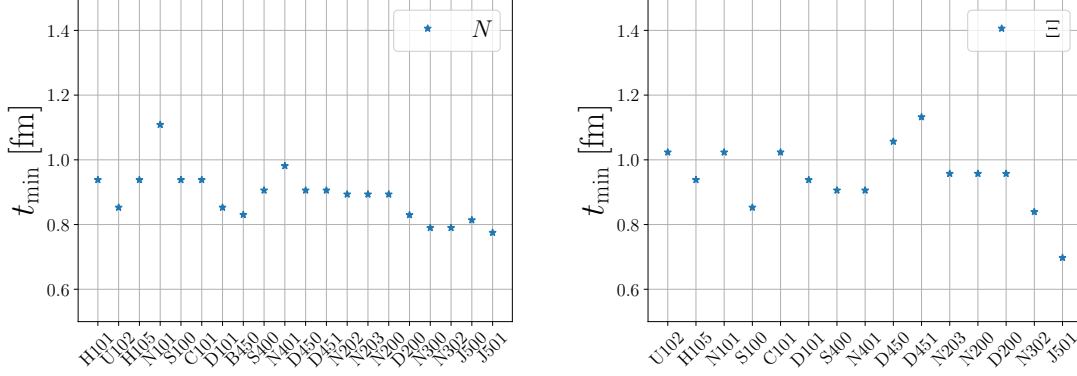


Figure 33. Starting times t_{\min} of the one-state fits for the nucleon N (left) and the Ξ baryon (right) for the subset of ensembles with high statistics.

in this case the two-point functions for the two baryons are the same. With our smearing and statistics, t_{\min} typically varies between 0.8 fm and 1 fm for the nucleon and on average it is somewhat larger for the Ξ baryon.

E.3 Tables of the masses and t_0/a^2

In table 17 we list for the $m_s = m_\ell$ ensembles the pseudoscalar meson mass $M_P = M_\pi = M_K$, the AWI quark mass $\tilde{m}_q = \tilde{m}_\ell = \tilde{m}_s$, the octet baryon mass $m_O = m_N = m_\Lambda = m_\Sigma = m_\Xi$ and the decuplet baryon mass $m_D = m_\Delta = m_{\Sigma^*} = m_{\Xi^*} = m_\Omega$ as well as the scale parameter t_0 , all in lattice units. In table 18 the pseudoscalar meson masses M_π and M_K , the AWI quark masses \tilde{m}_ℓ and \tilde{m}_s as well as the scale parameter t_0 are displayed for the ensembles not listed in table 17 (i.e. for $m_s \neq m_\ell$). In table 19 the octet baryon masses m_N , m_Λ , m_Σ and m_Ξ are shown for the ensembles not already listed in table 17. In table 20 the decuplet baryon masses m_Δ , m_{Σ^*} , m_{Ξ^*} and m_Ω are collected for the ensembles with $m_s \neq m_\ell$. We regard two of the Δ and two of the Σ^* entries as unreliable since the respective mass values are larger than those of non-interacting pairs of a nucleon or a Λ and a pion in a P -wave for these volumes. The corresponding entries are displayed in *Italics*. A much larger number of decuplet baryon entries will become unstable at the given quark masses in an infinite volume. We indicate these cases, where one would expect large volume effects, in *underlined Italics*.

Table 17: The pseudoscalar mass aM_P , the AWI quark mass $a\tilde{m}_q$, the octet baryon mass am_O and the decuplet baryon mass am_D as well as the scale parameter t_0/a^2 in lattice units for the ensembles with equal light and strange quark masses $m_s = m_\ell$. The decuplet baryon will become unstable in the infinite volume for the two entries indicated in *underlined Italics*.

trajectory	id	aM_P	$a\tilde{m}_q$	am_O	am_D	t_0/a^2
$\beta = 3.34, a = 0.098 \text{ fm}$						
$m_s = m_\ell$	A651	0.27507(87)	0.017314(93)	0.6715(44)	0.8033(63)	1.9200(47)
	A652	0.2140(10)	0.010782(97)	0.5842(41)	0.689(13)	2.1697(56)
	A650	0.1835(13)	0.00803(10)	0.5469(54)	0.663(13)	2.2878(72)

Continued on next page

Table 17: List of masses for $m_s = m_\ell$ (continued).

trajectory	id	aM_P	$a\tilde{m}_q$	am_O	am_D	t_0/a^2
$\bar{m} = m_{\text{symm}}$	A653	0.21245(93)	0.010663(88)	0.5855(37)	0.7168(73)	2.1729(50)
$\beta = 3.4, a = 0.085 \text{ fm}$						
$m_s = m_\ell$	rqcd019	0.26281(66)	0.018095(73)	0.6268(23)	0.7353(54)	2.4795(81)
	rqcd021	0.14702(88)	0.005983(59)	0.4508(47)	0.566(12)	3.032(15)
	rqcd017	0.1022(15)	0.002793(89)	0.388(13)	<u>0.514(20)</u>	3.251(13)
$\bar{m} = m_{\text{symm}}$	U103	0.18158(60)	0.008936(42)	0.5193(30)	0.638(10)	2.8815(57)
	H101	0.18286(57)	0.009197(39)	0.5074(18)	0.6178(71)	2.8545(81)
$\beta = 3.46, a = 0.075 \text{ fm}$						
$m_s = m_\ell$	rqcd029	0.27253(52)	0.021714(49)	0.6169(22)	0.7162(42)	2.976(11)
	rqcd030	0.12221(68)	0.004750(40)	0.3957(90)	0.466(22)	3.914(15)
	X450	0.10144(62)	0.003300(28)	0.3764(61)	<u>0.4902(68)</u>	3.9935(92)
$\bar{m} = m_{\text{symm}}$	B450	0.16103(49)	0.008118(33)	0.4582(24)	0.5619(47)	3.663(11)
$\beta = 3.55, a = 0.064 \text{ fm}$						
$m_s = m_\ell$	B250	0.23052(70)	0.018769(37)	0.5237(29)	0.6104(35)	4.312(18)
	X250	0.11321(39)	0.004899(21)	0.3597(51)	0.435(28)	5.283(28)
	X251	0.08684(40)	0.002877(23)	0.3185(85)	0.382(42)	5.483(26)
$\bar{m} = m_{\text{symm}}$	H200	0.13653(53)	0.006865(23)	0.3968(30)	0.4792(67)	5.150(16)
	N202	0.13389(35)	0.006856(15)	0.3799(18)	0.4637(61)	5.165(14)
$\beta = 3.7, a = 0.049 \text{ fm}$						
$m_s = m_\ell$	N303	0.16153(30)	0.012570(12)	0.3742(21)	0.4391(40)	7.743(23)
$\bar{m} = m_{\text{symm}}$	N300	0.10647(38)	0.0055137(68)	0.3035(13)	0.3711(54)	8.576(21)
$\beta = 3.85, a = 0.039 \text{ fm}$						
$m_s = m_\ell$	N500	0.11862(67)	0.0084940(80)	0.2878(22)	0.3333(55)	12.912(72)
$\bar{m} = m_{\text{symm}}$	J500	0.08119(34)	0.0042100(37)	0.2313(26)	0.2834(35)	14.013(34)

Table 18: The pion mass aM_π , the kaon mass aM_K , the light AWI quark mass $a\tilde{m}_\ell$, the strange AWI quark mass $a\tilde{m}_s$ and the scale parameter t_0/a^2 in lattice units for the ensembles with $m_s \neq m_\ell$. Results for the other ensembles are shown in table 17.

trajectory	id	aM_π	aM_K	$a\tilde{m}_\ell$	$a\tilde{m}_s$	t_0/a^2
$\beta = 3.34, a = 0.098 \text{ fm}$						
$\bar{m} = m_{\text{symm}}$	A654	0.1673(11)	0.22719(91)	0.006501(83)	0.018108(90)	2.1950(77)
$\beta = 3.4, a = 0.085 \text{ fm}$						
$\bar{m} = m_{\text{symm}}$	U102	0.15498(84)	0.19251(61)	0.006380(59)	0.013791(58)	2.8932(63)
	H102a	0.15321(98)	0.19091(78)	0.006436(67)	0.013789(61)	2.8840(89)
	H102b	0.15499(92)	0.19194(77)	0.006554(60)	0.013866(54)	2.8792(90)
	U101	0.1184(24)	0.2005(13)	0.00362(11)	0.018393(95)	2.934(11)
	H105	0.1215(13)	0.20234(64)	0.003976(68)	0.018714(58)	2.8917(65)
	N101	0.12133(58)	0.20156(30)	0.003972(33)	0.018685(23)	2.8948(39)
	S100	0.0929(31)	0.20551(57)	0.00229(11)	0.02117(10)	2.9212(91)
	C101	0.09589(63)	0.20561(33)	0.002427(27)	0.021210(33)	2.9176(38)
	D101	0.0958(11)	0.20572(45)	0.002500(35)	0.021280(33)	2.910(10)
	D150	0.05500(79)	0.20834(17)	0.000799(20)	0.023643(24)	2.9476(30)

Continued on next page

Table 18: List of pseudoscalar and AWI quark masses (continued).

trajectory	id	aM_π	aM_K	$a\tilde{m}_\ell$	$a\tilde{m}_s$	t_0/a^2
$\tilde{m}_s = \tilde{m}_{s,\text{ph}}$	H107	0.15921(73)	0.23746(53)	0.006656(47)	0.023976(52)	2.7193(76)
	H106	0.1182(20)	0.22472(67)	0.003799(62)	0.024031(68)	2.8227(68)
	C102	0.09647(77)	0.21783(36)	0.002468(39)	0.023958(37)	2.8682(47)
$\beta = 3.46, a = 0.075 \text{ fm}$						
$\bar{m} = m_{\text{symm}}$	S400	0.13554(42)	0.17035(38)	0.005679(28)	0.012605(28)	3.6919(74)
	N401	0.10987(56)	0.17759(37)	0.003795(28)	0.016460(35)	3.6844(52)
	D450	0.08256(41)	0.18354(12)	0.002077(18)	0.019429(19)	3.7076(75)
$\tilde{m}_s = \tilde{m}_{s,\text{ph}}$	B451	0.16141(57)	0.22047(32)	0.007893(32)	0.022061(32)	3.4265(72)
	B452	0.13492(47)	0.20973(34)	0.005525(30)	0.022001(26)	3.5286(66)
	N450	0.10967(31)	0.20176(18)	0.003659(18)	0.022044(19)	3.5920(42)
	D451	0.08371(31)	0.19385(15)	0.002120(16)	0.021843(19)	3.6684(36)
$\beta = 3.55, a = 0.064 \text{ fm}$						
$\bar{m} = m_{\text{symm}}$	N203	0.11249(30)	0.14399(24)	0.004739(16)	0.011051(13)	5.1465(63)
	S201	0.09453(47)	0.15228(37)	0.003135(19)	0.014142(17)	5.1638(91)
	N200	0.09244(29)	0.15061(24)	0.003156(12)	0.014146(12)	5.1600(71)
	D200	0.06544(33)	0.15652(15)	0.0015521(84)	0.0172194(86)	5.1793(39)
	E250	0.04228(23)	0.159370(61)	0.0006446(73)	0.0188850(74)	5.2027(41)
$\tilde{m}_s = \tilde{m}_{s,\text{ph}}$	N204	0.11427(33)	0.17734(29)	0.004792(13)	0.018906(12)	4.9473(79)
	N201	0.09276(31)	0.17040(22)	0.003149(14)	0.018853(14)	5.0427(75)
	D201	0.06476(42)	0.16302(18)	0.001551(15)	0.018872(15)	5.1378(66)
$\beta = 3.7, a = 0.049 \text{ fm}$						
$\bar{m} = m_{\text{symm}}$	N302	0.08716(41)	0.11373(36)	0.0037228(78)	0.0090864(78)	8.539(19)
	J303	0.06488(19)	0.11975(16)	0.0020511(61)	0.0123411(47)	8.615(14)
	E300	0.04403(20)	0.12397(15)	0.0009277(55)	0.0145418(80)	8.6241(74)
$\tilde{m}_s = \tilde{m}_{s,\text{ph}}$	N305	0.10719(35)	0.14598(34)	0.0054860(88)	0.0152409(83)	8.181(19)
	N304	0.08855(33)	0.13961(31)	0.0037156(93)	0.0152961(80)	8.322(20)
	J304	0.06545(18)	0.13181(14)	0.0020500(61)	0.0152663(44)	8.497(12)
$\beta = 3.85, a = 0.039 \text{ fm}$						
$\bar{m} = m_{\text{symm}}$	J501	0.06599(26)	0.08799(23)	0.0027380(36)	0.0071717(31)	13.928(39)

Table 19: The octet baryon masses am_O , $O \in \{N, \Lambda, \Sigma, \Xi\}$, in lattice units for the ensembles with $m_s \neq m_\ell$. Results for the other ensembles are shown in table 17.

trajectory	id	am_N	am_Λ	am_Σ	am_Ξ
$\beta = 3.34, a = 0.098 \text{ fm}$					
$\bar{m} = m_{\text{symm}}$	A654	0.5423(65)	0.5711(48)	0.5850(40)	0.6070(30)

Continued on next page

Table 19: List of octet baryon masses (continued).

trajectory	id	am_N	am_Λ	am_Σ	am_Ξ
$\beta = 3.4, a = 0.085 \text{ fm}$					
$\overline{m} = m_{\text{symm}}$	U102	0.4899(43)	0.5059(49)	0.5150(41)	0.5287(31)
	H102a	0.4797(28)	0.4986(26)	0.5079(26)	0.5235(23)
	H102b	0.4747(39)	0.4948(34)	0.5046(32)	0.5201(27)
	U101	0.456(11)	0.4888(80)	0.5108(64)	0.5432(53)
	H105	0.4397(66)	0.4845(33)	0.5096(22)	0.5392(17)
	N101	0.4412(38)	0.4873(18)	0.5050(18)	0.5376(11)
	S100	0.4219(91)	0.4731(60)	0.5019(33)	0.5465(21)
	C101	0.4237(35)	0.4788(17)	0.5026(19)	0.5433(11)
	D101	0.427(10)	0.4775(66)	0.5053(59)	0.5416(42)
	D150	0.4033(88)	0.4594(40)	0.4997(25)	0.5482(14)
$\tilde{m}_s = \tilde{m}_{s,\text{ph}}$	H107	0.4997(45)	0.5408(36)	0.5632(35)	0.5941(28)
	H106	0.4594(54)	0.5053(44)	0.5325(37)	0.5687(33)
	C102	0.4341(48)	0.4927(58)	0.5179(48)	0.5588(33)
$\beta = 3.46, a = 0.075 \text{ fm}$					
$\overline{m} = m_{\text{symm}}$	S400	0.4261(22)	0.4441(17)	0.4530(17)	0.4665(14)
	N401	0.3965(38)	0.4309(26)	0.4492(25)	0.4758(17)
	D450	0.3653(50)	0.4252(21)	0.4479(24)	0.4865(13)
$\tilde{m}_s = \tilde{m}_{s,\text{ph}}$	B451	0.4721(42)	0.5043(31)	0.5203(26)	0.5452(22)
	B452	0.4403(52)	0.4764(39)	0.4975(29)	0.5290(20)
	N450	0.3985(68)	0.4471(43)	0.4678(48)	0.5105(29)
	D451	0.3694(49)	0.4335(27)	0.4566(28)	0.4986(16)
$\beta = 3.55, a = 0.064 \text{ fm}$					
$\overline{m} = m_{\text{symm}}$	N203	0.3624(18)	0.3782(15)	0.3863(15)	0.3980(13)
	S201	0.3549(69)	0.3799(56)	0.3942(49)	0.4151(31)
	N200	0.3423(22)	0.3727(14)	0.3863(13)	0.4084(10)
	D200	0.3156(17)	0.3605(13)	0.3816(14)	0.41547(84)
	E250	0.3020(48)	0.3497(33)	0.3764(30)	0.4188(14)
$\tilde{m}_s = \tilde{m}_{s,\text{ph}}$	N204	0.3721(24)	0.4056(19)	0.4201(21)	0.4469(16)
	N201	0.3415(32)	0.3870(22)	0.4029(27)	0.4352(21)
	D201	0.3200(50)	0.3709(36)	0.3875(48)	0.4243(22)
$\beta = 3.7, a = 0.049 \text{ fm}$					
$\overline{m} = m_{\text{symm}}$	N302	0.2862(19)	0.2992(16)	0.3065(16)	0.3161(14)
	J303	0.2583(16)	0.2862(11)	0.3012(12)	0.32079(82)
	E300	0.2384(40)	0.2784(23)	0.2972(25)	0.3258(14)
$\tilde{m}_s = \tilde{m}_{s,\text{ph}}$	N305	0.3092(18)	0.3325(16)	0.3414(17)	0.3595(14)
	N304	0.2892(36)	0.3175(26)	0.3299(27)	0.3509(21)
	J304	0.2674(22)	0.2996(17)	0.3169(17)	0.3395(13)

Continued on next page

Table 19: List of octet baryon masses (continued).

trajectory	id	am_N	am_Λ	am_Σ	am_Ξ
$\beta = 3.85, a = 0.039 \text{ fm}$					
$\bar{m} = m_{\text{symm}}$	J501	0.2165(17)	0.2304(15)	0.2351(17)	0.2442(14)

Table 20: The decuplet baryon masses am_D , $D \in \{\Delta, \Sigma^*, \Xi^*, \Omega\}$, in lattice units for the ensembles with $m_s \neq m_\ell$. Results for the other ensembles are shown in table 17. Masses for decuplet baryons that can strongly decay into pairs of octet baryons and pions in the finite volume are unreliable and displayed in *Italics*. Additional entries for baryons that will become unstable in the infinite volume are indicated in underlined Italics.

trajectory	id	am_Δ	am_{Σ^*}	am_{Ξ^*}	am_Ω
$\beta = 3.34, a = 0.098 \text{ fm}$					
$\bar{m} = m_{\text{symm}}$	A654	0.6954(74)	0.7115(59)	0.7289(69)	0.7459(67)
$\beta = 3.4, a = 0.085 \text{ fm}$					
$\bar{m} = m_{\text{symm}}$	U102	0.6131(79)	0.6276(63)	0.6417(53)	0.6563(56)
	H102a	0.588(11)	0.6092(52)	0.6258(40)	0.6417(32)
	H102b	0.5866(69)	0.6046(52)	0.6220(41)	0.6388(34)
	U101	0.586(13)	0.600(21)	0.633(11)	0.6734(82)
	H105	<u>0.576(13)</u>	0.6033(89)	0.6360(79)	0.6689(69)
	N101	<u>0.577(14)</u>	0.6028(80)	0.6359(46)	0.6681(31)
	S100	<u>0.567(11)</u>	<u>0.597(11)</u>	<u>0.6429(69)</u>	0.6838(40)
	C101	<u>0.556(17)</u>	<u>0.6020(66)</u>	0.6394(43)	0.6817(27)
	D101	<u>0.5833(91)</u>	<u>0.587(19)</u>	0.634(12)	0.676(14)
	D150	<u>0.477(22)</u>	<u>0.578(13)</u>	<u>0.6402(51)</u>	0.6892(38)
$\tilde{m}_s = \tilde{m}_{s,\text{ph}}$	H107	0.637(10)	0.6712(54)	0.7055(41)	0.7378(40)
	H106	<u>0.581(21)</u>	0.613(12)	0.6662(68)	0.7066(53)
	C102	<u>0.5846(44)</u>	<u>0.606(10)</u>	<u>0.6579(65)</u>	0.7078(47)
$\beta = 3.46, a = 0.075 \text{ fm}$					
$\bar{m} = m_{\text{symm}}$	S400	0.5473(56)	0.5539(69)	0.5635(51)	0.5759(40)
	N401	<u>0.5141(84)</u>	<u>0.5428(53)</u>	0.5728(43)	0.5979(32)
	D450	<u>0.488(10)</u>	<u>0.5362(60)</u>	<u>0.5730(48)</u>	0.6111(44)
$\tilde{m}_s = \tilde{m}_{s,\text{ph}}$	B451	0.584(12)	0.6142(51)	0.6414(38)	0.6683(30)
	B452	0.556(20)	0.5879(91)	0.6196(75)	0.6476(59)
	N450	0.508(12)	<u>0.5600(94)</u>	0.6059(61)	0.6417(41)
	D451	<u>0.5096(96)</u>	<u>0.5429(85)</u>	<u>0.5866(50)</u>	0.6285(33)

Continued on next page

Table 20: List of decuplet baryon masses (continued).

trajectory	id	am_Δ	am_{Σ^*}	am_{Ξ^*}	am_Ω
$\beta = 3.55, a = 0.064 \text{ fm}$					
$\bar{m} = m_{\text{symm}}$	N203	0.4467(89)	0.4620(67)	0.4743(60)	0.4871(45)
	S201	0.467(14)	0.467(14)	0.477(12)	0.5035(74)
	N200	0.426(13)	0.4575(69)	0.4845(39)	0.5083(24)
	D200	<u>0.4228(47)</u>	<u>0.4581(41)</u>	<u>0.4898(27)</u>	0.5247(18)
	E250	<u>0.374(19)</u>	<u>0.4503(83)</u>	<u>0.4906(49)</u>	0.5287(29)
$\tilde{m}_s = \tilde{m}_{s,\text{ph}}$	N204	0.470(10)	0.4996(55)	0.5271(42)	0.5519(34)
	N201	<u>0.4441(81)</u>	0.4763(68)	0.5109(48)	0.5451(33)
	D201	<u>0.433(11)</u>	<u>0.4575(81)</u>	<u>0.4948(62)</u>	0.5308(55)
$\beta = 3.7, a = 0.049 \text{ fm}$					
$\bar{m} = m_{\text{symm}}$	N302	0.368(11)	0.3754(72)	0.3846(44)	0.3943(32)
	J303	<u>0.3330(91)</u>	<u>0.3572(50)</u>	0.3811(28)	0.4034(16)
	E300	<u>0.332(10)</u>	<u>0.3651(55)</u>	<u>0.3920(30)</u>	0.4191(23)
$\tilde{m}_s = \tilde{m}_{s,\text{ph}}$	N305	0.3901(42)	0.4085(33)	0.4258(28)	0.4426(24)
	N304	0.3610(74)	0.3865(55)	0.4098(29)	0.4331(36)
	J304	<u>0.3445(71)</u>	<u>0.3704(44)</u>	0.4010(31)	0.4257(26)
$\beta = 3.85, a = 0.039 \text{ fm}$					
$\bar{m} = m_{\text{symm}}$	J501	0.2796(42)	0.2877(32)	0.2945(27)	0.3010(27)

F Statistical analysis

We detail our statistical methods, starting with an exposition on jackknife [209, 210] and bootstrap [211, 212] resampling techniques that are used with respect to primary (correlation functions), secondary (masses determined on individual ensembles) and tertiary (extrapolated masses, LECs etc.) observables. In appendix F.2 we then explain how we take into account autocorrelations in the Monte Carlo time series both for the variances of observables and for the reduced correlation matrices between observables by means of a binning and extrapolation procedure. This is illustrated for some examples in appendix F.3. Finally, in appendix F.4 we detail how we take into account the errors of the arguments of our fit functions as well as correlations between the fitted masses and the arguments, also incorporating prior information on t_0/a^2 and the Ξ baryon mass into the fits to secondary data. We also employ a model averaging procedure which is explained in section 6.4 of the main text.

F.1 Resampling: jackknife and bootstrap analysis

We assume that a particular ensemble contains N gauge configurations and that I different observables A^i , $i = 1, \dots, I$ are computed on these configurations, with the set of results given as $\{A_1^i, A_2^i, \dots, A_N^i\}$. These could, e.g., be correlation functions $C_H(t)$ for a hadron H at a time t , where H and t are encoded as the superscript i . For these observables we

define ensemble averages

$$\langle A^i \rangle = \frac{1}{N} \sum_{n=1}^N A_n^i. \quad (\text{F.1})$$

We can then move on to compute secondary observables (also known as derived observables), e.g., hadron masses, from these ensemble averages:

$$f_k = f_k(\{\langle A^i \rangle\}) = f_k(\langle A \rangle), \quad (\text{F.2})$$

where the dependence on the arguments could be non-parametric, e.g., the result of a least squares fit. Above, we introduced the short-hand notation $\langle A \rangle = \{\langle A^i \rangle\}$. Within the remainder of this subsection we will omit the superscripts i but keep in mind that in general the secondary observables f_k will depend on several primary observables A .

In addition to the original sample $\{A_1, \dots, A_N\}$ we can also introduce a single elimination jackknife sample $\{A_1^{(J)}, \dots, A_N^{(J)}\}$, where

$$A_j^{(J)} = \frac{1}{N-1} (N\langle A \rangle - A_j). \quad (\text{F.3})$$

In this case the number of jackknives equals the number of configurations: $J = N$. Note that

$$\frac{1}{N} \sum_{j=1}^N A_j^{(J)} = \langle A \rangle,$$

however, for secondary quantities in general

$$f_k^{(J)} = \frac{1}{N} \sum_{j=1}^N f_{k,j}^{(J)} \neq f_k(\langle A \rangle), \quad \text{where} \quad f_{k,j}^{(J)} = f_k(A_j^{(J)}).$$

It can easily be checked that the single elimination jackknife error of A is identical to its standard deviation, where for the moment being we neglect autocorrelations:

$$\Delta A^2 = \frac{N-1}{N} \sum_j \left(A_j^{(J)} - \langle A \rangle \right)^2 = \frac{1}{N(N-1)} \sum_n (A_n - \langle A \rangle)^2. \quad (\text{F.4})$$

For secondary quantities no error propagation is needed but the jackknife error

$$\left(\Delta^{(J)} f_k \right)^2 = \frac{N-1}{N} \sum_j \left(f_{k,j}^{(J)} - f_k^{(J)} \right)^2 \quad (\text{F.5})$$

or the covariance matrix

$$C_{k\ell}^{(J)} = \frac{N-1}{N} \sum_j \left(f_{k,j}^{(J)} - f_k^{(J)} \right) \left(f_{\ell,j}^{(J)} - f_\ell^{(J)} \right), \quad (\text{F.6})$$

where $C_{kk}^{(J)} = \left(\Delta^{(J)} f_k \right)^2$, can be computed directly.

Instead of single elimination jackknife, one can “block” the N original measurements into $J < N$ bins, averaging over $S = \lfloor N/J \rfloor \in \mathbb{N}$ subsequent configurations and construct

jackknives out of these J bins. This will reduce — or if $S \gg \tau_{\text{int}}$ (where τ_{int} is the largest integrated autocorrelation time of the f_k) effectively remove — autocorrelations. It turns out that due to the reduced variance between jackknife samples, the jackknife is a more stable procedure than the bootstrap explained below. Therefore, at the initial stage of the analysis, different bin sizes are realized, and the jackknife errors of the f_k are computed as a function of the bin size. These are then extrapolated to infinite bin size (as will be detailed in appendix F.2 below), giving the scale factors

$$s_k = \lim_{S \rightarrow \infty} \frac{\Delta^{(J)} f_k[S]}{\Delta^{(J)} f_k} \approx \sqrt{2\tau_{k,\text{int}}}, \quad (\text{F.7})$$

where $\Delta^{(J)} f_k[S]$ is the jackknife error on f_k , obtained for the bin size S , and $\tau_{k,\text{int}}$ is the integrated autocorrelation time of f_k .

We wish to combine information from different ensembles with different numbers of configurations to perform various extrapolations and interpolations. The binning approach would require a bin size S that is larger than twice the maximal integrated autocorrelation time that we encounter for any of our observables. In addition, a fixed dimension of the resampled data across ensembles is preferable. Our strategy to achieve this is to resample all data into a bootstrap ensemble of a fixed dimension $B = 500$ but to rescale the resulting distributions of f_k by the scale factors s_k introduced above. For correlated fits, in addition the extrapolated covariance matrices eq. (F.6) are needed, see appendix F.2.

The bootstrap sets are generated, randomly dialling $b_n \in \{1, \dots, N\}$ for each $b = 1, \dots, B$. The bootstrap sample b then contains $\{A_{b_1}, A_{b_2}, \dots, A_{b_N}\}$. We do not require the whole sample but only the corresponding bootstrap averages

$$A_b^{(B)} = \frac{1}{N} \sum_n^N A_{b_n}, \quad (\text{F.8})$$

which can be generated directly from the original data with a well-defined random number sequence. This sequence is stored so that additional observables can be added when they are computed at a later time.

As discussed above, prior to any analysis we rescale the bootstrap distributions of f_k by the scale factor s_k :

$$f_{k,b}^{(B)} = f_k + s_k \left[f_k(A_b^{(B)}) - f_k \right]. \quad (\text{F.9})$$

We then define the bootstrap average of f_k as

$$f_k^{(B)} = \frac{1}{B} \sum_b^B f_{k,b}^{(B)}. \quad (\text{F.10})$$

In the limit $N \rightarrow \infty$ and for sufficiently large B : $f_k^{(B)} \rightarrow f_k$, up to $1/N$ corrections. There is a bias between the true (but unknown) result f_k^* and the estimate f_k , obtained using a finite sample size: $b_k = f_k - f_k^*$. Assuming that a similar skew exists between the average of the resampled distribution $f_k^{(B)}$ and the original ensemble average, one obtains [212] $b_k \approx f_k^{(B)} - f_k$. Subtracting this bias gives the so-called “unbiased estimate”:

$$f_k^* \approx 2f_k - f_k^{(B)}. \quad (\text{F.11})$$

We have decided to quote as our central values either the original ensemble averages f_k or the (statistically more robust) median of the bootstrap histogram, since the bias can only amount to a fraction of the statistical error.

In the absence of autocorrelations, one can determine the covariance matrix from the bootstrap ensemble instead of the jackknife sample. However, the results for the off-diagonal matrix elements would be incorrect if obtained from the rescaled bootstrap ensemble. Therefore, we also keep the binned jackknife samples, from which the relevant covariance matrix elements can be reconstructed if needed, extrapolating the definition (F.6) to infinite bin size, as will be detailed below.

The above errors and the covariance matrix (which will assume a block-diagonal form when data from different ensembles are combined) are needed for subsequent fits to the secondary f_k data. However, it is also possible to quote an (in general asymmetric) error range, by sorting the bootstrap results and discarding the upper and lower 16% of the distribution, resulting in upper and lower 68% confidence limits ($\pm 1\sigma$ error band).²² We monitor the differences b_k between $f_k^{(B)}$ and f_k as well as the deviation of the width of the confidence band from $2\Delta f_k^{(B)}$, as a measure of the non-Gaussianity of the resampled distribution.

The analysis described above factorizes into two stages. The output of the first stage is the ensemble average f_k , the resampled (and rescaled, see eq. (F.9)) bootstrap distribution $\{f_{k,b}^{(B)}, b = 1, \dots, B\}$ and jackknife ensembles for different bin sizes. From this the errors and covariance matrix can be reconstructed and further fits carried out. In principle, one could compute sub-bootstraps on the individual bootstrap ensembles, aiming at constructing separate covariance matrices for each bootstrap. These will be subject to larger statistical fluctuations, potentially resulting in non-positive or unusually small eigenvalues on some of the samples. Instead, we implement the more robust frozen covariance matrix approach, employing one and the same matrix on all the bootstraps in the subsequent fits to the secondary data. This approximation is justified by the fact that differences between the two methods should be of order $1/N$ in the sample size N .

F.2 Binning and autocorrelation times

We consider the autocorrelation function of the covariance matrix element between two primary observables A and B , i.e. in the notation of the previous subsection $A = A^1$ and $B = A^2$:

$$\begin{aligned}\Gamma_{AB}(t) &= \frac{1}{N-t} \sum_{t_0=1}^{N-t} (A_{t+t_0} - \langle A \rangle) (B_{t_0} - \langle B \rangle), \\ \Gamma_{BA}(-t) &= \Gamma_{AB}(t) \quad \text{for } t \geq 0,\end{aligned}\tag{F.12}$$

where $t \in \mathbb{Z}$, $|t| \ll N$ and the Monte Carlo time series is defined by $\{A_n, B_n\}$, $n = 1, \dots, N$. $\langle A \rangle$ is the ensemble average defined in eq. (F.1). Above, we assume phase conventions such that $\langle A \rangle, \langle B \rangle \in \mathbb{R}$ and we have taken into account that the length of the time series available

²²Note that if the unbiased estimate f_k^* rather than the ensemble average f_k is quoted, the 68% confidence range should be shifted accordingly.

for a given value of t is $N - t$. Note that $B = A$ is included as a special case. The discussion for the primary observables below can easily be generalized to secondary observables. We remark that estimates of the errors of (normalized) autocorrelation functions (which are errors of errors), including the case of secondary observables, can, e.g., be obtained following the procedure detailed in Appendix C of ref. [213], see also refs. [214, 215].

Next we define the normalized autocorrelation function,²³

$$\rho_{AB}(t) = \frac{\Gamma_{AB}(t)}{\sqrt{\Gamma_{AA}(0)\Gamma_{BB}(0)}} = \sum_k c_{A,k} c_{B,k} e^{-|t|/\tau_k}, \quad (\text{F.13})$$

where τ_k is the autocorrelation time of the mode k of the system and the largest exponential autocorrelation time is defined as $\tau_{\text{exp}} = \max_k \{\tau_k\}$. The coefficients $c_{A,k}$ and $c_{B,k}$ that describe the couplings of the observables A and B to the mode k are normalized: $\sum_k c_{A,k}^2 = \sum_k c_{B,k}^2 = 1$.

Extending the autocorrelation function to infinite times, the integrated autocorrelation time is defined as

$$\begin{aligned} \tau_{AB,\text{int}} &= \frac{1}{2} \int_{-\infty}^{\infty} dt \rho_{AB}(t) = \int_0^{\infty} dt \frac{1}{2} [\rho_{AB}(t) + \rho_{BA}(t)] \\ &= \sum_k c_{A,k} c_{B,k} \int_0^{\infty} dt e^{-t/\tau_k} = \sum_k c_{A,k} c_{B,k} \tau_k : \end{aligned} \quad (\text{F.14})$$

It corresponds to the weighted average of autocorrelation times of modes contributing both to A and B . We remark that for $A \neq B$ in principle $\tau_{AB,\text{int}}$ can be negative. The Cauchy–Schwarz inequality implies that

$$\tau_{AB,\text{int}}^2 \leq \tau_{A,\text{int}} \tau_{B,\text{int}}, \quad (\text{F.15})$$

where $\tau_{A,\text{int}} = \tau_{AA,\text{int}}$ is the integrated autocorrelation time of the observable A , needed to compute the scale factor $s_A \approx 2\tau_{A,\text{int}}$ of eqs. (F.7) and (F.9).

The variance of A can be obtained from $\Gamma_{AA}(t)$:

$$\begin{aligned} \text{var}(A) &= \int_{-\infty}^{\infty} dt \Gamma_{AA}(t) = \left\langle (A - \langle A \rangle)^2 \right\rangle \int_{-\infty}^{\infty} dt \rho_{AA}(t) \\ &= (2\tau_{A,\text{int}}) (N - 1) \sigma_A^2[1], \end{aligned} \quad (\text{F.16})$$

where the argument “[1]” denotes the bin size $S = 1$ (no binning) and

$$\sigma_A^2[1] = \frac{1}{N - 1} \left\langle (A - \langle A \rangle)^2 \right\rangle = C_{AA}[1] \quad (\text{F.17})$$

is the naive squared standard deviation, ignoring autocorrelation effects. In appendix F.1 we referred to it as ΔA^2 .

It is well known that autocorrelation times can also be estimated employing a binning procedure: we define J bins of length $S = \lfloor N/J \rfloor$ with $1 \leq S \ll N$ and we will only average

²³This equation is justified by the fact that the HMC algorithm is ultra-local in the Monte Carlo time, i.e. only the configuration at the time t is used to obtain the $t + 1$ result. Note that our convention differs for $A \neq B$ from $\rho_{AB}(t) = \Gamma_{AB}(t)/\Gamma_{AB}(0)$, which is sometimes found in the literature.

over the first $N' = JS$ measurements. We define $\delta A_n = A_n - \langle A \rangle$ and compute the standard deviation on the binned ensemble:

$$\begin{aligned}
\sigma_A^2[S] &= \frac{1}{J(J-1)} \sum_{j=0}^{J-1} \left(\frac{1}{S} \sum_{s=1}^S \delta A_{jS+s} \right)^2 \\
&= \frac{1}{N'(N'-S)} \sum_{j=0}^{J-1} \sum_{s,t=1}^S \delta A_{jS+s} \delta A_{jS+t} \approx \frac{(N-1)\sigma_A^2[1]}{S(N'-S)} 2 \int_0^S ds \int_s^S dt \rho_{AA}(t-s) \\
&= \frac{2(N-1)\sigma_A^2[1]}{N'-S} \sum_k c_{A,k}^2 \tau_k \left[1 - \frac{\tau_k}{S} \left(1 - e^{-S/\tau_k} \right) \right] \\
&= \frac{(N-1)\sigma_A^2[1]}{N'-S} 2\tau_{A,\text{int}} \left[1 - \sum_k c_{A,k}^2 \frac{\tau_k}{\tau_{A,\text{int}}} \frac{\tau_k}{S} \left(1 - e^{-S/\tau_k} \right) \right]. \tag{F.18}
\end{aligned}$$

In the approximate step²⁴ we replaced the autocorrelation function $\Gamma_{AA}(t)$ by the normalized autocorrelation function $\rho_{AA}(t)$ times $(N-1)\sigma_A^2[1]$, whereas in the second last step we employed eq. (F.13). Using $N-1 \approx N'-S$ gives the leading order expectation

$$\frac{\sigma_A^2[S]}{\sigma_A^2[1]} \approx 2\tau_{A,\text{int}} \left(1 - \frac{c_A}{S} \right), \tag{F.19}$$

where $c_A = \sum_k c_{A,k}^2 \tau_k^2 / \tau_{\text{int}} \geq 0$. Therefore, up to $1/S$ corrections in the bin length, the ratio of binned over unbinned squared standard deviations approaches twice the integrated autocorrelation time. This suggests, in a first step, to compute this ratio in a self-consistent way, e.g., at $S_0 \approx 2\tau_{\text{int}}$ and then to estimate the remaining ratio $\sigma_A^2[\infty]/\sigma_A^2[S_0]$ via a fit to the data obtained with bin sizes $S \geq S_0$. We remark that for $\tau = \tau_k = \tau_{\text{int}}$ one can write:

$$\frac{\sigma^2[S]}{\sigma^2[1]} \approx 2\tau \left[1 - \frac{\tau}{S} \left(1 - e^{-S/\tau} \right) \right]. \tag{F.20}$$

Taking into account the exponential corrections to eq. (F.19), we obtain

$$\frac{\sigma_A^2[S]}{\sigma_A^2[1]} \approx 2\tau_{A,\text{int}} \left[1 - \frac{c_A}{S} + \frac{1}{S\tau_{A,\text{int}}} \sum_k (c_{A,k}\tau_k)^2 e^{-S/\tau_k} \right], \tag{F.21}$$

which suggests the three-parameter fit

$$\frac{\sigma_A^2[S]}{\sigma_A^2[1]} \approx 2\tau_{A,\text{int}} \left(1 - \frac{c_A}{S} + \frac{d_A}{S} e^{-S/\tau_{A,\text{int}}} \right), \tag{F.22}$$

where $c_A > d_A \geq 0$. The rationale for this parametrization is that on the one hand large values of $\tau_{A,\text{int}}$ imply large couplings to slow modes, in which case one may be unable to resolve the exponential correction to the coefficient of the leading $1/S$ decay. In this case eq. (F.19) should be adequate, unless of course only one mode dominates, see eq. (F.20). If, however, $\tau_{A,\text{int}}$ is dominated by the faster modes then effectively replacing the smaller

²⁴This approximation is valid for $S, \tau_k \gg 1$. The most general case can be obtained by employing incomplete geometric sums: $\sum_{t=s+1}^S e^{-t/\tau} = (e^{-s/\tau} - e^{-S/\tau})/(e^{1/\tau} - 1) \approx \tau(e^{-s/\tau} - e^{-S/\tau})$.

τ_k -values by $\tau_{A,\text{int}}$ in eq. (F.22), thereby reducing the number of fit parameters, should be a sensible approximation.

The above equations also hold for jackknifed primary data and therefore, within the jackknife approach, generalize identically to secondary observables such as hadron masses. Therefore, this method can directly be used to determine the corresponding integrated autocorrelation times from binned jackknife estimates. We remark that the Γ -method of ref. [214] has the advantage of exponential as opposed to power-law corrections. However, binning provides smaller errors at a given value of S and is more robust in the case of limited statistics. For a recent discussion of the Γ -method and its application to secondary observables, see ref. [215]. As pointed out above, the generalization to secondary observables is trivial.

Assuming a normal distribution of independent measurements, i.e. $S \gtrsim 2\tau_{\text{int}}$, the error on $\sigma_A^2[S]$, that is needed to fit the $1/S$ tail, can be estimated as [216]

$$\Delta(\sigma_A^2[S]) = \sqrt{\frac{2(J-1)}{J^2}} \sigma_A^2[S], \quad (\text{F.23})$$

where $J = N'/S \approx J - 1$ is the number of bins.

The same binning can be performed for off-diagonal elements of the covariance matrix. We define unbinned covariance matrix elements $C_{AB}[1]$, see eq. (F.6) for the jackknife definition of the covariance matrix, where A and B can also be secondary data. For observables that are simple ensemble averages the relation $C_{AB}[1] = \Gamma_{AB}(t=0)/(N-1) = \rho_{AB}(0)\sigma_A[1]\sigma_B[1]$ holds. The autocorrelation time-corrected covariance matrix is given as $C_{AB}[\infty]$, where $C_{AB}[S]$ denotes the covariance matrix, computed for the bin size S . The resulting expression reads:

$$C_{AB}[S] \approx 2\tau_{AB,\text{int}}\sigma_A[1]\sigma_B[1] \left(1 - \frac{c_{AB}}{S} + \sum_k c_{A,k}c_{B,k} \frac{\tau_k}{\tau_{AB,\text{int}}} \frac{\tau_k}{S} e^{-S/\tau_k} \right), \quad (\text{F.24})$$

where, for $A \neq B$, c_{AB} is not necessarily semi-positive and $\tau_{AB,\text{int}}$ may be negative.

Naively reconstructing the autocorrelation time-corrected covariance matrix from the rescaled bootstrap data eq. (F.9) would amount to assuming $\tau_{AB,\text{int}} > 0$ and $\tau_{AB,\text{int}}^2 C_{AB}[1] = \tau_{A,\text{int}}\tau_{B,\text{int}}\sigma_A[1]\sigma_B[1]$, which in general does not hold. Therefore, to facilitate correlated fits to secondary data, in addition to the diagonal integrated autocorrelation times, giving us the rescaling factors, we need to estimate the off-diagonal elements of $C[\infty]$, using eq. (F.24). Combining the inequality (F.15) with $C_{AB}^2[1] \leq \sigma_A^2[1]\sigma_B^2[1]$ is consistent with the necessary condition $C_{AB}^2[\infty] \leq \sigma_A^2[\infty]\sigma_B^2[\infty]$, which we take as an upper limit for our extrapolation. In the end we store the normalized covariance matrices $\overline{C}_{jk} = C_{jk}[\infty]/(\sigma_{f_j}[\infty]\sigma_{f_j}[\infty])$ for the secondary data $\{f_j\}$. Since we also keep the binned jackknife distributions, this matrix can be enlarged to incorporate further observables at a later stage.

F.3 Examples of infinite bin size extrapolations

We show some examples for the extrapolation discussed above of statistical errors to infinite bin sizes, starting with t_0/a^2 . In the case of this observable our data, including the smallest

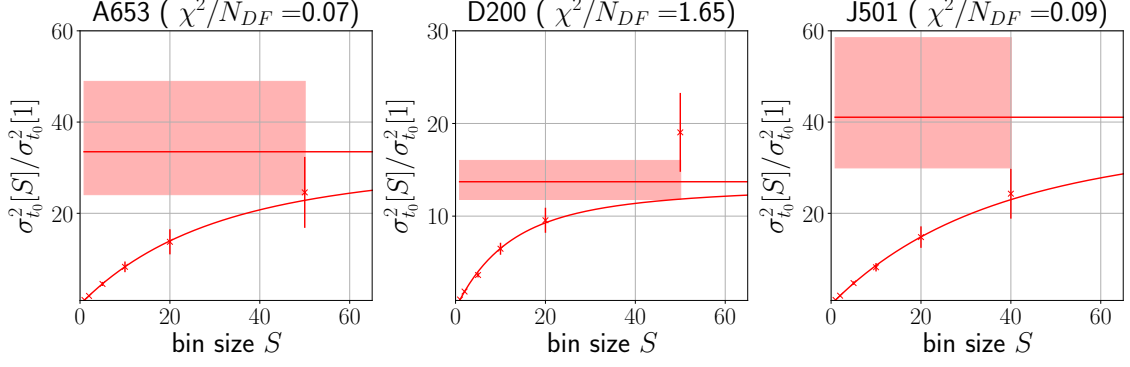


Figure 34. Bin size extrapolation of the variance of t_0/a^2 according to the one-parameter fit eq. (F.20) for the ensembles A653 (left), D200 (centre) and J501 (right). The bin size S is in units of 4 MDU. The error bands indicate the extrapolated values. Note that the central plot has a different scale on the y -axis than the other two panels. The respective simulation parameters can be found in tables 1, 2 and 21 (for D200 in table 2 of ref. [78]). An overview in terms of the pion masses and lattice spacings is also provided in the middle panel of figure 1.

bin size $S = 1$, are well-described by the one-parameter fit eq. (F.20), indicating that this quantity basically only couples to one — possibly the slowest — mode of the system. In figure 34 we show the extrapolation for three representative examples: A653, at the coarsest lattice spacing ($\beta = 3.34$, $a \approx 0.098$ fm) and a large pion mass $M_\pi \approx 429$ MeV, D200, a finer lattice ($\beta = 3.55$, $a \approx 0.064$ fm) at a small pion mass $M_\pi \approx 202$ MeV and J501, at the finest lattice spacing ($\beta = 3.85$, $a \approx 0.039$ fm) at an intermediate pion mass $M_\pi \approx 336$ MeV. A653 has periodic boundary conditions in time while the other two ensembles have open boundary conditions. Note that the data for different bin sizes are highly correlated. Therefore, the uncorrelated χ^2/N_{DF} -values are all much smaller than one.

The integrated autocorrelation times (which in this case seem to coincide with the exponential autocorrelation times) in units of four MDUs can be read off the figures by dividing the extrapolated results (error bands) by a factor of two. The general trend for the autocorrelation times is to increase with β towards smaller lattice spacings, with the exception of $\beta = 3.34$, which, being about the coarsest lattice spacing that we can simulate with our action, also suffers from large autocorrelations. Some time series are depicted in figure 6. We list the extracted autocorrelation times for t_0 and their errors in the last column of table 1 in section 2. In some cases our statistics are insufficient for a reliable estimation of the error of the autocorrelation time (indicated in *Italics*). Note that the ensembles that are labelled as “rqcd0mn” have been generated using BQCD [85] instead of OPENQCD [89].

The hadron masses couple to more than just one mode and cannot be described in terms of eq. (F.20). However, the data are in agreement with two- and three-parameter fits according to eqs. (F.19) and (F.22), starting from some minimum bin size. We find that the results from these parametrization usually agree, however, the three-parameter fits turn out to be more stable. Therefore, we extrapolate the error according to eq. (F.22), where we self-consistently start the fit range at a bin size that is larger than thrice the extracted integrated autocorrelation time. As a general pattern, we find larger autocorrelation times

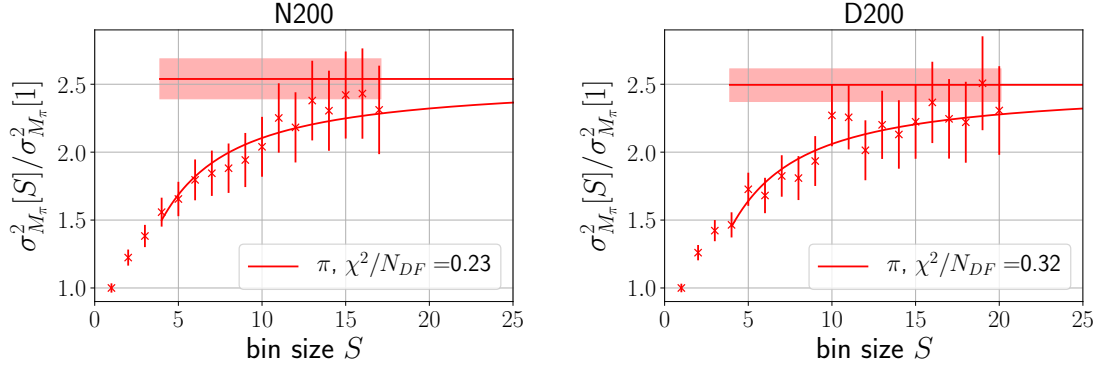


Figure 35. Bin size extrapolation of the variance of the pion mass M_π according to the three-parameter fit eq. (F.22) for the ensembles N200 (left, $M_\pi \approx 280$ MeV) and D200 (right, $M_\pi \approx 200$ MeV), both at $a \approx 0.064$ fm. Successive measurements are separated by 4 MDUs and the fit starts at thrice the integrated autocorrelation time. The red error band indicates the fit range and the extrapolated value.

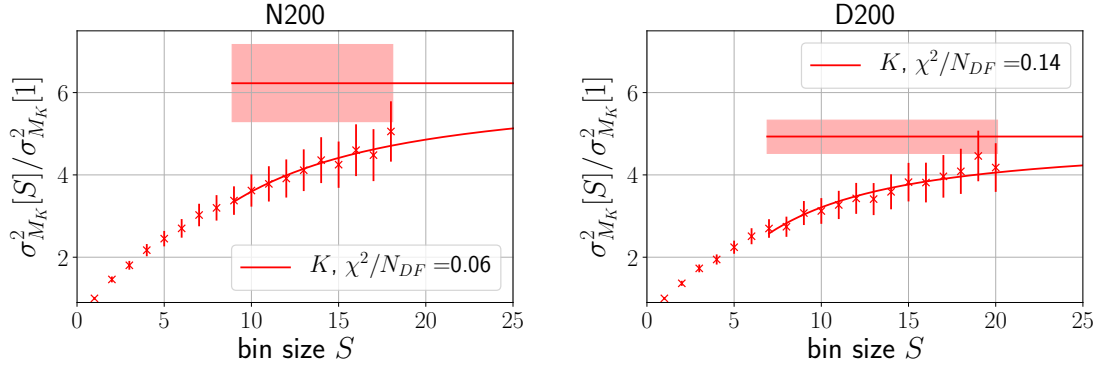


Figure 36. The same as figure 35 for the kaon mass M_K .

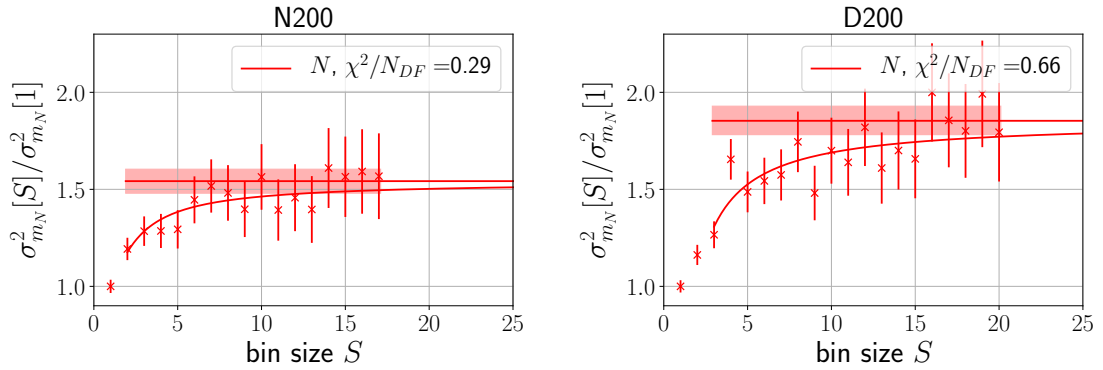


Figure 37. The same as figure 35 for the nucleon m_N .

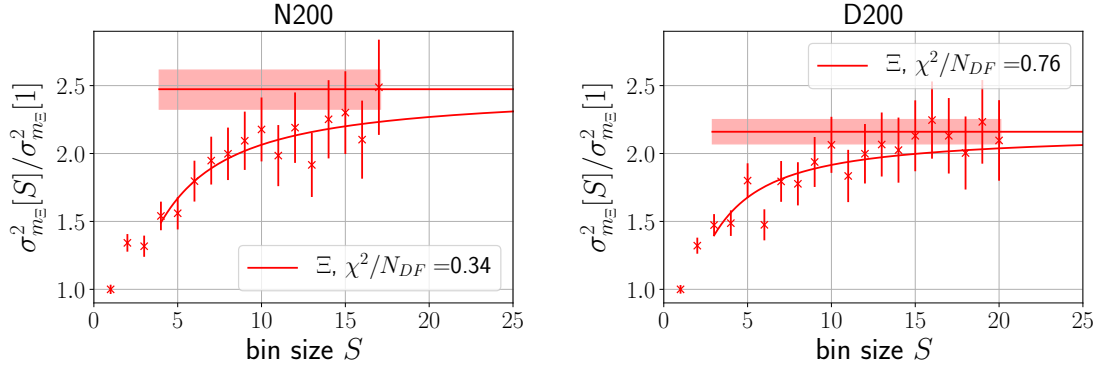


Figure 38. The same as figure 35 for the cascade mass m_Ξ .

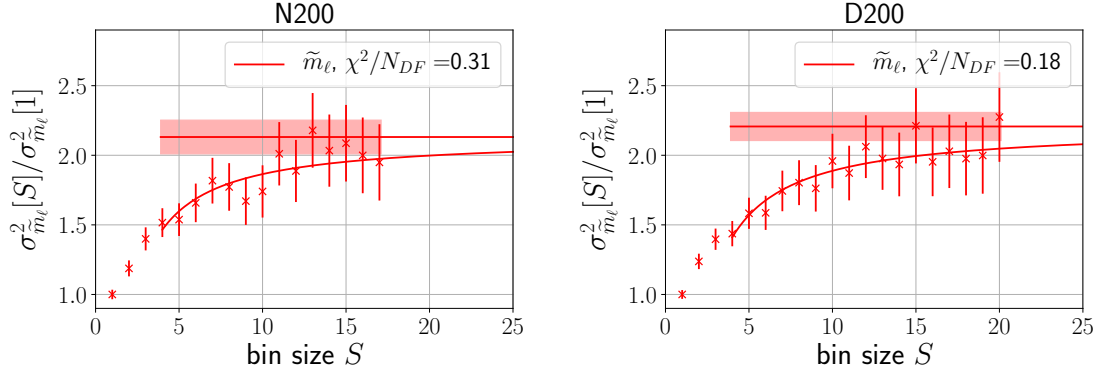


Figure 39. The same as figure 35 for the light AWI quark mass \tilde{m}_ℓ . However, the two-parameter fit (F.19) was employed, starting at four times the integrated autocorrelation time.

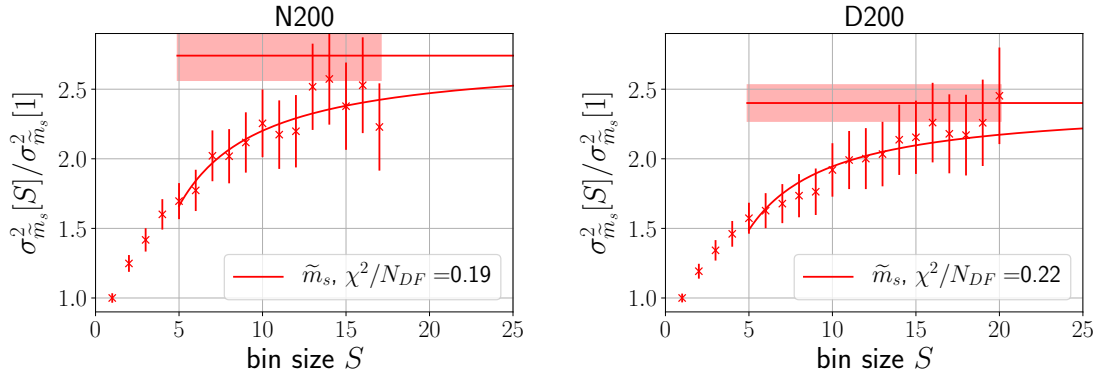


Figure 40. The same as figure 39 for the strange AWI quark mass.

for hadrons that contain strange quarks and also the autocorrelation times for pseudoscalar mesons are larger than those for baryons. In all the cases the integrated autocorrelation

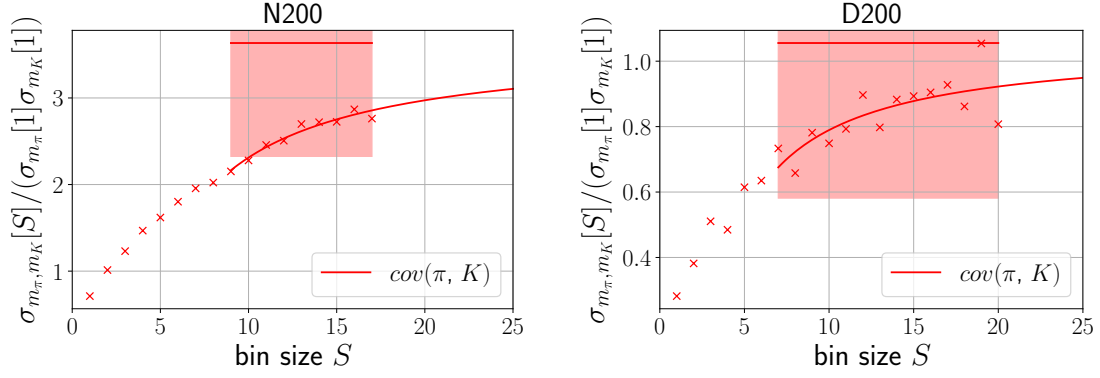


Figure 41. Bin size extrapolation of the covariance of the pion mass M_π with the kaon mass M_K according to the three-parameter fit eq. (F.22) for the ensembles N200 (left, $M_\pi \approx 280$ MeV) and D200 (right, $M_\pi \approx 200$ MeV), both at $a \approx 0.064$ fm. Successive measurements are separated by 4 MDUs.

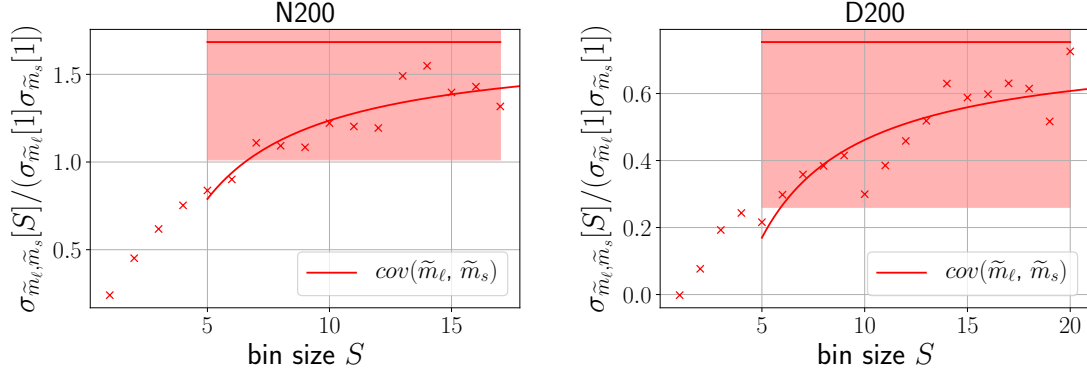


Figure 42. The same as figure 41 for the strange AWI quark mass \tilde{m}_s . However, the two-parameter fit (F.19) was employed.

times turn out to be much smaller than for t_0/a^2 .

In figures 35–40 we illustrate the extrapolations for the examples of N200 ($M_\pi \approx 280$ MeV) and D200 ($M_\pi \approx 200$ MeV), both at $a \approx 0.064$ fm, with successive measurements separated by 4 MDUs. Regarding the AWI quark masses (figures 39 and 40) the data show a preference for the two-parameter fits (F.19), which we carry out using the $S \gtrsim 4\tau_{\text{int}}$ data. Finally, in figures 41 and 42 we extrapolate the covariance matrix elements between the pion and the kaon masses and between the light and strange quark AWI masses, respectively. The starting bin size of the fit always corresponds to the maximum of the starting bin sizes for the corresponding fits to the two corresponding diagonal elements. In the first case the data are well described by the three-parameter fit (F.22), while for the AWI masses we employ the two-parameter fit (F.19). In some cases (not shown) we also encountered covariances that became smaller or changed sign when the bin size was increased, which is

to be expected. These were then parameterized according to eq. (F.24).

F.4 Least squares fits with errors on the arguments and priors

We wish to fit expectation values y_e , e.g., a baryon masses determined on an ensemble e , $e \in \{1, \dots, n_e\}$, to a parametrization $f(x_e; \{a^\ell\})$, where x_e could be the expectation value of the pion mass on ensemble e . The function depends on a set of parameters $\{a^\ell\}$, $\ell \in \{1, \dots, n_p\}$. The baryon mass has an error Δy_e , the pion mass an error Δx_e and, for the moment being, we neglect correlations between the two. The result can be obtained using Orear’s “effective variance method” [217, 218] by minimizing the functional

$$\chi^2[\{a^\ell\}] = \sum_{e=1}^{n_e} \frac{[y_e - f(x_e; \{a^\ell\})]^2}{\Delta y_e^2 + [df(x_e; \{a^\ell\})/dx_e \Delta x_e]^2} \quad (\text{F.25})$$

with respect to the parameters $\{a^\ell\}$. This is easily generalizable to simultaneous fits to several baryon masses, which may also depend on more than one parameter, e.g., on the pion as well as on the kaon mass. Correlations can easily be taken into account too. The drawback of this method is that derivatives of the function(s) with respect to the argument(s) have to be computed for each update of a parameter value a^ℓ and, in the case of correlated fits, the resulting new covariance matrix needs to be inverted each time.

While the x -errors affect the weights within the Orear χ^2 -functional, it is the y -difference that is minimized. It appears more natural to minimize the shortest (weighted) distance between the curve and a data point instead. We remark that within the Gaussian approximation both views are equivalent. A more efficient and stable class of algorithms that are based on the latter minimization strategy was suggested in ref. [219]. Here we describe a related approach, which we employ in our study, in a form that is as general as needed within the present analysis. This method places the expectation value(s) that appear as argument(s) of the fit function(s) on an equal footing with the expectation value(s) that are to be approximated by the fit function(s). The χ^2 -functional is then constructed such as to minimize the ℓ^2 -distance between the fitted parametrization and the data, where the distance is defined through a scalar product involving the inverse covariance matrix. We remark that the uncorrelated case of this generalized least squares method is actually the starting point of Orear’s derivation [218] of his effective variance method.

We define expectation values x_e^i , e.g., the mass of the baryon i , $i \in \{1, \dots, n\}$ on ensemble e .²⁵ These are parameterized in terms of functions

$$f_e^i(\{a^\ell\}) := f^i(x_e^{n+1}, \dots, x_e^N; \{a^\ell\}) \quad (\text{F.26})$$

that depend on a set of parameters $\{a^\ell\}$ as well as on the arguments x_e^j , $j \in \{n+1, \dots, N\}$, e.g., the pion and the kaon mass on ensemble e . So the first n elements of x_e are functions of the subsequent $N - n$ elements. We define the $N \times N$ covariance matrix C_e on ensemble e whose elements $C_e^{ii'}$ are computed according to eq. (F.6) (and extrapolated to infinite bin size, e.g., via eq. (F.24)). There exist no correlations between different ensembles.

²⁵These x_e^i correspond to the expectation values of secondary observables f_k for an ensemble e , as introduced in section F.1.

Instead of minimizing the differences $|x^i - f_e^i(\{a^\ell\})|$ using, e.g., the Orear effective variance method outlined above, we define a parametrization p_e^k , $k \in \{1, \dots, N - n\}$, both of the functions f_e^i and of the original arguments x_e^j , $j > n$. The functional forms in terms of the p_e^k are defined as follows:

$$f_e^i(\{a^\ell\}) := \begin{cases} f^i(p_e^1, \dots, p_e^{N-n}; \{a^\ell\}) , & i \leq n \\ p_e^{i-n} , & n < i \leq N \end{cases} . \quad (\text{F.27})$$

Then the differences $\delta f_e^i = x_e^i - f_e^i(\{a^\ell\})$, $i \in \{1, \dots, N\}$, are minimized via the χ^2 -functional

$$\chi^2[\{a^\ell, p_e^k\}] = \sum_{e=1}^{n_e} \sum_{i,i'=1}^N \delta f_e^i (C_e^{-1})^{ii'} \delta f_e^{i'} \quad (\text{F.28})$$

with respect to $\{a^\ell\}$ and $\{p_e^k\}$. Note that the f_e^i for $i \leq n$ contain products of the p_e^k and a^ℓ parameters. Therefore, this is not a linear fit. However, the $n_e(N - n)$ additional parameters are not overly problematic in terms of the fit stability or the algorithmic efficiency since these directions alone have a well defined minimum at the start values $p_e^k = x_e^{n+k}$. (For $i > n$: $\delta f_e^i = x_e^i - p_e^{i-n}$.) The additional multipliers do not alter the number of degrees of freedom $N_{\text{DF}} = n_e n - n_p$. We remark that in our case, for the ensembles along the symmetric line where $M_K = M_\pi$ and all octet (or decuplet) baryons collapse to one mass value, the sums over i and i' only run up to two. Therefore, the number of degrees of freedom is $N_{\text{DF}} = (n_e - n_{\text{symm}})n + n_{\text{symm}} - n_p$, where n_e is the total number of ensembles, n_{symm} is the number of ensembles along symmetric lines, n is the number of different baryons included in the fit and n_p is the number of fit parameters. In the case of joint octet and decuplet fits the second n_{symm} in the above formula has to be multiplied by two.

We rescale all dimensionful data and fit parameters into units of t_0/a^2 , set the lattice spacing using t_0^*/a^2 separately for each β -value and use m_Ξ/GeV to set the overall scale. We incorporate these additional measurements and information as “priors” into our fits. We are not able to resolve any correlations between t_0/a^2 and our masses. This is not surprising, given the fact that t_0/a^2 has a much larger autocorrelation time, coupling to very different modes. Therefore, we may treat t_0/a^2 as independent measurements. For each of the priors q_e^k we add a term $(r_e^k - q_e^k)^2/(\Delta q_e^k)^2$ to the χ^2 -functional. The central values q_e^k are drawn on a bootstrap by bootstrap basis according to a Gaussian pseudo-bootstrap distribution with variance Δq_e^k , while the r_e^k are additional fit parameters that modify the fit functions f_e^i . Since the number of additional parameters equals the number of additional measurements/priors, this procedure leaves the number of degrees of freedom invariant. After the minimization one may compare the bootstrap histograms for the r_e^k and the priors q_e^k . In our case these turn out to be fairly similar which means that the additional knowledge of the hadron masses has little impact on the favoured values for t_0/a^2 or t_0^*/a^2 .

G HMC simulation parameters and reweighting towards the target action

The CLS simulations are carried out with an action that differs from the target action in terms of the rational approximation made for the $N_f = 1$ strange quark contribution and

a twisted mass term that is introduced to stabilize the $N_f = 2$ light fermion part of the simulation. The difference is corrected for by reweighting the observables. For details see ref. [78]. We list the simulation parameters for some of the ensembles in appendix G and explain aspects of the computation of the reweighting factors in appendix G.2.

Table 21. Simulation parameters for selected ensembles, which (to the best of our knowledge) have not been reported elsewhere. The *ensemble id* consists of the id used for the ensemble plus a suffix (r000, ...) to distinguish different replica runs. $a\mu_0$ and $a\mu_i$ are the final and intermediate masses used in the twisted mass reweighting and factorization, respectively, where $N_{\text{mf},2}$ of the lightest twisted mass values are integrated on the coarsest time scale. N_p is the number of poles in the range $[r_a, r_b]$, used for the rational approximation for the single quark flavour. N'_p poles are represented as single pseudo-fermions of which $N_{p,2}$ are integrated on the coarsest time scale using $N_{s,2}$ steps at this level in the MD integrator. N_{MD} is the number of MDUs produced for this replica and $\langle P_{\text{acc}} \rangle$ is the average acceptance rate.

ensemble id	$a\mu_0$	$a\mu_i$	$N_{\text{mf},2}$	N_p	$[r_a, r_b]$	N'_p	$N_{p,2}$	$N_{s,2}$	N_{MD}	$\langle P_{\text{acc}} \rangle$
A651r000	0.0	(0.0005,0.005,0.05,0.5)	1	11	[0.01, 6.5]	5	2	7	4152	0.94
A651r001	0.0	(0.0005,0.005,0.05,0.5)	1	11	[0.01, 6.5]	5	2	7	16252	0.94
A652r000	0.0	(0.0005,0.005,0.05,0.5)	1	11	[0.01, 6.5]	5	2	6	3988	0.87
A652r001	0.0	(0.0005,0.005,0.05,0.5)	1	11	[0.01, 6.5]	5	2	6	15992	0.85
A650r000	0.0	(0.0005,0.005,0.05,0.5)	1	12	[0.005, 6.5]	5	2	7	2520	0.94
A650r001	0.0	(0.0005,0.005,0.05,0.5)	1	12	[0.005, 6.5]	5	2	7	17728	0.94
A653r000	0.0	(0.0005,0.005,0.05,0.5)	1	11	[0.01, 6.5]	5	2	7	20200	0.92
A654r000	0.001	(0.005,0.05,0.5)	1	11	[0.01, 6.5]	5	2	7	20722	0.95
D150r000	0.003	(0.00045,0.0006,0.0055,0.06,0.7)	3	16	[0.001, 7.8]	9	3	20	1616	0.80
D150r001	0.003	(0.00045,0.0006,0.0055,0.06,0.7)	3	16	[0.001, 7.8]	9	3	20	796	0.77
X450r001	0.00065	(0.005,0.05,0.5)	1	15	[0.001, 7.2]	8	3	8	1604	0.95
B450r000	0.001	(0.005,0.05,0.5)	1	13	[0.002, 7.5]	7	4	7	6448	0.95
S400r000	0.00065	(0.005,0.05,0.5)	1	12	[0.01, 7.3]	6	3	7	3488	0.92
S400r001	0.00065	(0.005,0.05,0.5)	1	12	[0.01, 7.3]	6	3	7	8004	0.93
N401r000	0.00065	(0.005,0.05,0.5)	1	14	[0.002, 7.5]	6	3	8	4400	0.87
B451r000	0.001	(0.005,0.05,0.5)	1	13	[0.002, 7.5]	7	4	7	8032	0.97
B452r000	0.001	(0.005,0.05,0.5)	1	13	[0.002, 7.5]	7	4	7	7776	0.98
N450r000	0.00065	(0.005,0.05,0.5)	1	14	[0.002, 7.5]	6	3	8	3232	0.91
N450r001	0.00065	(0.005,0.05,0.5)	1	14	[0.002, 7.5]	6	3	8	1548	0.87
D451r000	0.0003	(0.0007,0.007,0.07,0.5)	1	13	[0.006, 7.8]	6	5	12	4112*	0.87
N305r000	0.001	(0.005,0.05,0.5)	1	13	[0.008, 7.0]	6	3	6	4004	0.95
N305r001	0.001	(0.005,0.05,0.5)	1	13	[0.008, 7.0]	6	3	6	4000	0.95
N304r000	0.001	(0.005,0.05,0.5)	1	13	[0.008, 7.0]	6	3	6	3896	0.95
N304r001	0.001	(0.005,0.05,0.5)	1	13	[0.008, 7.0]	6	3	6	3008	0.94
J304r000	0.00075	(0.002625,0.009187,0.032156,0.112547,0.5)	1	13	[0.008, 7.0]	7	3	6	3320	0.90
J304r001	0.00075	(0.002625,0.009187,0.032156,0.112547,0.5)	1	13	[0.008, 7.0]	7	3	6	3216	0.90
N500r000	0.0005	(0.01,0.05,0.5)	1	13	[0.0038, 7.0]	6	3	6	3912	0.97
J500r004	0.0005	(0.01,0.05,0.5)	1	13	[0.0038, 7.0]	6	3	6	6312	0.94
J500r005	0.0005	(0.01,0.05,0.5)	1	13	[0.0038, 7.0]	6	3	6	2020	0.94
J501r001	0.0005	(0.01,0.05,0.5)	1	13	[0.0038, 7.0]	6	3	6	6540	0.93
J501r002	0.0005	(0.01,0.05,0.5)	1	13	[0.0038, 7.0]	6	3	6	1588	0.94

*300 MDUs at the beginning were excluded since the run was insufficiently thermalized.

G.1 Technical HMC parameters

In table 21 we list the technical parameters for some of the recently performed simulations. This table is a continuation of table 2 of ref. [78]. For details on the simulation of ensemble E250 we refer to ref. [169]. The table includes the value of the twisted mass parameter $a\mu_0$ used to stabilize the two flavour part of the simulation. The generated configurations are reweighted accordingly when expectation values of observables are computed. The table also includes the intermediate twisted mass values $a\mu_i$ ($i > 0$) employed in the corresponding factorization of the fermion determinant. $N_{\text{mf},2}$ denotes the number of (lightest) pseudo-fermion flavours that are integrated on the coarsest timescale in the multi-scale integration scheme. The rational approximation of the one flavour part of the fermionic action utilizes N_p poles in the range $[r_a, r_b]$. N'_p of these poles are represented as single pseudo-fermions in the simulation of which $N_{p,2}$ are integrated on the coarsest timescale, using $N_{s,2}$ steps (at this timescale). Also the effect of the rational approximation is corrected for by a reweighting factor during the measurement. The trajectory length is set to two molecular dynamics units (MDUs). These notational conventions are the same as those used in ref. [78] (in particular, in table 2). The ensembles named “rqcd0mn” (with anti-periodic fermionic and periodic gluon field boundary conditions in time) are not part of the CLS project as these have been generated using the BQCD code [85] on the (now decommissioned) QPACE computer.

G.2 Reweighting

We define the difference between the target action and the simulated action on a given configuration i as s_i . The strange quark reweighting factor usually does not vary significantly. However, there is an issue regarding the strange quark reweighting which is addressed in ref. [220] and has been taken into account in the results presented in this article too. Here we restrict the discussion to the factor that is associated with the twisted mass reweighting, which can fluctuate considerably, in particular, at coarse lattice spacings and light quark masses. By definition $s_i \geq 0$ for this latter contribution. The weight factors $w_i = \exp(-s_i)$ are stochastically estimated for each configuration. We remark that it is also possible to estimate w_i in a multi-step procedure. The discussion below trivially generalizes to this case.

Once the reweighting factors are known, expectation values of an observable A are given as

$$\langle A \rangle = \frac{\sum_i w_i A_i}{\sum_i w_i}. \quad (\text{G.1})$$

In the special case $w_i = w$ this corresponds to the usual ensemble average. It is straightforward to incorporate the reweighting into the construction of the jackknife and bootstrap ensembles discussed above.

The potential problem that we face is that the inclusion of some configurations with small but imprecisely determined weights can significantly affect ensemble average. While this is more frequently observed for three-point functions than for two-point functions, we shall also address this issue here. One (expected) observation is that the statistical error σ_{w_i} of the estimate w_i is much bigger for small reweighting factors than it is for those that are

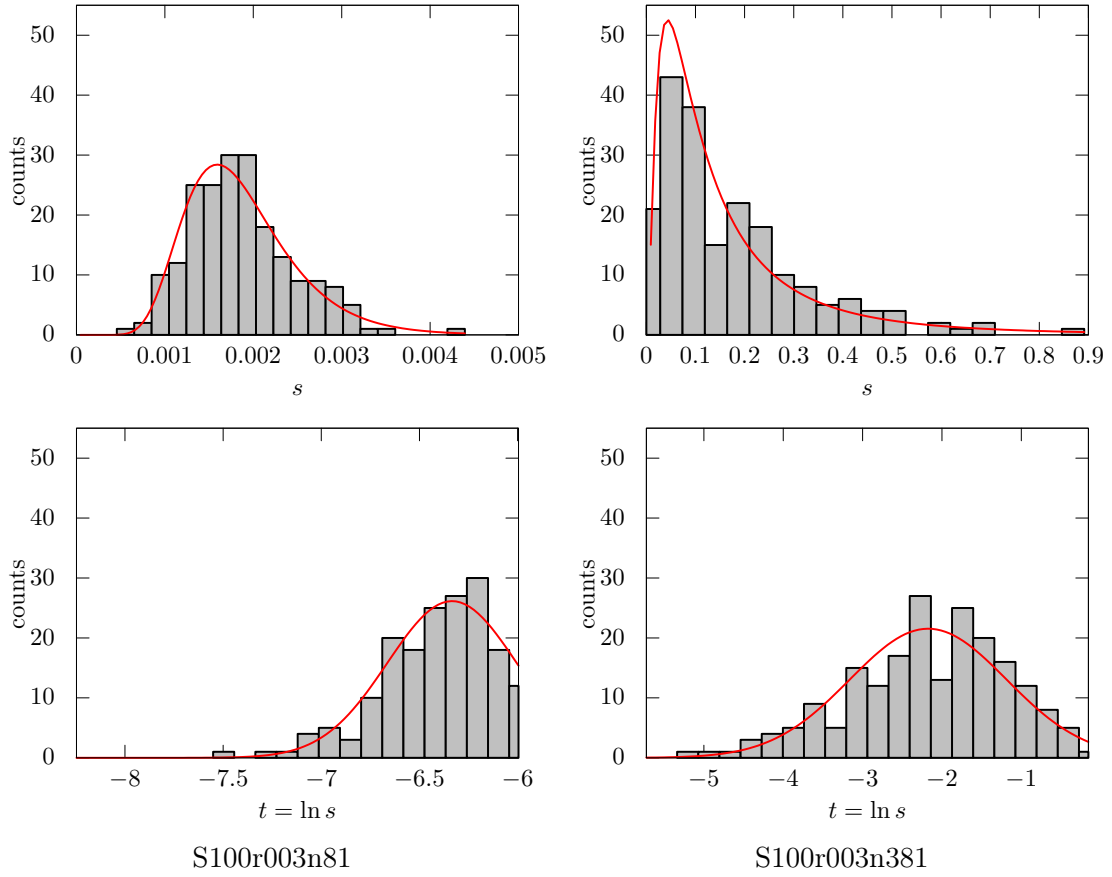


Figure 43. Examples of histograms of s (top row) and $t = \ln s$ (bottom row) for S100r003n81 (left) and S100r003n381 (right). To study the distribution 200 estimates were computed. While the distribution of s for reweighting factors close to one (S100r003n81: $w = \langle e^{-s} \rangle \approx 0.998$, left) typically resembles a Gaussian, for only slightly smaller reweighting factors (S100r003n381, $\langle e^{-s} \rangle \approx 0.851$, right) the distribution is in fact closer to a log-normal distribution. The curves in the bottom row show a normal distribution $\phi(t)$, using mean and variance of t . The curves in the top row $\phi(\log s)/s$ correspond to this assumption.

close to unity. In some of these cases the error on the reweighting factor even exceeds its estimated value. Our strategy is two-fold. First, we introduce a more robust estimate. Then, rather than keeping the number of estimates fixed, we increase it on a given configuration i until we would expect $\sigma_{w_i} < 0.01$. This is achieved by extrapolating the squared error $\sigma_{w_i}^2$ for large n_i linearly in the inverse number of estimates $1/n_i$, where $n_i \leq n_{\max}$ with n_{\max} fixed. In the cases where these target values are larger than n_{\max} , additional estimates are generated. In view of avoiding a bias, it is important that the targeted number of estimates is predicted beforehand, based on existing measurements, rather than continuing until the error has reached a certain threshold.

Table 22. Skewness, $\mu_3/\mu_2^{3/2}$, and kurtosis, μ_4/μ_2^2 , of the distribution of the logarithm of the estimates used to compute the reweighting factors, $t = \ln s$ at two different values of the coupling, $\beta = 3.4$ and $\beta = 3.7$, for ensembles along the $\text{Tr } M = \text{const}$ line. We also display the approximate pion mass and the volume. For a Gaussian distribution, one would expect $\mu_3/\mu_2^{3/2} = 0$ and $\mu_4/\mu_2^2 = 3$.

$\beta = 3.4$					$\beta = 3.7$				
id	M_π/MeV	$N_t \cdot N_s^3$	$\mu_3/\mu_2^{3/2}$	μ_4/μ_2^2	id	M_π/MeV	$N_t \cdot N_s^3$	$\mu_3/\mu_2^{3/2}$	μ_4/μ_2^2
U103	420	$128 \cdot 24^3$	0.142(7)	2.629(5)	N300	425	$128 \cdot 48^3$	0.071(9)	2.769(31)
H101	423	$96 \cdot 32^3$	0.163(10)	2.574(26)					
U102	357	$128 \cdot 24^3$	0.120(18)	2.619(18)	N302	348	$128 \cdot 48^3$	0.071(9)	2.731(16)
H102a	359	$96 \cdot 32^3$	0.132(18)	2.524(52)					
U101	271	$128 \cdot 24^3$	0.032(14)	2.669(12)	J303	259	$192 \cdot 64^3$	0.119(17)	2.777(26)
H105	281	$96 \cdot 32^3$	0.094(17)	2.665(24)					
N101	281	$128 \cdot 48^3$	0.201(12)	2.757(15)					
S100	214	$128 \cdot 32^3$	0.018(16)	2.578(23)					
C101	222	$96 \cdot 48^3$	0.109(7)	2.684(15)					
D101	222	$128 \cdot 64^3$	0.162(10)	2.683(15)					
D150	127	$128 \cdot 64^3$	-0.078(21)	2.701(35)					

In the usual definition, w (where we drop the index i) is estimated on each configuration:

$$w := \langle e^{-s} \rangle = \int d\mu(s) e^{-s} \approx \frac{1}{n} \sum_j^n e^{-s(j)}, \quad (\text{G.2})$$

where $s(j)$ is the j th estimate of s . $d\mu(s)$ denotes the measure associated with the probability distribution of the random variable s . We define the probability density $p_s(s)$: $d\mu(s) = p_s(s)ds$, $\int ds p_s(s) = 1$. One can easily change the random variable. The substitution $s = f(t)$ implies that $p_s(s) = p_t(t)/|f'(t)|$, i.e. $d\mu(s) = |f'(t)|d\mu(t)$. Ideally, $p_w(w)$ with $s = -\ln w$ would be a Gaussian of width Δw . This would guarantee uniform convergence of the average, with an error $\sigma_w = \Delta w/\sqrt{n-1}$. Clearly, this is not the case for our distribution as $s \geq 0$. So one may anticipate a slow onset of the asymptotic convergence behaviour, in particular, in the cases where w is not close to unity and the variance may be large.

One possibility would be that $p_w(w)$ is log-normal distributed, i.e. that $p_s(s)$ is a Gaussian distribution centred about s_0 , with a width Δs :

$$p_s(s) = \frac{1}{\sqrt{2\pi\Delta s^2}} \exp \left[-\frac{(s-s_0)^2}{2\Delta s^2} \right]. \quad (\text{G.3})$$

It is easy to see that in this case

$$w = \langle e^{-s} \rangle = \exp \left(-s_0 + \frac{\Delta s^2}{2} \right), \quad (\text{G.4})$$

i.e. we could obtain w from the average $s_0 = \langle s \rangle$ and its second moment $\Delta s^2 = \langle (s - s_0)^2 \rangle$. It turns out that also this is not the correct statistical model. Instead, the distribution of s itself appears to be close to log-normal. We demonstrate this for two configurations of ensemble S100 in figure 43, where in the second row we show histograms of $t = \ln s$. To further quantify the approximate log-normality, we compute $t_0 = \langle t \rangle$ and moments $\mu_n = \langle (t - t_0)^n \rangle$ for $n = 2, 3, 4$ ($\mu_1 = 0$ by definition). For a log-normal distribution of s one would expect $\mu_3/\mu_2^{3/2} \approx 0$ and $\mu_4/\mu_2^2 \approx 3$. The averages for some of our ensembles are shown in table 22. Skewness and kurtosis are not universal but somewhat vary between ensembles. However, we are unable to detect any patterns, regarding the pion mass, the volume or the twisted mass parameter (not shown). Mostly the skewness is slightly positive while the kurtosis is a bit smaller than three. While the distributions are not perfectly log-normal, they are close to it.

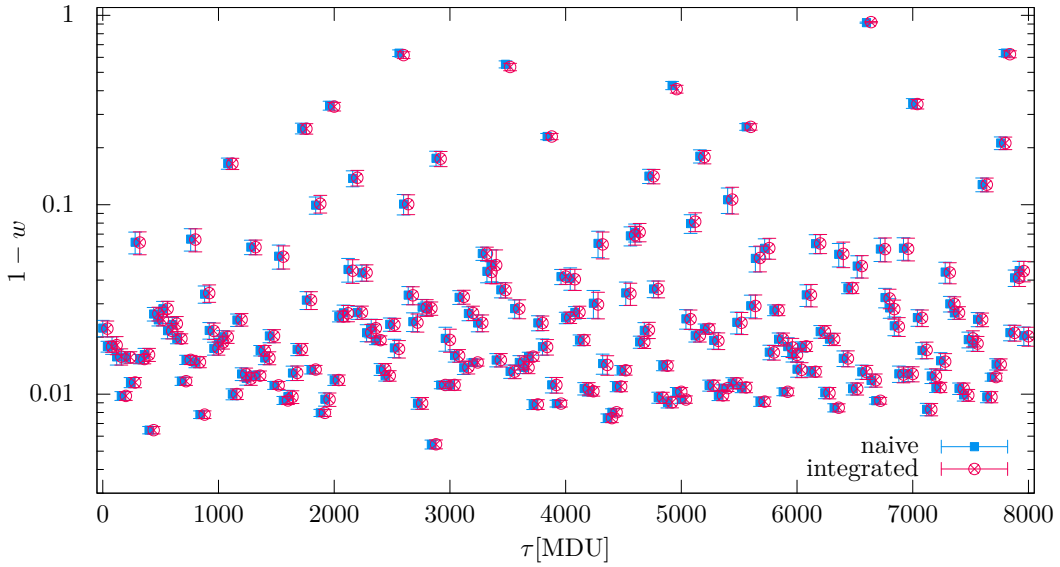


Figure 44. Deviations of the reweighting factors from one for ensemble C101 ($M_\pi \approx 222$ MeV, $a \approx 0.085$ fm), computed using the naive definition, eq. (G.2) and the definition assuming a log-distribution of the estimates, eq. (G.6). The reweighting factors have been computed with the target precision $\sigma_w < 0.01$, as predicted employing a smaller number of estimates. For better readability we shifted the points horizontally and plotted only every 40th MDU.

The approximate log-normality of s suggests to estimate w by computing

$$t_0 \approx \frac{1}{n} \sum_j^n \ln s(j), \quad \Delta t^2 = \mu_2 \approx \frac{1}{n} \sum_j^n [t_0 - \ln s(j)]^2 \quad (\text{G.5})$$

and then numerically integrating

$$\begin{aligned} w &= \frac{1}{\sqrt{2\pi\Delta t^2}} \int_{-\infty}^{\infty} dt \exp \left[-\frac{(t - t_0)^2}{2\Delta t^2} - e^t \right] \\ &\approx \frac{1}{\sqrt{2\pi\Delta t^2}} \int_{-6\Delta t}^{\min(3-t_0, 6\Delta t)} dt \exp \left[-\frac{t^2}{2\Delta t^2} - e^{(t+t_0)} \right]. \end{aligned} \quad (\text{G.6})$$

Note that this exponential integral cannot be solved in closed form. In the last step above, subsequent to the substitution $t - t_0 \mapsto t$, we neglected contributions from the regions $t > 3 - t_0$, which gives a numerical precision better than 10^{-8} . We remark that for $t < -(3 + t_0)$, it is safe to approximate the integrand by a Gaussian.

The error of this improved estimate (which we coin the “integrated” method) is determined by resampling over the stochastic estimates. In figure 44 we compare the results of the two methods for ensemble C101 where a particularly large number of reweighting factors is small. As expected, the two sets of reweighting factors agree within errors. The integrated procedure should be more reliable in terms of the error estimate, in particular, whenever w is close to zero. However, with the increased number of estimates that we employ, only for very few configurations are differences visible between the two definitions on the scale of the figure.

References

- [1] M. Lüscher, *Properties and uses of the Wilson flow in Lattice QCD*, *JHEP* **08** (2010) 071 [Erratum *ibid.* **03** (2014) 092], [[1006.4518](#)].
- [2] M. Bruno, T. Korzec and S. Schaefer, *Setting the scale for the CLS 2 + 1 flavor ensembles*, *Phys. Rev. D* **95** (2017) 074504 [[1608.08900](#)].
- [3] PACS-CS collaboration, S. Aoki et al., *Physical point simulation in 2 + 1 flavor Lattice QCD*, *Phys. Rev. D* **81** (2010) 074503 [[0911.2561](#)].
- [4] S. Capitani, M. Della Morte, G. von Hippel, B. Knippschild and H. Wittig, *Scale setting via the Ω baryon mass*, *PoS LATTICE2011* (2011) 145 [[1110.6365](#)].
- [5] BMW collaboration, S. Borsányi et al., *High-precision scale setting in Lattice QCD*, *JHEP* **09** (2012) 010 [[1203.4469](#)].
- [6] RBC AND UKQCD collaborations, T. Blum et al., *Domain Wall QCD with physical quark masses*, *Phys. Rev. D* **93** (2016) 074505 [[1411.7017](#)].
- [7] HADRON SPECTRUM collaboration, D. J. Wilson, R. A. Briceno, J. J. Dudek, R. G. Edwards and C. E. Thomas, *The quark-mass dependence of elastic πK scattering from QCD*, *Phys. Rev. Lett.* **123** (2019) 042002 [[1904.03188](#)].
- [8] N. Miller et al., *Scale setting the Möbius Domain Wall fermion on gradient-flowed HISQ action using the Ω baryon mass and the gradient-flow scales t_0 and w_0* , *Phys. Rev. D* **103** (2021) 054511 [[2011.12166](#)].
- [9] BMW collaboration, S. Dürer et al., *Ab-initio determination of light hadron masses*, *Science* **322** (2008) 1224 [[0906.3599](#)].
- [10] PACS collaboration, K. I. Ishikawa, N. Ishizuka, Y. Kuramashi, Y. Nakamura, Y. Namekawa, E. Shintani et al., *Finite size effect on vector meson and baryon sectors in 2 + 1 flavor QCD at the physical point*, *Phys. Rev. D* **100** (2019) 094502 [[1907.10846](#)].
- [11] QCDSF collaboration, G. S. Bali et al., *Nucleon mass and sigma term from Lattice QCD with two light fermion flavors*, *Nucl. Phys. B* **866** (2013) 1 [[1206.7034](#)].
- [12] ETM collaboration, C. Alexandrou et al., *Simulating twisted mass fermions at physical light, strange and charm quark masses*, *Phys. Rev. D* **98** (2018) 054518 [[1807.00495](#)].

- [13] QCDSF AND UKQCD collaborations, V. G. Bornyakov et al., *Wilson flow and scale setting from Lattice QCD*, [1508.05916](#).
- [14] HPQCD collaboration, R. J. Dowdall et al., *The Upsilon spectrum and the determination of the lattice spacing from Lattice QCD including charm quarks in the sea*, *Phys. Rev. D* **85** (2012) 054509 [[1110.6887](#)].
- [15] R. J. Dowdall, C. T. H. Davies, G. P. Lepage and C. McNeile, *V_{us} from π and K decay constants in full Lattice QCD with physical u , d , s and c quarks*, *Phys. Rev. D* **88** (2013) 074504 [[1303.1670](#)].
- [16] ETM collaboration, C. Alexandrou et al., *Ratio of kaon and pion leptonic decay constants with $N_f = 2 + 1 + 1$ Wilson-clover twisted-mass fermions*, *Phys. Rev. D* **104** (2021) 074520 [[2104.06747](#)].
- [17] S. Borsanyi, Z. Fodor, C. Hoelbling, S. D. Katz, S. Krieg and K. K. Szabo, *Full result for the QCD equation of state with $2 + 1$ flavors*, *Phys. Lett. B* **730** (2014) 99 [[1309.5258](#)].
- [18] MILC collaboration, A. Bazavov et al., *Gradient flow and scale setting on MILC HISQ ensembles*, *Phys. Rev. D* **93** (2016) 094510 [[1503.02769](#)].
- [19] FERMILAB LATTICE, MILC and TUMQCD collaborations, A. Bazavov et al., *Up-, down-, strange-, charm-, and bottom-quark masses from four-flavor Lattice QCD*, *Phys. Rev. D* **98** (2018) 054517 [[1802.04248](#)].
- [20] CLS community effort, B. Straßberger et al., *Scale setting for CLS $2 + 1$ simulations*, *PoS LATTICE2021* (2022) 135 [[2112.06696](#)].
- [21] N. Carrasco, V. Lubicz, G. Martinelli, C. T. Sachrajda, N. Tantalo, C. Tarantino et al., *QED corrections to hadronic processes in Lattice QCD*, *Phys. Rev. D* **91** (2015) 074506 [[1502.00257](#)].
- [22] V. Lubicz, G. Martinelli, C. T. Sachrajda, F. Sanfilippo, S. Simula and N. Tantalo, *Finite-volume QED corrections to decay amplitudes in Lattice QCD*, *Phys. Rev. D* **95** (2017) 034504 [[1611.08497](#)].
- [23] A. Patella, *QED corrections to hadronic observables*, *PoS LATTICE2016* (2017) 020 [[1702.03857](#)].
- [24] R. Sommer, *Scale setting in Lattice QCD*, *PoS LATTICE2013* (2014) 015 [[1401.3270](#)].
- [25] H. W. Hamber and G. Parisi, *Numerical estimates of hadronic masses in a pure $SU(3)$ gauge theory*, *Phys. Rev. Lett.* **47** (1981) 1792.
- [26] D. Weingarten, *Monte Carlo evaluation of hadron masses in lattice gauge theories with fermions*, *Phys. Lett.* **109B** (1982) 57.
- [27] C. W. Bernard, T. Draper and K. Olynyk, *Hadron mass calculations in QCD*, *Phys. Rev.* **D27** (1983) 227.
- [28] P. de Forcrand, R. Gupta, S. Güsken, K.-H. Mütter, A. Patel, K. Schilling et al., *Exploring hadron masses in Lattice QCD with light quarks and an improved fermion action*, *Phys. Lett. B* **200** (1988) 143.
- [29] APE collaboration, S. Cabbasino et al., *$\beta = 6.0$ quenched Wilson fermions*, *Phys. Lett. B* **258** (1991) 195.
- [30] APE collaboration, M. Guagnelli, M.-P. Lombardo, E. Marinari, G. Parisi and G. Salina,

The quenched mass spectrum in Lattice QCD on a 1-gigaflops computer, *Nucl. Phys. B* **378** (1992) 616.

- [31] M.-P. Lombardo, G. Parisi and A. Vladikas, *Lattice QCD spectroscopy with an improved Wilson fermion action*, *Nucl. Phys. B* **395** (1993) 388 [[hep-lat/9206023](#)].
- [32] UKQCD collaboration, C. R. Allton et al., *Quenched light hadron mass spectrum and decay constants: The effects of $O(a)$ improvement at $\beta = 6.2$* , *Nucl. Phys. B* **407** (1993) 331 [[hep-lat/9307009](#)].
- [33] GF11 collaboration, F. Butler, H. Chen, J. Sexton, A. Vaccarino and D. H. Weingarten, *Hadron masses from the valence approximation to Lattice QCD*, *Nucl. Phys. B* **430** (1994) 179 [[hep-lat/9405003](#)].
- [34] QCD-TARO collaboration, K. Akemi et al., *Quenched Wilson hadron spectroscopy on a $32^3 \times 48$ lattice at $\beta = 6.3$* , *Nucl. Phys. Proc. Suppl.* **34** (1994) 338.
- [35] T. Bhattacharya, R. Gupta, G. Kilcup and S. R. Sharpe, *Hadron spectrum with Wilson fermions*, *Phys. Rev. D* **53** (1996) 6486 [[hep-lat/9512021](#)].
- [36] QCDPAX collaboration, Y. Iwasaki, K. Kanaya, T. Yoshie, T. Hoshino, T. Shirakawa, Y. Oyanagi et al., *Hadron masses and decay constants with Wilson quarks at $\beta = 5.85$ and $\beta = 6$* , *Phys. Rev. D* **53** (1996) 6443 [[hep-lat/9512031](#)].
- [37] C. R. Allton, V. Gimenez, L. Giusti and F. Rapuano, *Light quenched hadron spectrum and decay constants on different lattices*, *Nucl. Phys. B* **489** (1997) 427 [[hep-lat/9611021](#)].
- [38] F. X. Lee and D. B. Leinweber, *Light hadron spectroscopy on coarse lattices with $O(a^2)$ mean field improved actions*, *Phys. Rev. D* **59** (1999) 074504 [[hep-lat/9711044](#)].
- [39] CP-PACS collaboration, S. Aoki et al., *Quenched light hadron spectrum*, *Phys. Rev. Lett.* **84** (2000) 238 [[hep-lat/9904012](#)].
- [40] CP-PACS collaboration, S. Aoki et al., *Light hadron spectrum and quark masses from quenched Lattice QCD*, *Phys. Rev. D* **67** (2003) 034503 [[hep-lat/0206009](#)].
- [41] K. D. Born, E. Laermann, N. Pirsch, T. T. F. Walsh and P. M. Zerwas, *Hadron Properties in Lattice QCD With Dynamical Fermions*, *Phys. Rev. D* **40** (1989) 1653.
- [42] MT_c collaboration, R. Altmeyer, K. D. Born, M. Göckeler, R. Horsley, E. Laermann and G. Schierholz, *The Hadron spectrum in QCD with dynamical staggered fermions*, *Nucl. Phys. B* **389** (1993) 445.
- [43] K. M. Bitar et al., *Hadron spectrum in QCD at $6/g^2 = 5.6$* , *Phys. Rev. D* **42** (1990) 3794.
- [44] K. M. Bitar et al., *Hadron spectrum in QCD with valence Wilson fermions and dynamical staggered fermions at $6/g^2 = 5.6$* , *Phys. Rev. D* **46** (1992) 2169 [[hep-lat/9204008](#)].
- [45] M. Fukugita, N. Ishizuka, H. Mino, M. Okawa and A. Ukawa, *Full QCD hadron spectroscopy with two flavors of dynamical Kogut-Susskind quarks on the lattice*, *Phys. Rev. D* **47** (1993) 4739.
- [46] HEMCGC collaboration, K. M. Bitar et al., *Hadron spectrum and matrix elements in QCD with dynamical Wilson fermions at $6/g^2 = 5.3$* , *Phys. Rev. D* **49** (1994) 3546 [[hep-lat/9309011](#)].
- [47] $T\chi L$ collaboration, N. Eicker et al., *Light and strange hadron spectroscopy with dynamical Wilson fermions*, *Phys. Rev. D* **59** (1999) 014509 [[hep-lat/9806027](#)].

- [48] UKQCD collaboration, C. R. Allton et al., *Light hadron spectroscopy with $O(a)$ improved dynamical fermions*, *Phys. Rev. D* **60** (1999) 034507 [[hep-lat/9808016](#)].
- [49] CP-PACS collaboration, A. Ali Khan et al., *Light hadron spectroscopy with two flavors of dynamical quarks on the lattice*, *Phys. Rev. D* **65** (2002) 054505 [Erratum *ibid.* **67** (2003) 059901], [[hep-lat/0105015](#)].
- [50] JLQCD collaboration, S. Aoki et al., *Light hadron spectroscopy with two flavors of $O(a)$ improved dynamical quarks*, *Phys. Rev. D* **68** (2003) 054502 [[hep-lat/0212039](#)].
- [51] ETM collaboration, C. Alexandrou et al., *Light baryon masses with dynamical twisted mass fermions*, *Phys. Rev. D* **78** (2008) 014509 [[0803.3190](#)].
- [52] ETM collaboration, C. Alexandrou, R. Baron, J. Carbonell, V. Drach, P. Guichon, K. Jansen et al., *Low-lying baryon spectrum with two dynamical twisted mass fermions*, *Phys. Rev. D* **80** (2009) 114503 [[0910.2419](#)].
- [53] A. Chowdhury, A. K. De, S. De Sarkar, A. Harindranath, J. Maiti, S. Mondal et al., *Pion and nucleon in two flavour QCD with unimproved Wilson fermions*, *Nucl. Phys. B* **871** (2013) 82 [[1212.0717](#)].
- [54] BGR collaboration, G. P. Engel, C. B. Lang, D. Mohler and A. Schäfer, *QCD with two light dynamical chirally improved quarks: Baryons*, *Phys. Rev. D* **87** (2013) 074504 [[1301.4318](#)].
- [55] ETM collaboration, C. Alexandrou and C. Kallidonis, *Low-lying baryon masses using $N_f = 2$ twisted mass clover-improved fermions directly at the physical pion mass*, *Phys. Rev. D* **96** (2017) 034511 [[1704.02647](#)].
- [56] MILC collaboration, C. W. Bernard, T. Burch, K. Orginos, D. Toussaint, T. A. DeGrand, C. E. Detar et al., *The QCD spectrum with three quark flavors*, *Phys. Rev. D* **64** (2001) 054506 [[hep-lat/0104002](#)].
- [57] A. Walker-Loud et al., *Light hadron spectroscopy using domain wall valence quarks on an Asqtad sea*, *Phys. Rev. D* **79** (2009) 054502 [[0806.4549](#)].
- [58] PACS-CS collaboration, S. Aoki et al., *2 + 1 flavor Lattice QCD toward the physical point*, *Phys. Rev. D* **79** (2009) 034503 [[0807.1661](#)].
- [59] HADRON SPECTRUM collaboration, H.-W. Lin et al., *First results from 2+1 dynamical quark flavors on an anisotropic lattice: Light-hadron spectroscopy and setting the strange-quark mass*, *Phys. Rev. D* **79** (2009) 034502 [[0810.3588](#)].
- [60] MILC collaboration, A. Bazavov et al., *Nonperturbative QCD simulations with 2+1 flavors of improved staggered quarks*, *Rev. Mod. Phys.* **82** (2010) 1349 [[0903.3598](#)].
- [61] PACS-CS collaboration, K.-I. Ishikawa et al., *$SU(2)$ and $SU(3)$ chiral perturbation theory analyses on baryon masses in 2+1 flavor Lattice QCD*, *Phys. Rev. D* **80** (2009) 054502 [[0905.0962](#)].
- [62] QCDSF AND UKQCD collaborations, W. Bietenholz et al., *Flavour blindness and patterns of flavour symmetry breaking in lattice simulations of up, down and strange quarks*, *Phys. Rev. D* **84** (2011) 054509 [[1102.5300](#)].
- [63] NPLQCD collaboration, S. R. Beane, E. Chang, W. Detmold, H.-W. Lin, T. C. Luu, K. Orginos et al., *High statistics analysis using anisotropic clover lattices: (IV) Volume dependence of light hadron masses*, *Phys. Rev. D* **84** (2011) 014507 [[1104.4101](#)].

- [64] UKQCD AND QCDSF collaborations, R. Horsley, J. Najjar, Y. Nakamura, D. Pleiter, P. E. L. Rakow, G. Schierholz et al., *Isospin breaking in octet baryon mass splittings*, *Phys. Rev. D* **86** (2012) 114511 [[1206.3156](#)].
- [65] OPEN LATTICE Initiative, F. Cuteri, A. S. Francis, P. Fritzsche, G. Pederiva, A. Rago, A. Schindler et al., *Properties, ensembles and hadron spectra with Stabilised Wilson Fermions*, *PoS LATTICE2021* (2022) 118 [[2201.03874](#)].
- [66] ETM collaboration, C. Alexandrou, V. Drach, K. Jansen, C. Kallidonis and G. Koutsou, *Baryon spectrum with $N_f = 2 + 1 + 1$ twisted mass fermions*, *Phys. Rev. D* **90** (2014) 074501 [[1406.4310](#)].
- [67] N. Miller et al., *The hyperon spectrum from Lattice QCD*, *PoS LATTICE2021* (2022) 448 [[2201.01343](#)].
- [68] BMW collaboration, S. Borsányi et al., *Isospin splittings in the light baryon octet from Lattice QCD and QED*, *Phys. Rev. Lett.* **111** (2013) 252001 [[1306.2287](#)].
- [69] BMW collaboration, S. Borsányi et al., *Ab initio calculation of the neutron-proton mass difference*, *Science* **347** (2015) 1452 [[1406.4088](#)].
- [70] QCDSF AND UKQCD collaborations, R. Horsley et al., *Isospin splittings of meson and baryon masses from three-flavor Lattice QCD + QED*, *J. Phys.* **G43** (2016) 10LT02 [[1508.06401](#)].
- [71] ALPHA collaboration, M. Bruno, J. Finkenrath, F. Knechtli, B. Leder and R. Sommer, *Effects of heavy sea quarks at low energies*, *Phys. Rev. Lett.* **114** (2015) 102001 [[1410.8374](#)].
- [72] ALPHA collaboration, A. Athenodorou, J. Finkenrath, F. Knechtli, T. Korzec, B. Leder, M. Krstić Marinković et al., *How perturbative are heavy sea quarks?*, *Nucl. Phys. B* **943** (2019) 114612 [[1809.03383](#)].
- [73] N. Husung, P. Marquard and R. Sommer, *Asymptotic behavior of cutoff effects in Yang–Mills theory and in Wilson’s Lattice QCD*, *Eur. Phys. J. C* **80** (2020) 200 [[1912.08498](#)].
- [74] RBC AND UKQCD collaborations, Y. Aoki et al., *Continuum limit physics from $2 + 1$ flavor Domain Wall QCD*, *Phys. Rev. D* **83** (2011) 074508 [[1011.0892](#)].
- [75] S. Aoki et al., *$1 + 1 + 1$ flavor QCD + QED simulation at the physical point*, *Phys. Rev. D* **86** (2012) 034507 [[1205.2961](#)].
- [76] J. Finkenrath, F. Knechtli and B. Leder, *One flavor mass reweighting in Lattice QCD*, *Nucl. Phys. B* **877** (2013) 441–456 [Erratum *ibid.* **880** (2014) 574], [[1306.3962](#)].
- [77] QCDSF AND UKQCD collaborations, W. Bietenholz et al., *Tuning the strange quark mass in lattice simulations*, *Phys. Lett. B* **690** (2010) 436 [[1003.1114](#)].
- [78] CLS community effort, M. Bruno et al., *Simulation of QCD with $N_f = 2 + 1$ flavors of non-perturbatively improved Wilson fermions*, *JHEP* **02** (2015) 043 [[1411.3982](#)].
- [79] RQCD collaboration, G. S. Bali, E. E. Scholz, J. Simeth and W. Söldner, *Lattice simulations with $N_f = 2 + 1$ improved Wilson fermions at a fixed strange quark mass*, *Phys. Rev. D* **94** (2016) 074501 [[1606.09039](#)].
- [80] ALPHA collaboration, S. Schaefer, R. Sommer and F. Viotto, *Critical slowing down and error analysis in Lattice QCD simulations*, *Nucl. Phys. B* **845** (2011) 93 [[1009.5228](#)].
- [81] M. Lüscher and S. Schaefer, *Lattice QCD without topology barriers*, *JHEP* **07** (2011) 036 [[1105.4749](#)].

- [82] B. Sheikholeslami and R. Wohlert, *Improved continuum limit lattice action for QCD with Wilson fermions*, *Nucl. Phys. B* **259** (1985) 572.
- [83] J. Bulava and S. Schaefer, *Improvement of $N_f = 3$ Lattice QCD with Wilson fermions and tree-level improved gauge action*, *Nucl. Phys. B* **874** (2013) 188 [[1304.7093](#)].
- [84] P. Weisz, *Continuum limit improved lattice action for pure Yang-Mills theory. 1.*, *Nucl. Phys. B* **212** (1983) 1.
- [85] Y. Nakamura and H. Stüben, *BQCD - Berlin quantum chromodynamics program*, *PoS LATTICE2010* (2010) 040 [[1011.0199](#)].
- [86] J. Bulava, M. Della Morte, J. Heitger and C. Wittemeier, *Nonperturbative renormalization of the axial current in $N_f = 3$ Lattice QCD with Wilson fermions and a tree-level improved gauge action*, *Phys. Rev. D* **93** (2016) 114513 [[1604.05827](#)].
- [87] ALPHA collaboration, I. Campos, P. Fritzsche, C. Pena, D. Preti, A. Ramos and A. Vladikas, *Non-perturbative quark mass renormalisation and running in $N_f = 3$ QCD*, *Eur. Phys. J. C* **78** (2018) 387 [[1802.05243](#)].
- [88] P. Korcyl and G. S. Bali, *Non-perturbative determination of improvement coefficients using coordinate space correlators in $N_f = 2 + 1$ Lattice QCD*, *Phys. Rev. D* **95** (2017) 014505 [[1607.07090](#)].
- [89] M. Lüscher and S. Schaefer, *Lattice QCD with open boundary conditions and twisted-mass reweighting*, *Comput. Phys. Commun.* **184** (2013) 519 [[1206.2809](#)].
- [90] K. Jansen, C. Liu, M. Lüscher, H. Simma, S. Sint, R. Sommer et al., *Nonperturbative renormalization of Lattice QCD at all scales*, *Phys. Lett. B* **372** (1996) 275 [[hep-lat/9512009](#)].
- [91] M. Lüscher, S. Sint, R. Sommer and P. Weisz, *Chiral symmetry and $O(a)$ improvement in Lattice QCD*, *Nucl. Phys. B* **478** (1996) 365 [[hep-lat/9605038](#)].
- [92] T. Bhattacharya, R. Gupta, W. Lee, S. R. Sharpe and J. M. S. Wu, *Improved bilinears in Lattice QCD with non-degenerate quarks*, *Phys. Rev. D* **73** (2006) 034504 [[hep-lat/0511014](#)].
- [93] G. S. Bali, K. G. Chetyrkin, P. Korcyl and J. Simeth, *Non-perturbative determination of quark-mass independent improvement coefficients in $n_f = 2 + 1$ Lattice QCD, in preparation* (2023) .
- [94] Y. Taniguchi and A. Ukawa, *Perturbative calculation of improvement coefficients to $O(g^2a)$ for bilinear quark operators in Lattice QCD*, *Phys. Rev. D* **58** (1998) 114503 [[hep-lat/9806015](#)].
- [95] M. Constantinou, R. Horsley, H. Panagopoulos, H. Perlt, P. E. L. Rakow, G. Schierholz et al., *Renormalization of local quark-bilinear operators for $N_f = 3$ flavors of stout link nonperturbative clover fermions*, *Phys. Rev. D* **91** (2015) 014502 [[1408.6047](#)].
- [96] J. Heitger, F. Joswig, P. L. J. Petrak and A. Vladikas, *Ratio of flavour non-singlet and singlet scalar density renormalisation parameters in $N_f = 3$ QCD with Wilson quarks*, *Eur. Phys. J. C* **81** (2021) 606 [[2101.10969](#)].
- [97] ALPHA collaboration, G. M. de Divitiis, P. Fritzsche, J. Heitger, C. C. Köster, S. Kuberski and A. Vladikas, *Non-perturbative determination of improvement coefficients b_m and $b_A - b_P$ and normalisation factor $Z_m Z_P / Z_A$ with $N_f = 3$ Wilson fermions*, *Eur. Phys. J. C* **79** (2019) 797 [[1906.03445](#)].

- [98] G. S. Bali, S. Bürger, S. Collins, M. Göckeler, M. Gruber, S. Piemonte et al., *Nonperturbative renormalization in Lattice QCD with three flavors of clover fermions: Using periodic and open boundary conditions*, *Phys. Rev. D* **103** (2021) 094511 [Erratum *ibid.* **107** (2023) 039901], [[2012.06284](#)].
- [99] M. Constantinou, M. Hadjiantonis, H. Panagopoulos and G. Spanoudes, *Singlet versus nonsinglet perturbative renormalization of fermion bilinears*, *Phys. Rev. D* **94** (2016) 114513 [[1610.06744](#)].
- [100] A. Skouroupathis, M. Constantinou and H. Panagopoulos, *Two-loop additive mass renormalization with clover fermions and Symanzik improved gluons*, *Phys. Rev. D* **77** (2008) 014513 [[0801.3146](#)].
- [101] S. Aoki and Y. Kuramashi, *Determination of the improvement coefficient c_{SW} up to one loop order with the conventional perturbation theory*, *Phys. Rev. D* **68** (2003) 094019 [[hep-lat/0306015](#)].
- [102] S. Aoki, R. Frezzotti and P. Weisz, *Computation of the improvement coefficient c_{SW} to one loop with improved gluon actions*, *Nucl. Phys. B* **540** (1999) 501 [[hep-lat/9808007](#)].
- [103] O. Bär and M. Golterman, *Chiral perturbation theory for gradient flow observables*, *Phys. Rev. D* **89** (2014) 034505 [Erratum *ibid.* **89** (2014) 099905], [[1312.4999](#)].
- [104] ALPHA collaboration, M. Bruno, M. Dalla Brida, P. Fritzsch, T. Korzec, A. Ramos, S. Schaefer et al., *The Λ -parameter in 3-flavour QCD and $\alpha_s(m_Z)$ by the ALPHA collaboration*, *PoS LATTICE2016* (2016) 197 [[1701.03075](#)].
- [105] A. Skouroupathis and H. Panagopoulos, *Λ -parameter of Lattice QCD with Symanzik improved gluon actions*, *Phys. Rev. D* **76** (2007) 114514 [[0709.3239](#)].
- [106] ALPHA collaboration, M. Bruno, M. Dalla Brida, P. Fritzsch, T. Korzec, A. Ramos, S. Schaefer et al., *QCD Coupling from a nonperturbative determination of the three-flavor Λ parameter*, *Phys. Rev. Lett.* **119** (2017) 102001 [[1706.03821](#)].
- [107] RQCD collaboration, G. S. Bali, S. Collins, W. Söldner and S. Weishäupl, *Leading order mesonic and baryonic $SU(3)$ low energy constants from $N_f = 3$ Lattice QCD*, *Phys. Rev. D* **105** (2022) 054516 [[2201.05591](#)].
- [108] N. Husung, P. Marquard and R. Sommer, *The asymptotic approach to the continuum of Lattice QCD spectral observables*, *Phys. Lett. B* **829** (2022) 137069 [[2111.02347](#)].
- [109] FLAVOUR LATTICE AVERAGING GROUP, Y. Aoki et al., *FLAG Review 2021*, *Eur. Phys. J. C* **82** (2022) 869 [[2111.09849](#)].
- [110] J. Gasser and H. Leutwyler, *Light quarks at low temperatures*, *Phys. Lett. B* **184** (1987) 83.
- [111] J. Gasser and H. Leutwyler, *Spontaneously broken symmetries: Effective Lagrangians at finite volume*, *Nucl. Phys. B* **307** (1988) 763.
- [112] J. Bijnens and T. Rössler, *Finite volume at two-loops in chiral perturbation theory*, *JHEP* **01** (2015) 034 [[1411.6384](#)].
- [113] M. Gell-Mann, *Symmetries of baryons and mesons*, *Phys. Rev.* **125** (1962) 1067.
- [114] S. Okubo, *Note on unitary symmetry in strong interactions*, *Prog. Theor. Phys.* **27** (1962) 949.
- [115] E. E. Jenkins and A. V. Manohar, *Baryon chiral perturbation theory using a heavy fermion Lagrangian*, *Phys. Lett. B* **255** (1991) 558.

- [116] J. Gegelia and G. S. Japaridze, *Matching heavy particle approach to relativistic theory*, *Phys. Rev. D* **60** (1999) 114038 [[hep-ph/9908377](#)].
- [117] T. Fuchs, J. Gegelia, G. S. Japaridze and S. Scherer, *Renormalization of relativistic baryon chiral perturbation theory and power counting*, *Phys. Rev. D* **68** (2003) 056005 [[hep-ph/0302117](#)].
- [118] B. C. Lehnhart, J. Gegelia and S. Scherer, *Baryon masses and nucleon sigma terms in manifestly Lorentz-invariant baryon chiral perturbation theory*, *J. Phys.* **G31** (2005) 89 [[hep-ph/0412092](#)].
- [119] L. Geng, *Recent developments in $SU(3)$ covariant baryon chiral perturbation theory*, *Front. Phys. (Beijing)* **8** (2013) 328 [[1301.6815](#)].
- [120] P. J. Ellis and K. Torikoshi, *Baryon masses in chiral perturbation theory with infrared regularization*, *Phys. Rev. C* **61** (2000) 015205 [[nucl-th/9904017](#)].
- [121] J. Gasser, M. E. Sainio and A. Švarc, *Nucleons with chiral loops*, *Nucl. Phys. B* **307** (1988) 779.
- [122] V. Bernard, N. Kaiser, J. Kambor and U.-G. Meißner, *Chiral structure of the nucleon*, *Nucl. Phys. B* **388** (1992) 315.
- [123] X.-L. Ren, L.-S. Geng, J. Martin Camalich, J. Meng and H. Toki, *Octet baryon masses in next-to-next-to-next-to-leading order covariant baryon chiral perturbation theory*, *JHEP* **12** (2012) 073 [[1209.3641](#)].
- [124] B. C. Tiburzi and A. Walker-Loud, *Decuplet baryon masses in partially quenched chiral perturbation theory*, *Nucl. Phys. A* **748** (2005) 513 [[hep-lat/0407030](#)].
- [125] V. Bernard, T. R. Hemmert and U.-G. Meißner, *Chiral extrapolations and the covariant small scale expansion*, *Phys. Lett. B* **622** (2005) 141 [[hep-lat/0503022](#)].
- [126] J. Martin Camalich, L.-S. Geng and M. J. Vicente Vacas, *The lowest-lying baryon masses in covariant $SU(3)$ -flavor chiral perturbation theory*, *Phys. Rev. D* **82** (2010) 074504 [[1003.1929](#)].
- [127] X.-L. Ren, L.-S. Geng and J. Meng, *Decuplet baryon masses in covariant baryon chiral perturbation theory*, *Phys. Rev. D* **89** (2014) 054034 [[1307.1896](#)].
- [128] T. R. Hemmert, B. R. Holstein and J. Kambor, *Chiral Lagrangians and $\Delta(1232)$ interactions: formalism*, *J. Phys.* **G24** (1998) 1831 [[hep-ph/9712496](#)].
- [129] M. Procura, B. U. Musch, T. Wollenweber, T. R. Hemmert and W. Weise, *Nucleon mass: From Lattice QCD to the chiral limit*, *Phys. Rev. D* **73** (2006) 114510 [[hep-lat/0603001](#)].
- [130] B. C. Tiburzi and A. Walker-Loud, *Strong isospin breaking in the Nucleon and Delta masses on the lattice*, *Nucl. Phys. A* **764** (2006) 274 [[hep-lat/0501018](#)].
- [131] V. Pascalutsa and M. Vanderhaeghen, *The nucleon and Δ -resonance masses in relativistic chiral effective-field theory*, *Phys. Lett. B* **636** (2006) 31 [[hep-ph/0511261](#)].
- [132] E. E. Jenkins and A. V. Manohar, *Chiral corrections to the baryon axial currents*, *Phys. Lett. B* **259** (1991) 353.
- [133] A. Walker-Loud, *Octet baryon masses in partially quenched chiral perturbation theory*, *Nucl. Phys. A* **747** (2005) 476 [[hep-lat/0405007](#)].
- [134] S. R. Beane, *Nucleon masses and magnetic moments in a finite volume*, *Phys. Rev. D* **70** (2004) 034507 [[hep-lat/0403015](#)].

- [135] V. Bernard, U.-G. Meißner and A. Rusetsky, *The Δ -resonance in a finite volume*, *Nucl. Phys. B* **788** (2008) 1 [[hep-lat/0702012](#)].
- [136] H. Akaike, *Information theory and an extension of the maximum likelihood principle*, in *2nd International Symposium on Information Theory, Tsahkadsor, Armenia, USSR, September 2–8, 1971*, eds. B.N. Petrov, F. Csáki, Akadémiai Kiadó, Budapest (1973) 267; reprinted in *Selected Papers of Hirotugu Akaike. Springer Series in Statistics (Perspectives in Statistics)*, eds. E. Parzen et al., Springer, New York (1998) 199–213.
- [137] BMW collaboration, S. Borsanyi et al., *Leading hadronic contribution to the muon magnetic moment from Lattice QCD*, *Nature* **593** (2021) 51–55 [[2002.12347](#)].
- [138] W. I. Jay and E. T. Neil, *Bayesian model averaging for analysis of lattice field theory results*, *Phys. Rev. D* **103** (2021) 114502 [[2008.01069](#)].
- [139] P. E. Shanahan, A. W. Thomas and R. D. Young, *Sigma terms from an $SU(3)$ chiral extrapolation*, *Phys. Rev. D* **87** (2013) 074503 [[1205.5365](#)].
- [140] BMW collaboration, S. Dürr et al., *Lattice computation of the nucleon scalar quark contents at the physical point*, *Phys. Rev. Lett.* **116** (2016) 172001 [[1510.08013](#)].
- [141] M. F. M. Lutz, R. Bavontaweepanya, C. Kobdaj and K. Schwarz, *Finite volume effects in the chiral extrapolation of baryon masses*, *Phys. Rev. D* **90** (2014) 054505 [[1401.7805](#)].
- [142] M. F. M. Lutz, Y. Heo and X.-Y. Guo, *On the convergence of the chiral expansion for the baryon ground-state masses*, *Nucl. Phys. A* **977** (2018) 146 [[1801.06417](#)].
- [143] P. L. J. Petrak, G. Bali, S. Collins, J. Heitger, D. Jenkins, S. Weishäupl et al., *Towards the determination of sigma terms for the baryon octet on $N_f = 2 + 1$ CLS ensembles*, *PoS LATTICE2021* (2022) 072 [[2112.00586](#)].
- [144] R. F. Dashen and A. V. Manohar, *$1/N_c$ corrections to the baryon axial currents in QCD*, *Phys. Lett. B* **315** (1993) 438–440 [[hep-ph/9307242](#)].
- [145] PARTICLE DATA GROUP, R. L. Workman, *Review of Particle Physics*, *PTEP* **2022** (2022) 083C01.
- [146] M. Hoferichter, J. Ruiz de Elvira, B. Kubis and U.-G. Meißner, *Roy–Steiner-equation analysis of pion–nucleon scattering*, *Phys. Rept.* **625** (2016) 1–88 [[1510.06039](#)].
- [147] M. Hoferichter, J. Ruiz de Elvira, B. Kubis and U.-G. Meißner, *High-Precision determination of the pion-nucleon σ term from Roy–Steiner equations*, *Phys. Rev. Lett.* **115** (2015) 092301 [[1506.04142](#)].
- [148] Y.-B. Yang, J. Liang, Y.-J. Bi, Y. Chen, T. Draper, K.-F. Liu et al., *Proton mass decomposition from the QCD energy momentum tensor*, *Phys. Rev. Lett.* **121** (2018) 212001 [[1808.08677](#)].
- [149] PNDME collaboration, Y.-C. Jang, R. Gupta, H.-W. Lin, B. Yoon and T. Bhattacharya, *Nucleon electromagnetic form factors in the continuum limit from $(2 + 1 + 1)$ -flavor lattice QCD*, *Phys. Rev. D* **101** (2020) 014507 [[1906.07217](#)].
- [150] MILC collaboration, A. Bazavov et al., *Lattice QCD ensembles with four flavors of highly improved staggered quarks*, *Phys. Rev. D* **87** (2013) 054505 [[1212.4768](#)].
- [151] Y. Lin, A. S. Meyer, C. Hughes, A. S. Kronfeld, J. N. Simone and A. Strelchenko, *Nucleon mass with highly improved staggered quarks*, *Phys. Rev. D* **103** (2021) 034501 [[1911.12256](#)].

- [152] FERMILAB LATTICE, HPQCD and MILC collaborations, C. T. H. Davies et al., *Hadronic-vacuum-polarization contribution to the muon's anomalous magnetic moment from four-flavor lattice QCD*, *Phys. Rev. D* **101** (2020) 034512 [[1902.04223](#)].
- [153] K. Ottnad, D. Djukanovic, H. B. Meyer, G. von Hippel and H. Wittig, *Mass and isovector matrix elements of the nucleon at zero-momentum transfer*, *PoS LATTICE2022* (2023) 117 [[2212.09940](#)].
- [154] Y.-H. Chen, D.-L. Yao and H. Q. Zheng, *Analyses of pion-nucleon elastic scattering amplitudes up to $O(p^4)$ in extended-on-mass-shell subtraction scheme*, *Phys. Rev. D* **87** (2013) 054019 [[1212.1893](#)].
- [155] J. Ruiz de Elvira, M. Hoferichter, B. Kubis and U.-G. Meißner, *Extracting the σ -term from low-energy pion-nucleon scattering*, *J. Phys. G* **45** (2018) 024001 [[1706.01465](#)].
- [156] ETM collaboration, A. Abdel-Rehim, C. Alexandrou, M. Constantinou, K. Hadjiyiannakou, K. Jansen, C. Kallidonis et al., *Direct evaluation of the quark content of nucleons from Lattice QCD at the physical point*, *Phys. Rev. Lett.* **116** (2016) 252001 [[1601.01624](#)].
- [157] RQCD collaboration, G. S. Bali, S. Collins, D. Richtmann, A. Schäfer, W. Söldner and A. Sternbeck, *Direct determinations of the nucleon and pion σ terms at nearly physical quark masses*, *Phys. Rev. D* **93** (2016) 094504 [[1603.00827](#)].
- [158] χ QCD collaboration, Y.-B. Yang, A. Alexandru, T. Draper, J. Liang and K.-F. Liu, *πN and strangeness sigma terms at the physical point with chiral fermions*, *Phys. Rev. D* **94** (2016) 054503 [[1511.09089](#)].
- [159] JLQCD collaboration, N. Yamanaka, S. Hashimoto, T. Kaneko and H. Ohki, *Nucleon charges with dynamical overlap fermions*, *Phys. Rev. D* **98** (2018) 054516 [[1805.10507](#)].
- [160] A. Agadjanov, D. Djukanovic, G. von Hippel, H. B. Meyer, K. Ottnad and H. Wittig, *The nucleon sigma terms with $N_f = 2 + 1$ $O(a)$ -improved Wilson fermions*, [2303.08741](#).
- [161] ETM collaboration, C. Alexandrou, S. Bacchio, M. Constantinou, J. Finkenrath, K. Hadjiyiannakou, K. Jansen et al., *Nucleon axial, tensor, and scalar charges and σ -terms in Lattice QCD*, *Phys. Rev. D* **102** (2020) 054517 [[1909.00485](#)].
- [162] BMW collaboration, S. Borsanyi, Z. Fodor, C. Hoelbling, L. Lellouch, K. K. Szabo, C. Torrero et al., *Ab-initio calculation of the proton and the neutron's scalar couplings for new physics searches*, [2007.03319](#).
- [163] R. Gupta, S. Park, M. Hoferichter, E. Mereghetti, B. Yoon and T. Bhattacharya, *The pion-nucleon sigma term from Lattice QCD*, *Phys. Rev. Lett.* **127** (2021) 242002 [[2105.12095](#)].
- [164] M. F. M. Lutz, Y. Heo and X.-Y. Guo, *Low-energy constants in the chiral Lagrangian with baryon octet and decuplet fields from Lattice QCD data on CLS ensembles*, [2301.06837](#).
- [165] M. Göckeler, R. Horsley, M. Lage, U. G. Meißner, P. E. L. Rakow, A. Rusetsky et al., *Scattering phases for meson and baryon resonances on general moving-frame lattices*, *Phys. Rev. D* **86** (2012) 094513 [[1206.4141](#)].
- [166] W. Detmold and A. Nicholson, *Low energy scattering phase shifts for meson-baryon systems*, *Phys. Rev. D* **93** (2016) 114511 [[1511.02275](#)].
- [167] C. W. Andersen, J. Bulava, B. Hörz and C. Morningstar, *Elastic $I = 3/2$ p -wave nucleon-pion scattering amplitude and the $\Delta(1232)$ resonance from $N_f = 2 + 1$ Lattice QCD*, *Phys. Rev. D* **97** (2018) 014506 [[1710.01557](#)].

- [168] G. Silvi et al., *P-wave nucleon-pion scattering amplitude in the $\Delta(1232)$ channel from Lattice QCD*, *Phys. Rev. D* **103** (2021) 094508 [[2101.00689](#)].
- [169] CLS collaboration, D. Mohler, S. Schaefer and J. Simeth, *CLS 2 + 1 flavor simulations at physical light- and strange-quark masses*, *EPJ Web Conf.* **175** (2018) 02010 [[1712.04884](#)].
- [170] G. S. Bali, S. Collins, P. Korcyl, R. Rödl, S. Weishäupl and T. Wurm, *Hyperon couplings from $N_f = 2 + 1$ Lattice QCD*, *PoS LATTICE2019* (2019) 099 [[1907.13454](#)].
- [171] RQCD collaboration, G. S. Bali, L. Barca, S. Collins, M. Gruber, M. Löffler, A. Schäfer et al., *Nucleon axial structure from Lattice QCD*, *JHEP* **05** (2020) 126 [[1911.13150](#)].
- [172] Jülich Supercomputing Centre, *JUWELS: Modular Tier-0/1 Supercomputer at the Jülich Supercomputing Centre*, *J. of large-scale research facilities* **5** (2019) A135.
- [173] Jülich Supercomputing Centre, *JURECA: Modular supercomputer at Jülich Supercomputing Centre*, *J. of large-scale research facilities* **4** (2018) A132.
- [174] P. Arts et al., *QPACE 2 and Domain Decomposition on the Intel Xeon Phi*, *PoS LATTICE2014* (2015) 021 [[1502.04025](#)].
- [175] Jülich Supercomputing Centre, *HDF Cloud – Helmholtz Data Federation cloud resources at the Jülich Supercomputing Centre*, *J. of large-scale research facilities* **5** (2019) A137.
- [176] SCIDAC, LHP AND UKQCD collaborations, R. G. Edwards and B. Joó, *The Chroma software system for Lattice QCD*, *Nucl. Phys. B Proc. Suppl.* **140** (2005) 832 [[hep-lat/0409003](#)].
- [177] S. Heybrock, M. Rottmann, P. Georg and T. Wettig, *Adaptive algebraic multigrid on SIMD architectures*, *PoS LATTICE2015* (2016) 036 [[1512.04506](#)].
- [178] P. Georg, D. Richtmann and T. Wettig, *DD- α AMG on QPACE 3*, *EPJ Web Conf.* **175** (2018) 02007 [[1710.07041](#)].
- [179] A. Frommer, K. Kahl, S. Krieg, B. Leder and M. Rottmann, *Adaptive aggregation based Domain Decomposition Multigrid for the lattice Wilson Dirac operator*, *SIAM J. Sci. Comput.* **36** (2014) A1581 [[1303.1377](#)].
- [180] M. Lüscher, *Deflation acceleration of Lattice QCD simulations*, *JHEP* **12** (2007) 011 [[0710.5417](#)].
- [181] J. Bijnens, *Violations of Dashen’s theorem*, *Phys. Lett. B* **306** (1993) 343 [[hep-ph/9302217](#)].
- [182] B. Moussallam, *A sum rule approach to the violation of Dashen’s theorem*, *Nucl. Phys. B* **504** (1997) 381 [[hep-ph/9701400](#)].
- [183] J. Gasser, A. Rusetsky and I. Scimemi, *Electromagnetic corrections in hadronic processes*, *Eur. Phys. J.* **C32** (2003) 97 [[hep-ph/0305260](#)].
- [184] FLAVOUR LATTICE AVERAGING GROUP, S. Aoki et al., *Review of lattice results concerning low-energy particle physics*, *Eur. Phys. J.* **C77** (2017) 112 [[1607.00299](#)].
- [185] S. R. Coleman and S. L. Glashow, *Electrodynamical properties of baryons in the unitary symmetry scheme*, *Phys. Rev. Lett.* **6** (1961) 423.
- [186] R. F. Dashen, *Chiral $SU(3) \times SU(3)$ as a symmetry of the strong interactions*, *Phys. Rev.* **183** (1969) 1245.
- [187] QCDSF AND UKQCD collaborations, R. Horsley, J. Najjar, Y. Nakamura, H. Perlt,

- D. Pleiter, P. E. L. Rakow et al., *Lattice determination of Σ - Λ mixing*, *Phys. Rev. D* **91** (2015) 074512 [[1411.7665](#)].
- [188] QCDSF AND UKQCD collaborations, R. Horsley, J. Najjar, Y. Nakamura, H. Perlt, D. Pleiter, P. E. L. Rakow et al., *Reply to “Comment on ‘Lattice determination of Σ - Λ mixing’”*, *Phys. Rev. D* **92** (2015) 018502 [[1507.07825](#)].
- [189] QCDSF AND UKQCD collaborations, A. Ali Khan et al., *The nucleon mass in $N_f = 2$ Lattice QCD: Finite size effects from chiral perturbation theory*, *Nucl. Phys. B* **689** (2004) 175 [[hep-lat/0312030](#)].
- [190] L.-S. Geng, X.-L. Ren, J. Martin-Camalich and W. Weise, *Finite-volume effects on octet-baryon masses in covariant baryon chiral perturbation theory*, *Phys. Rev. D* **84** (2011) 074024 [[1108.2231](#)].
- [191] W. Detmold and C. D. Lin, *Twist-two matrix elements at finite and infinite volume*, *Phys. Rev. D* **71** (2005) 054510 [[hep-lat/0501007](#)].
- [192] J. Gasser and H. Leutwyler, *Chiral perturbation theory: Expansions in the mass of the strange quark*, *Nucl. Phys. B* **250** (1985) 465.
- [193] A. Meurer, C. P. Smith, M. Paprocki, O. Čertík, S. B. Kirpichev, M. Rocklin et al., *SymPy: symbolic computing in Python*, *PeerJ Computer Science* **3** (2017) e103.
- [194] MILC collaboration, A. Bazavov et al., *Results for light pseudoscalar mesons*, *PoS LATTICE2010* (2010) 074 [[1012.0868](#)].
- [195] RQCD collaboration, G. S. Bali, V. Braun, S. Collins, A. Schäfer and J. Simeth, *Masses and decay constants of the η and η' mesons from Lattice QCD*, *JHEP* **08** (2021) 137 [[2106.05398](#)].
- [196] J. Bijnens and G. Ecker, *Mesonic low-energy constants*, *Ann. Rev. Nucl. Part. Sci.* **64** (2014) 149 [[1405.6488](#)].
- [197] S. Güsken, U. Löw, K. H. Mütter, R. Sommer, A. Patel and K. Schilling, *Nonsinglet axial vector couplings of the baryon octet in Lattice QCD*, *Phys. Lett. B* **227** (1989) 266.
- [198] S. Güsken, *A Study of smearing techniques for hadron correlation functions*, *Nucl. Phys. Proc. Suppl.* **17** (1990) 361.
- [199] APE collaboration, M. Falcioni, M. L. Paciello, G. Parisi and B. Taglienti, *Again on $SU(3)$ glueball mass*, *Nucl. Phys. B* **251** (1985) 624.
- [200] G. S. Bali, B. Lang, B. U. Musch and A. Schäfer, *Novel quark smearing for hadrons with high momenta in Lattice QCD*, *Phys. Rev. D* **93** (2016) 094515 [[1602.05525](#)].
- [201] R. Sommer, *Leptonic decays of B and D mesons*, *Nucl. Phys. Proc. Suppl.* **42** (1995) 186 [[hep-lat/9411024](#)].
- [202] UKQCD collaboration, M. Foster and C. Michael, *Hadrons with a heavy color adjoint particle*, *Phys. Rev. D* **59** (1999) 094509 [[hep-lat/9811010](#)].
- [203] S. Bernardson, P. McCarty and C. Thron, *Monte Carlo methods for estimating linear combinations of inverse matrix entries in Lattice QCD*, *Comput. Phys. Commun.* **78** (1993) 256.
- [204] T χ L collaboration, J. Viehoff, N. Eicker, S. Güsken, H. Hoerber, P. Lacock, T. Lippert et al., *Improving stochastic estimator techniques for disconnected diagrams*, *Nucl. Phys. Proc. Suppl.* **63** (1998) 269 [[hep-lat/9710050](#)].

- [205] UKQCD collaboration, C. McNeile and C. Michael, *Decay width of light quark hybrid meson from the lattice*, *Phys. Rev. D* **73** (2006) 074506 [[hep-lat/0603007](#)].
- [206] ALPHA collaboration, B. Blossier, M. Della Morte, N. Garrón, G. von Hippel, T. Mendes, H. Simma et al., *HQET at order $1/m$: II. Spectroscopy in the quenched approximation*, *JHEP* **05** (2010) 074 [[1004.2661](#)].
- [207] H. W. Hamber, E. Marinari, G. Parisi and C. Rebbi, *Considerations on numerical analysis of QCD*, *Nucl. Phys. B* **225** (1983) 475.
- [208] G. P. Lepage, *The analysis of algorithms for lattice field theory*, in *From actions to answers. Proceedings, Theoretical Advanced Study Institute in Elementary Particle Physics, Boulder, CO, USA, June 5–30, 1989*, eds. T. A. DeGrand and D. Toussaint, World Scientific, Singapore (1990) 97–120.
- [209] M. H. Quenouille, *Approximate tests of correlation in time-series*, *J. of the Royal Statistical Society. Series B (Methodological)* **11** (1949) 68 [<https://www.jstor.org/stable/2983696>].
- [210] M. H. Quenouille, *Notes on bias in estimation*, *Biometrika* **43** (1956) 353.
- [211] B. Efron, *Bootstrap methods: another look at the Jackknife*, *Annals of Statistics* **7** (1979) 1.
- [212] B. Efron, *The Jackknife, the Bootstrap and other resampling plans*. SIAM CBMS-NSF Regional Conference Series in Applied Mathematics (Book 38), Reading, MA, 1982, [10.1137/1.9781611970319](#).
- [213] N. Madras and A. D. Sokal, *The pivot algorithm: A highly efficient Monte Carlo method for selfavoiding walk*, *J. Statist. Phys.* **50** (1988) 109.
- [214] ALPHA collaboration, U. Wolff, *Monte Carlo errors with less errors*, *Comput. Phys. Commun.* **156** (2004) 143 [Erratum *ibid.* **176** (2006) 383], [[hep-lat/0306017](#)].
- [215] A. Ramos, *Automatic differentiation for error analysis of Monte Carlo data*, *Comput. Phys. Commun.* **238** (2019) 195 [[1809.01289](#)].
- [216] J. F. Kenney and E. S. Keeping, *Mathematics of Statistics, Part 2*. D. Van Nostrand Company, 2nd edition, Princeton, NJ, 1951.
- [217] D. R. Barker and L. M. Diana, *Simple method for fitting data when both variables have uncertainties*, *Am. J. Phys.* **42** (1974) 224.
- [218] J. Orear, *Least squares when both variables have uncertainties*, *Am. J. Phys.* **50** (1982) 912 [Erratum *ibid.* **52** (1984) 278].
- [219] S. L. Marshall and J. G. Blencoe, *Generalized least squares fit of multiequation models*, *Am. J. Phys.* **73** (2005) 69.
- [220] D. Mohler and S. Schaefer, *Remarks on strange-quark simulations with Wilson fermions*, *Phys. Rev. D* **102** (2020) 074506 [[2003.13359](#)].